Design, synthesis and characterisation of novel allosteric modulators for the prostaglandin EP_2 receptor.

Constance Dalton, MSc

Thesis submitted to the University of Nottingham for the degree of Doctor of Philosophy

March 2026

Declaration of own work

This thesis is entirely the candidate's own work. The experiments described in this thesis were performed by the author between September 2021 and March 2026 at the University of Nottingham within the Division of Biomolecular Sciences and Medicinal Chemistry, School of Pharmacy, in Nottingham. No part of this material has been previously submitted for a degree or any other qualification at any university.

i) Abstract

The prostaglandin E_2 (PGE_2) receptor subtype 2 (EP_2), a G protein-coupled receptor, is a key mediator of inflammatory response regulating pro-inflammatory cytokine expression and modulation of Th17 cell function. The EP_2 receptor is reportedly upregulated in chronic inflammation and as a result its inhibition is a potential strategy for the treatment of cancer and chronic inflammatory neurodegenerative diseases such as Alzheimer's and Parkinson's. Anti-inflammatory therapeutics, such as non-steroidal anti-inflammatory drugs (NSAIDs), inhibit cyclooxygenase (COX) enzymes upstream of the prostanoid synthesis pathway but are not approved by the Food and Drug Administration (FDA) for treatment of the above diseases due to numerous adverse effects associated with long term use.

(Tetrahydrofuran-2-yl)methyl 2-amino-1-(2,3-dihydrobenzo[b][1,4]dioxin-6-yl)-1*H*-pyrrolo[2,3-b]quinoxaline-3-carboxylate (**25a**) is the first reported EP_2 antagonist with a reversible agonist-dependent allosteric mode of action (Jiang *et al*., 2020). Compound **25a** demonstrated selectivity against other prostanoid receptors: prostaglandin E_2 receptor subtype 4 (EP_4), prostaglandin I_2 receptor (IP) and prostaglandin D_2 receptor subtype 1 (DP_1) and limited structure-activity relationships (SARs) of only fourteen analogues identified the 2,3-dihydrobenzo[*b*][1,4]dioxine motif as essential for EP_2 modulation.

Herein, this thesis reports the design, synthesis and pharmacological characterisation of 33 novel analogues of **25a**, with a focus on modifications at the (tetrahydrofuran-2-yl) methyl ester moiety. From this SAR dataset, numerous analogues demonstrating an improvement in EP_2 binding affinity and functional potency, compared to **25a**, were identified. These parameters were determined utilising NanoBRET competition binding assays for the EP_2 G protein binding site, and NanoBiT complementation assays reporting EP_2 recruitment of beta-arrestin2, respectively. Additionally, these ligands displayed classical allosteric insurmountable antagonism in agonist concentration response curves (CRCs) with decreasing agonist maximal effect proportional to increasing concentrations of our negative allosteric modulators (NAMs). The

development of a new computational model, based on the recently reported cryo-EM structure of EP_2 (protein data base (PDB) 7CX2) which was evaluated using the SAR dataset, is also reported. This model supports that these ligands bind to an intracellular binding pocket on EP_2 which is predicted to sterically block the recruitment of the heterotrimeric $G\alpha_s$ protein and thus inhibit downstream signalling. Overall, the findings presented in this thesis highlight the synthesis and pharmacological characterisation of fourteen novel NAMs of the prostanoid EP_2 receptor and provides an insight into their allosteric mechanism of action.

ii) Acknowledgements

Firstly, I would like to thank my PhD supervisors Dr Shailesh Mistry, Dr Nicholas Holliday and Prof Charles Laughton for all their guidance, support and knowledge they imparted to me throughout the course of my PhD. I have learnt so much under their collective supervision and I have thoroughly enjoyed all the challenges and opportunities that have been provided.

I owe a big thankyou to both Dr James Farmer and Dr Nicola Dijon for all their support in developing and teaching of the pharmacology reported in this thesis. You both taught me a wide range of new skills which encouraged me to pursue a 3-month pharmacology placement as part of my PhD scholarship requirements.

To all the Mistry lab group and C-floor family both past and present, I want to thank you not only for all the chemistry support but for providing such a welcoming, fun, friendly and social environment. Morgan, Rhys and Ziah, thank you for letting me drag you to watch ice hockey every few weeks, your support and friendship has been invaluable to me, and I am grateful to have made some lifelong friends.

Furthermore, I would also like to thank the numerous Masters and Undergraduate students who worked alongside me during this project and contributed a significant amount of chemical synthesis in the development of my compound library.

I must give a special thankyou to my amazing family, specifically my Mum, Dad, grandma Shirley, grandma Beryl and both grandad Ken's. Thank you for putting up with me living at home for four years! I cannot put into words how much your belief in me means, not to mention all the emotional and financial support over the years which is very much appreciated. Though you may not understand a lot of the science, I hope you appreciate that your encouragement has made this thesis possible. Michael, thank you for your continued love and support and for making the effort to check all the grammar in my thesis.

Finally (and most importantly in my opinion), I want to thank all the many emotional support pet chickens I have had over the years. There were many occasions in which a cuddle with Rocky, Star, PB, Poppy, Maple, Cloud and many more got me through challenging times during my PhD and thesis writing.

This work was funded by the UKRI and BBSRC as part of the Nottingham BBSRC Doctoral Training Programme.

iii) List of abbreviations

AA	Arachidonic acid
AD	Alzheimer's disease
AI	Artificial intelligence
ALS	Amyotrophic lateral sclerosis
APP	Amyloid precursor protein
ATP	Adenosine triphosphate
β2AR	β2 adrenergic receptor
BBB	Blood brain barrier
BLAST	Basic local alignment search tool
BRET	Bioluminescence resonance energy transfer
cAMP	5',3'-cyclic adenosine monophosphate
CCR	CC chemokine receptor
CK2	Casein kinase 2
CNS	Central nervous system
COPD	Chronic obstructive pulmonary disease
COX	Cyclooxygenases
CRC	Concentration response curve
Cryo-EM	Cryo-electron microscopy
CREB	cAMP-response element binding protein
CTLA-4	Cytotoxic T-lymphocyte-associated protein 4
CV	Column volumes
CXCR	C-X-C motif chemokine receptor
DBU	Diazabicyclo[5.4.0]undec-7-ene
DCC	*N,N*'-dicyclohexylcarbodiimide
DCM	Dichloromethane
DEAD	Diethyl azodicarboxylate
DGK	Diacylglycerol kinase
DIPEA	*N*,*N*-diisopropylethylamine
DMAP	4-Dimethylaminopyridine
DMF	*N*,*N*-dimethylformamide
DMSO	Dimethyl sulfoxide
DGK	Diacylglycerol kinase
ECL	Extracellular loops
EDC	1-Ethyl-3-(3-dimethylaminopropyl)carbodiimide
EGFR	Epidermal growth factor receptor
EMBL-EBI	EMBL's European bioinformatic institute
EPAC	Exchange proteins regulated by cAMP
ERK	Extracellular signal-regulate kinase
FDA	Food and drug administration
FRET	Förster resonance energy transfer
GDP	Guanosine diphosphate

GI	Gastrointestinal
GPCR	G protein-coupled receptor
GRK	G protein-coupled receptor kinases
GTP	Guanosine triphosphate
HATU	1-[Bis(dimethylamino)methylene]-1*H*-1,2,3-triazolo[4,5-*b*]pyridinium 3-oxid hexafluorophosphate
HBA	Hydrogen bonding acceptor
HBD	Hydrogen bond donor
HBTU	*N,N,N',N'*-tetramethyl-*O*-(1*H*-benzotriazol-1-yl)uronium hexafluorophosphate
HEK	Human embryonic kidney
HPLC	High-performance liquid chromatography
HRMS	High resolution mass spectra
HTRF	Homogeneous time-resolved fluorescence
HTS	High-throughput screening
IAM	Immobilised artificial membrane
IBD	Inflammatory bowel disease
ICL	Intracellular loops
IDF	Induced docking fit
IL	Interleukin
IP3	Inositol 1,4,5-triphosphate
LCMS	Liquid chromatography mass spectrometry
LgBiT	Large BiT, fragment of Nanoluciferase
MAPK	Mitogen-activated kinase
MOM-Cl	Chloromethyl methyl ether
mregDC-Treg	Mature dendritic cell enriched in immunoregulatory molecules regulatory T cell
NAM	Negative allosteric modulator
NF- kB	Nuclear factor kappa-light-chain-enhancer of activated B cells.
NLuc	Nanoluciferase
NMP	*N*-methylpyrrolidone
NMR	Nuclear magnetic resonance
NSAID	Non-steroidal anti-inflammatory drug
NSF	*N*-ethylmaleimide-sensitive fusion protein
OMAN	Operational model of allosterically modulated agonism
PAM	Positive allosteric modulator
PAMP	Pathogen associated molecular patterns
PD	Parkinson’s disease
PDB	Protein database
PD-1	Programmed cell death protein 1
PD-L1	Programmed cell death ligand 1
PDE	Phosphodiesterase

PG	Prostaglandin
PI3K/Akt	Phosphoinositide 3-kinase/protein kinase B
PKA	Protein kinase A
PKC	Protein kinase C
PRR	Pattern recognition receptor
RA	Rheumatoid arthritis
ROS	Reactive oxygen species
SAR	Structure activity relationship
S_NAr	Nucleophilic aromatic substitution
SmBiT	Small BiT, fragment of Nanoluciferase
TBAF	2-(Trimethylsilyl)ethoxycarbonyl]
TBDMS-Cl	Tertbutyldimethylsilyl chloride
Teoc	2-(Trimethylsilyl)ethoxycarbonyl
Th2	T-helper cell type 2
THF	Tetrahydrofuran
TLC	Thin-layer chromatography
TLR	Toll-like receptor
TM	Transmembrane
TMR	Tetramethylrhodamine
TME	Tumour microenvironment
TNF	Tumour necrosis factor
TRAF	TNF receptor associated factor
tsNluc	Thermostable nanoluciferase
TXA_2	Thromboxane A_2
UV	Ultraviolet
3D	Three dimensional

iV) Table of contents

Chapter 1- General Introduction

1.1 Chronic inflammation

1.1.1 An introduction to chronic inflammation

Arguably one of the most important scientific discoveries in recent decades is the identification of inflammation as playing a significant role in both the development and progression of diseases which currently dominate worldwide morbidity and mortality rates[1, 2]. Inflammation is the body's protective response by the immune system to a tissue injury, infectious agent or a foreign body to eliminate the harmful stimulus and begin the healing process. Typically, symptoms of inflammation only last a few days until the injury or infection is healed and the inflammatory process ends (see Figure 1) [3-6]. However, chronic inflammation occurs when an inflammatory response continues past the point of healing or begins when there is no infection/injury. Over time, chronic inflammation can damage healthy cells, tissues and organs and has been identified as a key contributor to disease progression in cardiovascular disease, cancer, diabetes, rheumatoid arthritis (RA), allergic asthma, chronic obstructive pulmonary disease (COPD), Alzheimer's disease (AD), chronic kidney disease and inflammatory bowel disease (IBD) [3, 5, 6]. As a result, chronic inflammatory diseases have been recognised as the most significant cause of mortality worldwide, accounting for more than 50 % of all deaths [7, 8]. Therefore, inhibition of inflammatory pathways utilising small molecule inhibitors could provide therapeutic benefits to patients by both reducing the severity and the progression of these life threatening diseases.

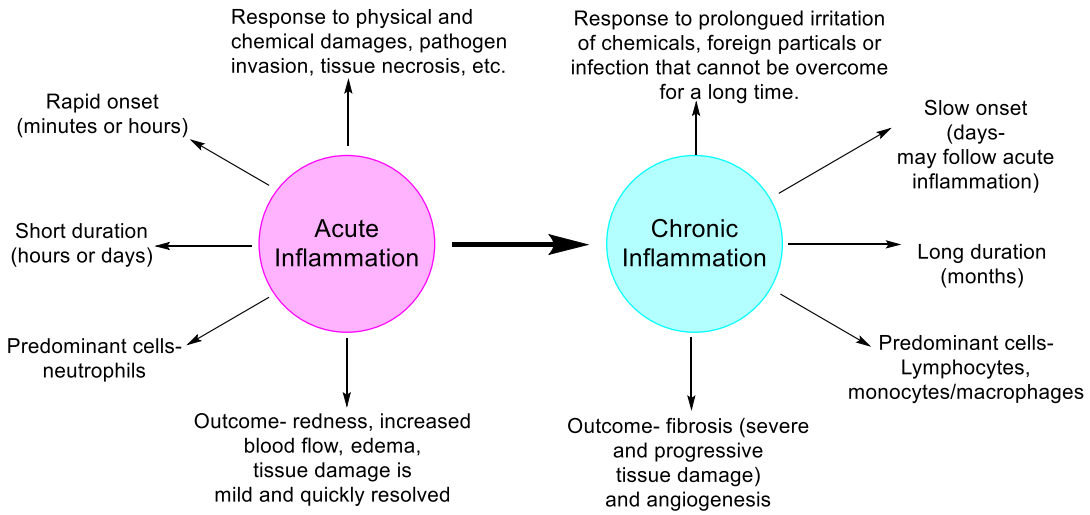

Figure 1- *Hallmarks of acute and chronic inflammation [3-6].*

Numerous causes of chronic inflammation have been identified. For example, these include a failure to eliminate the agent causing acute inflammation (e.g. infectious organisms, foreign material or exposure to low level irritant), autoimmune disorders in which the immune system recognises a normal body component as a foreign antigen and attacks healthy tissue (e.g. RA) and defects in immune cells responsible for mediating inflammation (auto inflammatory disorders e.g. Familial Mediterranean Fever). Additionally, recurrent episodes of acute inflammation and inflammatory or biochemical inducers (e.g. free radicals, uric acid crystals) causing oxidative stress and mitochondrial dysfunction have also been found to cause chronic inflammation [3]. Numerous risk factors are associated with chronic inflammation including old age, obesity, poor diet (rich in saturated fats and processed foods) and smoking. Additionally, low sex hormones, stress and sleep disorders have also be linked to the development of chronic inflammation [3].

Inflammation is a complex biological process and involves both an innate and adaptive immune response to combat harmful stimuli (see Figure 2).

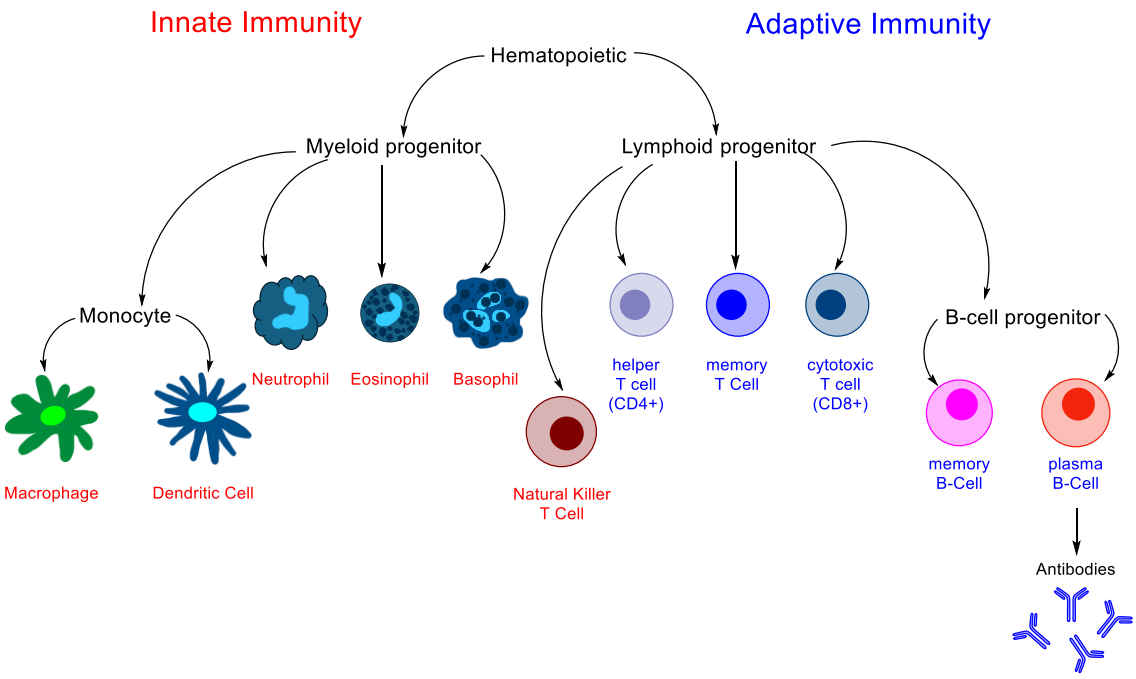

Figure 2- *The innate versus adaptive immune responses and the cells involved. [9]*

The innate immune response is the host's first defence mechanism found in all multicellular organisms. It includes physical barriers such as skin and mucosa as well as effector cells and cytokines [9]. When a pathogen first enters the body, macrophages and dendritic cells recognise specific pathogen associated molecular patterns (PAMPs) present on the pathogen surface via complementary pattern recognition receptors (PRRs) e.g. toll-like receptors (TLRs). This binding triggers the release of cytokines such as interleukin-1 (IL-1) and tumour necrosis factor α (TNF-α). These cytokines induce the injury-site endothelial cells to express selectins and integrins which stimulate the chemotaxis and diapedesis of circulating myeloid cells [3]. As well as releasing cytokines, tissue macrophages and dendritic cells also clear antigens by phagocytosis and serve as antigen presenting cells [9]. Neutrophils are the initial and most prominent myeloid cells to be recruited to the local site of injury during acute inflammation [10]. They contain granules rich with lysozyme, matrix metalloproteinases and myeloperoxidase which are released on the foreign or self-antigen leading to its destruction. Neutrophils also destroy the antigen by phagocytosis, release of reactive oxygen species and produce a wide range of cytokines (both pro-and anti-inflammatory) [11].

The next line of defence, part of the adaptive immune response, involves the activation and recruitment of lymphocytes, including B-cells and T-cells, to the site of injury [3, 12, 13]. B-cells play a crucial role in mediating inflammation; plasma B cells produce antibodies to form immune antigen-antibody complexes neutralizing pathogens and marking them (opsonization) for destruction by cytotoxic T-cells (CD8+). Furthermore, activation of B cells and T cells generates the formation of memory B cells and memory T cells for a more robust immune response on rechallenge of the antigen [14]. Two other types of T-cells are involved in adaptive immunity including helper T cells (CD4+) and regulatory T cells. Helper T cells produce pro-inflammatory cytokines and stimulate B-cells to generate antibodies. Whereas regulatory T cells are responsible for maintaining immune balance, dampening excessive inflammation by suppressing activation, proliferation and effector function of T cells and preventing the immune system from attacking native cells [14]. Additionally, the complement system, classically activated by the formation of antigen-antibody complexes, is another crucial part of the innate immune system response against common pathogens. It is a rapid and non-specific defence involving plasma and membrane associated serum proteins (C-reactive proteins) that activate in a cascade to tag (opsonize), engulf and destroy pathogens directly (lysis) through the assembly of membrane attack complexes [15, 16].

Three key pro-inflammatory cytokines (protein-based mediators) are prevalent during acute and chronic inflammation including IL-1, IL-6 and TNF-α, which work synergistically to mediate the inflammatory response (see Figure 3).

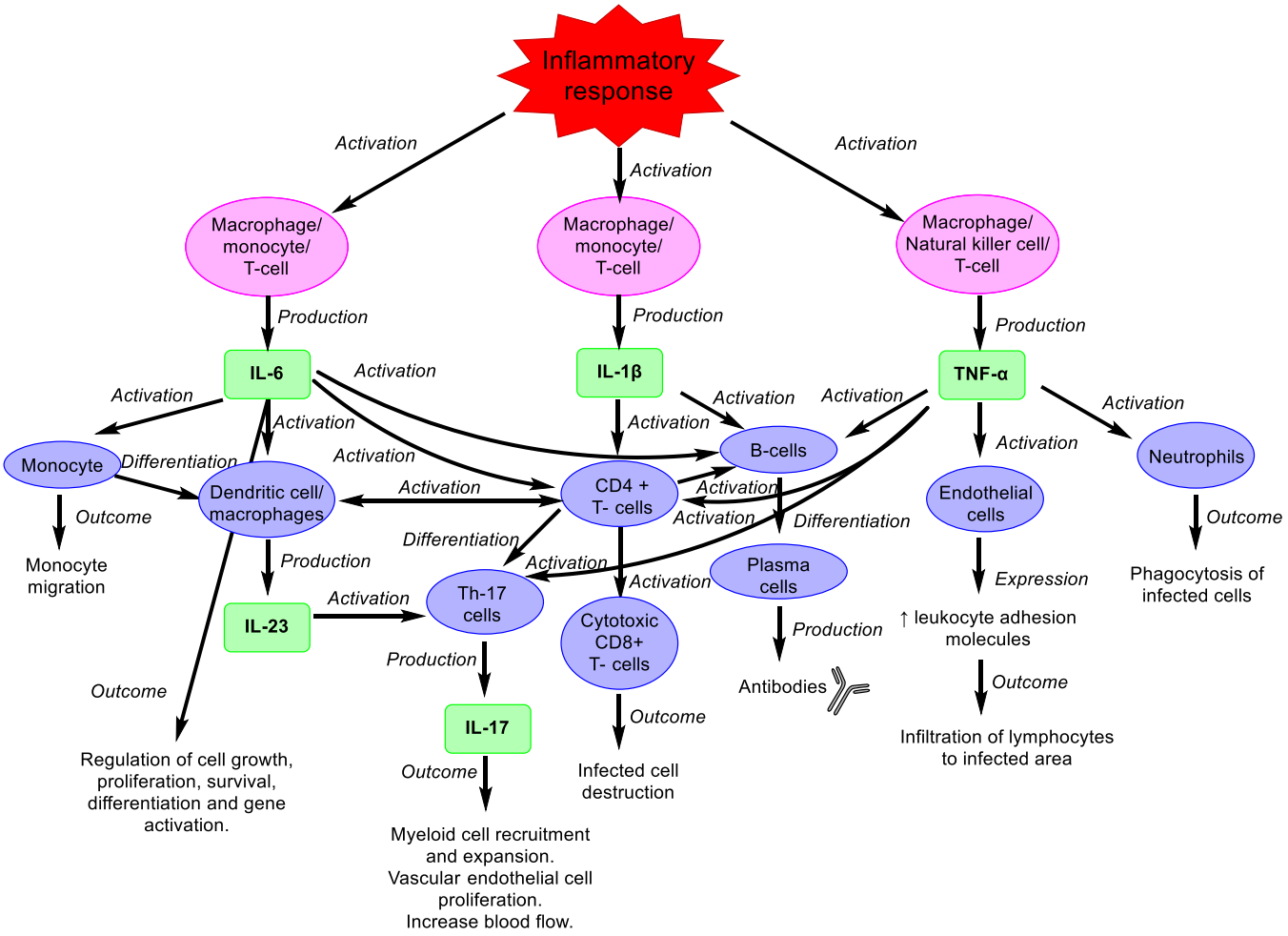

Figure 3- *A summary diagram of the production and signalling of key pro-inflammatory cytokines IL-1β, IL-6 and TNF-α during an inflammatory response. [17-23]*

The cytokine IL-1 can be subdivided into IL-1α, which is constitutively expressed, and IL-1β mainly produced by macrophages, monocytes and T-cells [17]. IL-1β is reported to activate CD4+ T-cells which in turn stimulate infected cell destruction by cytotoxic CD8+ T-cells and the production of antibodies by B-cells. Additionally, IL-1β promotes CD4+ T-cell differentiation into memory T-helper17 (Th17) cells. Th17 have been identified as key pro-inflammatory immune cells due to their production of IL-17; IL-17 promotes the recruitment and expansion of myeloid cells and proliferation of vascular endothelial cells, expanding blood flow and delivering myeloid cells to the target area to combat pathogens [18]. In contrast, IL-6 is a pleiotropic cytokine produced by monocytes, fibroblasts and endothelial cells. It induces B-cell differentiation into plasma cells, induces production of acute-phase proteins in the liver (e.g. C-reactive

proteins in the classical complement pathway) and promotes myeloid cell infiltration [19]. During chronic inflammation IL-6 has been linked to the migration of monocytes, which differentiate into macrophages and dendritic cells in response to inflammation, at the site of injury [20]. Furthermore, IL-6 is also responsible for sustaining Th17 cell function via upregulation of Interleukin-23 (IL-23) which binds and activates the immune cell [18]. In addition to its pro-inflammatory action, IL-6 regulates cell growth, gene activation, proliferation, survival and differentiation [19]. The final pro-inflammatory cytokine TNF-α is mainly produced by macrophages, T-lymphocytes and natural killer cells [21]. In addition to activating neutrophils and lymphocytes, TNF-α enhances expression of the leukocyte adhesion molecules on endothelial cells that stimulate infiltration of lymphocytes to the infection area [22]. Furthermore, similarly to IL-17, TNF-α triggers the proliferation of endothelial cells and increases their permeability to improve blood flow to the injury site [23].

Most features of acute inflammation continue in chronic conditions. These include vasodilation, increased blood flow, capillary permeability and migration of neutrophils to the infected tissue. However, the composition of white blood cells differs in chronic inflammation with macrophages and lymphocytes being prevalent replacing the short-lived neutrophils [3]. Two types of chronic inflammation have been reported; nonspecific proliferative and granulomatous inflammation [3]. Nonspecific proliferative chronic inflammation is characterised by the formation of new non-specific granulation tissue, including connective tissue and blood vessels, formed by infiltration of mononuclear cells such as lymphocytes and macrophages. Proliferation of fibroblasts and epithelial cells also occurs in nonspecific proliferative chronic inflammation. Diseases featuring nonspecific proliferative chronic inflammation include RA, Asthma, COPD, IBD, tuberculosis and some cancers [3, 24]. Granulomatous inflammation is characterized by the presence of distinct granulomas formed from an aggregation of activated macrophages, epithelial cells and lymphocytes. There are two types of granulomas that can form, either due to the presence of a foreign body (foreign body granuloma) or due to chronic infection (infection granuloma) such as tuberculosis [3, 25].

1.1.1 Inhibition of the COX pathway as a treatment for chronic inflammation

Non-steroidal anti-inflammatory drugs (NSAIDs) have long been utilised to treat the symptoms of RA, menstrual cramps, migraines and influenza through reducing inflammation, pain and fever [26, 27]. An estimated 40% of people age 65 years and older fill one or more prescriptions for NSAIDs each year [28]. Some common examples approved by the U.S. Food and Drug Administration (FDA) for clinical treatment include aspirin (**1**), celecoxib (**2**), indomethacin (**3**), ibuprofen (**4**) and diclofenac (**5**) (see Figure 4)[26].

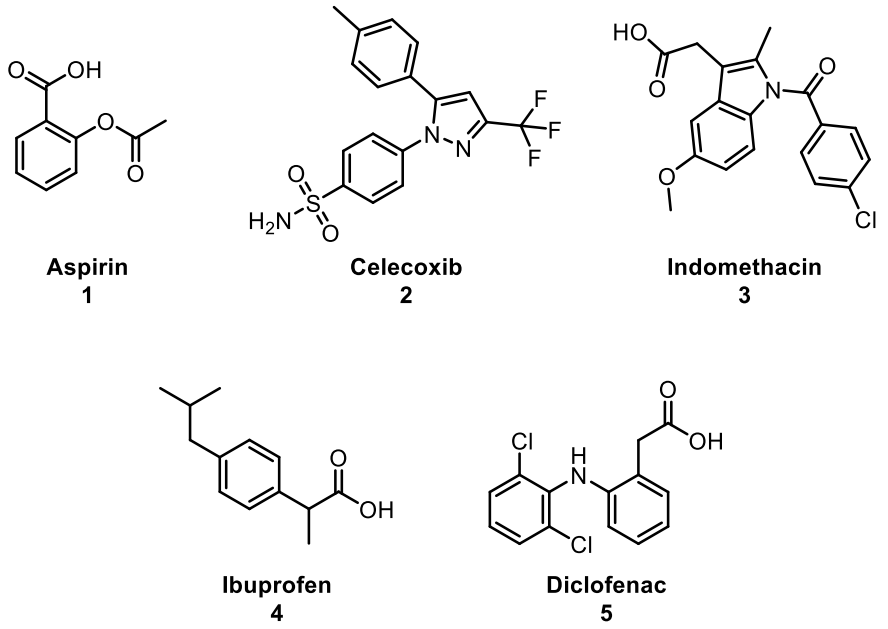

Figure 4- *Chemical structures of Aspirin, Celecoxib, Indomethacin, Ibuprofen and Diclofenac [26].*

NSAIDs reduce inflammation by competitively inhibiting the activity of cyclooxygenases (COXs) which are responsible for the conversion of arachidonic acid (AA, **6**) into prostaglandin (PG) intermediate PGH_2 in a two-step process involving either COX-1 or COX-2 (see Figure 5) [26, 29]. First, COX isozymes catalyse the cyclisation of AA to PGG_2 (**7**) which is followed by a reduction of the 15-hydroperoxy group forming PGH_2 (**8**) by the same enzymes [30-32]. COX-1 is constitutively expressed in most tissues unlike COX-2 which is typically present at undetectable levels in most cells except when upregulated

during inflammation by cytokines IL-1, IL-6 and TNF-α [30, 33]. The constitutive expression of COX-1 promotes gastric mucosal protection and increased mucosal blood flow through signalling via PGE_2 and PGI_2 [34, 35]. Five primary bioactive prostanoids PGD_2 (**9**), PGE_2 (**10**), $PGF_{2\alpha}$ (**11**), PGI_2 (**12**) and thromboxane A_2 (TXA_2, **13**) are generated by specific PG synthases from PGH_2 (see Figure 5)[29].

Prostanoids are defined as the cyclooxygenase metabolites of AA which are synthesized and released upon cell stimulation. They act locally on cells and tissue to contribute to a wide variety of physiological responses and pathological processes including immune regulation, inflammation, vascular control/airway smooth muscle tone and gastrointestinal function and secretion [29, 32]. AA is also utilized in a COX independent pathway called the 5-lipoxygenase pathway to produce leukotrienes (e.g. leukotriene B4 and cysteinyl leukotrienes) which are potent inflammatory mediators typically produced by myeloid cells [36, 37].

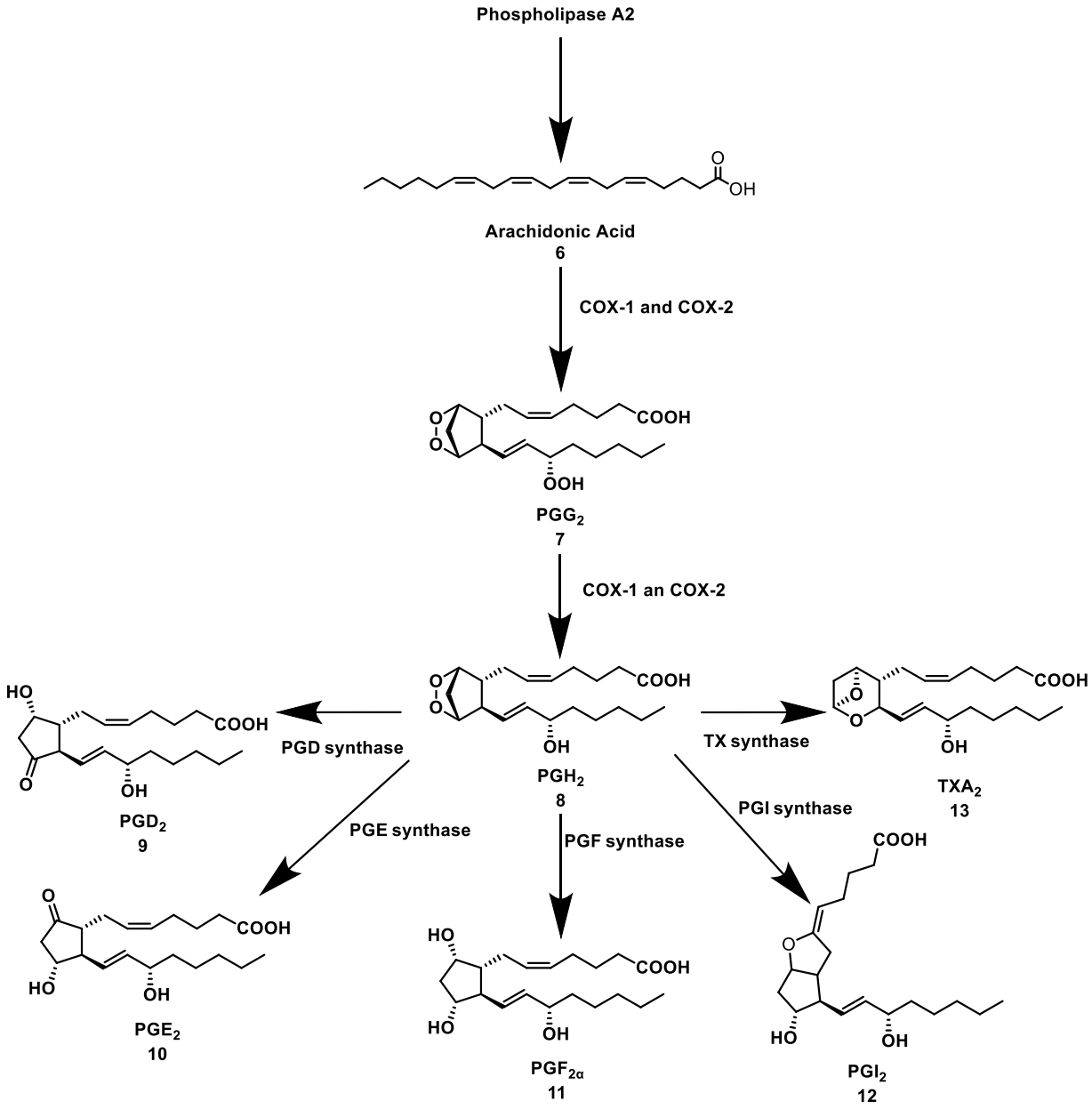

***Figure 5**- Biosynthetic pathways of prostanoids PGD_2, PGE_2, $PGF_{2\alpha}$, PGI_2 and TXA_2 from arachidonic acid via PGG_2 and PGH_2 including the associated enzymes [29, 31, 32].*

One clinically important example is the use of unselective COX inhibitor aspirin in low doses to reduce thrombosis risk in patients by inactivating PG mediated platelet clotting via platelet COX-1 [38, 39]. However, despite the common application of NSAIDs to reduce inflammation they have been found to exacerbate numerous chronic inflammatory diseases and produce life-threatening adverse effects [27, 40]. As a result, NSAID use has been reported to cause an estimated 41,000 hospitalizations and

3300 deaths each year among older adults in the US [41]. A wide range of gastrointestinal (GI) adverse effects have been reported upon use of non-selective NSAIDs which inhibit COX-1 (e.g. ibuprofen, aspirin, naproxen) ranging from dyspepsia (10-20% of patients) to life-threatening gastric bleeding (1.5% of patients) [41, 42]. The development of COX-2 selective inhibitors (e.g. celecoxib, rofecoxib and valdecoxib) which are associated with fewer GI complications, provided an alternative approach to treatment of inflammation [43]. However, numerous additional adverse effects leading to multiple organ pathologies were still prevalent across all NSAIDs preventing their widespread adoption in the clinic [27]. Most notably for COX-2 selective inhibitors the risk of cardiovascular events has limited their use, with thrombotic events, increased blood pressure, congestive heart failure and palpitations all being reported [35]. Additionally, long term NSAID therapy has been found to induce renal dysfunction in an estimated 2.5 million people in the US in 2006, ranging from decreased glomerular perfusion, decreased glomerular filtration rate and acute renal failure [40, 44]. Furthermore, central nervous system (CNS) adverse effects, including headaches, fatigue, insomnia, vertigo and seizures, has also been linked to COX inhibition. Other common adverse effects of NSAIDs include bleeding, asthma attacks, Reye's syndrome, urticaria and neutropenia [27, 35]. The occurrence of these life-threatening adverse effects by NSAIDs has been linked to the inhibition of downstream prostanoid production in a non-selective and unbalanced manner. As each specific prostanoid activates downstream signalling at numerous receptors to induce a variety of different physiological responses the elimination of all prostanoid production by COX-inhibitors results in these unwanted side-effects. Secondly, inhibition of the COX pathway may shift the balance to other local mediators produced from arachidonic acid, such as the leukotrienes produced from 5-lipooxygenase activity. Therefore, the production of small molecule inhibitors acting at specific prostanoid receptors downstream of the COX pathway might generate more selective actions and could mitigate chronic inflammation whilst eliminating these adverse effects.

1.2 Prostaglandin EP_2 receptor

1.2.1 An introduction to GPCRs and the prostanoid receptors

Prostanoid receptors belong to the G protein-coupled receptors (GPCRs) family and are the largest and most diverse group of membrane receptors in eukaryotes mediating cellular responses to most hormones, metabolites, cytokines and neurotransmitters through effector proteins [45]. These receptors form a superfamily of membrane proteins and are comprised of five distinct classes in vertebrates; Rhodopsin-like (class A), Secretin (class B), Glutamate (class C), Adhesion (class B2) and Frizzled/Smoothened (class F) [46]. The Rhodopsin-like family is the most diverse and largest, comprising approximately 400 proteins in the human genome [47]. Typically, members are characterized by conserved sequence motifs that are indicative of shared structural features and activation mechanisms. However, individual GPCRs have unique modes of signal-transduction which can involve multiple G-protein subtypes, G-protein independent signalling pathways and complex regulatory processes [47]. As GPCRs employ such diverse signalling mechanisms involving a variety of G-protein and β-arrestin subtypes, they can modulate a wide variety of physiological responses and provide attractive targets for pharmacological exploitation. To date GPCRs are the most intensively studied drug targets with a total of 481 drugs (~38% of all drugs approved by the FDA) acting at 107 GPCRs and accounting for ~27% of the global market share of therapeutic drugs [48, 49]. Despite this success, 57% of non-olfactory GPCRs have yet to be explored in clinical trials, indicating significant therapeutic potential not yet exploited. With the rapid advancements in structural biology, receptor pharmacology assays and improvements in structural elucidation techniques, the development of small molecule ligands targeting novel GPCRs has become more viable [49].

All GPCRs span the membrane with seven transmembrane (TM) α-helices (TM1-TM7) connected by three extracellular loops (ECL1-ECL3), three intracellular loops (ICL1-ICL3), an extracellular *N*-terminal domain (NH_3^+) and an intracellular *C*-terminal domain (COO^-) (see Figure 6) [46, 50].

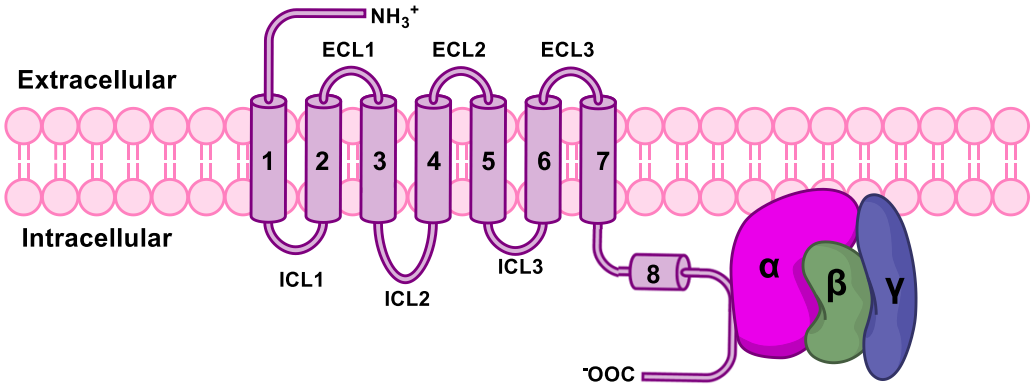

***Figure 6**- Generic structure of a GPCR showing the 7 TM α-helices and separately the three subunits of the heterotrimeric G-protein (α, β and γ) [47, 51]. Made using ChemDraw 19.1.*

The main feature of many GPCRs is their interaction with heterotrimeric G proteins composed of Gα and Gβγ subunits (see Figure 6). Individual receptors typically select from a subset of G protein isoforms for activation including, $G\alpha_s$, $G\alpha_q$, $G\alpha_{i/o}$ and $G\alpha_{12/13}$, each of which regulates distinct signalling pathways, resulting in the functional diversity of GPCRs [52, 53].

The five primary bioactive prostanoids previously discussed PGD_2, PGE_2, $PGF_{2\alpha}$, PGI_2 and TXA_2 act locally on nine GPCRs, each classified as selective on the basis of their natural prostanoid (which is at least one order of magnitude more potent than the other four) [54, 55]. These GPCR families are designated as DP, EP, FP, IP, and TP for the PGD_2, PGE_2, $PGF_{2\alpha}$, PGI_2 and TXA_2 prostanoids respectively (see Table 1). The EP receptors exist as four subtypes $EP_{1\text{-}4}$ all producing a different physiological response upon activation [32, 56]. The nine prostanoid receptors can also be classified into three subfamilies in accordance with their structural similarities and the intracellular signalling they induce (see Table 1) [32, 57]. The 'relaxant' receptors consist of DP_1, EP_2, EP_4 and IP subfamilies and are $G\alpha_s$ coupled mediating cyclic adenosine monophosphate (cAMP) production and leading to the relaxation of smooth muscles. The 'contractile' receptors include EP_1, FP and TP receptors are $G\alpha_q$ coupled and mediate cytosolic Ca^{2+} mobilization inducing smooth muscle contractions. In contrast, the EP_3 subfamily member is $G\alpha_i$ coupled and primarily mediates a decrease in cAMP

and are therefore classified as ‘inhibitory’ receptors [32, 57]. Each prostanoid receptor is responsible for the modulation of various physiological processes and abnormal receptor expression can be linked to the pathology of numerous disease states.

***Table 1**- Prostanoid receptors, their endogenous prostanoids, coupled G-protein, second messenger effect, subfamily classification and biological response [32, 57].*

Prostanoid receptor	Endogenous prostanoid	G-protein	Second messenger effect	Prostanoid receptor subtype	Immune cell expression	Biological response
DP_1	PGD_2	$G\alpha_s$	↑ cAMP (↑ Ca^{2+})	Relaxant	Mast cells, basophils, eosinophils, t-helper cell type 2 (Th2) cells, dendritic cells, macrophages.	Regulates allergic and inflammatory responses (both pro- and anti- inflammatory role dependent on phase of allergic response), vasodilation, bronchodilation, sleep regulation and the inhibition of platelet aggregation [32, 58-60]. The pro-inflammatory role of DP_1 involves the polarisation of T-helper cell type 2 (Th2- stimulates B cells) during sensitization stage of inflammation [61]. Inhibits apoptotic cascade for survival of eosinophils [62]. Anti-inflammatory role by inhibiting signalling pathways decreasing the production of pro-inflammatory cytokines Il-1β, IL-6 and TNF-α [59]. Additionally, suppresses dendritic cell maturation and function during effector phase reducing activation of antigen specific Th2 cells [61].

DP_2	PGD_2	$G\alpha_i$	↓ cAMP (↑ Ca^{2+})	Contractile	Th2 cells, eosinophils, basophils and mast cells.	Inflammatory mediator- recruits and activates Th2 cells, eosinophils and basophils to the site of inflammation [63]. DP_2 plays a key role in the pathophysiology of asthma promoting release of cytokines IL-4, IL-5 and IL-14 which drive eosinophilic inflammation, goblet cell hyperplasia and mucus hypersecretion [64]. DP_2 activation also remodels airways through promoting the proliferation and migration of airway smooth muscle cells [65].
EP_1	PGE_2	$G\alpha_q$	↑ Ca^{2+}	Contractile	T cells (CD4 + and CD8+), dendritic cells, B cells and macrophages.	Mediator of pain perception, neuroinflammation, neuronal death, cardiovascular homeostasis and plays a role in cancer cell proliferation and progression [66-68]. Regulates sensitization stage of inflammation by facilitating differentiation of naïve T cells into Th1[69]. EP_1 receptors can interact with COX-2 to facilitate its Ubiquitination and degradation (negative feedback loop) [70].

EP_2	PGE_2	$G\alpha_s$	↑ cAMP	Relaxant	T cells (CD4+ and CD8+), B cells, macrophages, monocytes, microglia and neutrophils.	Inflammatory mediator regulating Th17 cell differentiation, function through production of IL-23 and is linked to Th17 cell production of IL-17 leading to angiogenesis. Role in smooth muscle regulation and cell growth. Implicated in progression of cancer and neurodegenerative diseases [51, 71, 72]. EP_2 signalling in macrophages and microglia (CNS resident macrophage like cells) promotes the expression and release of pro-inflammatory cytokines. Part of a positive feedback loop upregulating COX-2 expression and thus amplifying the inflammatory response [73, 74].
EP_3	PGE_2	$G\alpha_i$ ($G\alpha_s$ /$G\alpha_q$)	↓ cAMP (↑ Ca^{2+})	Inhibitory	Macrophages, dendritic cells, B cells and neutrophils.	Role in thermoregulation, smooth muscle contraction, GI function (inhibits secretion of gastric acid) and neuroinflammation [75-77]. Highly expressed in the kidney where it regulates fluid metabolism by inhibiting water and sodium reabsorption [78]. Activation of EP_3 receptors has been linked to antinociception (reduction in **i**nflammatory pain) [79].

EP_4	PGE_2	$G\alpha_s$ ($G\alpha_i$)	↑ cAMP	Relaxant	T cells (CD4+ and CD8+), eosinophils macrophages, dendritic cells, natural killer cells and microglia.	Vascular relaxation, angiogenesis, bone remodelling and both pro- and anti- inflammatory role in macrophages. EP_4 suppresses macrophage production of TNF-α, IL-12 and MCP-1 but promotes pro-inflammatory cytokine IL-6 via the MAPK pathway. EP_4 works in tandem with EP_2 to modulate Th17 cells (via IL-6) to produce IL-17. IL-17 is responsible for the recruitment and expansion of myeloid cells and inducing proliferation of vascular endothelial cells leading to angiogenesis [80]. IL-17 is upregulated in cancer and linked to tumour cell proliferation, migration and metastasis [80, 81].
FP	$PGF_{2\alpha}$	$G\alpha_q$	↑ Ca^{2+}	Contractile	Macrophages	Mediates smooth muscle contraction, regulates reproductive processes like luteolysis and parturition. Regulates intraocular and blood pressure. Implicated in hypertension, age-related cardiac fibrosis and can promote angiogenesis in some cancers [82].
IP	PGI_2	$G\alpha_s$	↑ cAMP (↑ Ca^{2+})	Relaxant	T-cells (CD4+), dendritic cells,	IP is a key vasodilator to regulate cardiovascular functions including blood pressure. Primarily

					macrophages, neutrophils and eosinophils.	associated with pulmonary arterial hypertension and atherothrombosis [83]. Additionally, inhibits platelet activation, adhesion and aggregation by inhibiting production of 1,4,5-trisphosphate (IP_3) and subsequent Ca^{2+} release [84, 85]. Influences endothelial cell function and vascular permeability during inflammation [86, 87]. IP signalling supresses Th2-mediated allergic inflammatory response by enhancing its production of anti-inflammatory cytokine IL-10 [88]. IP present on sensory neurons and linked with inflammatory pain and induction of hyperalgesia [89].
TP	TXA_2	$G\alpha_q$ ($G\alpha_s$ /$G\alpha_{12/13}$)	↑ Ca^{2+} (↑ cAMP)	Contractile	Platelets, T cells (CD4+ and CD8+), macrophages and dendritic cells.	Promote platelet activation and aggregation, vasoconstriction, vascular smooth muscle cell proliferation and promotes inflammation.[90, 91] Role in cardiovascular diseases including atherosclerosis, thrombosis and hypertension. Linked to cancer progression (angiogenesis, cell survival and metastasis) and asthma [91, 92].

All prostanoid receptors have been reported to play complex roles in the promotion of chronic inflammation and can be linked to the progression of cancer and neurodegenerative diseases [93, 94]. For the purpose of this report only the role of prostanoid receptor EP_2 in the inflammatory process will be discussed in detail.

1.2.2 Prostaglandin EP_2 signalling

The prostaglandin EP_2 receptor is a $G\alpha_s$ coupled GPCR which is commonly expressed in the human small intestine, lungs, media of the arteries, arterioles of the kidney, thymus, uterus, cerebral cortex and immune cells (T-cells, myeloid and dendritic cells) [51]. All G-protein isoforms function via a GTPase cycle in which agonist binding (e.g. endogenous agonist PGE_2) to the EP_2 receptor results in a conformational change to the 'active state' mediating interactions with the G protein. Once bound, the G protein acts as a guanine nucleotide exchange factor exchanging guanosine diphosphate (GDP) for guanosine triphosphate (GTP) on the surface of the Gα subunit. As a result, the G-protein uncouples from the receptor forming two functional subunits, membrane bound Gβγ and $G\alpha_s$-GTP, which induce downstream signalling. Subsequent termination of $G\alpha_s$ signalling occurs when GTP is hydrolysed into GDP and inorganic phosphate by inherent GTPase activity, facilitating the reassembly of the Gα-GDP complex with the βγ subunit. Subsequently, the dissociation of the agonist from EP_2 triggers a conformational change returning both EP_2 and the G protein to their inactive state and terminating signal transduction [95].

The EP_2 $G\alpha_s$ signalling pathway regulates cAMP production through the activation of adenylate cyclase which converts adenosine triphosphate (ATP) to cAMP (see Figure 7) [51, 96]. Increasing concentrations of cAMP can bind, activate and induce the signalling of cAMP sensitive binding proteins such as protein kinase A (PKA) and exchange proteins regulated by cAMP (EPACs). PKA regulates gene transcription, cell survival and migration and extracellular signal-regulated kinase (ERK) signalling via the mitogen-activated kinase (MAPK) cascade pathway [97, 98]. For example, PKA phosphorylates downstream transcription factors such as cAMP-response element binding protein (CREB), a downstream target of the MAPK cascade, and nuclear factor kappa-light-

chain-enhancer of activated B cells (NF-kB, see Chapter 1.2.3). CREB reportedly mediates neuronal plasticity, long-term memory formation, neuronal survival and neurogenesis in the brain [73, 99]. In comparison, cAMP activated EPACs modulate hormone secretion, formation of cell junctions, cell differentiation/proliferation and gene expression via activation of the Ras superfamily small GTPases Rap1 and Rap2 [100].

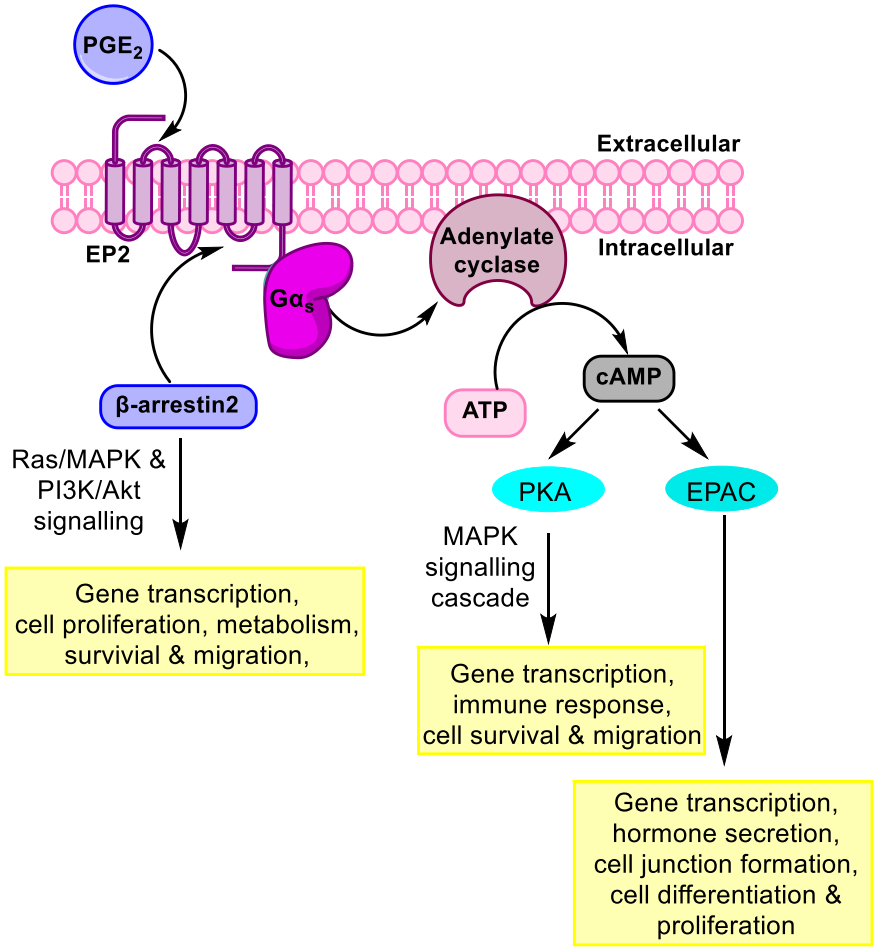

***Figure 7**- EP_2 receptor signalling pathways detailing $G\alpha_s$ dependent and independent β-arrestin signalling and their downstream biological response [51, 96-98, 100]. Made using ChemDraw 19.1.*

GPCRs can also be regulated and signal independently of G proteins, for example through the direct recruitment of β-arrestins. β-arrestin-dependent signalling is extremely diverse, having been originally described classically for GPCR inactivation (desensitisation) and receptor internalisation [101]. Four main isoforms of arrestin are reported (arrestins 1-4) with only arrestin-2 and 3, termed β-arrestin 1/2 respectively,

being involved in classical signalling due to their ubiquitous expression. Arrestin-1 and 4 denoted as 'visual' arrestins are almost exclusively located within photoreceptive cells [102].

Recruitment of β-arrestin to the GPCR and subsequent signalling is promoted upon receptor activation by agonists. Agonist-occupied GPCRs are rapidly phosphorylated at select serine and threonine amino acids within the *C*-terminal tail and/or intracellular loop by specific GPCR kinases (GRKs). The pattern of phosphorylation dictates the duration, stability and subtype of β-arrestin-GPCR association [101]. The recruitment of β-arrestin to the GPCR facilitates receptor inactivation and reduces the downstream effects of G-protein signalling by numerous mechanisms. Firstly, the binding of β-arrestin to an intracellular pocket on the GPCR sterically inhibits G-protein binding and signalling resulting in receptor desensitisation. This desensitisation is often referred to as "homologous" as the mechanism ensures that only agonist activated and occupied receptors are inactivated. In contrast, heterologous desensitisation mechanisms, for example receptor phosphorylation by second messenger kinase PKA, PKC or casein kinase 2 (CK2), affect both inactive and active receptor populations [103-105]. Secondly, β-arrestin undergoes conformational rearrangement upon recruitment to GPCRs promoting binding to both clathrin endocytic machinery (e.g. clathrin, β2-adaptin and N-ethylmaleimide-sensitive fusion protein (NSF) and E3 ubiquitin ligases) to induce receptor internalisation and degradation respectively. Furthermore, the β-arrestin receptor complex scaffolds enzymes such as phosphodiesterase (PDE) and diacylglycerol kinase (DGK) that degrade second messengers generated by G protein activity such as cAMP, further contributing to GPCR desensitization [101, 106]. In addition to these inhibitory mechanisms EP_2 activation is also known to engage β-arrestin2 in a G protein-independent signalling pathway. The formation of an EP_2-β -arrestin2 complex has been reported to scaffold proteins and induce signalling via Ras/MAPK and phosphoinositide 3-kinase/protein kinase B (PI3K/Akt), including activation of Src, EGFR and ERK1/2. The PI3K/Akt signalling pathway is essential for processes like cell migration, glucose metabolism, immune cell development and cell growth, survival and proliferation. Dysregulation of this EP_2-β -arrestin2 signalling

pathway is strongly linked to migration, adhesion and proliferation of tumour cells [73, 107]. This implies β-arrestin recruitment to EP_2 plays a larger role in cellular signalling than just desensitization and internalisation.

1.2.3 EP_2 and inflammation

Prostanoid receptor EP_2 plays an essential role in the inflammatory process by promoting the expression of pro-inflammatory cytokines from leukocytes, macrophages and lymphocytes [71, 108]. During inflammation, PKA activates NF-kB transcription factors upon phosphorylation to regulate genes involves in inflammation, immune response, cell survival and proliferation [109]. For example, NF-kB signalling in macrophages leads to the production of pro-inflammatory cytokines IL-1, IL-6, IL-12, TNF-α and chemokines. Additionally, NF- kB is the main downstream signalling pathway of cytokine receptors TNF-α, IL-1 and TLRs further driving immune response. As a result, dysregulation of NF-kB signalling is a hallmark of chronic inflammatory diseases [109].

Furthermore, EP_2 receptor signalling has been identified as one of the most essential GPCRs for the modulation of Th17 cell function [73, 110]. The stimulation and differentiation of $CD4^+$ into Th17 cells is induced by the cytokine IL-1β whose receptors are upregulated by EP_2 induced PKA/EPAC signalling [111]. Additionally, working synergistically with EP_4, EP_2 receptors activate and sustain Th17 cell function through the upregulation of IL-23 induced by cytokine IL-6. Cytokine IL-6 is produced by EP_2 induced Akt and NF-kB signalling, whilst IL-23 receptors are upregulated by the EP_2 induced cAMP-PKA signalling cascade [111-113]. Furthermore, Th17 production of cytokine IL-17 has been linked to EP_2 activation via upregulation of the IL-17 transcription factor ROR-yt [111]. As previously discussed, IL-17 increases blood flow to the site of inflammation delivering myeloid cells and lymphocytes to combat disease/pathogens (see Chapter 1.1.1) [18, 73, 110]. EP_2 induced production of IL-6 is also responsible for B-cell differentiation and migration of monocytes to the site of inflammation. The exacerbation of inflammation has been linked to EP_2 signalling via cAMP suppression of phagocytosis and antimicrobial function by pulmonary macrophages thus dampening innate antibacterial responses [73, 114].

The upregulation and increased expression of prostanoid EP_2 receptors has been reported in numerous disease states including cancer, arthritis, IBD, epilepsy, amyotrophic lateral sclerosis (ALS) and chronic inflammatory neurodegenerative diseases including AD and Parkinsons (PD) [115, 116]. Therefore, targeted inhibition of EP_2 receptors is an attractive therapeutic approach for the treatment of these diseases either by mitigating chronic inflammatory induced disease progression or removing immunosuppression in cancer (see Chapter 1.2.4 and 1.2.5) [116]. To date only a single EP_2 orthosteric agonist omidenepag (**14**), has been approved for clinical use in a non-immune indication as its pro-drug omidenepag isopropyl in the treatment of glaucoma and ocular hypertension, (see Figure 9) [117]. Omidenepag reduces intraocular pressure through an EP_2 induced increase in both trabecular and uveoscleral outflow via smooth muscle relaxation.

1.2.4 EP_2 and chronic inflammation in cancer.

The EP_2 signalling pathway has been identified as a key modulator of various physiological functions in cancer, including tumour occurrence, invasion and metastasis, angiogenesis, chronic inflammation, tumour immunity, cell apoptosis and immunosuppression [51, 118]. Upregulation of EP_2 receptors has been reported in various cancers including gastric, prostate, skin, colon, brain and cervical cancer [72, 99, 119]. Notably, individuals with existing chronic inflammatory diseases have an increased risk of cancer development, for example IBD is a well-known precancerous lesion to colorectal cancer [120].

Approximately 60% of solid cancers are associated with an immunosuppressive tumour microenvironment (TME) occurring in parallel with active inflammation [120, 121]. An immunosuppressive TME can facilitate tumour progression and treatment resistance. It is a common characteristic of malignancy and is generated by promoting the activation of oncogenes and the release of reactive oxygen species (ROS). ROS lead to DNA/protein damage and affects multiple signalling pathways including NF-kB (EP_2 induced), K-Ras and P53 [120, 121]. Under these TME conditions it appears that PGE_2-EP_2/ EP_4 signalling is immunosuppressive, driving the mature dendritic cell enriched in

immunoregulatory molecules regulatory T cell (mregDC-Treg) axis and hampering the bioenergetics and ribosome biogenesis both in lymphocytes and tumour-infiltrating myeloid cells [122]. For example, EP_2 signalling has been linked to the suppression of antigen presentation by dendritic cells resulting in subsequent suppression of cytotoxic T cell responses [123]. Overall, in the TME immune cells have reduced migration activity, poor survival and expansion capacity as a result of PGE_2-EP_2/EP_4 signalling [124]. Therefore, in these circumstances, EP_2 antagonists acting on immune cells in the TME may help remove immunosuppression and improve the effectiveness of anti-cancer treatments which aim to harness the immune response to destroy cancer cells [125]. One anti-cancer treatment that would theoretically benefit from combination therapy with an EP_2 antagonist is immune checkpoint inhibitors. These drugs bind and block the function of checkpoint proteins such as programmed cell death protein 1 (PD-1), programmed death ligand 1 (PD-L1) and cytotoxic T-lymphocyte-associated protein 4 (CTLA-4) thereby reactivating T cells to recognise and destroy cancer cells [125, 126].

In addition to the immunosuppression action of PGE_2-EP_2/EP_4 signalling, EP_2 simultaneously promotes active inflammation through NF-kB induced transcription which is responsible for more than 500 cancer related genes. One example includes the regulation of anti-apoptotic genes TNF receptor-associated factor (TRAF) 1 and TRAF2 which are found to be chronically active in inflammatory diseases and cancer [109, 120]. Furthermore, the production of pro-inflammatory cytokines (IL-6 & IL-17) via EP_2 signalling promotes malignant cell survival, proliferation, angiogenesis and metastasis [127, 128]. The elimination of EP_2 receptors has been reported to supress the growth of tumours and prolong survival in syngeneic mouse tumour models [123]. As a result, the modulation of EP_2 is an attractive target for development of cancer therapies currently not exploited. COX inhibitors are not FDA approved for cancer treatment due to the requirement for high doses and prolonged use which results in a high risk of toxic adverse effects [129, 130].

1.2.5 EP_2 and neurodegenerative diseases.

1.2.5.1 EP_2 and Alzheimer's disease

More than 10% of people over 65 years of age and 30% of people >85 are affected by AD which clinically manifests as progressive cognitive impairment [131, 132]. Pathologically AD is characterized by the formation of both extracellular amyloid plaques, formed of amyloid beta (Aβ), and intracellular neurofibrillary tangles, formed of the hyperphosphorylated microtubule-binding protein tau. These plaques are surrounded by immune cells which could pose as a potential target for immunomodulation [133]. In the earliest stages of AD the formation of Aβ occurs due to abnormal cleavage of amyloid precursor protein (APP) by β- and γ- secretases. Aβ intrinsically oligomerise and aggregate to form plaques because of genetic mutations in the APP gene. It is thought that Aβ binds and activates microglia to phagocytose plaques and protect neurons [134]. However, a failure in Aβ clearance leads to persistent chronic inflammation and chronically activated microglia which then increase APP expression and plaque formation in a feedback loop [131, 135]. The activation of EP_2 receptors at microglia reportedly regulates APP expression, via Ras/MAPK signalling, and has been shown to reduce their ability to phagocytose Aβ plaques [136, 137]. Additionally, the hyperphosphorylation of tau proteins occurs by kinases which are activated by inflammatory cytokines such as IL-6 produced from the EP_2 signalling pathway. Therefore, EP_2 signalling contributes to the production of tau tangles and neuronal cell death [131]. A 1995 study found that individuals on long-term NSAIDs had up to 50 % reduction in risk of developing AD, therefore development of anti-inflammatory EP_2 antagonists, without COX inhibitor side effects, is an attractive approach for treatment of AD [138].

1.2.5.2 EP_2 and Parkinson's disease

PD is the second most common neurodegenerative disease, afflicting 1% of the population greater than 60 years old. PD is a multi-system disorder resulting in motor deficits, neuro inflammation, immune disfunction, sleep and GI dysfunction. It is pathologically characterized by the presence of Lewy bodies, composed of aggregated

α-synuclein, and the loss of dopaminergic neurons in the substantia nigra [131, 139]. Excessive α-synuclein in neurons is transported to the mitochondria where its phosphorylation and aggregation leads to mitochondrial dysfunction and neuron damage, the central progression of PD. Excessive aggregation of α-synuclein and failure to clear from the neuron results in its direct or exosomal release, activating microglia and amplifying neurotoxicity by spreading α-synuclein to neighbouring healthy neurons. Cytokine production by EP_2 signalling pathways in chronically activated microglia results in upregulation of α-synuclein expression, α-synuclein phosphorylation and increased mitochondrial dysfunction further exacerbating PD [131]. With evidence suggesting that the adaptive immune system plays an important role in approximately 40 % of PD cases, inhibition of the EP_2 receptor is an attractive therapeutic target [131].

Overall, chronic inflammation, modulated by the prostanoid EP_2 receptor, plays a central role in the initiation and progression of neurodegeneration in both AD and PD. With no curative treatment to prevent disease progression available current treatments focus on managing symptoms using cholinesterase inhibitors and dopaminergic drugs for AD and PD respectively [140]. The development of EP_2 inhibitors to combat chronic inflammation in the brain may provide an alternative therapeutic strategy to eliminate disease progression.

1.3 EP_2 receptor antagonists.

1.3.1 GPCR ligand pharmacology

Therapeutic ligands targeting GPCRs can be defined first by the molecular site of action being either the same binding site as the endogenous agonist (orthosteric) or through a topographically distinct (allosteric) binding site. In either case, the direct action of a ligand at a receptor can be classed as an agonist/partial agonist, antagonist or inverse agonist [141]. Agonists have both the ability to bind to the GPCR (affinity) and to activate it through conformational change (intrinsic efficacy). The simplest model to describe receptor agonism involves an equilibrium between inactive (R) and active (R*)

conformations (D+R↔DR↔DR*, where D is the therapeutic ligand, see section 1.4.1). Agonist efficacy in this model is therefore represented by the extent of the shift in equilibrium to the R* active conformation once the agonist has bound. Agonists at GPCRs commonly display differing efficacies. In functional assays lower efficacy can be revealed as partial agonism, in which a submaximal response is observed compared to a reference agonist. In contrast, antagonists have receptor affinity but act to inhibit the biological response of an agonist and do not activate the receptor. For competitive reversible antagonists, the antagonist competes non-covalently for the orthosteric binding site, which results in a reduction in potency of the agonist response. Inverse agonists represent a subset of antagonists, in which the ligands actively stabilise the inactive R conformation of the receptor. Therefore, under conditions where the receptor displays constitutive basal activity, inverse agonists can induce an opposite functional response to that of an agonist, as well as antagonising agonist responses [142, 143].

Traditionally most drugs on the market target orthosteric sites, with ligands exerting their effect through competition with the endogenous agonist binding site. The extent of inhibition depends on the respective affinities and concentrations of the competing ligands. For orthosteric antagonists where interaction with the receptors is reversible and conditions are at equilibrium, surmountable antagonism is observed, in which increasing agonist concentrations outcompete the antagonist and are able to restore the maximal response (with a reduced potency compared to the no antagonist control) [143]. Despite a large portion of GPCR-targeting drugs operating through this mechanism, designing orthosteric ligands that are both safe and effective under diverse biological conditions presents a significant challenge [144]. The occurrence of off-target side effects and poor selectivity of many orthosteric drugs is a result of the highly conserved structure of the orthosteric binding pockets between closely related GPCRs and has contributed to many drug candidates failing to reach the clinic [145].

Allosteric ligands offer an alternative route for manipulation of GPCR responses and attempts to mitigate the challenges associated with orthosteric ligands. Allosteric drugs bind at a topographically distinct site in the receptor protein from the endogenous

ligands, offering potentially increased subtype selectivity and tunability of receptor function [141]. Allosteric ligands demonstrate multiple modes of action to modulate receptor activity. The binding of allosteric modulators can indirectly affect protein activity by changing the conformation of the receptor; this can impact the orthosteric agonist affinity (often referred to as α co-operativity), or its efficacy in activating downstream pathways (often referred to as β co-operativity), in a positive, negative or neutral manner [143, 146, 147]. Allosteric ligands may enhance the activity of an orthosteric agonists (positive allosteric modulation, PAM), inhibit their activity (NAM) or have no impact on the orthosteric agonist effect (silent allosteric modulation) [143]. Direct effects on GPCR efficacy (intrinsic efficacy, τβ) can also be exhibited with the allosterically induced conformation change modulating receptor G-protein/β-arrestin binding affinities and/or the formation of the ligand-receptor complex sterically hindering their recruitment. Unlike classical orthosteric ligands, allosteric ligands may have a ceiling to their modulation on the orthosteric agonist function, their inhibitory effect reaches a maximum saturation point even with increased drug concentration as allosteric sites become fully occupied, which can be a useful property to titrate the magnitude of their effect and prevent overdose [148]. For allosteric ligands without intrinsic efficacy of their own, their pharmacological action depends on the presence of the orthosteric ligand- thereby generating use dependence. For example, the anti-inflammtory effect of a drug only occur if immune cells are stimulated by existing concentrations of local orthosteric mediator PGE_2.

Both allosteric and orthosteric modulators have the potential to induce signalling bias and probe dependence at GPCRs, further contributing to the possibility to develop drugs with precise pharmacological modulation [149]. Signalling bias occurs when different ligands activate the same GPCR but preferentially trigger distinct downstream pathways, either G-protein or β-arrestin, rather than both pathways equally. This leads to drugs with unique cellular responses and the potential for reduced side effects [150]. In comparison probe dependence is where the extent of the allosteric effect is dependent on the nature of the orthosteric agonist used [151].

Four druggable allosteric hotspots have been identified for GPCRs termed; the extracellular vestibule, the intracellular and extracellular faces of the transmembrane helices/domains and outside and at the intracellular surface, (see Figure 8) [152]. Some notable examples of ligands binding to these allosteric hotspots include 'LSN3160440' (**15**) a PAM targeting the extracellular vestibule of glucagon-like peptide-1 receptor (GLP-1R), as well as, 'Compound-6FA' (**16**, PAM) and 'AS408' (**17**, NAM) both targeting binding pockets located outside the transmembrane domain of the beta-2 adrenergic receptor (β2AR) [153-155]. Typically, these drugs have high lipophilicity with rigid lipophilic regions to anchor the ligand within the lipid cell membrane. Additionally, 'HTL14242' (**18**) is an advanced orally active NAM, binding inside the transmembrane domain, of metabotropic glutamate (mGlu) receptor type 5 in early clinical testing [156]. Finally, both Navarixin (**19**) and 'Compound 15' (**20**) are intracellular NAMs, binding between TM1-3 and 6-8, at the C-X-C motif chemokine receptor 2 (CXCR2) and β2AR receptors respectively [157, 158]. These ligands must be sufficiently lipophilic to passively diffuse across the hydrophobic cell membrane (but not too high to avoid becoming trapped in lipid bilayer) and generally have smaller molecular weights to prevent steric hinderance and promote intracellular penetration [159].

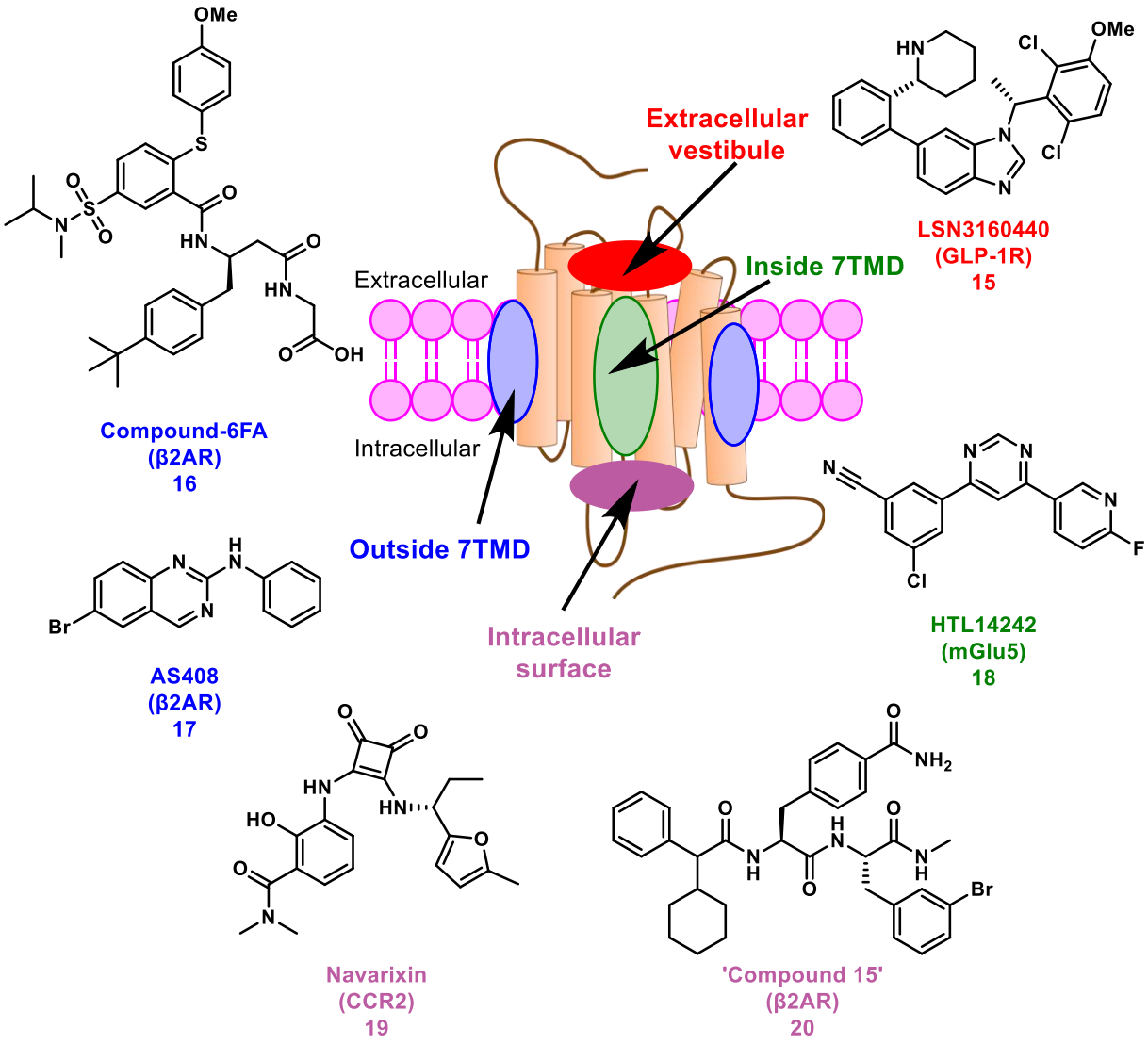

***Figure 8**- Diagram demonstrating the location of the four druggable allosteric pockets reported across GPCRs. Structures of LSN3160440, HTL14242, 'Compound 15', Navarixin, AS408 and 'Compound-6FA' are also included and colour coded according to their reported allosteric pocket binding type [152-158]. Made using ChemDraw 19.1.*

1.3.2 Targeting the EP_2 receptor

Numerous considerations must be made when developing antagonists targeting the EP_2 receptor. Firstly, developing antagonists with EP_2 selectivity is desirable to minimise off-target adverse effects. Despite the relatively low overall sequence homology between EP subtypes of 28-33 %, a conserved α chain carboxyl recognition motif at the endogenous agonist PGE_2 binding site, containing essential amino acids $Tyr^{2.65}$, Thr^{ECL2}, $Arg^{7.40}$, $Met^{3.32}$/$Leu^{3.32}$ and $Leu^{7.36}$/$Phe^{7.36}$ (Ballesteros-Weinstein numbering), shared by all

prostanoid receptors except DP_2 has been reported [29, 160, 161]. Potential adverse effects of non-selective EP_2 antagonists include vasoconstriction leading to stoke and heart attack via EP_4/IP antagonism, over-activation of platelets resulting in thrombosis via IP/DP_1 antagonism, and increased ischemic injury following stroke as well as an interference with sleep regulation via DP_1 antagonism [162-166]. The complexity of chronic conditions also needs considered with PGE_2 induced signalling resulting in a balance of different effects, both positive and negative in relation to disease progression. To develop a therapeutic there is a need to identify the precise effect for which EP_2 antagonism is beneficial and whether this is dependent on the stage and/or nature of the chronic disease [167]. As a result, it may be beneficial to titrate the effect of the antagonist with a ceiling, protecting patients from excessive inhibition (overdose) seen in competitive antagonism, to regulate immune pathways [168]. Therefore, development of allosteric as well as orthosteric EP_2 ligand approaches may be beneficial due to their tendency for increased selectivity, ability for use dependence and ceiling effect.

1.3.3 Orthosteric antagonists of EP_2.

Numerous orthosteric antagonists for EP_2 have been reported in the literature and can be divided into four structural classes; cinnamic amides e.g.TG4-155 (**21**), carbamothioacrylamide e.g. TG6-129 (**22**), azetidine-carboxylic acid derivatives e.g. PF-04418948 (**23**) and benzoxapine derivatives e.g. benzoxapine 52 (**24**), (see Figure 9) [169-172]. TG6-129 was identified as part of a new acrylamide class of selective antagonists through a high-throughput screening (HTS) approach [170]. TG6-129 demonstrates inhibition of PGE_2 induced EP_2 receptor activation in a concentration dependent manner with PGE_2 and has an equilibrium dissociation constant (K_D) value of 8.8 nM [170]. PF-04418948 has also been determined to be a potent *in vitro*, selective EP_2 receptor antagonist against EP_1, EP_3, DP_1 and TP in recombinant cell-based systems, and smooth muscle preparations from human non-pregnant myometrium (EP_2 expression heavily regulated by hormonal cycles and pregnancy), dog bronchiole (robust EP_2 expression, closely homologous) and mouse trachea (robust EP_2 expression,

significantly larger protein with extended and divergent intracellular/extracellular loops) [171]. Inhibition of EP_2 by TG6129 in a mouse model containing xenografts from human neuroblastoma cell line SK-N-AS demonstrated antiangiogenic, anti-inflammatory and apoptotic effects [173]. In comparison, PF-04418948 inhibited PGE_2-induced cAMP increase in cells expressing EP_2 receptors (K_B = 1.8 nM in functional cAMP assays utilising a Chinese Hamster Ovary (CHO-EP_2) receptor cell line). CHO cells are widely used in prostanoid receptor pharmacology as they offer minimal interference from other prostaglandin receptors due to negligible expression, however as they lack specific human glycosyltransferases this leads to alterations in the hydrodynamic volume, stability and conformation of the extracellular loops [174]. Increasing concentrations of PF-04418948 caused parallel rightward shifts of PGE_2 curves with no significant reduction in maximal response, indicating surmountable antagonism, consistent with competitive reversible antagonism [171]. In a dextran sodium sulphate-induced colitis mice model for the study of IBD, inhibition of EP_2 by PF-04418948 was found to protect against excessive inflammatory responses and intestinal tissue damage [175].

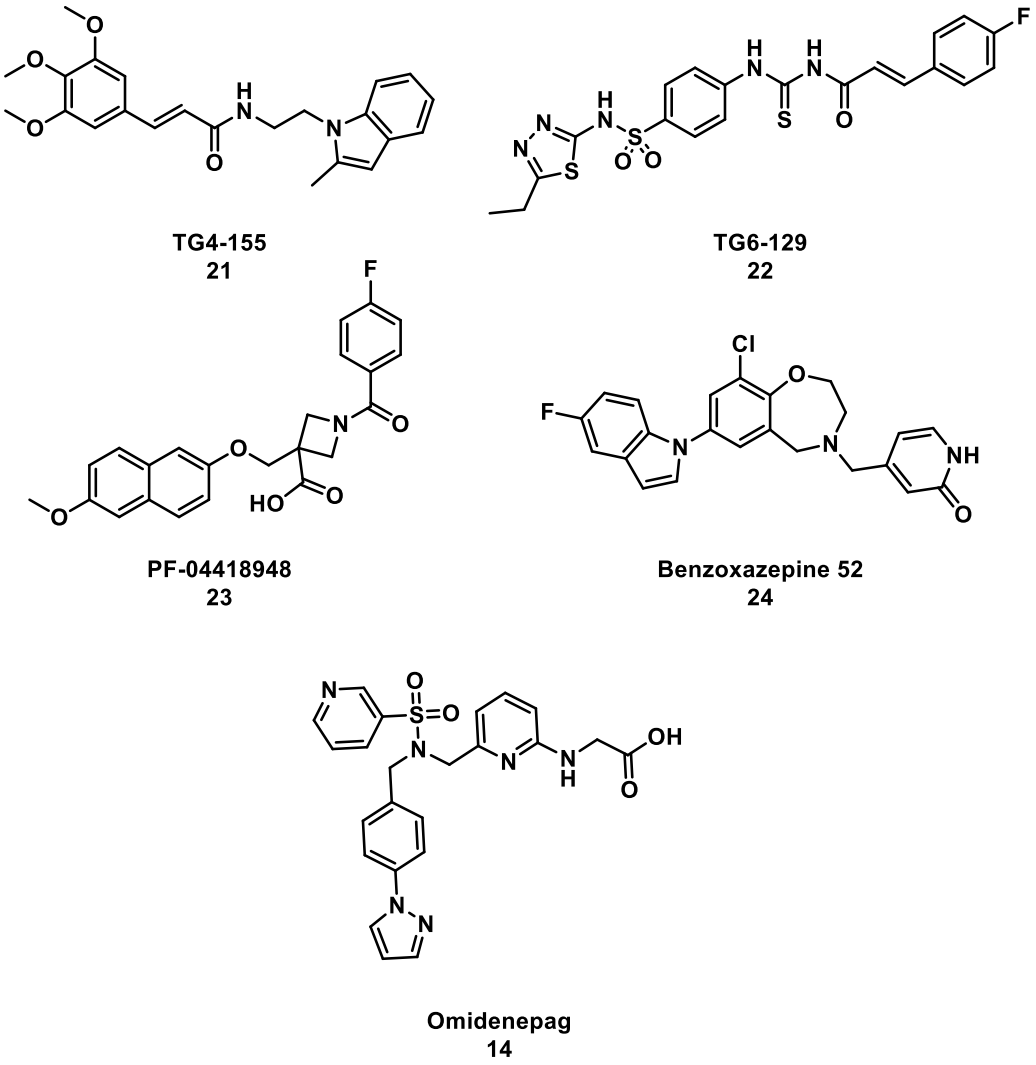

Figure 9- *Chemical structure of clinical orthosteric agonist omindenepag and examples of the four structural classes of EP_2 orthosteric antagonists reported in the literature: TG4-155, TG6-129, PF-04418949 and benzoxazepine 52 [117, 169-172].*

However, the development of safe and effective orthosteric drugs for clinical use can be challenging due to their tendency to cause side effects *in vivo* due to poor selectivity [148]. For example, TG4-155 displayed approximately 14-fold selectivity for EP_2 (K_D = 2.4 nM) over DP_1 (K_D =34.5 nM) in time resolved fluorescence resonance energy transfer (TR-FRET) cAMP assays using stably transfected human embryonic kidney (HEK)293 cells. Additionally, TG4-155 also displayed weak off target activity inhibiting the serotonin 5-HT_{2B} receptor with an IC_{50}= 2.6 μM and hERG with IC_{50}= 12 μM, assessed by either enzyme assays or radioligand binding assays [99]. hERG channels are essential voltage-

gated potassium ion channels primarily expressed in the heart and play a crucial role in heart muscle electrical activity regulation. Therefore, off target inhibition of hERG can trigger potentially fatal ventricular arrhythmia [176].

1.3.4 *Allosteric antagonists of EP_2.*

The development of allosteric modulators has the potential to minimise problems associated with orthosteric ligands through their topographically distinct mode of action, modulating the function of the receptor but, importantly, not engaging the orthosteric site.[148] The ligands bind in non-conserved regions between receptor subtypes, due to a lack of evolutionary pressure to engage with a common endogenous ligand (e.g. PGE_2), and can therefore achieve greater selectivity [177, 178].

In 2020 'Compound 1' the first prostaglandin EP_2 receptor antagonist with a reversible, agonist dependent allosteric mode of action was reported, herein termed **25a**, identified through HTS (see Figure 10) [179].

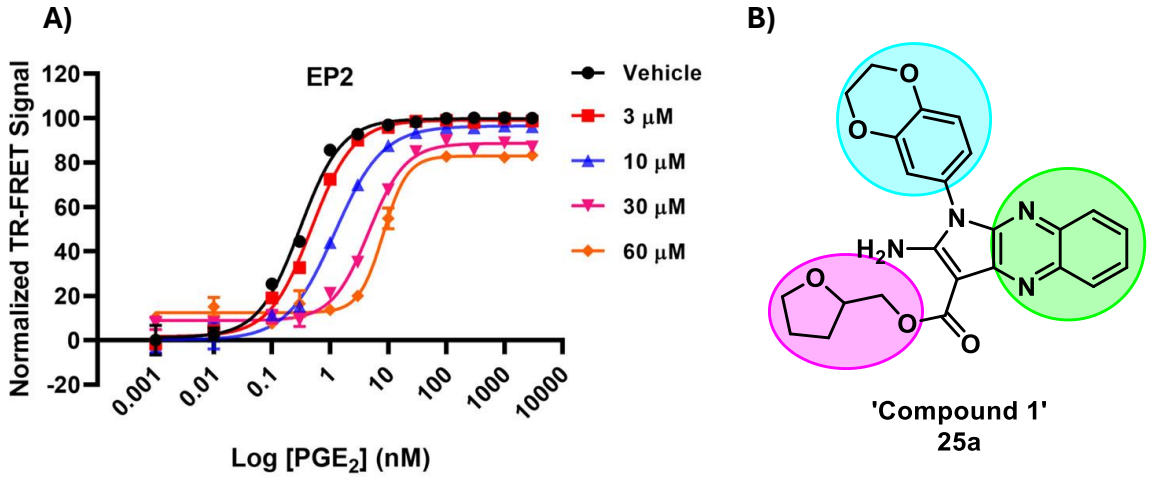

Figure 10*- *A) *Allosteric inhibition of EP_2 receptors by **25a** at various concentrations measured by cAMP production, PGE_2 was used as an orthosteric agonist in C6G-hEP_2 cells; both affinity and maximal response of PGE_2 is reduced (n=4).* ***B)*** *Structure of **25a** highlighting three regions of interest for structural modification; 1,4-benzodioxane (blue), tetrahydrofuran-2-yl methyl ester (pink) and quinoxaline (green) [179]. Adapted with permission from Jiang, et al. An Agonist Dependent Allosteric Antagonist of Prostaglandin EP_2 Receptors. ACS Chem. Neurosci. 2020. 11(10): p. 1436-1446. Copyright 2022 American Chemical Society.*

Antagonist **25a** displayed an insurmountable inhibition of cAMP accumulation in C6 glioma cells overexpressing human EP_2 when stimulated by multiple different EP_2 agonists, including PGE_2 (**10**), butaprost (**26**), evatanepag (CP533536, **27**), taprenepag (CP544326, **28**), ONO-AE1-259 (**29**) and ONO-4960073 (**30**) (see Figure 11) [179]. At 1-30 μM of **25a**, a graded rightward shift and downward displacement of all EP_2 agonist curves was produced, typical of an allosteric antagonist, with the extent of agonist potency and efficacy reduction dependent on the agonist employed. At an antagonist concentration of 30 μM butaprost, ONO-4960073, and ONO-AE1-259 had a stronger efficacy than PGE_2; however, the efficacy for ONO-AE1-259 and ONO-4960073 was similar. In the case of PGE_2 a 14-fold shift in EC_{50} was reported in the presence of **25a** (30 μM), with K_B = 2.6 ± 0.4 μM [179].

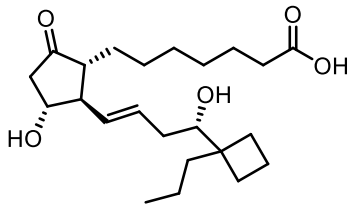

Butaprost (free acid)
26

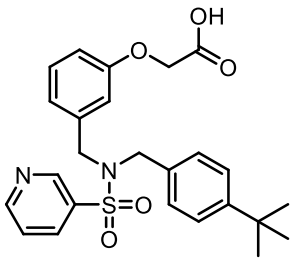

Evatanepag (CP533536)
27

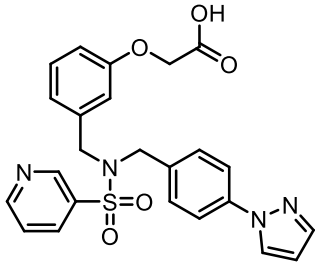

Taprenepag (CP544326)
28

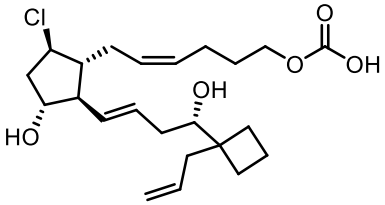

ONO-AE1-259
29

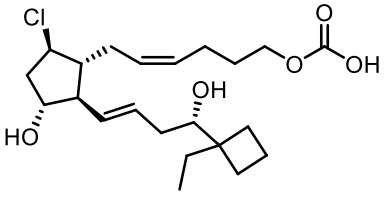

ONO-4960073
30

Figure 11- *Chemical structures of EP_2 orthosteric agonists butaprost, evatanepag (CP533536), taprenepag (CP544326), ONO-AE1-259 and ONO-4960073 [179].*

Due to the unique binding pocket of 'compound 1', not thought to be conserved across GPCR families, **25a** exhibited selectivity over other $G\alpha_s$ coupled prostaglandin receptors EP_4, IP and DP_1. At 30 μM **25a** showed a small reduction in the potency of PGE_2 at EP_4 receptors with a 2.20-fold-shift in the EC_{50} value with no change in the maximal response [179]. No effect on either the potency or maximal response of agonists BW245C and Iloprost was observed at both the DP_1 and IP receptors respectively upon addition of 30 μM **25a**. Jiang reported that out of 727 PubChem bioassays conducted, evaluating the selectivity of **25a** over other molecular targets, only a single assay involving $G\alpha_{15/16}$ mediated Ca^{2+} signalling reported inhibition by **25a** [179]. These results demonstrate that **25a** is a selective allosteric antagonist of EP_2 receptors and is unlikely to produce any off-target toxicity/side effects. Furthermore, an ATP-based luminescence assay, widely used to measure cytotoxicity in the drug discovery field as ATP is an indicator of metabolically active cells, determined that **25a** showed no observed cytotoxicity using doxorubicin as a positive control in BV2 microglia and C6G cells after 24 hr incubation [179, 180].

A homology model of *h*EP_2 was reported in the literature, developed using *h*EP_4 (PDB 5YWY) as a template, and predicting that the binding pocket of **25a** is located on the intracellular surface of EP_2, (see Figure 12) [179, 181]. Poor sequence homology (30 %) is reported between *h*EP_2 and *h*EP_4 receptors, with *h*EP_4 containing an additional 25 amino acids in ICL3 and a longer intracellular C terminus with an additional 108 amino acids reported [182]. This model predicts the binding pose of **25a** with the tetrahydrofuran methyl ester pointing up into the receptor pocket between TM2,3 & 6, the 1,4-benzodioxane moiety sits perpendicular to the receptor sitting between TM5 & 6, and the quinoxaline ring is solvent exposed directed away from the receptor. The enantiomer of **25a** docked into the homology model is not reported and no predicted ligand-receptor interactions are shown.

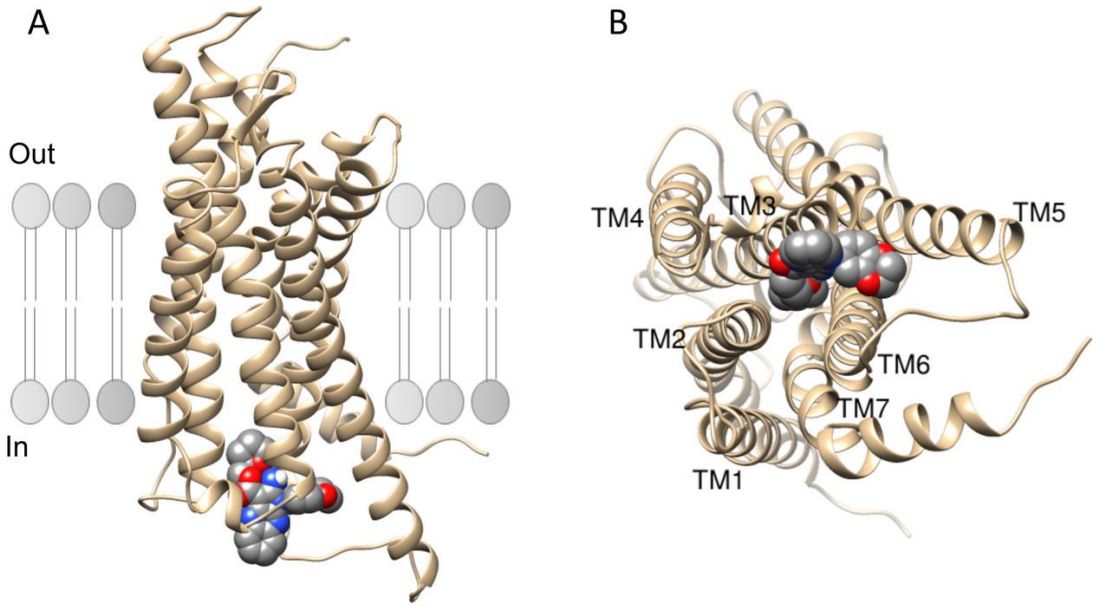

Figure 12- 25a *docked to a homology model of the human EP_2 receptor (by UCSF CHIMERA) including the predicted allosteric binding site.* ***A)*** *Structure is shown across the cell membrane.* ***B)*** *Structure looking up from the cytoplasmic surface of the receptor [179]. Reprinted with permission from Jiang, et al. An Agonist Dependent Allosteric Antagonist of Prostaglandin EP2 Receptors. ACS Chem. Neurosci. 2020. 11(10): p. 1436-1446. Copyright 2022 American Chemical Society.*

Multiple NAMs of GPCRs with similar binding mechanisms have been reported in the literature; these NAMs inhibit their receptors by binding to and stabilising the inactive conformation states and prevent coupling of the G proteins and β-arrestin eliminating downstream signalling. Examples include 'compound 15' (β2 adrenergic receptor (β2AR)), CCR2-RA-[*R*] (CC chemokine receptor 2 (CCR2)), Navarixin (C-X-C motif chemokine receptor 2 (CXCR2)) and Vercirnon (CC chemokine receptor 9 (CCR9)) [157, 158, 183, 184].

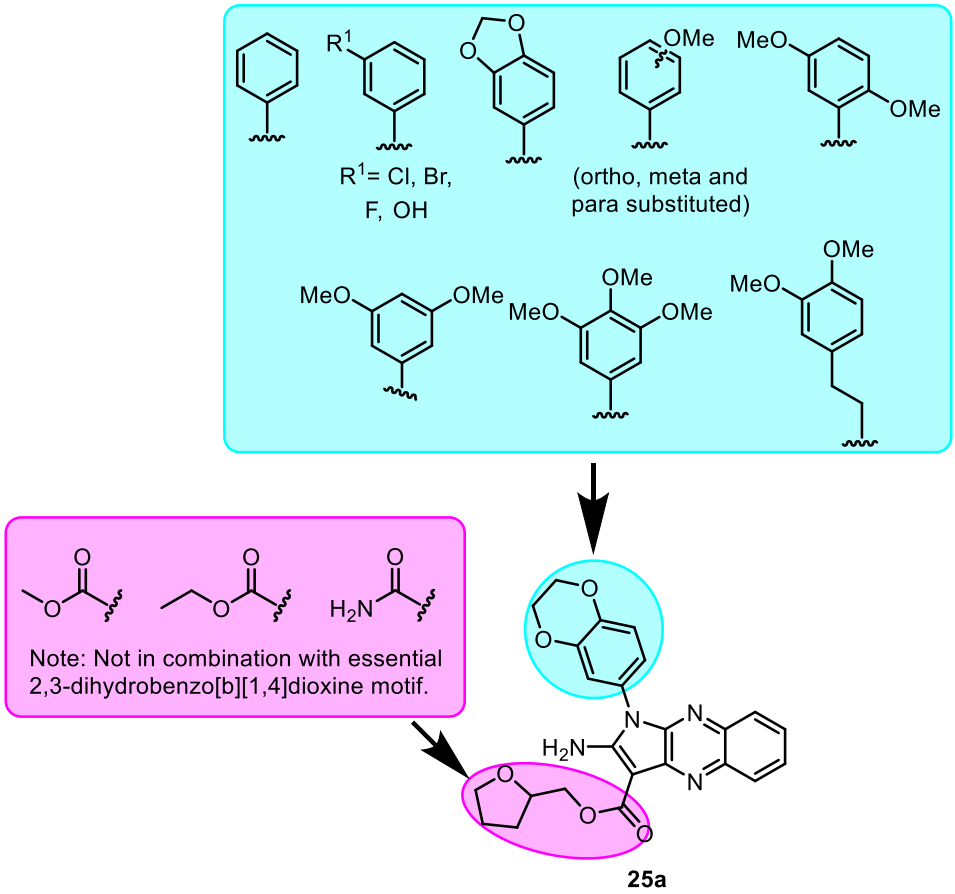

***Figure 13**- Diagram summarising the modifications made to **25a** reported in the literature [179].*

Fourteen analogues of **25a** were reported in the literature showing no modulation of potency nor reduction of maximal response in both PGE_2 and ONO-AE1-259 treated C6G-*h*EP_2 cells [179]. Most modifications were made at the 1,4-benxodioxane moiety inserting a variety of halides and ethers at various substitution patterns (see Figure 13). Three modifications were made to the tetrahydrofuran ester including insertion of a primary amide and replacement with a methyl/ethyl ester [179]. From this structure activity relationship (SAR) dataset it was determined that the 1,4-benzodioxane moiety is essential for ligand binding to EP_2 with any modifications in this region eliminating the ligands inhibitory activity. With such a limited SAR reported in the literature, there is a significant research opportunity for SAR dataset expansion exploring modifications at the three key regions of interest; 1,4-benzodioxane moiety, tetrahydrofuran methyl ester moiety and quinoxaline ring moiety (see Figure 13).

1.4 Exploring GPCR pharmacology- models and methods

1.4.1 Pharmacological models of ligand action at GPCRs

GPCRs can be modelled simply as molecular switches existing in dynamic equilibrium in unbound, bound and activated states. A simple two state model of drug receptor interaction is represented by:

$$D + R \rightleftharpoons DR \rightleftharpoons DR^*$$

Where R is the unoccupied receptor, DR is the occupied but inactive receptor and DR* is the active receptor. The ability of a ligand to bind to a receptor (D + R ⇌ DR) is termed the 'affinity' and the ability of a drug, following binding, to activate the receptor (DR ⇌ DR*) is termed the intrinsic efficacy [185, 186]. The affinity is dependent on the forward and reverse rates of interaction described by the law of mass action as association rate constant (k_{on}) and dissociation rate constant (k_{off}). At equilibrium both the forward and reverse binding rates are equal, and the receptor affinity of a ligand can be represented by the equilibrium dissociation constant (K_D). K_D is defined by the ratio of dissociation and association rate constants (k_{off}/k_{on}) and is related to the drug concentration and proportional receptor occupancy α according to the Hill-Langmuir equation: [187, 188]

$$\alpha = \frac{[D]}{[D] + K_D}$$

K_D is therefore also defined as the concentration of ligand to occupy 50 % of receptors at equilibrium (when K_D =[D], α=0.5). K_D can be referred to in different ways (e.g. K_B, K_i) depending on the type of experimental assay used to estimate it.

The two-state model provides a simplistic description of GPCR function and dynamics but does not incorporate the effector proteins and their allosteric effects on ligand binding, such as heterotrimeric G-proteins or β-arrestin, and is therefore incomplete.

The 'ternary complex model' was developed to account for these effectors (see Figure 14a). This model represents a three-way binding interaction that occurs at GPCRs; upon

ligand binding with the receptor a conformational change occurs, stabilizing the activate state and enabling allosteric coupling of the G-protein and formation of a ternary complex [189]. The 'extended ternary complex model' has evolved to incorporate both inactive and active receptor conformations (see Figure 14b). The consequence is that both low affinity (for the uncoupled receptor) and high affinity states (for the effector-coupled receptor) for agonist binding at the receptor can be measured under conditions which vary the amount of G protein coupling (e.g. presence of non-hydrolysable GTP nucleotides which disrupt R-G interactions). A 'high affinity agonist state' arises from the allosteric co-operativity between agonist and effector binding to the receptor in the ternary complex, and the extent to which agonists shift the equilibrium to receptor G protein coupling in this manner is a representation of their efficacy [190, 191]. This model was further modified to incorporate the thermodynamic interactions between the receptor and G-protein in the absence of an agonist to yield the 'cubic ternary complex model', (see Figure 14c) [192]. This model is the most complete theoretically but has limited experimental applications as measurement of the different populations is difficult to achieve. Furthermore, the activated GPCR can exist in several conformational states which is not considered by this model [193].

Finally the addition of an allosteric modulator to the system can be incorporated leading to the operational model of allosterically-modulated agonism (OMAN) which is a thermodynamically complete theoretical description of allosteric modulation of receptor activation, (see Figure 14d) [192, 194]. As for the cubic ternary complex model, in practice, measurement of all the individual rate constants in this model unambiguously is difficult to achieve.

A. $A + R \rightleftharpoons AR + G \rightleftharpoons ARG$

B.

$$\begin{array}{ccccc} AR + G & \rightleftharpoons & AR^* + G & \rightleftharpoons & AR^*G \\ \uparrow\downarrow & & \uparrow\downarrow & & \uparrow\downarrow \\ A + R + G & \rightleftharpoons & A + R^* + G & \rightleftharpoons & A + R^*G \end{array}$$

C.

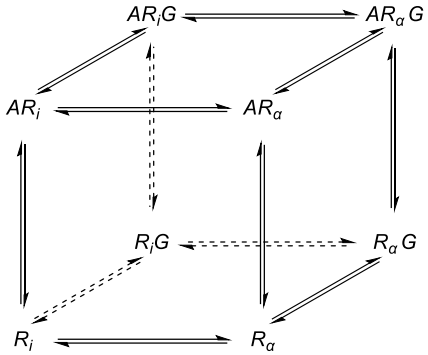

D.

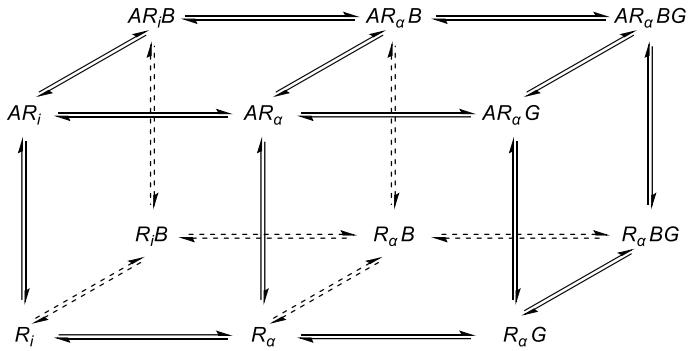

Figure 14*- Ternary complex models detailing interactions between receptors (R), agonists (A), G-proteins (G) and allosteric modulators (B).* ***A)*** *The original ternary complex model [189].* ***B)*** *The extended ternary complex model including constitutively active receptors (R*) [190, 191].* ***C)*** *The cubic tertiary complex model with receptors bound to either ligand (A) and/or a G-protein (G) and existing in either an active (R_α) or inactive (R_i) state [192].* ***D)*** *The cubic ternary complex model of allosteric modulation of receptor activation.*

1.4.2 Pharmacological quantification of receptor pharmacology.

There are two main aims of pharmacologically characterizing modulators of GPCRs experimentally: directly measuring the ligand binding parameters (e.g. K_D & B_{max}) and indirectly measuring receptor functional response in the presence and absence of different ligands (EC_{50}/IC_{50} & R_{max}).

B_{max} or maximal binding capacity represents the maximum number of molecules of a ligand (e.g. radiolabelled or fluorescent ligand probe) that can bind specifically to the receptor ligand binding sites and is often used as a representation of the total receptor density in the preparation. In a saturation binding assay that determines B_{max}, K_D is therefore the concentration of the probe that produces ½ B_{max} binding (concentration of drug to occupy 50% target population)[195]. As will be discussed below and in later chapters, K_D can also be estimated from competition binding studies or functional data for unlabelled ligands.

Both EC_{50} and R_{max} parameters are derived from agonist concentration-response curve analysis. The EC_{50}, a measure of agonist potency, is defined as the half maximal effective concentration of a ligand required to produced 50 % of its maximal biological response in a system, while R_{max} refers to the maximum response or effect a ligand can produce. Differences in agonist potency (EC_{50}) and full versus partial agonism (R_{max} differences) can then be assessed accordingly [195-197].

IC_{50} values represent the concentration of ligand that produces 50% of maximal inhibition in a binding or functional assay. They are typically used to determine the potency of a competing unlabelled ligand in preventing the binding of a fluorescent/radiolabelled ligand probe or, in a functional assay, the inhibition of a functional response by an antagonist to a specific concentration of agonist drug. For ligands that are competitive and reversible with the tracer in a binding assay format, the unlabelled ligand IC_{50} in binding studies can be converted to an estimate of its dissociation constant K_D using the Cheng-Prusoff correction [198-200].

1.4.3 Assays used to pharmacologically characterize ligand action at GPCRs

For GPCRs a wide variety of techniques have been developed to monitor ligand binding and functional responses at a cellular level. Direct ligand binding measurements have been most commonly studied using radioligand binding assays wherein membranes,

cells or tissue preparations containing the desired receptor of interest are incubated with radioligand (ligand containing a desired radioisotope) in the presence and absence of unlabelled competitor ligands to define non-specific binding. The specific relationship between the radiolabel emission and the amount of ligand present allows calculations of the amount of bound ligands directly, after separation of the receptor preparations (e.g. by filtration) from the free radiolabelled probe present in the assay solution [201]. However, due to the hazardous nature of radioligands (emission of ionizing radiation) and the inability to produce continuous experimental reads because of a bound/free separation step (new experiment for each timepoint required) the use of higher throughput fluorescent based methods has become more prevalent in drug discovery [202]. The use of resonance energy transfer within fluorescence based approaches provides a significant advantage as it enables continuous homogenous measurements to be taken over a time period, without bound/free separation and allowing kinetic as well as endpoint data to be collected. FRET is a technique utilising the transfer of non-radiative energy from one fluorescent molecule (donor fluorophore) to another (acceptor fluorophore) resulting in the release of detectable photons from the acceptor. Each fluorophore is required to have a distinct excitation and emission wavelength profile with a small degree of spectral overlap to enable FRET [203]. The proximity between donor and acceptor fluorophores is essential for FRET with an ideal range between 1-10 nm, this is most likely to occur during ligand-receptor interactions enabling real time measurements of ligand binding affinity. This distance constraint ensures that limited non-specific binding is detected, enabling binding studies to be performed without separation of the bound and free fluorescent ligands [204-206]. In GPCRs TR-FRET is commonly utilized to monitor various GPCR functions including second messenger accumulation (e.g. IP_1 and cAMP for calcium-sensing receptor CaSR), receptor oligomerization, receptor conformational changes and ligand binding [205, 207-210]. Typically receptors are N or C-terminally tagged (e.g. SNAP/CLIP/Halo-tag) with a fluorophore donor (e.g. europium, terbium or cyan fluorescent protein (CFP)) and the fluorescent probe/protein (e.g. Cy5, d2 or yellow fluorescent protein (YFP)) is labelled as acceptor [202, 208, 211].

Bioluminescence Resonance Energy Transfer (BRET) assays have a similar principle to FRET but rely on the production of donor emission by a luciferase enzyme tag on the receptor generating bioluminescence upon substrate addition. One example luciferase is the nanoluciferase (NLuc), a 19.1 kDa luciferase enzyme derived from a deep-sea shrimp *Oplophorus gracilirostris,* chosen for its high intensity, stability and long-term luminescence output [212]. NLuc catalyses an oxidation reaction converting its substrate furimazine (**31**) to furimamide (**32**)in its excited state; UV photons are emitted upon the decay of the amide to its ground state (see Figure 15a) [213, 214]. This change eliminates the need for fluorescent excitation (essential for FRET) and does not require expensive fluorophore labelling reagents (e.g. Terbium) [202, 215].

These assays can be conducted in both membranes and whole cells with a bioluminescent donor NLuc fused to either the C- or N-terminal tail of the receptor. Upon binding of an agonist to the GPCR a conformational change enables recruitment of the fluorescent probe bringing the luciferase and acceptor fluorophore into close proximity (<10 nm). Upon addition of substrate furimazine luminescence is produced and undergoes BRET to excite the acceptor fluorophore to emit light of a longer wavelength (see Figure 15b). The fluorescent tracer binding is quantified as the respective acceptor/donor emission ratios, termed BRET ratios. Upon insertion of an unlabelled intracellular ligand into the assay we would expect to see its competition with the fluorescent tracer for the binding site, leading to a reduction in the BRET ratio [216-219].

Fluorescent ligand BRET and FRET approaches for GPCR binding can then be analysed in the same manner as other binding studies. If the fluorescent probe concentration is varied (in the presence and absence of unlabelled competitor to determine specific binding), this generates a saturation binding curve from which the K_D and B_{max} for the probe can be estimated. Alternatively, competition binding studies using a set concentration of fluorescent probe can be performed, which measure competition for the probe with increasing concentrations of unlabelled ligand present. An IC_{50} value for the unlabelled ligand can then be determined from the concentration inhibition curves.

If it is assumed the competitor ligand acts competitively and reversibly with the probe, the IC_{50} values can be converted to a K_i estimate for the unlabelled ligands affinity, using the Cheng-Prusoff relationship [198].

In GPCRs NanoBRET has been used to monitor orthosteric ligand binding at Nluc-N terminally tagged β2AR using the fluorescent tracer (known binding ligand connected to a fluorophore via a linker) TAMRA-labelled β2AR antagonist alprenolol in HEK293 cells [217]. Another example includes the use of a NanoBRET ligand binding assay at NLuc-adenosine A3 receptor (A3AR) in HEK293 cells with two fluorescent ligands (antagonist xanthine amine congener linked to BODIPY (XAC-ser-tyr-X-BY630) or antagonist 1,2,4-triazolo[4,3-a]quinoxalin-1-one linked to BY630 (AV039)) to determine the rate constants of three unlabelled orthosteric antagonists (PSB-11, compound 5 and LUF7565) [206]. NanoBRET competition binding assays utilising a fluorescent tracer for the binding site of interest can also be exploited to determine unlabelled allosteric ligand binding affinities for desired GPCRs (see Figure 15b) [216-219].

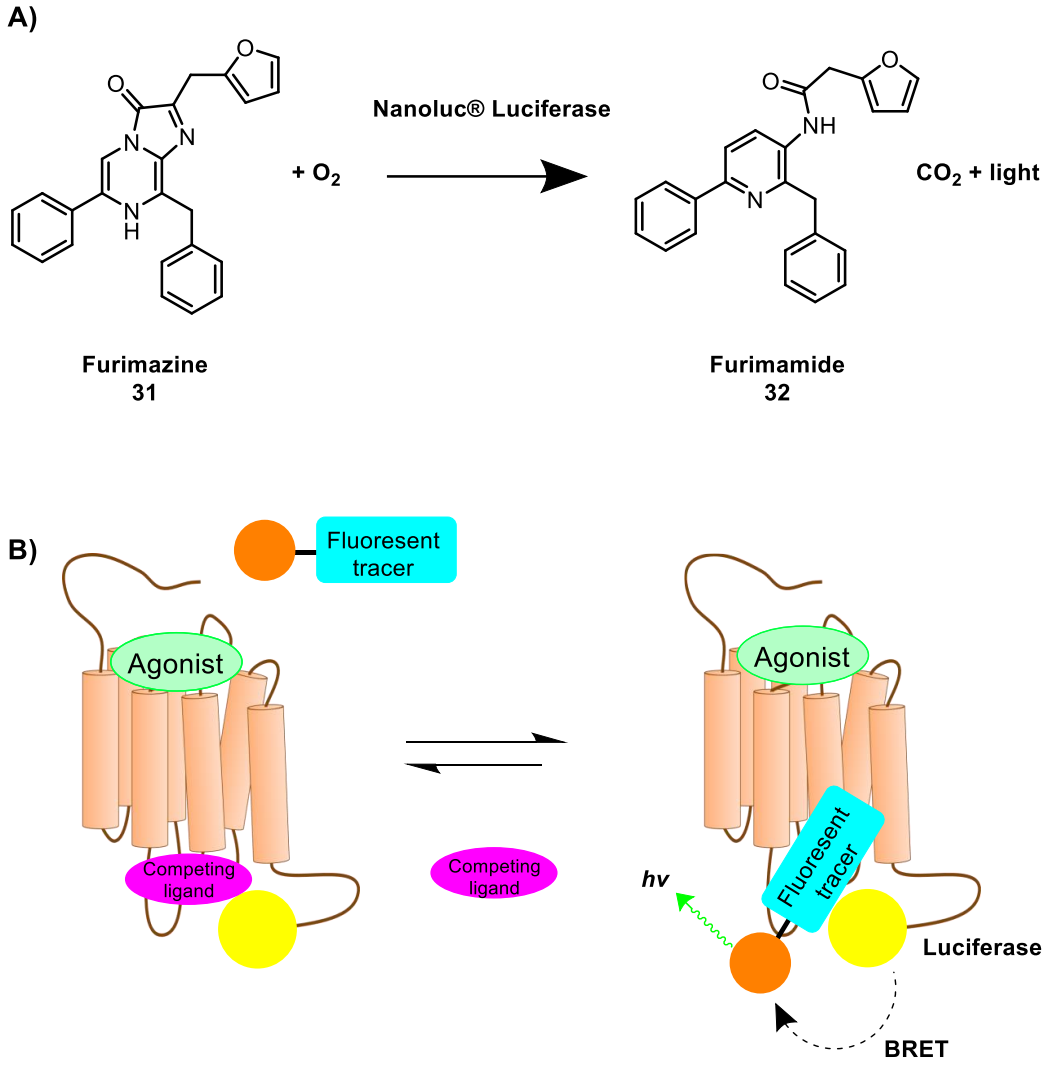

Figure 15- *A) Oxidation reaction of furimazine to furimamide catalysed by NanoLuc® luciferase.[220] B) Diagram of NanoBRET competition binding assay with a GPCR C-terminally tagged with luciferase in the presence of a fluorescent probe and competing unlabelled ligand [216-219]. Made using ChemDraw 19.1.*

Cell-based functional assays for GPCR activity can be performed in a wide variety of formats (for example, measurements of second messenger of downstream kinase cascade activity, G protein activation, reporter gene, or phenotypic responses). For analysis of ligand pharmacology, formats which measure the direct protein-protein interaction between the receptor of interest, and a downstream effector protein, can be useful. For example, NanoBiT complementation assays have been developed which monitor the recruitment of either heterotrimeric G-proteins or β-arrestins to the receptor providing an insight into downstream signalling [213, 221]. The NanoBiT

system utilises a NLuc split into two subunits, the 1.3 kDa peptide (SmBiT), and the 18 kDa (LgBiT) polypeptide which can weakly associate (K_D= 190 μM) and reversibly assemble into a functional NLuc complex dependent on the interaction characteristics of the proteins of interest [221, 222]. The LgBiT subunit is fused to the C-terminus of the receptor of interest and the effector is N-terminally tagged to SmBiT (see Figure 16) [222]. Effectors include β-arrestins and mini-Gα proteins that preserve the receptor-G protein binding interface [223, 224].

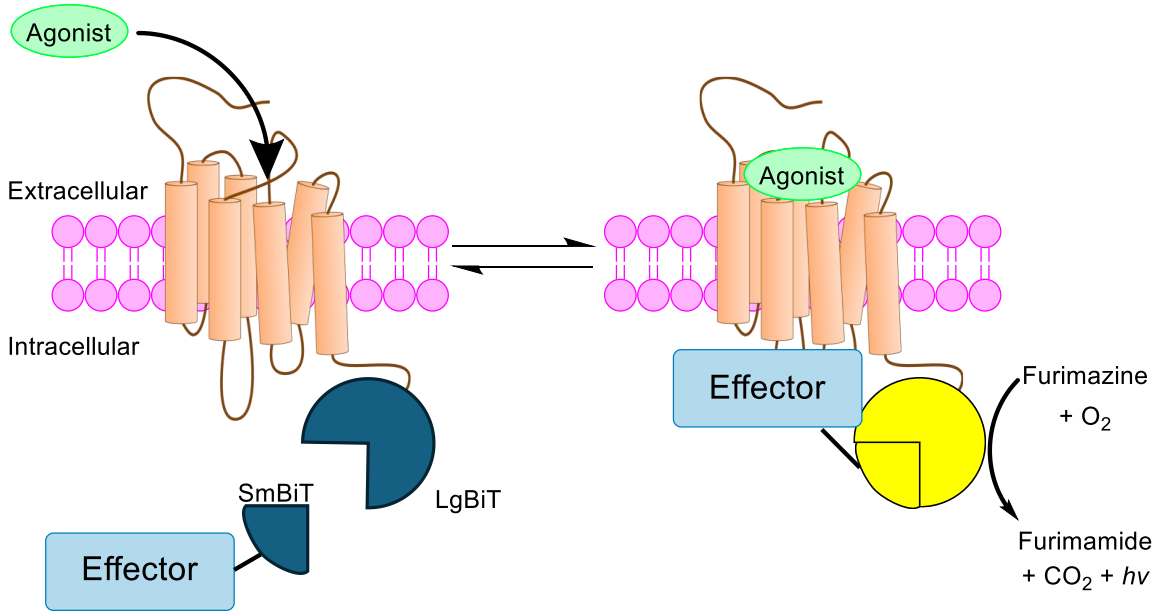

Figure 16- *NanoBiT luminescence complementation assay measuring β-arrestin or mini-Gα recruitment at GPCRs. The receptor recruits the effector, either constitutively or upon agonist simulation, which results in enzyme complementation and the production of luminescence on addition of furimazine substrate [221, 222]. Made using ChemDraw 19.1.*

Under basal conditions low level luciferase activity is observed, yet upon recruitment of the effector, either constitutively or upon agonist stimulation, the SmBiT and LgBiT subunits are brought into close proximity enabling assembly of the luminescent complex (see Figure 16). Upon addition of substrate furimazine which is converted to furimamide by NanoLuc luminescence is produced; this luminescence is proportional to GPCR activation and/or effector recruitment [222]. The mode of action of modulatory ligands can be assessed by generating agonist concentration response curves (CRCs) in the absence and presence of a range of modulator concentrations and calculating the

agonist EC_{50} and R_{max} values in each case. Alternatively functional antagonist IC_{50} values can also be determined through production of inhibitor concentration inhibition relationships in the presence of a set concentration of agonist [222, 225].

1.5 Thesis aims and objectives

This thesis has highlighted the key role of the prostanoid EP_2 receptor in the development and progression of chronic inflammatory diseases and has discussed their modulation as a potential therapeutic approach. With COX inhibitors not being FDA approved for the treatment of inflammation in cancer, AD, PD and IBD due to their associated adverse cardiovascular and GI effects, there is currently an unmet need for anti-inflammatory therapeutics [129, 130]. The improvement in selectivity and potential for inducing signalling bias of EP_2 NAMs for either G-protein or β-arrestin2 signalling, compared to current orthosteric antagonists, is proposed to eliminate toxic adverse effects and produce a more successful clinical candidate [226, 227]. Additionally, the complexity of the EP_2 receptor's role in disease pathogenesis and acute/chronic inflammatory processes means ongoing research to understand the intricacies of EP_2 signalling is essential to mitigate disease progression and guide development of novel therapeutic agents.

The recent publication of NAM **25a** targeting the EP_2 receptor provides a starting point for the development of a novel SAR dataset which serves as the main focus of this project [179]. The SAR dataset reported in the literature demonstrated a clear research gap; three modifications at the ester moiety, methyl-/ethyl ester and primary amide, were reported but were not present in combination with essential 2,3-dihydrobenzo[*b*][1,4]dioxine motif for EP_2 inhibition [179]. Therefore, resynthesis and further modification of these esters and amides analogues in combination with 2,3-dihydrobenzo[*b*][1,4]dioxine would explore a currently unknown branch of theorised EP_2 NAMs.

Firstly, the development of a synthetic route to novel analogues of **25a** was required to generate our compound library. The tetrahydrofuran-2yl methyl ester moiety of **25a** was the focal point of structural modifications, reported as the moiety occupying the deepest region of the EP_2 allosteric pocket from the literature *h*EP_2 homology model, whilst maintaining the essential binding 2,3-dihydrobenzo[*b*][1,4]dioxine motif [179]. Initial proposed novel analogues of **25a** aimed to vary the solubility and lipophilicity of our ligands as well as exploring potential new ligand-target interactions (see Figure 17, further detailed in Chapter 2.1).

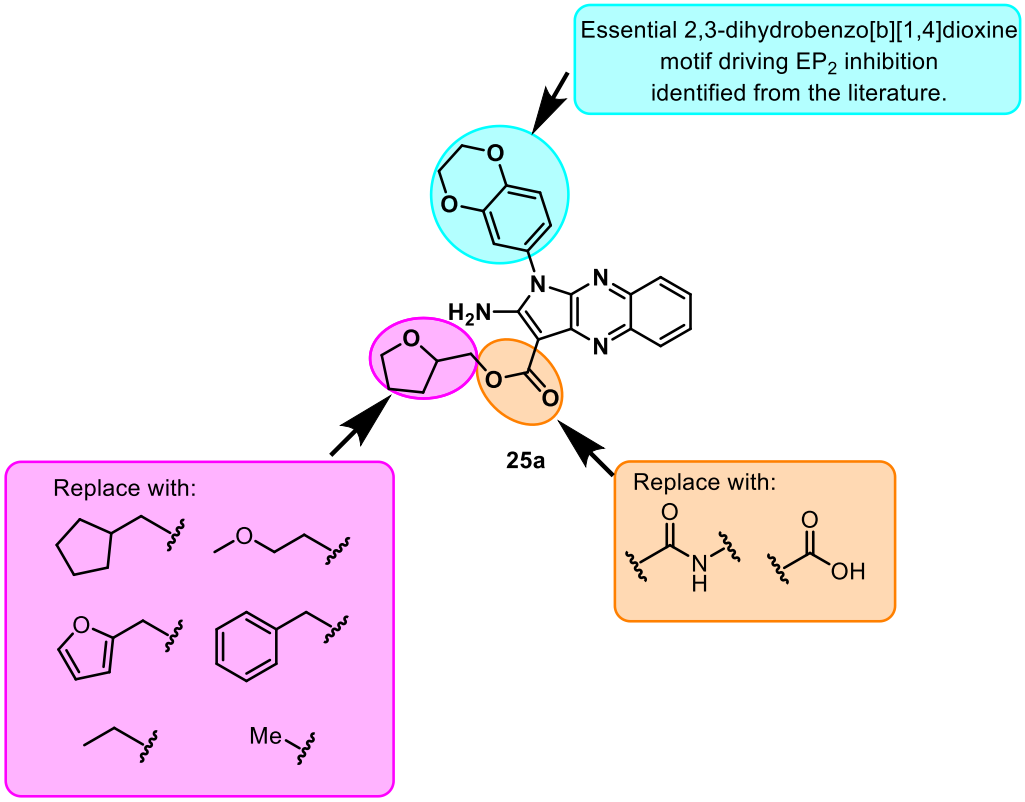

Figure 17- *Initial proposed synthetic lines of enquiry to produce a novel compound library of* ***25a*** *analogues. The removal of electronegative oxygen atoms at the tetrahydrofuran increases ligand lipophilicity (reducing aqueous solubility) and removes the ability to form hydrogen bonds. The methyl- and ethyl- esters explore the impact of decreasing ester chain length and the introduction of a benzyl ester explores binding site toleration of larger functionality. Additionally, introduction of aromaticity enables the formation of non-covalent interactions such as π- π stacking. Breaking of the tetrahydrofuran ring introduces a flexible alkyl chain whilst maintaining the hydrogen bonding oxygen. Replacement of the ester with a carboxylic acid or amide introduces a hydrogen bond donor hydrogen atom and explores the impact of removing the ester functionality.*

Pharmacological characterisation of this library, utilising both NanoBRET competition binding assays and NanoBiT complementation assays, would enable identification of the key ligand regions driving modulator binding and provide an insight into the modulator mechanism of action [216-219, 221, 222]. Furthermore, development of SAR could produce an analogue with improved binding affinity and functional potency, compared with **25a**, which could be advanced into a therapeutic agent.

The homology model presented by Jiang et. al. was developed from the crystal structure of related protstanoid receptor *h*EP_4. Utilising *h*EP_4 as a template for *h*EP_2 model development is not ideal having produced a low-quality model due to the poor sequence homology between these receptors (30 %); the respective amino acids and their conformations lining the predicted binding pocket may not be conserved across receptors [228]. Therefore, developing a new *h*EP_2 homology model, based upon the recently reported cryo-electron microscopy (cryo-EM) structure of the PGE_2-bound EP_2-$G\alpha_s$ complex (PDB 7CX2) and evaluating it using the expanded SAR dataset would produce a more accurate visualization of the EP_2 allosteric pocket bound to the NAMs [160].

Chapter 2- Synthesis of series 1

2.1 An introduction to series 1

Development of an allosteric antagonist targeting the emerging pro-inflammatory GPCR EP_2 is an attractive approach for therapeutics relating to both cancer and a variety of neurodegenerative diseases where chronic neuroinflammation may be mediated by the prostanoid system. The first reported ligand **25a** with this desired mechanism of action was identified from a high-throughput screening approach in 2020 by the Dingledine group, however, no synthetic route was published [179]. **25a** displayed insurmountable inhibition selectively at the EP_2 receptor, with efficacy varying dependent on the agonist employed, measured using a cAMP FRET assay monitoring cAMP production (see Chapter 1.3.4) [179]. Initial SAR data reported in the literature was limited to fourteen analogues of **25a**, with focus on modifications at the 2,3-dihydrobenzo[*b*][1,4]dioxine moiety. The alteration of this region was not tolerated and no additional active NAMs of the EP_2 receptor were identified in this screen [179].

The initial homology model developed in the literature predicted the binding pocket of **25a** to be at the intracellular surface of the EP_2 receptor (see Chapter 1.3.4) [179]. As a result **25a** is predicted to have a similar mechanism of action to previously reported NAM 'compound 15' which stabilises the inactive conformation of the β2-adrenoceptor (β2AR) preventing recruitment of both the Gs heterotrimeric G-protein and β-arrestin [158]. The proposed binding conformation of **25a** with EP_2 has the ester moiety oriented into the deepest region of the binding pocket between TM α-helices 2,3 and 6, the 2,3-dihydrobenzo[*b*][1,4]dioxine moiety posed perpendicular to the receptor towards TM5 and the quinoxaline ring is solvent exposed directed away from the receptor [179]. Due to the tight SAR around the 2,3-dihydrobenzo[*b*][1,4]dioxine motif you might expect the homology model to yield a different binding pose, for example with this moiety occupying the deepest binding pocket between the TM α-helices 2,3 and 6. Conducting an expanded SAR study focused on the ester moiety (currently occupying this pocket in the literature homology model) would provide further experimental evidence to prove or disprove this theory.

The predicted conformation of the ester moiety deep within the pocket was identified as an ideal starting point to explore ligand-receptor interactions and in theory presented a straightforward synthesis route to analogues. Only four examples of ester modifications were present in the literature SAR study but did not contain the essential 2,3-dihydrobenzo[*b*][1,4]dioxine moiety and displayed no inhibitory activity at EP_2. Therefore, in addition to resynthesis of **25a**, a series of ester analogues were designed and synthesised maintaining the key 2,3-dihydrobenzo[*b*][1,4]dioxine motif. A summary of the proposed SAR mini-library (compounds **25a**-**i**) and compound physiochemical properties is provided (see Table 2) [179]. Isolation of the *R*- and *S*- enantiomers of **25a** was not conducted to enable direct comparison to the literature data; a racemic mixture was utilised by Jiang et. al. [179].

This series has inserted a variety of new functionalities to modify ligand properties such as solubility and lipophilicity, as well as exploring potential new ligand-target interactions. Six esters were designed based on the original tetrahydrofuran-2-yl methyl ester in **25a**. Firstly the potential hydrogen bonding acceptor (HBA) oxygen atom was removed in the cyclopentylmethyl ester **25e** increasing lipophilicity (cLogP increase of 1.27, see Table 1) whilst maintaining the five membered ring system. In contrast, the 2-methoxyethyl analogue **25f** contains a linear more flexible alkyl chain maintaining the position of the HBA oxygen. The methyl- and ethyl- esters **25i**/**b** explore the impact of decreasing the ester chain length whilst the introduction of a larger benzyl ester **25h** explores the toleration of larger functionality in the binding pocket. Additionally, the introduction of aromaticity in both the furan-2-yl ester **25g** and the benzyl **25h** could enable engagement in non-covalent interactions. For example, π- π stacking occurs when the aromatic ring of a drug molecule stack with aromatic amino acid residues in the binding pocket, including Phe, Tyr and Trp [229, 230].

Furthermore, this series explores some modifications at the 2,3-dihydrobenzo[*b*][1,4]dioxine moiety, which was previously identified as an essential binding motif [179]. The shortening and breaking of the 1,4-dioxane bridge afforded analogues **25m**/**n** respectively, these each maintain two HBA oxygens whilst varying

their rigidity, positioning and flexibility due to differences in rotational freedom. Three compounds described in the literature **25j**-**l**, that demonstrated no inhibition of cAMP production at the EP_2 receptor, were resynthesized to act as negative controls for our pharmacological characterisation assays (see Chapter 1.3.4) [179]. These ligands contain *O*-methyl groups at various substitution patterns (3,5-dimethoxy, 2,5-dimethoxy and 3,4,5-trimethoxy) in place of the 2,3-dihydrobenzo[*b*][1,4]dioxine ring system which could all act as potential HBAs.

The corresponding amide analogues **25o**-**t** of esters **25a**,**b**,**e**-**h** were designed for series one. The insertion of an amide could increase ligand binding affinities and functional potency at the EP_2 receptor resulting from their stronger dual hydrogen bonding capability; the carbonyl group acts as a HBA and the amine a hydrogen bond donor (HBD) [231]. Direct comparison between ester and amide analogues with the same substituents would enable us to quantify any resulting change in NAM pharmacology. Furthermore, replacement of an ester with an amide would improve the metabolic stability of the compounds and reduce renal elimination/excretion of the drug [232]. Due to the electronic resonance effect of nitrogen donating electrons into the carbonyl, the amide bond is a poorer electrophile and less susceptible to nucleophilic attack and hydrolysis by liver enzymes such as carboxylesterases [233]. However, a successful synthetic approach to these amide analogues has not yet been identified and the desired compounds were not isolated.

An additional five compounds **25u**-**y** were purchased from Life Chemicals (Munich, Germany) to further expand the compound library. These analogues were deemed suitable for pharmacological characterization as they all contain the pyrrole[2,3,-*b*]quinoxaline core but have modifications at the 2,3-dihydrobenzo[*b*][1,4]dioxine and/or tetrahydrofuran-2-yl methyl ester. **25u**/**v**/**x** all maintain the ester but have a 2-ethyl thiophene, benzo[*d*][1,3]dioxole and 2-methoxyethyl group respectively in place of the benzyl dioxane. All three compounds contain an extended alkyl chain in this region, increasing the flexibility and potentially accessing new conformations within the binding pocket to improve binding affinity and selectivity. They also contain a minimum of one

HBA molecule, either oxygen or sulphur, whilst varying aromatic ring size in **25u** & **25v** or removing it entirely in **25x**. The substitution of the ester with an amide is explored by **25w**/**y**, primary and secondary amides typically exhibit stronger hydrogen bonding than esters.[234] Ligand **25w** has the same benzo[*d*][1,3]dioxole present in **25n** but contains an *N*-2-isopropoxyethyl amide in place of an ester. In contrast, **25y** contains a primary amide at the ester position and a 3-methyoxy phenyl group in place of the 2,3-dihydrobenzo[*b*][1,4]dioxine.

***Table 2**-Series 1 compound library structures including their calculated molecular weight, number of H-bond donors/acceptors, LogP, LogS, number of rotatable bonds and calculated total polar surface area (calculated using Marvinsketch version 25.1.75 by Chemaxon). Compounds in red were not successfully synthesized.*

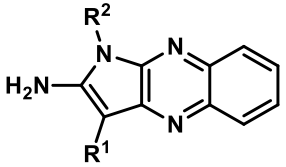

Compound	R^1	R^2	Molecular weight	H-bond acceptors	H-bond donors	LogP	LogS	Rotatable bonds	Total polar surface area (Å^2)
25a	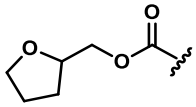	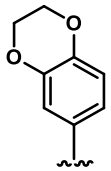	446.46	9	1	3.59	-5.31	6	110.7
25b	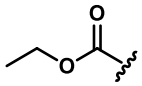	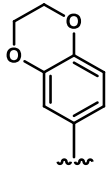	390.40	8	1	3.70	-5.09	6	101.5
25c	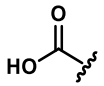	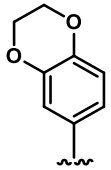	362.35	8	2	2.72	-4.62	3	112.4
25d		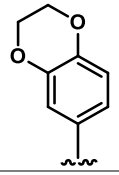	343.35	7	1	2.37	-4.84	2	99.0

25e	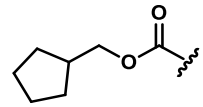	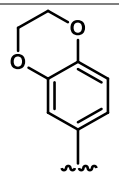	444.49	8	1	4.86	-6.68	6	101.5
25f	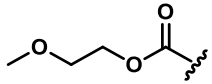	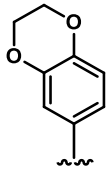	420.43	9	1	3.19	-4.72	8	110.7
25g	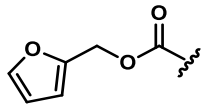	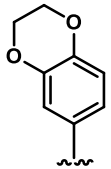	442.43	9	1	4.08	-5.76	6	114.6
25h	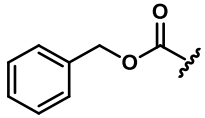	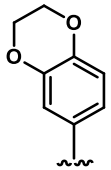	452.47	8	1	5.13	-6.39	6	101.5
25i	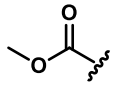	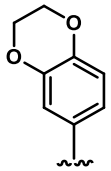	376.37	8	1	3.36	-4.79	5	101.5
25j	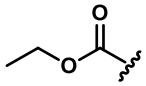	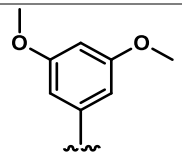	392.42	8	1	3.88	-4.61	10	101.5
25k	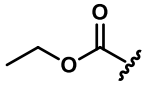	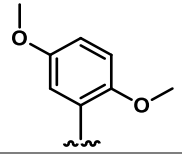	392.42	8	1	3.88	-4.61	10	101.5

25l	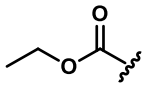	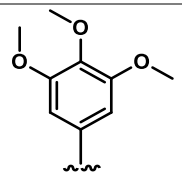	422.44	9	1	3.62	-4.55	12	110.7
25m	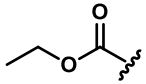	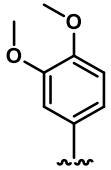	392.42	8	1	3.88	-4.61	10	101.5
25n	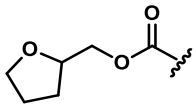	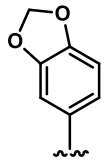	432.44	9	1	3.95	-5.31	6	110.7
25o	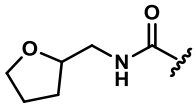	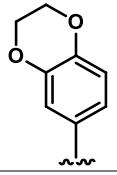	445.48	9	2	2.34	-5.27	5	113.5
25p	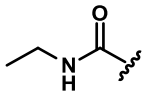	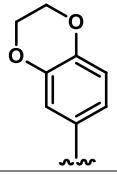	389.42	8	2	2.45	-4.96	5	104.3
25q	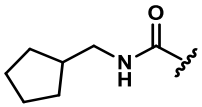	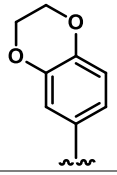	443.51	8	2	3.61	-6.54	5	104.3

25r	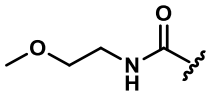	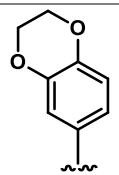	419.44	9	2	1.94	-4.68	7	113.5
25s	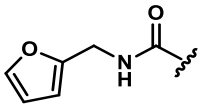	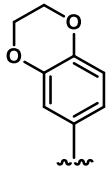	441.45	9	2	2.83	-5.71	5	117.4
25t	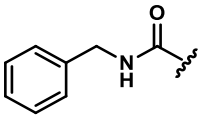	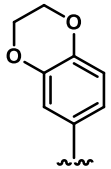	451.49	8	2	3.88	-6.25	5	104.3
25u	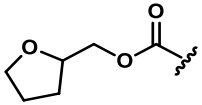	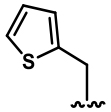	408.48	8	1	4.19	-4.76	6	92.3
25v	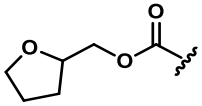	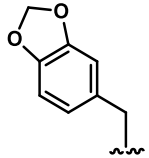	446.46	9	1	4.05	-5.11	6	110.7
25w	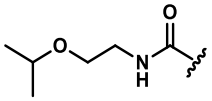	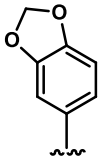	447.50	9	2	3.06	-5.10	8	113.5
25x	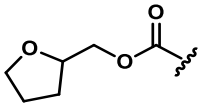	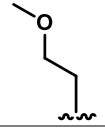	370.41	8	1	2.42	-3.03	8	101.5

25y	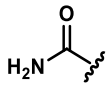	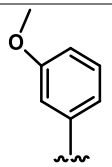	333.35	7	2	2.29	-4.27	4	109.1

Included in the above table are seven calculated parameters known to contribute to the physiochemical properties of our ligands. Lipinski's rule of 5 was developed to set 'drugability' guidelines for new molecular entities and was based on trends in the world drug index database containing ~2,000 drugs. It was observed that poor absorption or permeation is more likely when a molecule has more than 5 H-bond donors, 10 H-bond acceptors, a molecular weight >500 and the calculated LogP value >5 across this database [235]. Molecules that conform to these rules are thought to be more easily converted to orally active drugs. LogP is defined as the logarithm of the octanol-water partition coefficient and is a measure of the lipophilicity of a molecule, the higher the LogP value the more hydrophobic the compound and the less soluble in water. This single property impacts many aspects of drug pharmacokinetics such as aqueous solubility, absorption from the gastrointestinal tract, phospholipid membrane permeability, distribution via blood, blood-brain barrier (BBB) permeation and metabolism/clearance from the body [236]. Compounds in series one possess a wide range of calculated LogP values with over 1000-fold difference (1.94- 5.13). Except for **25h**, which has a LogP >5, the remaining analogues in series 1 fit within Lipinski's proposed rules and are predicted to display high drug-likeness. The six amide analogues are predicted to have a much lower range of LogP values between 1.94-3.88 compared to 3.36-5.13 for their corresponding ester analogues. This is a result of the amides stronger dual hydrogen bonding capability increasing water solubility. Whilst strict adherence to Lipinski's guidelines is important for developing a drug with a good pharmacokinetic profile (including absorption, distribution, metabolism and excretion) at this stage of a drug discovery campaign the development of ligands which fall outside the rule of five should be considered to probe the extremes of ligand-receptor interactions. However, ligand properties should still be compatible with pharmacological assay conditions to produce accurate and comparable data.

Physiochemical properties outside of Lipinski's rule of five have also been reported, (see Table 2). Rotatable bonds, single bonds in a molecule which can freely rotate around their axis, are a key determinant of a molecule's conformational flexibility. A more flexible ligand can more effectively induce optimal conformational changes within

the receptor binding pocket to create a more stable, high affinity complex [237, 238]. Molecules with too many rotatable bonds may be too flexible to bind tightly to their target, while molecules with too few are too rigid to adapt to the binding pocket [239, 240]. Whilst there is no set target number of rotatable bonds, a study suggests that drug candidates with 10 or fewer rotatable bonds and a polar surface area (PSA) equal to or less than 140 $Å^2$ will have a high probability of good oral bioavailability in rat studies [240]. In series 1, only analogue **25l** exceeds this limit.

The total surface area (tPSA) of a molecule that is contributed by its polar atoms (oxygen, nitrogen and attached hydrogens), is a crucial metric in drug discovery for the prediction of drug absorption, membrane permeability and BBB permeation [241]. Typically, a molecule with high tPSA >140 $Å^2$ has poor membrane permeability whilst those with <60 $Å^2$ are more likely to cross the BBB resulting in either therapeutic and/or adverse effects [242]. All analogues synthesized in series 1 are within the ideal PSA range.

LogS is defined as the logarithm of the intrinsic aqueous solubility of a compound, typically measured in mol/L, and is a key predictor of drug absorption. The higher the LogS value the greater the absorption in the gastrointestinal tract after oral administration. However, molecules that are too polar with high LogS values can struggle to cross the phospholipid bilayers of the cell membrane and reach their intended site of action [243]. Consequently, most drugs have reported LogS values between -5 and -1[244]. Series 1 has a predicted LogS range between -3.03 and -6.60 with twelve compounds outside of the desired range with LogS values <-5 including literature NAM **25a**. As a result, we can expect poor aqueous solubility for these analogues, likely a result of the large MW of these compounds, which could lead to poor drug absorption and permeation in vitro and in vivo studies.

2.2 Development of a convergent synthetic route to 25a and analogues.

Initial work was focused on the development of a synthetic route to the desired analogues; no synthesis was published in the literature with **25a** being obtained from a chemical library [179]. The synthesis of a 1,3-substituted pyrrolo[2,3-*b*]quinoxaline has been previously reported in the literature and formed the basis of our synthetic approach. In 2004 Obafemi and Pfleiderer first reported a nucleophilic aromatic substitution (S_NAr) reaction of 2,3-dichloroquinoxaline with malonitrile and ethylcyanoacetate [245]. The resulting product could then undergo cyclisation to form the desired pyrrolo-[2,3-*b*]quinoxalines as reported by Takahashi et. al. in 1970 [246]. A convergent approach based upon this literature was initially conducted, with the aim of inserting the variable ester functionality at the final reaction step (see Scheme 1).

Scheme 1*- Attempted development of a convergent synthesis to* ***25a*** *[245, 246].*

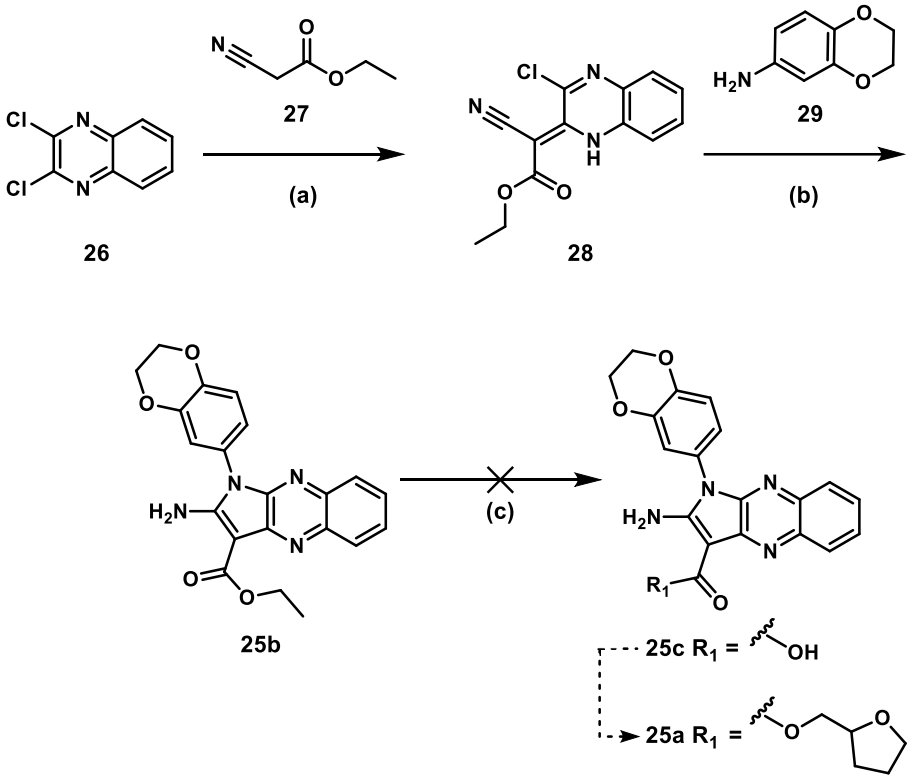

Reagents and conditions*- (a) Ethyl cyanoacetate, 60% NaH mineral oil, DME, 3h, rt-80 °C. 65-79 %, (b) Amine, EtOH: tetrahydrofuran (THF) (3:1), 19h, 78 °C. 45-91%, (c) NaOH/LiOH, THF/Water (1:1), 72 h, 70 °C.*

The first synthetic step in scheme 1 involved an S_NAr reaction of 2,3-dichloroquinoxaline (**26**) with ethyl cyanoacetate (**27**) to afford ethyl (*Z*)-2-(3-chloroquinoxalin-2(1*H*)-ylidene)-2-cyanoacetate (**28**) [245]. A cyclisation reaction with 2,3-dihydrobenzo[*b*][1,4]dioxin-6-amine (**29**) generated ethyl 2-amino-1-(2,3-dihydrobenzo[*b*][1,4]dioxin-6-yl)-1*H*-pyrrolo[2,3-b]quinoxaline-3-carboxylate (**25b**) [246]. Hydrolysis of **25b** was attempted using numerous hydrolysing agents, including NaOH and LiOH both with and without heating as well as acid catalysed conditions with 2M and 6M aq. Hydrochloric acid (HCl), but failed to yield the corresponding carboxylic acid **25c** [247, 248]. This work was undertaken by students Mohamed Khaki and Khai Sing Lim (School of Pharmacy, University of Nottingham) [249, 250]. Whilst this synthetic approach was found to be unviable, the ethyl ester intermediate **25b** was identified as a suitable analogue to be taken forward into pharmacological characterisation.

Intermediate **28** was determined to be present wholly in its enamine tautomer when characterised by ^{1}H NMR (see Figure 18a/b) [251]. This was identified due to the presence of the N***H*** broad peak at 14.50 ppm with an integration of ~1 and the lack of a hydrogen peak for the 2-cyanoacetate position, predicted at approximately 4.61 ppm. This is further supported by the ^{13}C nuclear magnetic resonance (NMR) which reported the cyanoacetate-2-C at shift 69.6 ppm compared to the predicted shift of 32.7 ppm for the methylene imine, calculated by CS ChemNMR Pro (see Figure 18c). This downfield shift is due to the increased de-shielding effect in a sp^2 hybridized carbon double bond vs the sp^3 hybridised single bond, resulting from a difference in the electronegativity and anisotropic effects of the pi system. The preference for the enamine tautomer was reported in the literature in both the solid state and in deuterated chloroform ($CDCl_3$) and dimethyl sulfoxide (DMSO-d_6), confirmed by ^{13}C-nuclear magnetic resonance (NMR) and ^{1}H-NMR experiments [245]. The presence of an intramolecular hydrogen bond between the carbonyl/nitrile and NH was postulated in the literature to stabilise the enamine tautomer shifting the equilibrium to favour its formation [245]. All the S_NAr substituted quinoxaline intermediates synthesized were identified exclusively in the enamine form.

A)

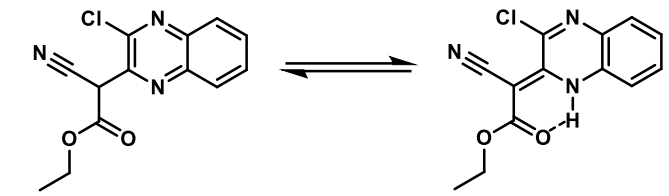

Methyline imine tautomer Enamine tautomer

B)

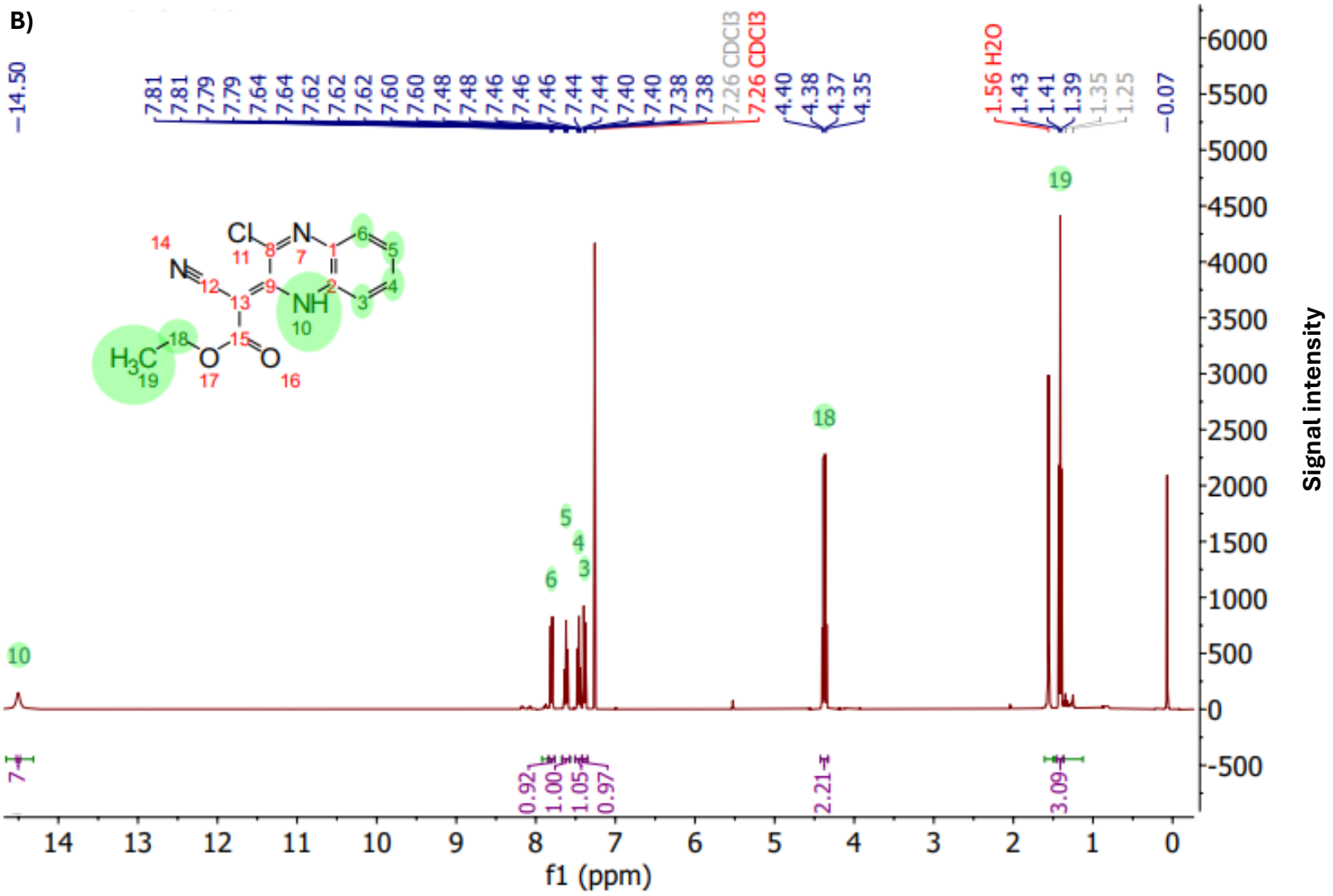
14.50
7.81
7.79
7.64
7.62
7.60
7.48
7.46
7.44
7.40
7.38
7.26 CDCl3
4.40
4.38
4.37
4.35
1.56 H2O
1.43
1.41
1.39
1.35
1.25
0.07
Cl
N
NH
H3C
O
O
10
19
18
6
5
4
3
0.92
1.00
1.05
0.97
2.21
3.09
f1 (ppm)
Signal intensity

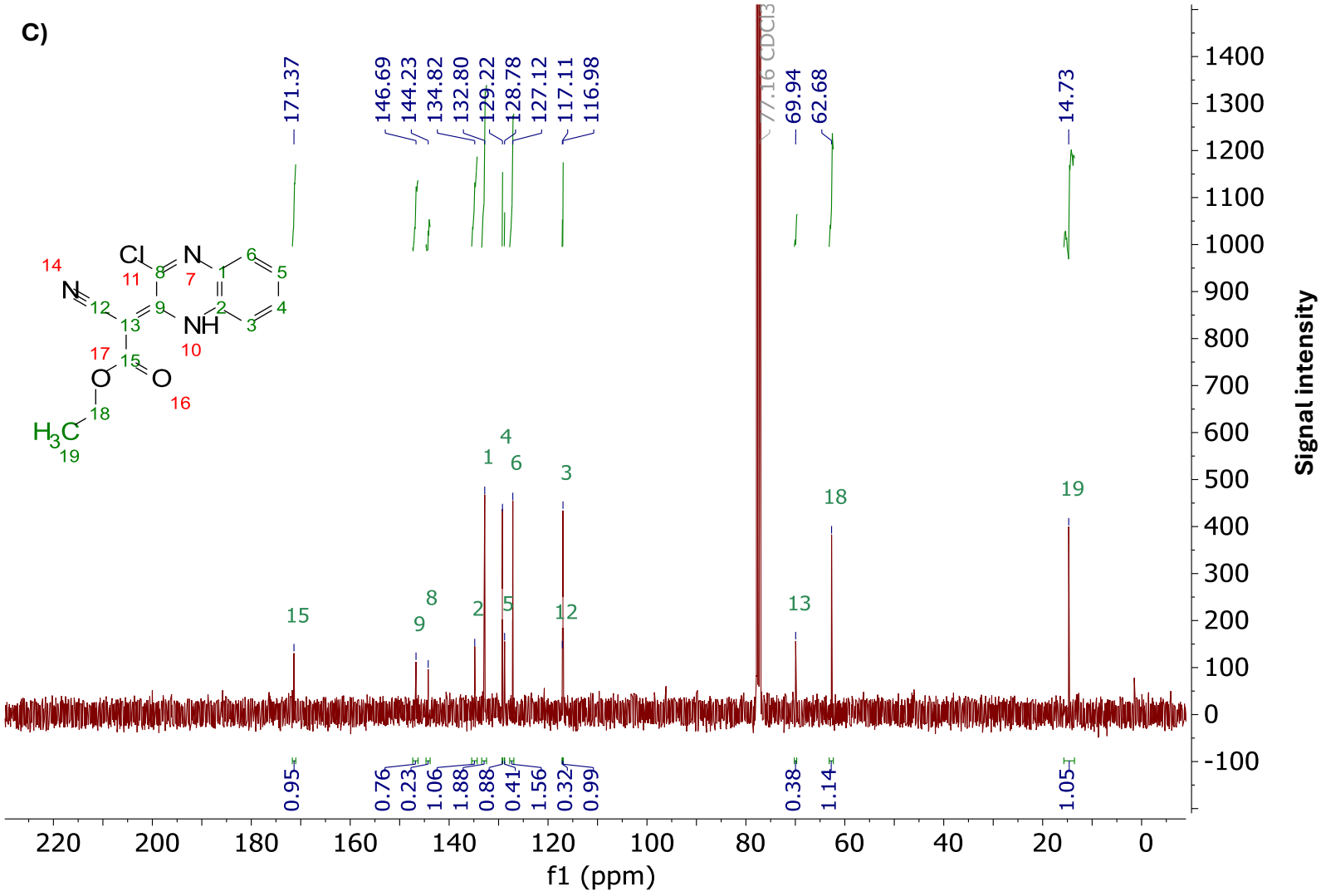

Figure 18- *A) The methyline imine and enamine tautomer forms of substituted quinoxaline intermediate* ***28*** *including stabilising hydrogen bonding. B)* ^{1}*H NMR of* ***28*** *at the enamine tautomer. C)* ^{13}*C NMR of* ***28*** *as the enamine tautomer [251].* H or C peak assignments are highlighted in green. F1= frequency axis (chemical shift).

An alternative convergent synthetic route (see Scheme 2) was devised and successful in resynthesizing **25a** and producing analogues **25c**-**e**.

Scheme 2*- Convergent synthetic route to* ***25a*** *and analogue* ***25e*** *[245, 246, 252-254].*

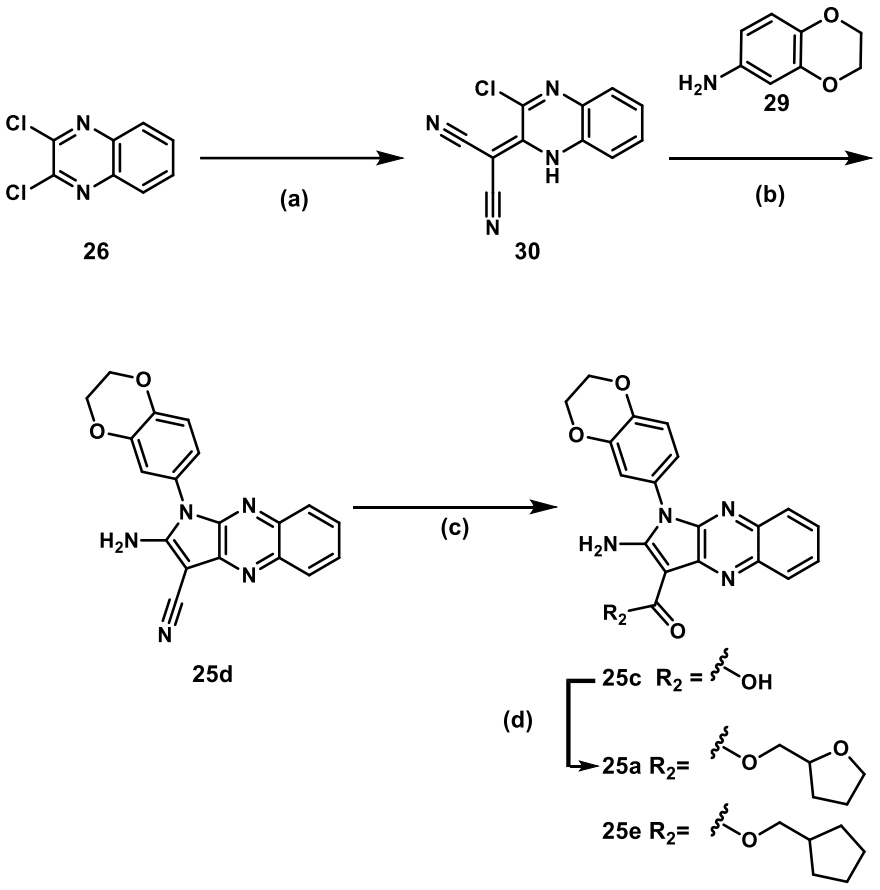

Reagents and conditions- *(a) Malonitrile, Cs_2CO_3, DMSO, rt, 24 h, 86-99 % (b) Amine, Ethanol/THF (3:1), 80 °C, 24 h, 69-96 % (c) 10M NaOH in H_2O: 1,4 dioxane (1:1), 120 °C, 8 h, microwave, 15-38 % (d) H_2SO_4, alcohol, 24 h, 110-160 °C, 8-21 %. Note: A small amount of intermediate* ***25c*** *was purified for pharmacological characterisation but was taken forward as crude material for the generation of* ***25a/e*** *due to purification challenges.*

Similarly to scheme 1, this synthesis scheme involves the S_NAr reaction of **26** with malonitrile followed by subsequent cyclisation of with 2,3-dihydrobenzo[*b*][1,4]dioxin-6-amine (**29**) to generate nitrile **25d**. Hydrolysis of **25d** was then conducted under basic conditions with vigorous heating to yield the corresponding carboxylic acid **25c**. A range of conditions were screened for hydrolysis step (c), (see Table 3). Methodical alterations were made to the reagents employed in this reaction, both acid- and base- catalysed hydrolysis was explored using concentrated H_2SO_4 or metal hydroxides such as NaOH,

LiOH and KOH. The solvent system was varied including both miscible solutions of water with DMSO/EtOH, immiscible mixtures of water with dioxane/cyclopentane methanol or MeOH alone. A range of temperatures were explored from a range of rt-180 °C and reactions were monitored between 0.75- 168 h. The use of a microwave was also investigated for this reaction step. The optimal conditions identified in experiment 13 were 10 M NaOH in a 1:1 mix of water and dioxane ran in the microwave at 120 °C for 8h.

***Table 3**- Reaction condition screen of hydrolysis of **25d** to form carboxylic acid **25c**. Experiment number 13 was chosen as it produced the best ratio of product to starting material measured by liquid chromatography-mass spectrometry (LCMS). [255-258]*

Experiment	Reagent	Solvent System (volume ratio)	Temperature (°C)	Time (h)	Microwave (Y/N)	Outcome (measured by LCMS)	Notes
1	Conc. H_2SO_4 (3 eq.)	Water: DMSO (2:1)	100-110	48	N	No product formation	Temp. increased at 24 h.
2	NaOH (3.5 eq.)	Water: DMSO (1:1)	80-180	168 (7 days)	N	Minor product formation but significant side reactions.	
3	NaOH (5 eq.)	Water: DMSO (1:1)	120-180	0.75 (45 min)	Y	No product formation	Increased temp by 15 °C at 15 min intervals.
4	10 M NaOH (Excess)	10 M NaOH in water: EtOH (1:1)	88	96 (4 days)	N	Minor product formation, side reaction present.	Side reaction caused by ethanol forming ester.
5	NaOH (1eq.) H_2O_2	MeOH	rt	36 (3 days)	N	No product formation.	

	(5 eq.)						
6	10 M NaOH (excess)	10 M NaOH in water: cyclopentane methanol (1:1)	100	120 (5 days)	N	1:1 ratio of starting material **25d**: carboxylic acid **15e**. No ester product present.	Attempt to directly form a desired ester.
7	10 M NaOH (excess)	10 M NaOH in water: cyclopentane methanol (1:1)	88	6	Y	Minor formation of **25e**. No ester product present.	
8	10 M NaOH (excess)	10 M NaOH in water: EtOH (4:1)	88	6	Y	2:1 ratio of starting material **25d**: product **25e**.	Reduction in ethanol volume to avoid side reaction.
9	10 M LiOH (excess)	10 M LiOH in water: EtOH (4:1)	88	1.75	Y	Minor product formation at 15 mins. No change after additional 1.5 h.	
10	10 M KOH (excess)	10 M KOH in water: EtOH (4:1)	88	2	Y	Minor product formation at 15 mins, no change after additional 1.75 h.	

11	10 M NaOH (excess)	10 M NaOH in water: dioxane (2:1)	100	12	Y	Major product formation. 3:1 ratio of product **25e** to starting material **25d**.	Dioxane improved solubility and ran no risk of ester formation. No change in starting material amount after 12 h (ran for additional 6h).
12	10 M NaOH (excess)	10 M NaOH in water: dioxane (1:1)	100	14	Y	Major product formation. 2:1 ratio of product **25e** to starting material **25d**.	23 mg and 34 mg of purified product **1e** was isolated from two separate 500 mg batches. The remainder was carried forward as a mixture.
13	10 M NaOH (excess)	10 M NaOH in water: dioxane (1:1)	120	8	Y	Major product formation. 3:1 ratio of product **25e** to starting material **25d**.	Increased temp. and decreased time gave the same product ratio as experiment 11 conditions.

Numerous purification techniques were employed to achieve separation between **25c/d**. Recrystallization was attempted using either MeOH, EtOH, EtOAc, toluene or acetone but proved unsuccessful due to poor solubility of both the product and starting material. Column chromatography was conducted employing various solvent conditions such as 0-5 % MeOH in dichloromethane (DCM) and 1.5 % methanolic ammonia in EtOAc over 14 column volumes (CV). In both cases product and starting material co-eluted and the loading of columns with the crude material proved challenging due to poor solubility. Overall, isolation of **25c** in large batches proved too labour intensive to be viable and was carried forward in the next reaction step as crude material.

The poor reactivity of both the carbonyl in **25b** and the nitrile in **25d** can be explained by the presence of a vinylogous carbamate system within the molecule; vinylogy is the transmission of electronic effects through a conjugated system [259, 260]. The lone pair of electrons on the primary amine can be delocalised across the conjugated system decreasing the electrophilicity of the nitrile and carbonyl, scheme 3 [261]. The unsuccessful hydrolysis of **25b** could be explained by the formation of a hydrogen bond between the enol hydroxy group and the imine nitrogen, (see Figure 19a). This interaction stabilises the enol tautomer, a poor electrophile, requiring a higher activation energy for nucleophilic attack by the hydroxide ion.

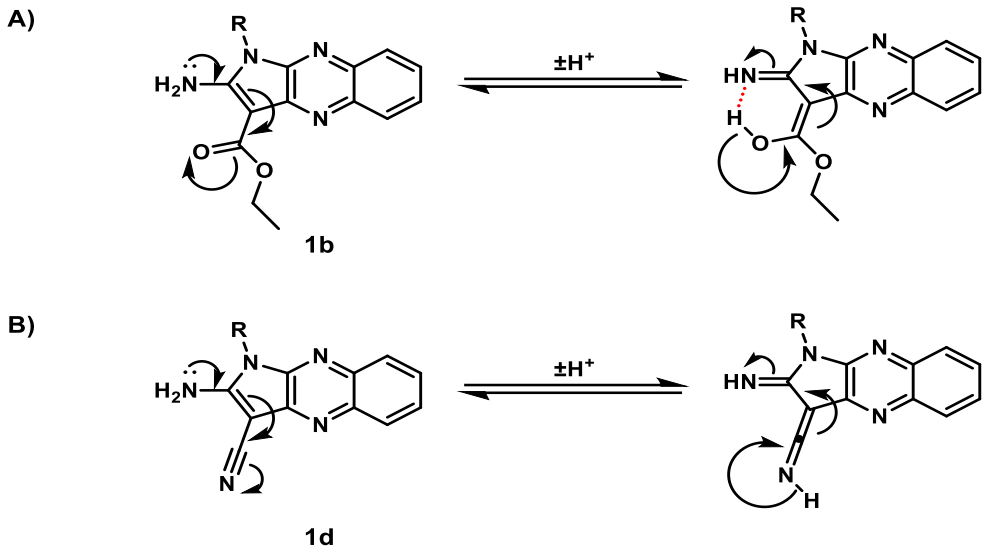

***Figure 19**- Vinylogy of the A) carbamate system including potential stabilising hydrogen bonding (red) and B) amino-nitrile conjugated system leading to a decrease in the nucleophilicity of the C=O and C-N bond [259, 260].*

Carboxylic acid **25c** underwent acid-catalysed esterification with (tetrahydrofuran-2-yl)methanol and cyclopentylmethanol to yield **25a** and **25e** respectively. However, due to the use of the desired alcohol as a solvent, high boiling points required for reflux and a tendency for side reactions to occur this approach produced poor yields (8-21 %). Alternative conditions were explored, aiming to generate both ester and amide analogues, including the formation of acyl chloride intermediates and traditional Steglich esterification using *N,N*'-dicyclohexylcarbodiimide (DCC) with 4-dimethylaminopyridine (DMAP), and triphenyl phosphine with diethyl azodicarboxylate (DEAD) [262, 263]. Furthermore, coupling reagents 1-[bis(dimethylamino)methylene]-1*H*-1,2,3-triazolo[4,5-*b*]pyridinium 3-oxid hexafluorophosphate (HATU) and *N,N,N′,N′*-tetramethyl-*O*-(1*H*-benzotriazol-1-yl)uronium hexafluorophosphate (HBTU) were trialled, all of the above proving unsuccessful with no formation of the desired products and only starting material present [264].

Overall, the convergent schemes described enabled the synthesis of a small number of desired analogues. However, due to low yields (7 % overall for **25a**), poor compatibility with alcohols for the esterification step and harsh conditions with incomplete formation of desired product in scheme 2 step c (~50% conversion), this route was determined as non-viable for the generation of the remaining desired analogues.

2.3 Development of a non-convergent synthetic route to 25a and analogues.

A non-convergent route was developed with the inclusion of various ester moieties within the first reaction step, (see Scheme 3). This approach was not initially explored due to the larger synthetic effort required. This route was used in the synthesis of **25f**-**25n** with good tractability, consistently high yields and ease of purification.

Scheme 3- *Non-convergent synthetic route to analogues* ***25f-n*** *[245, 246, 263].*

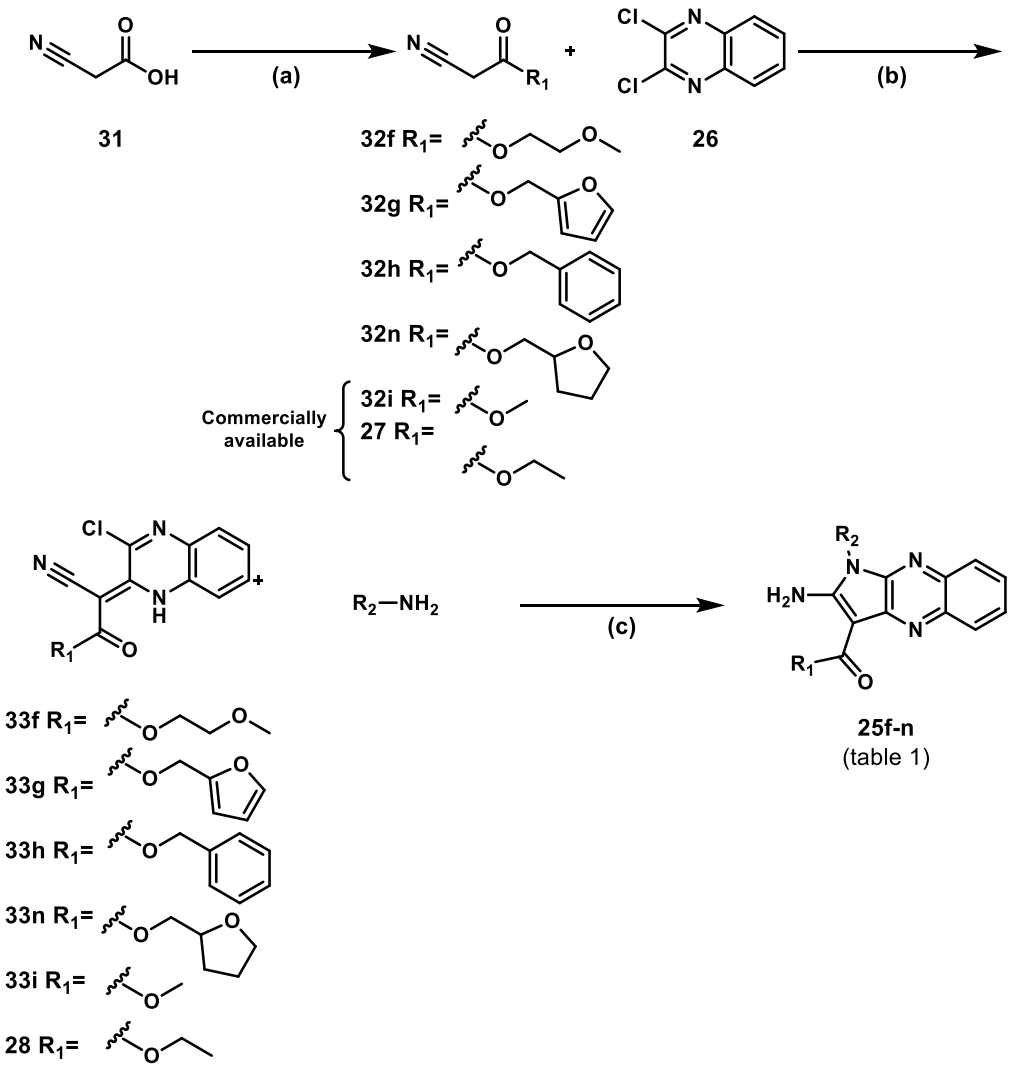

Reagents and conditions- (a) Alcohol, DCC, DMAP, DCM, 0 °C-rt, 24 h, 57-66 %. (b) 2,3-Dichloroquinoxaline, Cs_2CO_3, dimethylformamide (DMF), rt, 24 h, 37-90 %. (c) Amine, EtOH:THF (3:1), 80 °C, 24 h, 12-91 %.

In this method the insertion of various ester moieties occurs within the first reaction step, a 'Steglich esterification' with 2-cyanoacetic acid (**31**) and the desired alcohol using DCC and DMAP coupling conditions [263]. The resulting esters (**32f**-**i** & **k**) then react via S_NAr with **26** to yield **33f**-**l** & **3** followed by cyclisation with the desired amine as previously described [245, 246]. Overall, this non-convergent route was used to isolate sufficient quantities of **25f**-**n** at a purity >95 % (determined by LCMS and NMR) for pharmacological characterisation.

The non-convergent synthetic route proved more successful than the convergent scheme with calculated overall yield ranges between 2.5-54 % and 0.7-7.5 % respectively. Despite the success of scheme 3 for the generation of series 1, numerous drawbacks can be identified. Firstly, due to its non-convergent nature this route is less efficient with more reactions conducted to achieve the desired analogues. Secondly, the synthesis is limited to the generation of esters. A non-convergent approach was attempted for the generation of a benzyl amide analogue **25t**, (see Scheme 4), contributed to by student Fook Looeng Lai (School of Pharmacy, University of Nottingham) [265].

***Scheme 4**- Attempted non-convergent route to amide analogues [245, 246, 266, 267].*

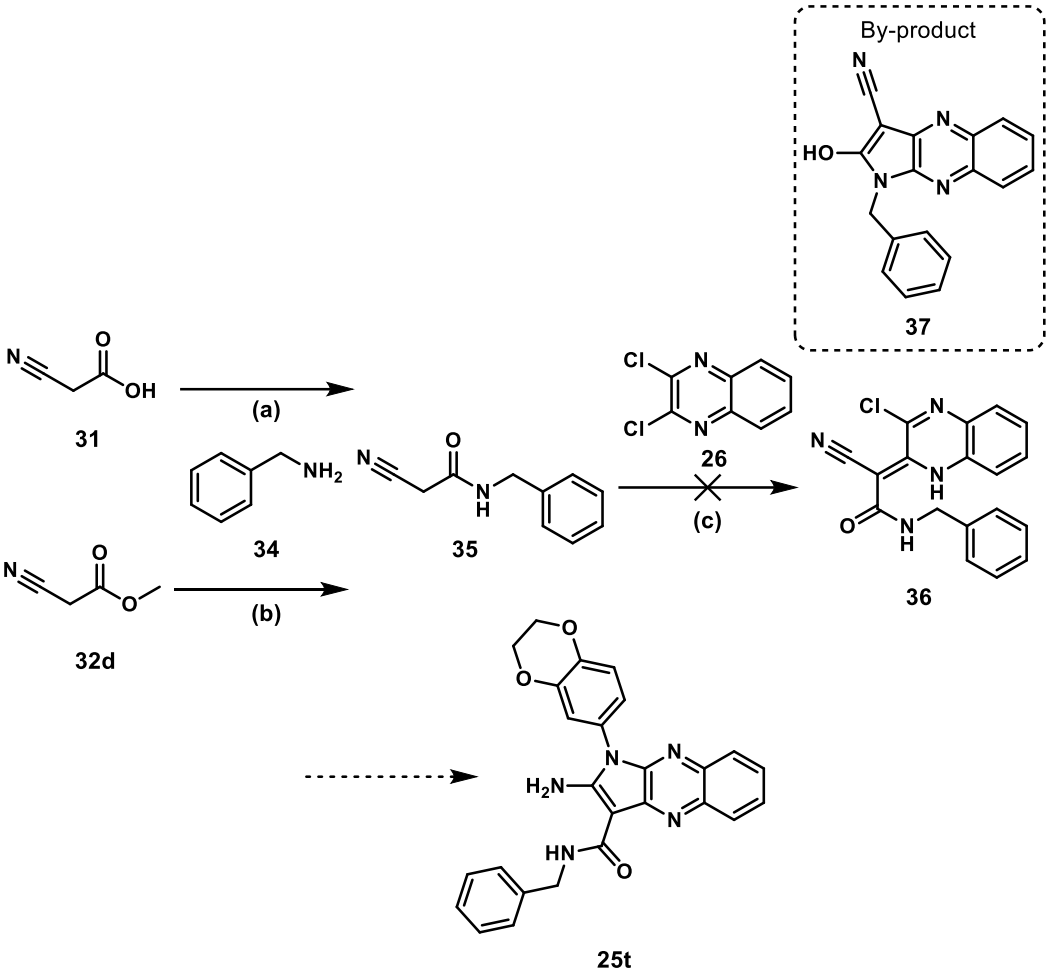

***Reagents and conditions**- (a) 2-Cyanoacetic acid, amine, DMAP, 1-Ethyl-3-(3-dimethylaminopropyl)carbodiimide (EDC), DCM, 48 h, rt, 23 %. (b) Methyl 2-cyanoacetate, amine, rt, 1 h, 35 %; (c) 2,3-Dichloroquinoxaline, **11**, Cs_2CO_3, DMF, reflux, 2 h, 42 % by-product.*

This scheme details two amide coupling reactions with benzyl amine **34** to produce *N*-benzyl-cyanoacetamide (**35**) either using EDC with the cyanoacetic acid or a direct aminolysis of the corresponding methyl ester **32d** [266, 267]. During the S_NAr reaction of step (c) there was no formation of the desired intermediate **36** and a cyclised by-product **37** was isolated. Therefore, this route is currently unviable for the generation of amide analogues. By-product **37** was determined a suitable analogue for pharmacological characterisation as it contains the pyrroloquinoxaline core but has modifications at both the 2,3-dihydrobenzo[*b*][1,4]dioxine and ester regions. A benzyl

group, increasing the number of rotatable bonds but eliminating the HBA oxygen atoms, has replaced the 2,3-dihydrobenzo[*b*][1,4]dioxane whilst the ester has been substituted for a weaker HBA nitrile.

By-product **37** is thought to be produced by a secondary S_NAr cyclisation reaction following the initial formation of **36**. Due to the presence of excess base (pKa 10.3) the nitrogen of the amide (pKa ~15) can be deprotonated forming a resonance stabilised anion that can act as a nucleophile to undergo a secondary S_NAr at the 3-chloro position, (see Figure 20). This is supported by the lack of cyclised by-products in the S_NAr reaction with an ester as the oxygen cannot be deprotonated to form a nucleophile to attack the quinoxaline-3 position.

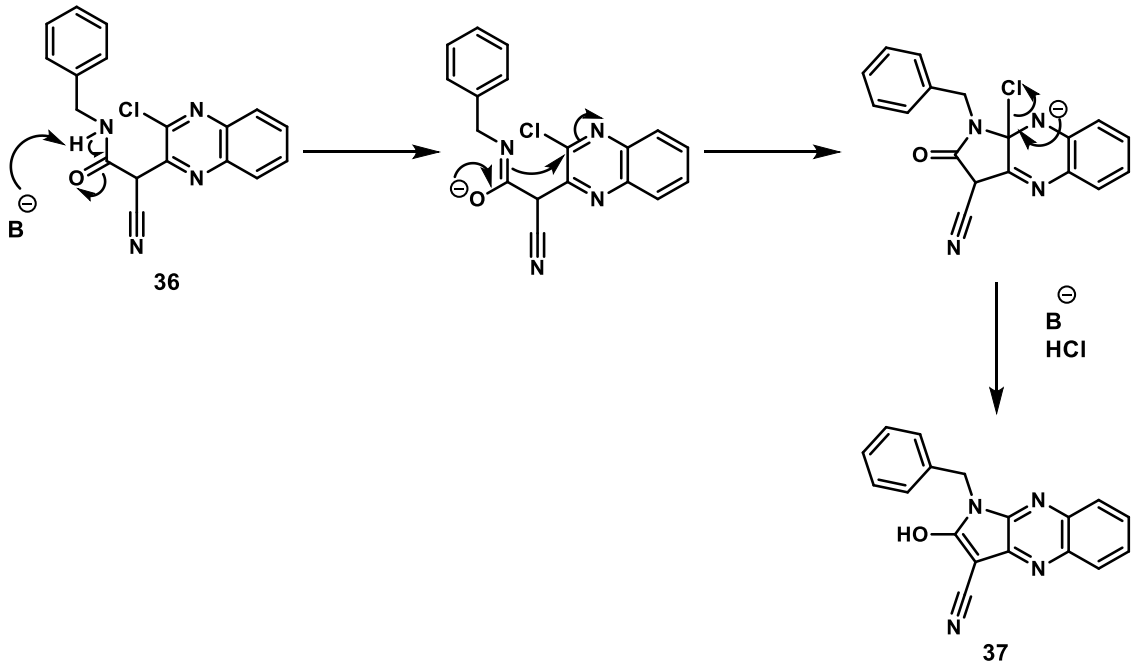

***Figure 20**- Proposed mechanism for the generation of by-product **37**.*

To circumvent the formation of **37** an alternative approach was explored with the initial S_NAr on 2,3-dichloroquinoxaline (**26**) conducted with amine **29**. Intermediate **38** could then undergo a second S_NAr and cyclisation with the desired amide **35** to form final compound **25t**, scheme 5. However, this reaction was unsuccessful due to no formation of the mono-substituted product **38**. Instead, the di-substituted by-product **39** was isolated and confirmed by NMR and LCMS. This was determined a suitable

analogue to take forward for pharmacological characterisation as it maintained the quinoxaline ring core structure whilst exploring the toleration of two 2,3-dihydrobenzo[*b*][1,4]dioxine moieties. The HBA ester has been replaced with two secondary amines with the ability to act as two new HBD sites.

Scheme 5*- Attempted convergent route to amide analogue* ***25t*** *[245, 246].*

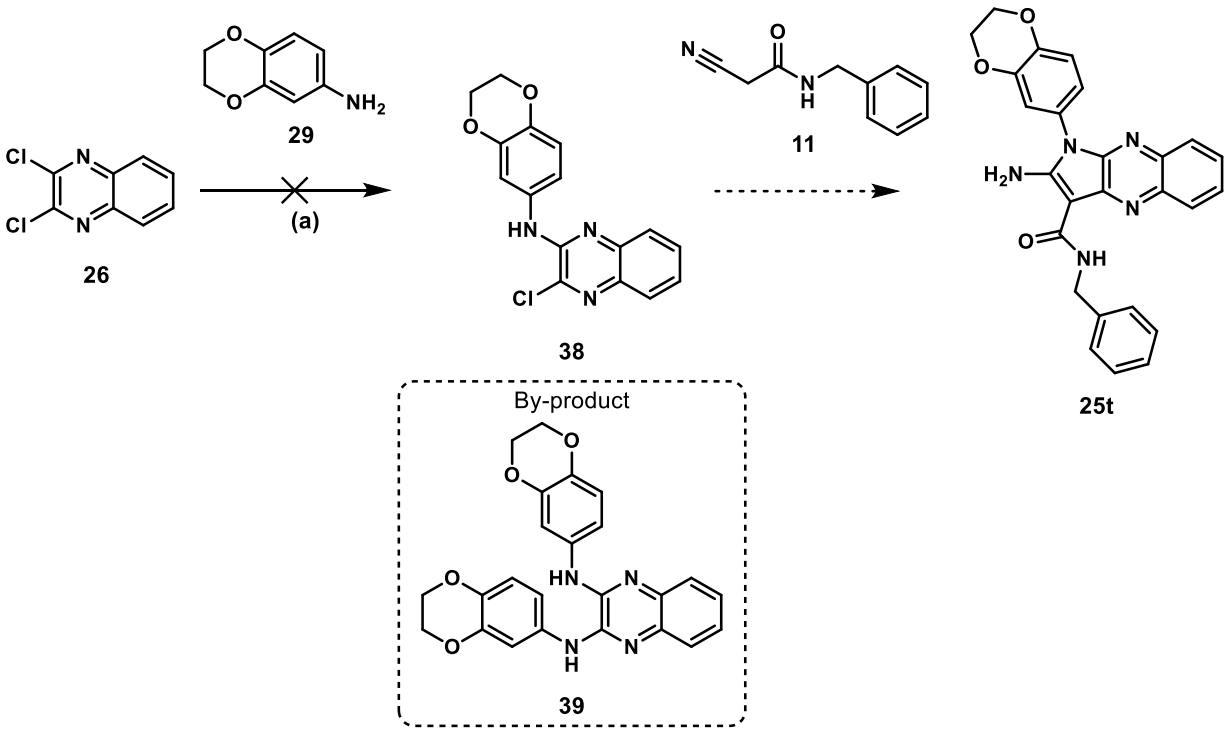

Reagents and conditions*- (a) 1. 2,3-dichloroquinoxaline, 2,3-dihydrobenzo[b][1,4]dioxin-6-amine, EtOH, 100 °C, 2 h microwave. 2. 110 °C, 1 h, microwave, 23 % by-product.*

A reaction conditions screen was conducted varying the ratio of starting materials, temperature and solvent, as well as using reagents such as $AlCl_3$ and sodium bis(trimethylsilyl amide) [268, 269]. $AlCl_3$ is a strong Lewis acid that can coordinate with the chlorine in 2,3-dichloroquinoxaline, this acts as a better leaving group and facilitates nucleophilic attack by the amine [270]. In contrast, sodium bis(trimethylsilyl amide) is a strong base that can deprotonate weakly acidic amines, this generates a more nucleophilic anion to undergo the S_NAr reaction [271]. In all cases, either no reaction occurred or a majority of by-product **39** was formed (see Table 4).

***Table 4**-Reaction conditions screen for scheme 5 reaction (a) [268, 269, 272].*

Experiment	Reagents	Solvent System	Temperature (°C)	Time (h)	Microwave (Y/N)	Outcome (monitored by LCMS and TLC)
1.	**26** (1 eq.), **29** (1.5 eq.)	EtOH	a) 100 b) 110	a) 2 b) 1	Y	23 % yield of by-product **39**
2.	**26** (1 eq.), **29** (1 eq.)	EtOH	79	24	N	At 3 h mixture of desired **38** and by-product **39**. identified. At 24 h only by-product **39**.
3.	**26** (1 eq.), **29** (1 eq.)	1,4-dioxane	rt	24	N	Incomplete reaction-small amount of **38** and **39** observed.
4.	**26** (1 eq.), **29** (1 eq.)	1,4-dioxane	50	48	N	Incomplete reaction-small amount of **38** and **39** observed.
5.	**26** (1 eq.), **29** (1 eq.), *N*,*N*-diisopropylethylamine (DIPEA, 1 eq.)	1,4-dioxane	a) rt b) 100	a) 24 b) 18	N	No reaction observed.
6.	**26** (1 eq.), **29** (1 eq.), Aluminium (III) chloride (1.25 eq.)	Anhydrous DCE	80	24	N	Incomplete reaction-minor formation of by-product **39**.

7.	**26** (1 eq.), **29** (1 eq.), Sodium bis(trimethylsilyl)amide (1.25 eq.)	Anhydrous THF	0-rt	40	N	No reaction observed

Due to the lack of a successful synthetic route and project time restrictions the production of a series of amide analogues was not further explored. However, some alternative approaches have been discussed. To prevent the cyclisation of secondary amides and the formation of by-product **37** (scheme 4) amine protection strategies, which remain intact under basic conditions, could be implemented. This strategy would eliminate deprotection at the nitrogen and the formation of any lone pairs of electrons, thus preventing nucleophilic attack at the 3-quinoxaline position. One example involves the synthesis of a series of *N*-methyl protected analogues which are stable under strong basic conditions and the secondary amine starting materials are commercially available. However, demethylation of the *N*-methyl amide analogues is chemically challenging and involves novel approaches such as copper-catalyzed radical *N*-demethylation and visible light-induced cerium catalysis [273, 274]. Both reactions are known for difficulty in achieving high selectivity and high yields due to the formation of highly reactive alkyl radical intermediates forming competing side reactions. Issues with over-oxidation by copper catalysts in copper-catalyzed radical *N*-demethylation and a sensitivity to water during visible light-induced cerium catalysis also contribute to low yields [273, 274]. An alternative approach involves silyl protecting groups such as 2-(trimethylsilyl)ethoxycarbonyl (teoc) a carbamate protecting group which is stable to strong acids and mild bases and is deprotected using a fluoride ion in tetra-n-butylammonium fluoride (TBAF) [275].

2.4 Synthesis of series 1 conclusions

In conclusion, series 1 was designed and synthesized with the future aim of investigating the ligand-receptor interactions of the previously unexplored ester moiety in NAM **25a**. This region was identified as a key starting point for SAR development from initial literature homology modelling, predicting the tetrahydrofuran-2-yl methyl ester as occupying an intracellular pocket between EP_2 TM α-helices 2-4 [179]. The 2,3-dihydrobenzo[*b*][1,4]dioxine moiety, previously reported as a key contributor to the

inhibition of EP_2 induced cAMP production, was also modified to expand the SAR dataset [179].

Three chemistry approaches were successfully used to resynthesize literature compounds **25a**,**j**-**l** and yield 12 novel analogues (**25b**-**i**,**m/n**) in sufficient quantities for pharmacological characterisation [179]. An additional five compounds (**25q**-**u**) purchased from Life Chemicals (Munich, Germany) further expand the series 1 compound library.

This series has inserted a variety of new functionalities to modify ligand properties such as solubility and lipophilicity, as well as exploring potential new ligand-target interactions. For example, this series explores the binding pocket being occupied by the 2,3-dihydrobenzo[*b*][1,4]dioxine through both the shortening of and the breaking of the dioxane bridge (**25n**/**m** respectively) maintaining two HBA oxygens but varying the rigidity, position and flexibility of this moiety. The substitution patterns of the resulting di-methoxy phenyl groups were also varied as 3,5-dimethoxy, 2,5-dimethoxy and 3,4,5-trimethoxy for **25j**/**k**/**l** respectively. Furthermore, the 2,3-dihydrobenzo[*b*][1,4]dioxine motif was completely replaced with a thiophene and 2-methoxyethyl in the purchased compounds **25u**/**x** but still maintained a HBA sulfur or oxygen.

Additionally, a range of ester analogues were explored. Firstly, we have covered the replacement of the ester with either a nitrile (**25d**) carboxylic acid (**25c**) or amide (**25w**/**y**) varying H-bond donor/acceptor strength. The tetrahydrofuran ring was broken in **25f**. Lipophilicity has also been increased through the removal of an oxygen in **25e** and the ester chain length has been shortened in the methyl/ethyl esters (**25i/b**). Finally, aromaticity was introduced through the replacement of the tetrahydrofuran with furan-2-yl (**25g**) and benzyl rings (**25h**). Enabling engagement in non-covalent interactions such as π- π stacking [230]. Two amide analogues containing either a *N*-2-isopropoxyethyl amide (**25w**) or a primary amide (**25y**) were purchased for SAR dataset expansion. However, these analogues do not maintain the essential 2,3-dihydrobenzo[*b*][1,4]dioxine moiety and therefore the direct impact of ester to amide replacement cannot be quantified by this series. Six amide analogues were designed as

part of this series (**25o**-**t**) with the aim of increasing ligand binding affinity and functional potency through their dual hydrogen-bonding capabilities [231]. Insertion of an amide would also improve the metabolic stability of our compounds as they are less susceptible to hydrolysis compared to the ester counterparts [232]. However, no successful synthetic route was established to produce these ligands via either convergent or non-convergent approaches due to side reactions yielding by-products **37** and **39**. These by-products were determined suitable compounds to pharmacologically characterise as they maintain the quinoxaline core structure but contain modifications at the ester and/or 2,3-dihydrobenzo[*b*][1,4]dioxine moieties. Future work could exploit an amide protecting group strategy such as *N*-methyl or silyl carbamate protecting group teoc to synthesize the desired analogues **25o**-**t** [275].

Despite the success of the convergent synthesis (scheme 2) to yield a small number of analogues its incompatibility with most desired alcohols in the final esterification step meant that future chemical syntheses did not employ this route. In contrast, the non-convergent approach, whilst requiring a larger synthetic effort, has been proven viable with a large variety of ester modifications and was applied in the production of a second series of analogues.

Chapter 3- Pharmacological assessment of series 1 analogues as EP_2 negative allosteric modulators

3.1 Introduction and aims of pharmacological characterization of series 1

3.1.1 Aims of pharmacological characterization of series 1

Typically, a lead compound in the drug discovery process displays desirable biological activity against a target. This is often characterised by improved binding affinity, functional potency, receptor selectivity and pharmacokinetic properties compared to the initial hit [179]. These lead compounds serve as a starting point for further optimization and are often taken forward into in vivo studies to assess their efficacy, safety and potential for development in the clinic [276]. In this work optimization of literature NAM **25a** for EP_2 was explored with 12 novel analogues designed and synthesized as part of series 1 (see Chapter 2). The pharmacokinetics and safety profile of our NAMs were not evaluated using in vivo assays as this falls outside the project scope focussed on evaluating ligand target interactions in model cell systems. Series 1 underwent in vitro pharmacological characterisation to identify a lead NAM of the prostaglandin EP_2 receptor, as a target mechanism for the treatment of inflammation.

The proposed mechanism of action of my series 1 compounds, based upon initial homology modelling from the literature (see Chapter 1.3.4), is through binding to an intracellular allosteric binding site of the EP_2 receptor, leading to antagonism of receptor-effector coupling. To experimentally demonstrate this, we first needed a measure that allows the assessment and ranking of our ligand binding affinities for this allosteric binding site. A NanoBRET competition binding assay in conjunction with a fluorescent probe for the desired intracellular binding site was utilized to produce these data.

Secondly, to confirm these ligands are functional antagonists in a cell-based assay our compound library was screened in the NanoBiT complementation binding assay. This experiment measures receptor-effector recruitment at the *h*EP_2 receptor using β-arrestin2 as the example effector protein. This assay can also be utilized for initial

exploration of our ligand selectivity by comparing their effects on *h*EP_2 versus *h*EP_4 receptors.

3.1.2 Introduction to NanoBRET competition binding assays at hEP$_2$ using TMR-Gαs19cha18

To use NanoBRET assays to evaluate the binding affinities of this series at the intracellular site, a probe that competes for binding at the same binding site on *h*EP_2 is required [216-219]. A potential option is utilising peptides based on the G protein Gα subunit C terminus that recognise and bind to the intracellular G-protein binding pocket of active GPCRs. These short Gα-protein peptides are produced from identifying key residues in the G-protein C-terminus that interact with the associated binding pocket of the receptor which determines their selectivity ($G\alpha_s$, $G\alpha_i$, $G\alpha_q$ etc.) [277-280]. Historically, these G-protein C-terminal peptides have been shown to functionally antagonise G-protein coupling of GPCRs when expressed in target cells [281, 282]. More recently, using the $G\alpha_s$ C-terminal peptide, Mannes *et al.* then optimised the sequence to improve its affinity for the $G\alpha_s$ coupled β2AR [283]. Notably, these authors demonstrated that such peptides can substitute for the G protein in supporting the high affinity agonist-receptor-G-peptide ternary complex. For example, the optimal peptide Gαs19Cha19 was demonstrated to increase the affinity of the orthosteric agonist isoprenaline for β2AR through stabilisation of its high affinity conformation [283].

In 2022 Farmer et al developed a tetramethylrhodamine (TMR) N-terminally labelled fluorescent tracer based on Gαs19cha18 (TMR-Gαs19cha18) and showed that its binding to both β2AR and EP_2 receptor could be detected and be utilised in competition binding assays to explore intracellular GPCR binding sites (see Figure 21) [219]. This tracer is based on the 19 amino acids Gαs subunit C-terminus with the conserved penultimate leucine substituted for a non-native amino acid cyclohexylalanine residue [219, 283]. The substitution, identified in a HTS approach, was found to increase the potency of the peptide in stabilising the original target β2AR high affinity active conformation bound to isoproterenol [284]. The TMR-Gαs19cha18 fluorescent probe is predicted to bind to the same intracellular EP_2 G-protein binding pocket as the Gαs

subunit C-terminus, reportedly between TM2,3,5&6 in the recent cryo-EM structure of PGE_2-bound EP_2-Gs complex, supported by mutagenesis studies conducted by Conklin in 1993 with predecessor G-protein C-terminus mimetics [280]. This overlaps with the proposed (but not proven) binding pocket of literature compound **25a** and its derivatives [160, 179].

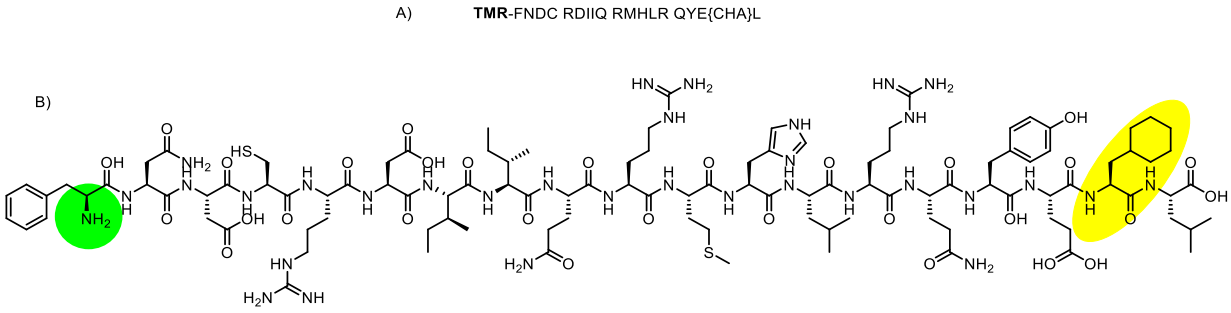

Figure 21- A) *TMR-Gαs19cha18 amino acid sequence (N-C terminus left to right).* ***B)*** *Structure of Gαs19cha18 including site of fluorophore addition (green) and non-natural amino acid cyclohexyl alanine substitution (yellow).*

The NanoBRET™ competition binding assay utilising TMR-Gαs19cha18 was used to directly determine the binding affinities of our ligands for the *h*EP_2 receptor (see Chapter 1.4.2) [199]. This assay was conducted using EP_2-thermostableNanoLuc (*ts*NLuc) expressing HEK293 cell membranes, in which the bioluminescent donor NLuc is fused to the intracellular C-terminal of the EP_2 receptor [285]. tsNLuc is a bioluminescent donor with a similar luminescence emission profile to Nluc but, due to mutations removing cysteine residues, has a ~30 °C improvement in thermostability and lower reported luminescence output compared to wild type [285]. The Nluc enzyme catalyses an oxidation reaction converting its substrate furimazine to furimamide in its excited state; UV photons are emitted upon the decay of the amide to its ground state [214]. The emitted donor luminescence, emission 420-550 nm, can then undergo BRET exciting a fluorescent acceptor in close proximity (within 10 nm) that in turn emits light of a different wavelength. The TMR-Gαs19cha18 probe emits light at a longer wavelength of ~550 nm [219]. Total binding is quantified as the respective acceptor/donor emission ratios (BRET ratios), and specific probe binding can be calculated through comparison

of the probe binding in the presence and absence of a high concentration of unlabelled competitor [216].

Unlike radioligand techniques, real time measurements of fluorescent probe binding for this site can be recorded in a homogenous format without traditional separation (e.g. by filtration) of the bound ligand-receptor complexes from free probe in solution [202]. Upon the addition of unlabelled intracellular ligands to the assay we would expect to see competition with the tracer for the intracellular site. This results in a reduction in the BRET ratio (acceptor TMR emission/ donor NLuc emission) and the inhibitory concentration for half maximal inhibition of specific binding is estimated as the IC_{50} value. The ligand equilibrium dissociation constant K_D/K_i (see Chapter 1.4.1) values respectively are calculated for the TMR-Gαs19cha18 tracer and unlabelled ligands according to saturation analysis (probe) or competition IC_{50} values with Cheng- Prusoff correction, which assumes a competitive reversible binding of the unlabelled ligands and the probe (see Chapter 8.2.2.3) [198, 199, 216, 219]. Therefore, NanoBRET™ competition binding assays using TMR-Gαs19cha18 enable direct assessment of the affinity of our unlabelled ligands in series 1 [219].

In addition to supporting an intracellular binding mode of action, the ability of our ligands to successfully compete with TMR-Gαs19cha18 can lead to the identification of key structural moieties participating in ligand-receptor interactions and determining affinity.

3.1.3 Introduction to NanoBiT complementation assays at hEP_2 and hEP_4 whole cells.

Th ligands demonstrating the highest binding affinities in the NanoBRET™ competition binding assays were then selected for further functional studies, focussed on identifying whether the compounds could induce receptor-arrestin interactions or disrupt receptor-effector signalling complexes. NanoBiT™ is a real time reversible complementation assay measuring agonist stimulated EP_2 receptor βarrestin2 recruitment in whole cells (see Chapter 1.4.2), which has previously been successfully

employed for many different GPCRs including β1AR and β2AR, dopamine D2 receptor and the CXCR4 chemokine receptor [222, 286, 287]. The NanoBiT™ system is composed of two subunits, the 1.3 kDa (SmBiT) peptide and the 18 kDa (LgBiT) polypeptide, which weakly associate and reversibly assemble into a functional NLuc complex dependent on the interaction characteristics of the proteins of interest [221, 288]. Here, a NanoBiT™ assay was established by co-expressing cDNA of (1) the *h*EP_2 receptor C-terminally fused to the LgBiT fragment, and (2) β-arrestin2 N-terminally tagged to SmBiT, previously generated by Dr Nicola Dijon [222]. In this assay the agonist activation of EP_2 receptor and β-arrestin2 effector recruitment is proportional to luminescence produced by the complemented NanoBiT.

3.2 Determination of the EP_2 binding affinity of series 1 compounds through the NanoBRET competition binding assay.

3.2.1 Saturation analysis to determine the affinity of TMR-Gαs19cha18 at the EP_2 receptor.

The tracer TMR-Gαs19cha18 was first characterized by saturation analysis, varying the concentrations of the probe, to determine its binding affinity for EP_2 *ts*NLuc in HEK293 membranes. These experiments were conducted by Dr James Farmer [289]. As observed for this probe at other G_s coupled GPCRs, TMR-Gαs19cha18 specific binding was only observed in the presence of the endogenous orthosteric agonist PGE_2 (10 μM), suggesting selective binding to an agonist-occupied EP_2 conformation, (see Figure 22a). Under these conditions, saturation analysis determined a K_d for TMR-Gαs19cha18 at the EP_2 receptor of 1.92 ± 0.19 μM, (see Figure 2b). Addition of unlabelled competitor **25b** showed effective competition with TMR-Gαs19cha18, (see Figure 22c), with a pIC_{50} value of 7.17 and a maximum inhibition of 98.3 % specific binding. Therefore, the NanoBRET competition binding assays utilising TMR-Gαs19cha18 could then successfully be used to demonstrate whether series 1 ligands were able to compete for the probe binding site in for EP_2 *ts*NLuc in HEK293 membranes, and if so determine their binding affinities. A low sodium buffer was utilized in this assay to mimic the

intracellular biochemical environment and minimise potential assay interference by sodium ions [290].

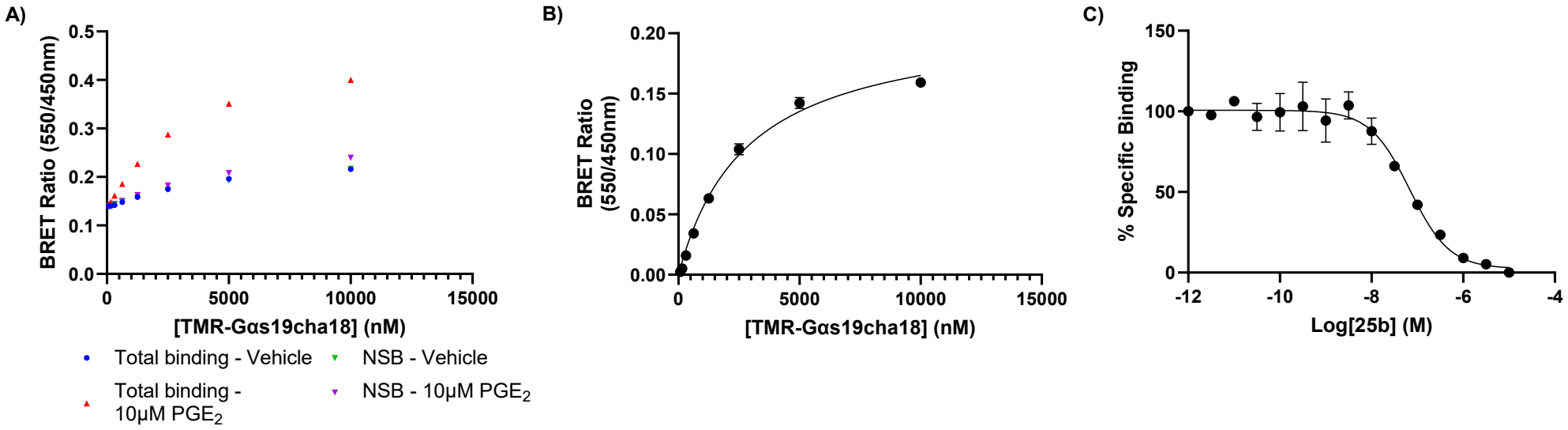

***Figure 22**- Agonist-dependent binding of TMR-Gαs19cha18 to EP_2-tsNLuc membranes determined by NanoBRET, using low sodium buffer at 37 °C, endpoint reads taken at 60- min incubation (experiments performed by Dr James Farmer). Non-specific binding (NSB) determined using 40 μM concentration of **25b**. **A)** Saturation binding of TMR-Gαs19cha18, demonstrating the increased total binding observed in the presence of 10 μM PGE_2. Data is a representative example from three independent experiments. **B)** Specific binding data in the presence of PGE_2 fitted with a one-site specific binding model to determine TMR-Gαs19cha18 affinity (K_d) quoted in the text. The data was normalised and pooled from three independent experiments. **C)** NanoBRET competition binding data shown as % specific binding against increasing concentrations of **25b** in the presence of 500 nM TMR-Gαs19cha18 and 10 μM PGE_2. Data is a representative example from three independent experiments [289].*

3.2.2 NanoBRET competition binding assays for series 1 ligands at hEP_2 in cell membranes.

Of the twenty-one compounds in series 1, nine ligands (including **25a**) successfully displaced the fluorescent tracer TMR-Gαs19cha18 in the NanoBRET™ competition binding assay, supporting a competitive binding mode at the intracellular site, (see Figure 23). The binding affinities of these modulators was calculated and reported as the negative log of the dissociation constant (pK_i); the higher the pK_i value the greater the binding affinity of the ligand, (see Table 5).

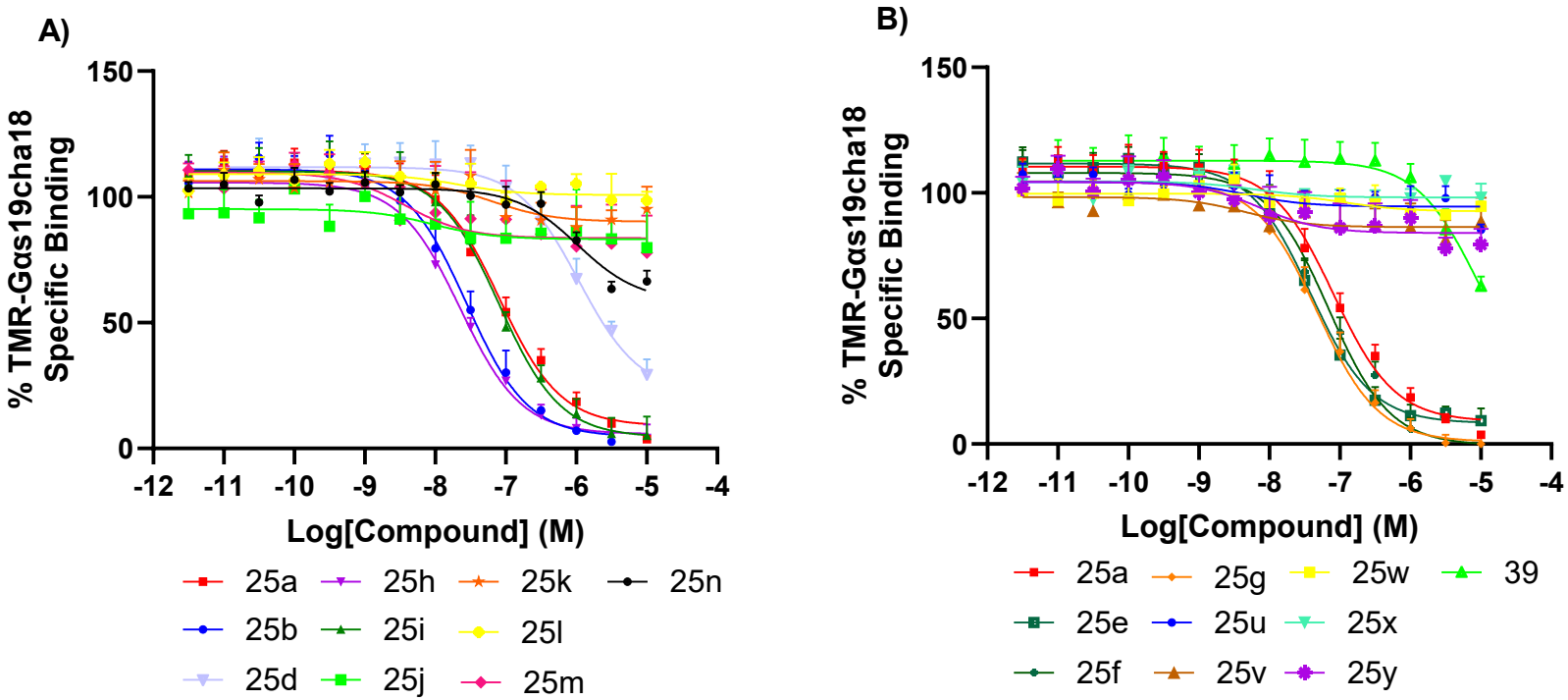

Figure 23- *A/B) NanoBRET® competition binding data shown as % specific binding against increasing concentrations of the competing ligand. The specific binding data shown was normalised and pooled from five independent experiments, with non-specific binding determined by addition of 10 μM of* ***25b****. Assay was performed using 1 μM TMR-Gαs19cha18 tracer in a low sodium buffer + 0.2 % bovine serum albumin, 1/960 Furimazine, 10 μM* PGE_2 *and varied concentrations of competing ligands, incubated at 37 °C for 1 h [219, 289].*

Table 5- *Mean pK_i values of series 1 unlabelled competing ligands pooled from five individual values from five independent NanoBRET competition binding experiments including the standard error of the mean (SEM), fold increase in pK_i from* ***25a*** *and compound structures. One way ANOVA followed by Dunnett's post test conducted for pK_i and % reduction in specific binding comparing to* ***25a*** *reference compound reported as *P<0.05, ** P<0.01 and ***P<0.001.*

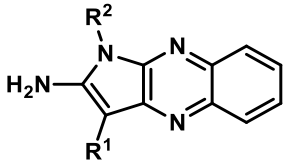

Compound	R^1	R^2	Mean pK_i ± SEM	Mean K_i (nM)	Fold change in K_i from 25a
25a	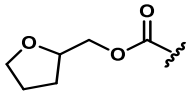	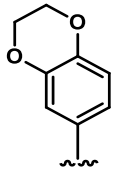	7.14 ± 0.11	73	1.00
25b	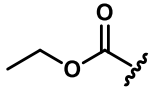	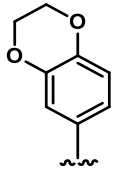	7.64 ± 0.18*	23	3.17
25d		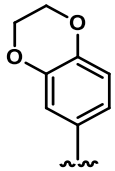	<6.00***	N/A	N/A
25e	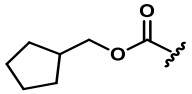	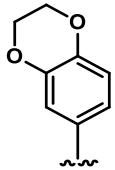	7.53 ±0.15	30	2.43

25f	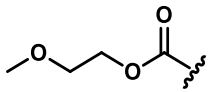	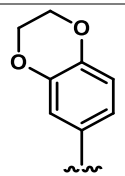	7.20 ± 0.11	63	1.16
25g	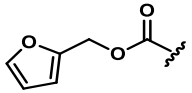	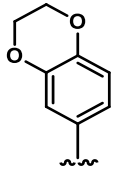	7.53 ± 0.12	30	2.43
25h	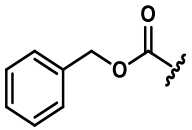	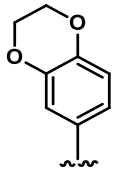	7.84 ± 0.11***	14	5.2
25i	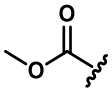	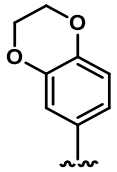	7.30 ± 0.12	50	1.46
25j	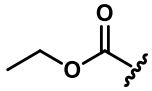	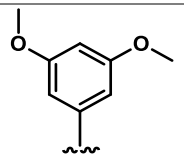	<6.00***	N/A	N/A
25k	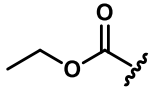	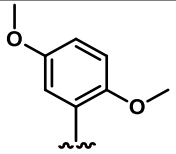	<6.00***	N/A	N/A

25l	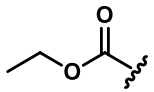	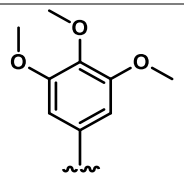	<6.00***	N/A	N/A
25m	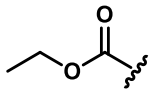	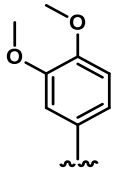	<6.00***	N/A	N/A
25n	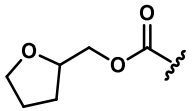	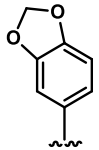	<6.00***	N/A	N/A
25u	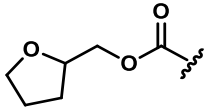	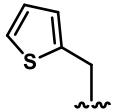	<6.00***	N/A	N/A
25v	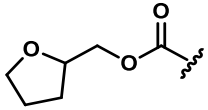	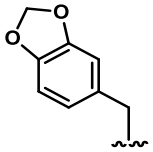	<6.00***	N/A	N/A
25w	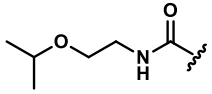	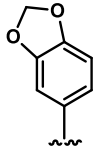	<6.00***	N/A	N/A

25x	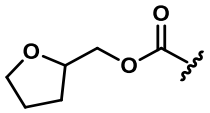	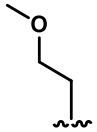	<6.00***	N/A	N/A
25y	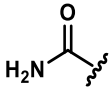	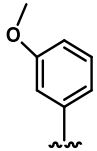	<6.00***	N/A	N/A
39	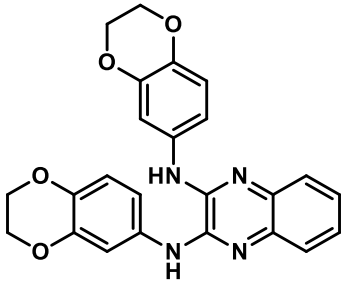		<6.00***	N/A	N/A

The seven reported active ligands had determined pK_i values within the range 7.14-7.84 (73-14 nM), displaying a relatively flat SAR for affinity based on the modifications tested. This implies that the presence of an ester is essential for ligand binding, potentially due to the formation of hydrogen bond donor interactions within the binding site, but the nature of the alkyl moiety has minimal impact [291]. This is further supported by ligands **25d** and **39** which do not contain an ester moiety but do have the essential 2,3-dihydrobenzo[*b*][1,4]dioxine motif; the rightward curve shift highlights these ligands as lower affinity binders. These analogues did not fully inhibit specific binding and therefore only minimum pK_i values could be calculated. The reduced affinity of **39** indicates that a replacement of the ester moiety with a larger secondary 2,3-dihydrobenzo[*b*][1,4]dioxine motif is sterically disfavoured for this pocket.

The benzyl ester analogue **25h** was identified as the ligand with the highest binding affinity for the intracellular Gs binding pocket in this series with a pK_i value five-fold higher than the literature compound **25a**. The potential to form pi-pi stacking interactions between the benzyl group and the aromatic side chains of amino acids within the binding pocket (e.g. Phe, Tyr, Trp and His) may contribute to this increase in binding affinity [292]. The increase in lipophilicity of **25h** (LogP of 5.13) could also be a contributing factor potentially interacting with hydrophobic pockets within the *h*EP_2 allosteric binding site.

The remaining eleven compounds, including three negative controls from the literature **25j**-**l**, failed to displace the fluorescent tracer TMR-Gαs19cha18 at concentrations up to 10 μM (see Table 5) [179]. This indicated these ligands had very low affinity for the G_s binding pocket. For most of these analogues, the detrimental effect on binding affinity can be attributed to modifications/removal of the essential 2,3-dihydrobenzo[*b*][1,4]dioxine. Negative controls **25j**-**l** contained di/tri- methoxy phenyl rings with various substitution patterns in place of the 1,4-dioxine moiety. Additionally, no tolerance was observed for ligands containing either a reduction in the ring size to a 1,3-dioxole in analogues **25n**/**v**/**w**. This highlights the importance of the ethylene bridge in either supporting the rigidity and positioning of the hydrogen bond acceptor oxygen

molecules or their direct involvement in van-der Waals interactions with the EP_2 receptor [293, 294]. Replacement of the benzo-1,4-dioxine with 2-ethyl thiophene in **25u**, 2-methoxyethyl in **25x** or 3-methyoxy phenyl in **25y** also demonstrated very low affinity for the G_s binding pocket.

For two remaining analogues **25c** and **37**, at high concentrations (above 10^{-6} M) a sharp increase in apparent TMR-Gαs19cha18 specific binding in the NanoBRET to over 400 % was observed. Subsequent emission spectrum recorded on 10^{-5} M solutions of compounds (with excitation 450 nm and recordings taken from 510-650 nm) highlighted an overlap with the tracer TMR-Gαs19cha18 emission, (see Figure 24). Therefore, assay interference limited accurate assessment of binding by BRET at these concentrations (> 1 μM), and as a result the affinity of **25c** and **37** for *h*EP_2 in the assay could not be accurately determined. Assay interference resulting from pharmacophores/functional groups with inherent fluorescent properties is a weakness of fluorescence/luminescence-based assays [295]. Traditional radioligand binding techniques are less prone to these issues, however the assays are not homogenous and require synthesis of a radioligand [201, 202].

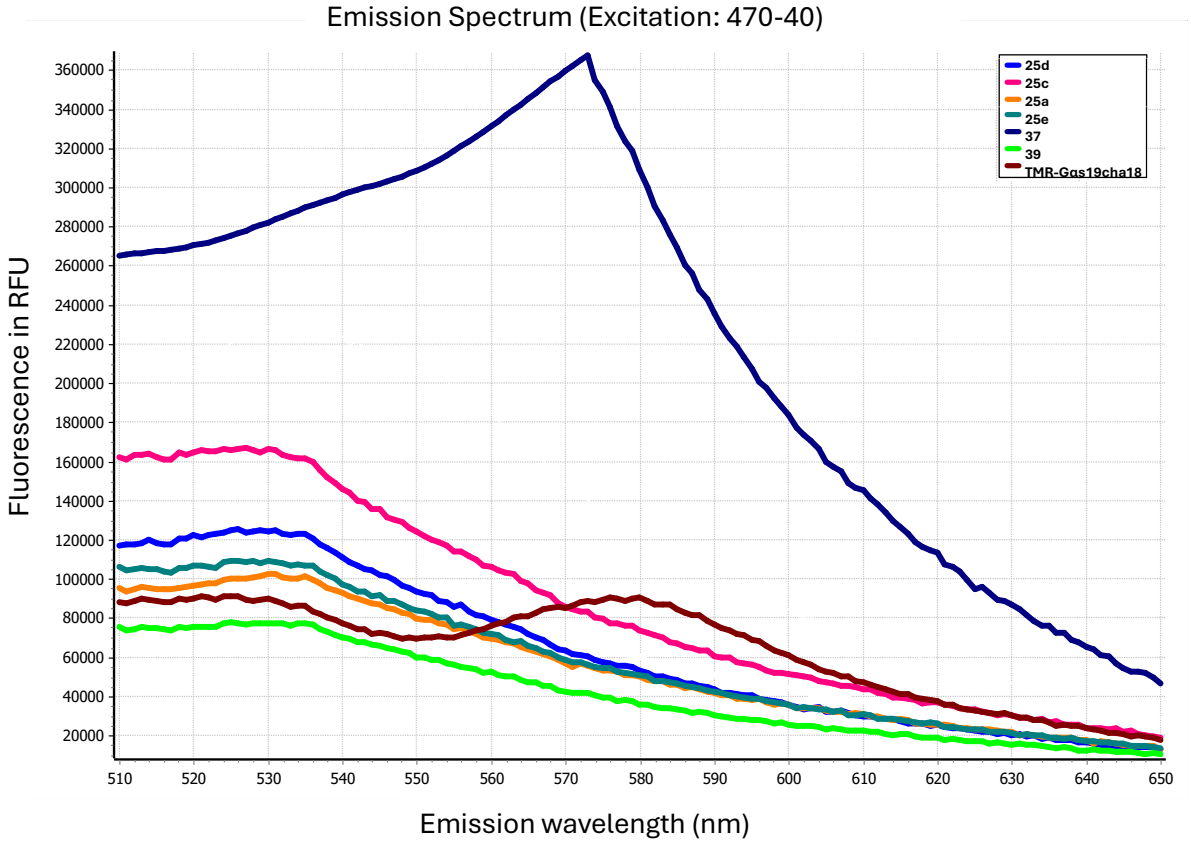

***Figure 24**-Emission spectrum of series 1 compounds **25a/c/d/e/n/39 (**10 μM**)** compared with TMR-Gαs19cha18, using excitation of 470 nm (bandpass 40 nm- measuring 450-490 nm emission) to represent BRET luminescence donor emission.*

For this assay we must consider it employs a G-protein mimetic probe not a full G-protein. Despite mimetics having the advantage of improved stability and easy modification for fluorophore addition, they may not perfectly replicate the binding characteristics of the full protein [296]. For example, proteins can adopt a large number of complex conformations which cannot easily be replicated by smaller mimetics [297]. Additionally, the substitution of a conserved penultimate leucine for the larger non-native amino acid cyclohexylalanine residue may introduce steric hinderance for mimetic binding. TMR-Gαs19cha18 was initially designed to target the β2AR which reportedly has a larger cytoplasmic pocket than EP_2 due to a larger separation of the TM3-TM6-TM7 bundles [160, 298].

3.3 Determination of the EP_2 functional potency of series 1 compounds through the NanoBiT complementation assays

3.3.1 Agonist responses in the NanoBiT arrestin assay

Firstly, the HEK293 EP_2-βarrestin2 NanoBiT™ cell line was used to generate CRCs for three agonists reported to have differing efficacies with respect to βarrestin2 recruitment; butaprost, evatanepag and endogenous agonist PGE_2, (see Figure 25a) [299-301]. The pEC_{50} values (the negative log of the concentration of agonist required to produce 50 % of the maximal biological response), R_{max} (maximum assay response produced by the agonist) and the Hill slope (determining the steepness of the concentration response curve) were recorded, (see Table 6). On this basis, agonist concentrations representing EC_{80} were determined for subsequent evaluation of inhibitors in the IC_{50} experiment (see Chapter 3.3.2). An EC_{80} concentration of agonist in such assays maximises the window to determine the inhibitor effect, avoiding higher concentrations which might adversely reduce inhibitor potencies. Normalised agonist EC_{80} time course data was generated to determine suitable assay read times post

agonist addition; when both agonist-receptor equilibrium is established and a suitable assay window, is retained (see Figure 25b). This was identified as 30 minutes post agonist addition for PGE_2, butaprost and evatanepag.

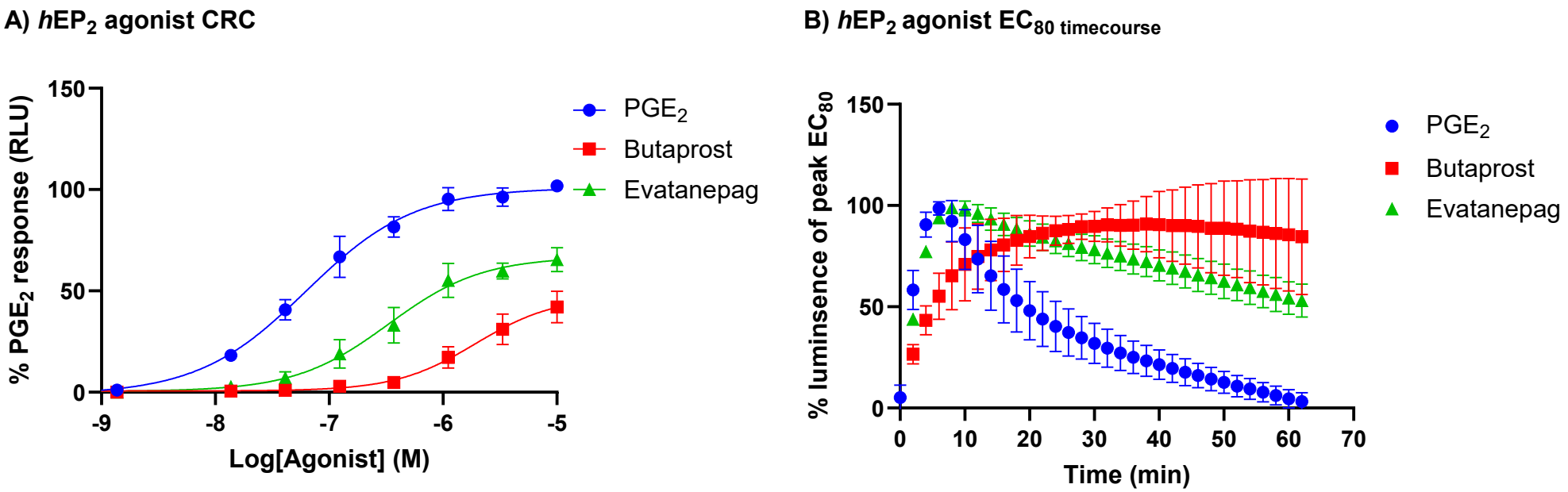

Figure 25- *NanoBiT complementation assay in EP_2-LgBiT, β-arrestin2-SmBiT tagged stably transfected HEK293 cells, 1x HEPES buffer + 0.1 % BSA, 1:750 furimazine, incubated at 37 °C for a total of 60 mins.* ***A)*** *NanoBiT complementation assay shown as % PGE_2 response (RLU) against increasing concentrations of agonists. Reading taken 30 minutes post agonist addition. The CRC curves shown were normalised and pooled from a minimum of five independent experiments.* ***B)*** *Agonist EC_{80} time course measuring β-arrestin2 recruitment by NanoBiT™ complementation assay for 60 minutes post agonist addition. Data is normalised and pooled from a minimum of five independent experiments [222].*

***Table 6**- Mean pEC_{50}, R_{max}, Hill slope and EC_{80} values of EP_2 agonists normalised and pooled from five independent NanoBiT complementation assays in EP_2-LgBiT, β-arrestin2-SmBiT tagged stably transfected HEK293 cells including the standard error of the mean (SEM) and compound structures. One way ANOVA followed by Dunnett's post test conducted for pEC_{50} and % Rmax comparing to PGE_2 reference compound reported as *P<0.05, ** P<0.01 and ***P<0.001.*

Agonist	pEC_{50} ± SEM	R_{max} ± SEM	Hill slope	EC_{80} (nM)	Structures
PGE_2	7.20 ± 0.06	102.0 ± 1.4	0.94 ± 0.10	208	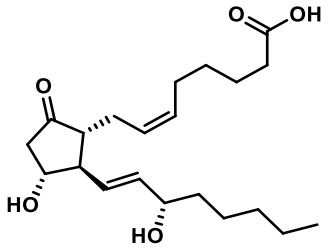
Butaprost	5.68 ± 0.18**	52.0 ± 8.7**	1.39 ± 0.12	4677	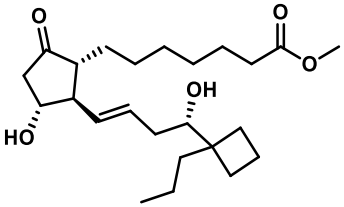
Evatanepag	6.46 ± 0.11**	67.8 ± 3.0**	1.10 ± 0.06	950	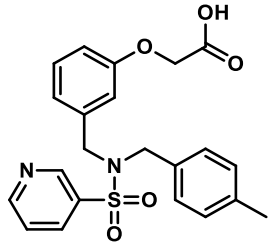

The endogenous agonist PGE_2 exhibited the highest functional potency with a pEC_{50} value of 7.20 compared to evatanepag and butaprost at 6.46 and 5.68 respectively. Additionally, the latter agonists demonstrated partial agonism with their R_{max} values, approximately 30 % for evatanepag and 50 % for butaprost, lower than PGE_2's value of 102 %. This partial agonism has been described previously in the literature, reflecting the lower intrinsic efficacy of butaprost and evatanepag to activate the EP_2 receptor-arrestin pathway once bound [300, 302]. This may also underpin the more sustained time-course for arrestin recruitment observed for butaprost and evatanepag (see Figure 25b) compared to PGE_2, as sustained signalling kinetics are characteristics of other GPCR partial agonists (e.g. levorphanol and tramadol as μ-opioid receptor partial agonists, and taprostene as IP receptor partial agonist) [303, 304]. Overall, this data demonstrated that all three agonists induced a quantifiable concentration dependent recruitment of β-arrestin2 to the *h*EP_2 receptor in whole HEK293 cells. At EC_{80} concentration, all three agonists were therefore suitable to provide an appropriate luminescence window for determining the functional potency of the unlabelled allosteric modulators in series 1. Initial data focused on use of the native agonist, PGE_2, as the stimulus.

To conduct selectivity studies for our series one ligands a HEK293 EP_4-βarrestin2 NanoBiT™ cell line was utilised; *h*EP_4 is also a $G\alpha_s$ coupled receptor similarly activated by the endogenous agonist PGE_2 and sharing 38% homology with hEP_2 (see Chapter 1.2.1) [182, 305]. As for *h*EP_2, CRCs and EC_{80} time course data was produced for the agonist PGE_2 (see Figure 26a/b) and the pEC_{50} and EC_{80} values are reported (see Table 7).

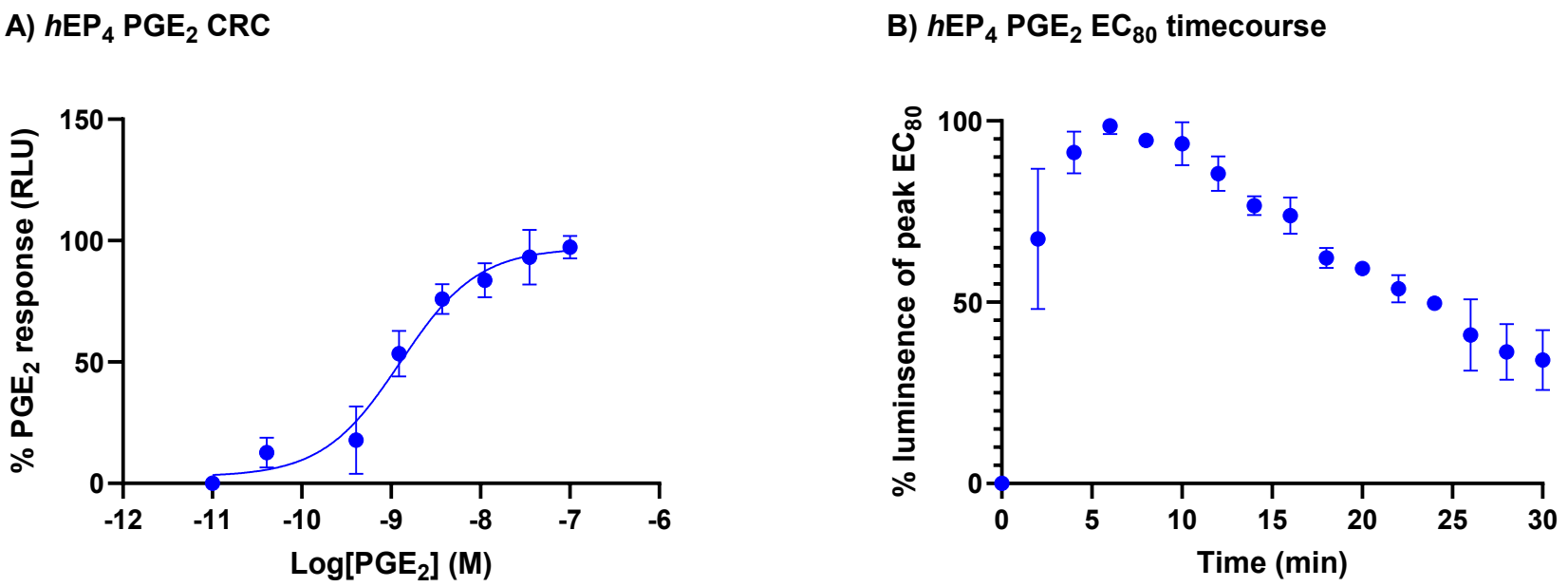

Figure 26- *NanoBiT complementation assay in EP_4-LgBiT, β-arrestin2-SmBiT tagged stably transfected Hek293 cells, 1x hepes buffer + 0.1 % BSA, 1:750 furimazine, incubated at 37 °C for a total of 60 mins.* ***A)*** *NanoBiT complementation assay shown as % PGE_2 response (RLU) against increasing concentrations of PGE_2. Readings taken 30 minutes post agonist addition. The CRC curves shown were normalised and pooled from a minimum of three independent experiments.* ***B)*** *PGE_2 EC_{80} time course measuring β-arrestin2 recruitment by NanoBiT™ complementation assay for 30 minutes post agonist addition. Data is normalised and pooled from a minimum of three independent experiments [222].*

***Table 7**- Mean pEC_{50}, EC_{80} and Hill slope values of EP_4 agonist PGE_2 normalised and pooled from three independent NanoBiT complementation assays in EP_4-LgBiT, β-arrestin2-SmBiT tagged stably transfected HEK293 cells including the standard error of the mean (SEM) and compound structure*.

Agonist	pEC_{50} ± SEM	Hill slope	EC_{80} (nM)	Structures
PGE_2	8.39 ± 0.11	1.28 ± 0.25	1.24	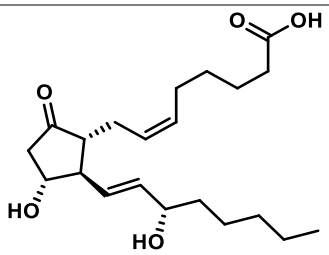

Endogenous agonist PGE_2 exhibits a higher functional potency, pEC_{50} of 8.39, at *h*EP_4 receptors compared to *h*EP_2, pEC_{50} of 7.20, indicating a difference in agonist selectivity (168 fold change) across receptor subtypes which is in line with recent literature [306]. This data demonstrated that PGE_2 induced a quantifiable concentration dependent recruitment of β-arrestin2 to the *h*EP_4 receptor in whole HEK293 cells. Additionally, the EC_{80} concentration (1.24 nM) provided an appropriate luminescence window, at the 30-minute timepoint read, to determine the functional potency of our unlabelled NAMs in series 1 and enabling direct comparison of ligand selectivity between receptor subtypes.

3.3.2 NanoBiT complementation assay for series 1 ligands at hEP_2 and hEP_4 in whole cells.

CRCs of our ligands were determined, following 30 minute NAM pre-treatment, by recording 30 minutes post stimulation using the EC_{80} concentration of PGE_2 (164 nM for EP_2 and 1.25 nM for EP_4), conducted in both EP_2-LgBiT, β-arrestin2-SmBiT and EP_4-LgBiT, β-arrestin2-SmBiT tagged stably transfected HEK293 whole cells using EP_2 agonist PGE_2 (see Figure 27) [222]. Functional potency is reported as pIC_{50} values, the negative logarithm of the IC_{50} value which represents the compounds concentration to inhibit an assay response by 50 % of its maximal inhibition, (see Table 8). The higher the pIC_{50} value the greater the functional potency of the compound [307].

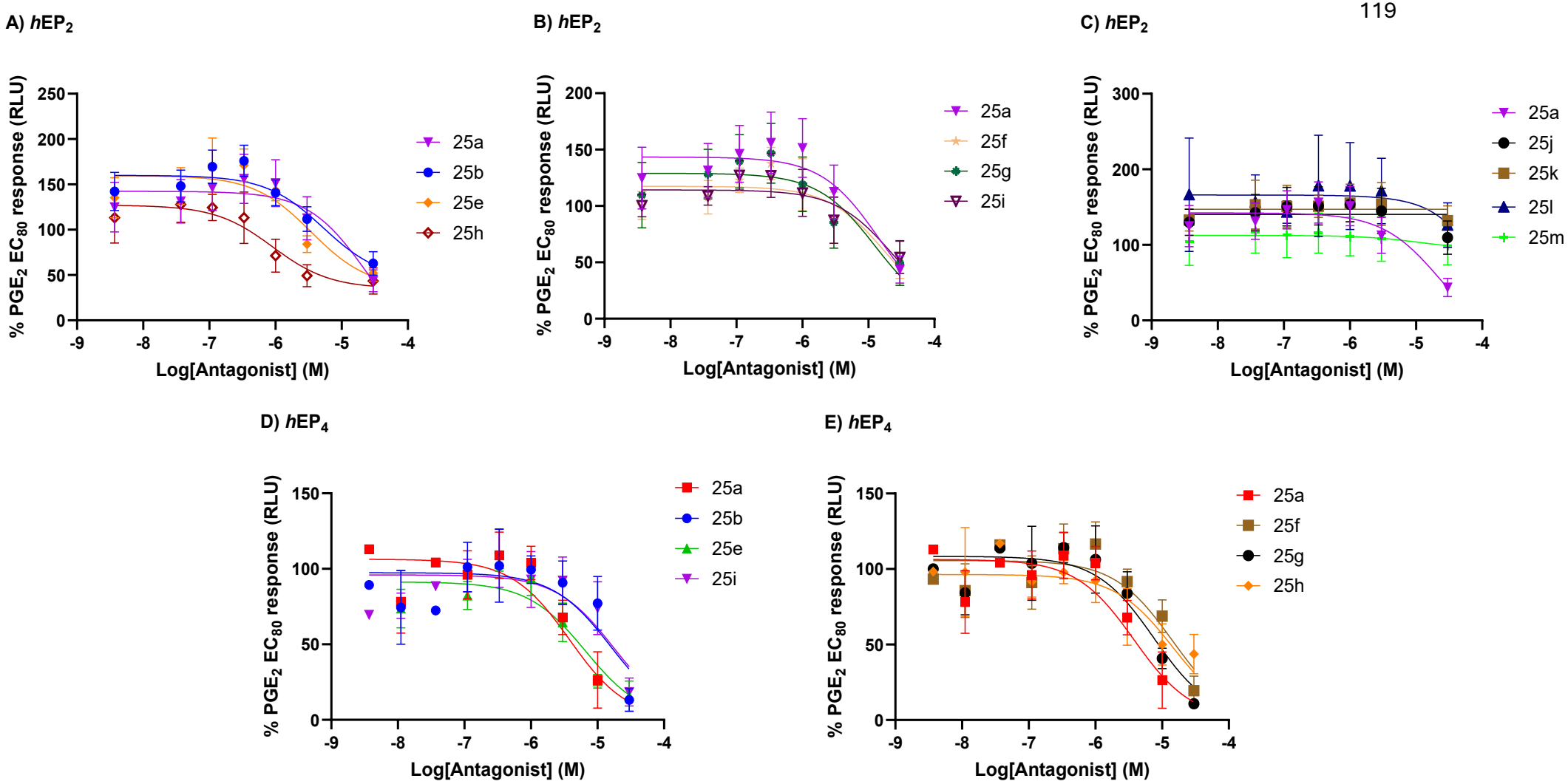

Figure 27- *β-arrestin2 NanoBiT complementation assay data in* ***A-C)*** *EP_2-LgBiT, β-arrestin2-SmBiT tagged or* ***D/E)*** *EP_4-LgBiT, β-arrestin2-SmBiT tagged stably transfected HEK293 cells. Compounds were preincubated with cells for 30 min prior to PGE_2 addition at approximately EC_{80} concentration (164 nM EP_2; 1.25 nM EP_4). Response data 30-min post PGE_2 addition are shown as % PGE_2 EC_{80} luminescence against increasing concentrations of competing ligand. Experiments were performed in 1x Hepes buffer + 0.1 % BSA and 1:750 furimazine. The functional data shown were normalised and pooled from either five (****A/B****) or three (****C-E****) independent experiments.*

Table 8- *Mean pIC_{50} values of series 1 unlabelled competing ligands normalised and pooled from five independent NanoBiT complementation experiments in hEP_2-LgBiT, β-arrestin2-SmBiT and hEP_4-LgBiT, β-arrestin2-SmBiT tagged stably transfected HEK293 whole cells including the standard error of the mean (SEM), fold selectivity and compound structures. One way ANOVA followed by Dunnett's post test conducted for pIC_{50} and % inhibition comparing to* ***25a*** *reference compound at both hEP_2 and hEP_4 reported as *P<0.05, ** P<0.01 and ***P<0.001.*

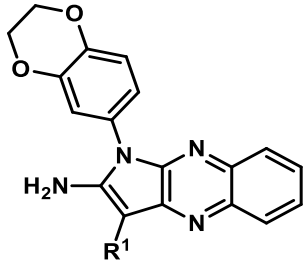

Compound	Structure R^1	Mean *h*EP_2 pIC_{50} ± SEM	Mean *h*EP_4 pIC_{50} ± SEM	Fold selectivity *h*EP_2 v *h*EP_4	% Inhibition at top concentration (30 uM) from vehicle control for EP_2 ± SEM	% Inhibition at top concentration (30 uM) from vehicle control for EP_4 ± SEM
25a	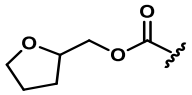	5.00 ± 0.08	4.65 ± 0.04	2.2	59.4 ± 4.0	91.6 ± 12.4
25b	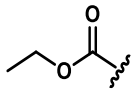	5.20 ± 0.07	4.43 ± 0.14	5.9	37.3 ± 5.8*	86.8 ± 4.4
25e	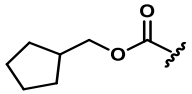	5.40 ± 0.09	5.01 ± 0.24	2.5	47.8 ± 3.7	84.3 ± 5.8

25f	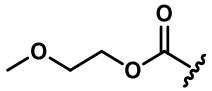	4.77 ± 0.29	4.54 ± 0.15	1.7	53.2 ± 5.1	80.6 ± 4.8
25g	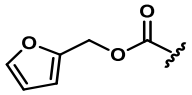	5.20 ± 0.14	4.55 ± 0.21	4.5	50.6 ± 8.1	89.2 ± 1.4
25h	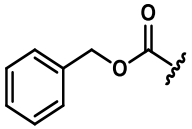	5.96 ± 0.08***	4.65 ± 0.03	20.4	56.5 ± 5.9	56.3 ± 6.5**
25i	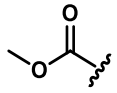	4.95 ± 0.25	4.49 ± 0.03	2.9	45.7 ± 6.5	81.6 ± 4.6

The *h*EP_2 NanoBiT™ complementation assay demonstrated that all ligands with known affinity for the Gαs allosteric binding pocket also displayed functional inhibition of β-arrestin2 recruitment at the *h*EP_2 receptor with pIC_{50} values ranging between 4.77-5.96 (1.1-17.0 μM). The maximal inhibition, reduction in NanoBiT™ luminescent response from the EC_{80} PGE_2 control response, by the highest concentration of compound was 56.5 % by NAMs tetrahydrofuran ester **25a** and benzyl ester **25h**. This is typical of a non-competitive mode of action for our NAMs as the maximal inhibition is <100 % (percentage of PGE_2 EC_{80} response does not reach 0 %). In contrast the ethyl ester **25b** has the lowest reported % inhibition at 37.3 ± 5.8 followed by methyl ester **25i** at 45.7 ± 6.5, the reduction in size of the ester moiety could be attributed to this trend in SAR. Unlike the flat nature of the previous binding affinity data, benzyl ester **25h** displayed the best inhibitory potency by approximately a half log unit compared to cyclopentane ester **25e** with the second-best reported functional potency. Therefore, from this SAR data we can determine that the inclusion of a benzyl ester in our NAMs plays a key role in improving functional inhibition of β-arrestin2 recruitment, however, its mechanism of action is currently unknown.

In comparison negative controls **25j-l** containing di/tri- methoxy phenyl rings with various substitution patterns, which were functionally inert in prior cAMP assays from the literature, failed to inhibit β-arrestin2 recruitment and pIC_{50} values could not be calculated (pIC_{50} <4.5) [179]. This poor functional potency (IC_{50} <4.5 and maximal inhibition <25%) is believed to be a result of modifications at the 2,3-dihydrobenzo[*b*][1,4]dioxine moiety; previously determined to be a key driver of ligand binding to the intracellular allosteric pocket by the NanoBRET competition binding SAR data (see Chapter 3.2.2). Therefore, the correlation between these SAR datasets demonstrates that the functional inhibition of β-arrestin2 recruitment is likely a direct result of ligand binding to the EP_2 receptor at the intracellular G-protein binding site.

The use of whole cells compared to membrane preparations for the functional potency and binding affinity assays respectively should be considered when comparing SAR data as this impacts the ability of compounds to access the intracellular site. All ligands

demonstrating functional potency at EP_2 are lipophilic with a cLogP range between 3.19-5.13 suggestive of good membrane permeation in whole cells. A high lipophilicity can enhance a ligand's ability to penetrate the cell membrane increasing the relative concentration at the target [308]. This range in lipophilicity may contribute to differing rates of membrane permeation in whole cells and vary the time taken for equilibrium across the membrane to be established. As a result, less lipophilic compounds with poor permeation will lead to a lower-than-actual quantity of ligand at the intracellular EP_2 binding pocket causing inaccuracies in the recorded data [309]. This effect may contribute to differences in SAR trends between the binding affinity and functional potency data, with lead **25h** having the highest calculated lipophilicity value (cLogP 5.13). However, the 60-minute total incubation of the NAMs with EP_2-LgBiT, β-arrestin2-SmBiT expressing whole HEK293 cells prior to data read provides sufficient time for all ligands to establish equilibrium across the cell membrane [310]. Thus, minimising the influence of membrane permeability on the functional potency data. Conducting immobilised artificial membrane (IAM) analysis to experimentally quantify the membrane permeability of our NAMs would provide evidence to determine if permeability is influencing the SAR functional potency data [311]. Furthermore, in whole cells there is also the possibility that our unlabelled NAMs are competing with native G-proteins driving a reduction in the displayed functional potency [279, 312, 313]. Additionally, the relative EP_2 receptor expression levels in whole cell assays can result in shifts in ligand potency and efficacy as well as baseline constitutive activity. High receptor expression creates a receptor reserve increasing the amount of antagonist required to block the agonist effect skewing assay results. Additionally, high receptor expression can produce a high basal signal that can mask the inhibitory effects of an antagonist [314]. Furthermore, in this assay the presence of serum proteins (e.g. bovine serum albumin) should also be taken into consideration, these proteins can bind to lipophilic small-molecule ligands lowering their effective concentration and therefore could lead to inaccuracies in the calculated pIC_{50} values [315].

Another key difference between the pharmacological assays that should be considered when comparing the binding affinity and functional potency data is the type of

transducer proteins utilised. Firstly, in the NanoBRET™ competition binding assay we measure the unlabelled ligands binding affinity for the G-protein binding site using the G-protein mimetic TMR-Gαs19cha18. In contrast, the NanoBiT assay provides functional characterisation of the effects of our ligands on β-arrestin2 recruitment. As both β-arrestin2 and the Gs heterotrimeric G-protein are recruited to the same intracellular region of the EP_2 receptor, their binding pockets are predicted to have significant overlap; supported by the recently reported cryo-EM structure of PGE_2 bound to the EP_2-Gs complex [160]. Therefore, binding of our NAMs is expected to induce a similar response in β-arrestin2 recruitment as for G protein binding. This is further supported by the inhibition of cAMP production, modulated by G-protein activated adenylate cyclase, demonstrated by **25a** in the literature [51, 96, 179]. However, it remains possible that our NAMs alter Gαs-protein and β-arrestin2 signalling to different degrees and may explain the differences in SAR dataset trends. For example, NAM **25h** could be more effective at functionally inhibiting β-arrestin2 recruitment specifically than **25a** because the increase in size of the ester moiety, through introduction of the phenyl ring, has an improved overlap of the ligand with the β-arrestin2 binding pocket. Recent literature at class A GPCR neurotensin receptor 1, has reported the ability of intracellular allosteric modulator SBI-533 (biased agonist) to be effector selective preferentially activating β-arrestins over the G protein $G\alpha_q$ preference [316].

In contrast, the NanoBRET competition binding assay identified that variation in the ester moiety had minimal impact on the binding affinity of our ligands for the Gαs peptide mimetic binding pocket. Therefore, the variation in SAR trends between the two datasets for different recruitment proteins supports the theory that our NAMs bind to an intracellular region overlapping both the β-arrestin2 and Gs binding pockets [160, 179]. The extent of ligand overlap with these binding pockets may result in our NAMs altering the signalling of β-arrestin2 and the heterotrimeric Gs protein to different degrees.

Future work may involve the development of new NanoBiT competition binding assays using EP_2-LgBiT, mGα-SmBiT expressing whole HEK293 cells to monitor Gs-protein recruitment and enable direct comparison to β-arrestin2 modulation. Mini-Gα proteins

are engineered GTPase domains of Gα subunits which preserve the GPCR receptor-G protein binding interface and have been applied to the NanoBiT system to measure interactions between GPCRs and their effector proteins [222, 223]. Alternatively, assays measuring downstream cAMP accumulation (e.g. homogeneous time-resolved fluorescence (HTRF) cAMP kit- Revvity) as G-protein dependent responses would provide comparable SAR data [317].

Furthermore, the conformational selectivity and kinetics could differ between binding and functional assays due to ligand-receptor co-operativity. Within the NanoBiT™ assay the 30-minute incubation with the NAMs prior to agonist addition requires binding to the inactive (PGE_2-unbound) conformation of the receptor [318, 319]. Therefore, a ligand's relative ability to bind and stabilise the inactive conformation, shifting the equilibrium in the presence of the orthosteric agonist, could explain the SAR trend in functional potency with **25h** proving the most effective. In contrast, PGE_2 agonist and unlabelled ligands are added concurrently in the NanoBRET assay eliminating this pre-established stabilisation and resulting in the observed flat SAR. However, as both assays achieve equilibrium prior to data recording this is an unlikely contributor to the SAR dataset. Additionally, the use of membranes compared to whole cells in the NanoBRET assay and the addition of a C-terminal NLuc modification could result in alterations to the EP_2 receptor conformation thus distorting our generated functional potency/binding affinity data.

Selectivity studies for the most efficacious *h*EP_2 compounds **25a-b** and **25e-i** were conducted using a NanoBiT complementation assay in the closely related EP_4 receptor. Overall, these ligands demonstrated lower functional potency for *h*EP_4, with pIC_{50} values between 4.43-5.01. Calculating the fold change in the pIC_{50} values between *h*EP_2 and *h*EP_4 identified **25h** as having the best selectivity at over 20-fold. Comparatively, literature compound **25a** demonstrated only 2.2 -fold selectivity and **25b**, the second best, a selectivity of 5.9-fold. While it would have been useful to establish a *h*EP_4 NanoBRET binding assay for additional comparisons with the *h*EP_2 binding data,

previous laboratory attempts using the TMR- Gαs19cha18 probe proved unsuccessful (Dr N Holliday, personal communication).

3.4 Series 1 pharmacology conclusions.

In summary, the NanoBRET™ competition binding assay demonstrated for the first time seven ligands **25a**-**b** and **25e**-**i** had nanomolar binding affinity (15-72 nM range) for the intracellular Gs binding site detected by fluorescent probe TMR-Gαs19cha18. Modifications focused on the ester region exhibited a flat SAR with a notable reduction in binding affinity occurring upon ester removal. This indicates the ester likely participates in a key hydrogen bonding interaction with the EP_2 intracellular binding pocket. The SAR dataset of series 1 further supports the 2,3-dihydrobenzo[*b*][1,4]dioxine motif as an essential driver of ligand binding to the allosteric site. Elimination/modification of this region resulted in very low ligand affinity for the receptor.

The NanoBiT™ complementation assay was first utilised to produce CRC curves for three known EP_2 receptor agonists; butaprost, evatanepag and PGE_2 [299-301]. The pEC_{80} and R_{max} values were calculated with endogenous agonist PGE_2 having the highest functional potency and being the only full agonist tested. Both butaprost and evatanepag demonstrated partial agonism at the EP_2 receptor with R_{max} values 30 % and 50 % lower respectively than for PGE_2 [300, 302]. Additionally, the generation of an agonist EC_{80} timecourse allowed for identification of suitable assay read times. Two agonists, PGE_2 and evatanepag, produced a suitable luminescence window for determination of our unlabelled allosteric modulators functional potency.

Five analogues in series 1 were identified as having micromolar range functional potency at EP_2-LgBiT, β-arrestin2-SmBiT tagged stably transfected HEK293 cells with pIC_{50} values >5. This confirms our NAMs permeate the cell membranes and reach the proposed allosteric binding pocket to functionally inhibit β-arrestin2 recruitment at the *h*EP_2 receptor. Selectivity studies, monitoring β-arrestin2 recruitment at *h*EP_4 in whole

cells, demonstrated that all NAMs of the *h*EP_2 receptor had lower functional potency at *h*EP_4 (pIC_{50} 4.4-5.0). From these assays benzyl ester analogue **25h** was identified as the NAM with both the best inhibitory potency, pIC_{50} value of 5.96, and the largest fold difference in selectivity, 20.4- fold difference in pIC_{50} value, for hEP_2 over hEP_4.

In conclusion benzyl ester analogue **25h** was identified as the allosteric antagonist of the *h*EP_2 receptor with the highest binding affinity, highest functional potency and best selectivity for EP_2 over EP_4 in series 1. A second compound library was designed and synthesize based upon this lead compound with modifications focused on the phenyl ring.

Chapter 4- Synthesis of series 2

4.1 An introduction to series 2

Pharmacological characterisation of our series 1 compound library identified seven analogues with binding affinity for the intracellular pocket of the *h*EP_2 receptor and a reported pK_i range of 7.14-7.84. Binding affinity was determined using NanoBRET™ competition binding assays in membrane suspensions observing the displacement of a G_s protein mimetic probe TMR-Gαs19cha18 by our unlabelled ligands [219, 289]. A relatively flat SAR dataset was produced with binding affinity being reduced upon replacement of the ester for a nitrile and eliminated with modifications at the 2,3-dihydrobenzo[*b*][1,4]dioxine moiety. The NanoBiT™ complementation assay, conducted in whole cells, demonstrated that all ligands with known binding affinity for the Gαs allosteric binding pocket displayed functional inhibition of β-arrestin2 recruitment at the *h*EP_2 receptor with pIC_{50} values ranging between 4.77-5.96 [222]. Selectivity studies conducted at the closely related *h*EP_4 receptor demonstrated lower functional potency with reported pIC_{50} values between 4.43-5.01.

From this data we identified ligand **25h** as an allosteric antagonist of the *h*EP_2 receptor displaying both the highest binding affinity (pK_i= 7.84 ± 0.11) and functional potency (pIC_{50}= 5.96 ± 0.08) of the compound library; an improvement compared to literature compound **25a** (pK_i= 7.14 ± 0.11, pIC_{50}=5.00 ± 0.08) [179]. Furthermore, **25h**

demonstrated the best selectivity in series 1 for the *h*EP_2 receptor over *h*EP_4 with a 20.4-fold difference in pIC_{50} values. Comparatively, the literature compound **25a** demonstrated only 2.2-fold selectivity in functional potency at *h*EP_2 vs *h*EP_4 in whole cells.

Using the pharmacological characterization results of series 1, a second compound library was designed and synthesized with modifications focused on the benzyl ester aromatic ring in **25h**, (see Table 9). Synthesis of the ortho-, meta- and para- analogues were conducted for each phenyl substituent to explore ligand toleration at the intracellular EP_2 binding pocket. The aim of this series was to vary physiochemical properties to ensure cell membrane permeability, good bioavailability and reducing lipophilicity to a value <5 to satisfy Lipinski's rules [235]. Additionally, adding new hydrogen bond donor/acceptor regions could potentially exploit additional interactions within the binding pocket. Analogues **40a-c** & **h**-**m** are predicted to satisfy Lipinski's rule of five, with a molecular weight below 500 g/mol, calculated logP of <5, <5 hydrogen bond donors and <10 hydrogen bond acceptors. This suggests these ligands have good drug-likeness and are predicted to have good absorption and permeability [235, 236]. The remaining analogues have a predicted LogP value >5 which may contribute to poor absorption, distribution, metabolism and excretion (ADME) properties in in-vivo studies. All ligands reported have <10 rotatable bonds and have a calculated tPSA within the ideal range of 60- 140 $Å^2$ [239-241]. These values predict the ligands can permeate the cell membrane to reach the intracellular Gs heterotrimeric G-protein binding site and have the conformational flexibility to undergo an induced fit binding mechanism at the target [237]. However, all compounds in this series demonstrate a calculated LogS value <-5, with a range between -5.22 and -8.07, predicting poor aqueous solubility [243, 244].

The first analogues explored involved the replacement of the phenyl ring with pyridine, analogues were generated varying the nitrogen between the 2, 3 and 4 positions (**40a**/**b**/**c** respectively). As pyridines contain a weakly basic polar nitrogen atom (pK_a= 5.20), which are ionizable and polarise the ring system, these ligands are predicted to

have an improved aqueous solubility (calculated LogS of -5.35 for **40a** and -5.22 **40b**/**c** compared to -6.39 for **25h**) [320, 321]. The addition of a strong hydrogen bond acceptor nitrogen, hydrogen bond basicity pK_{BHX}= 1.86 (logarithm of complexation constant *K* of 4-fluorophenol with bases, the higher the PK_{BHX} value the stronger the hydrogen bond acceptor) aims to explore new intermolecular interactions within the binding pocket [322-325].

Inclusion of halogens to the phenyl ring enables potential halogen-π bonding to occur with amino acids such as tyrosine, phenylalanine and tryptophan [326, 327]. Typical halogen-π bonding involves the aromatic benzene ring acting as donors and the C-X (where X= F, Cl, Br or I) act as the acceptors [328]. The reduction in size and increasing electronegativity difference between the chloride-substituted analogues **40d**-**f** and the fluoride-substituted analogues **40q**-**s** varies the strength of potential halogen-π bonding and explores what is tolerated in the binding pocket [329]. However, halogen atoms are hydrophobic and their addition to the phenyl ring is predicted to increase compound lipophilicity and decrease aqueous solubility in accordance to their atomic size. The larger less electronegative chloro- substituents increase the nonpolar character of the molecule and have a predicted LogS of -7.01, whereas, for the smaller fluoro-substituents this effect is reduced with a LogS of -6.62 [330, 331].

Aromaticity has been removed in the cyclohexyl ester **40g** inserting a non-planar ring and increasing conformational diversity (adopting either a chair or boat conformation) to better adapt to the intracellular binding pocket [332]. The inclusion of methoxy phenyl in various substitution patterns (**40h**-**j**) is a typical functionalization during lead optimisation [333]. Unlike purely electron-withdrawing atoms e.g. fluorine, the methoxy group exhibits both an electron donating (+M) mesomeric effect, with the oxygen atom lone pair of electrons being delocalised into the pi system, and an electron withdrawing (-I) inductive effect caused by the electronegativity of the oxygen [334]. As a result the oxygen atom displays a partial negative charge, whereas the methyl group has a partial positive charge. These varying electrostatic potentials could enable either hydrogen bonding with oxygen as the acceptor and/or Van der Waals interactions between the

ligand and the amino acid residues of the intracellular EP_2 pocket [333]. Furthermore, the bent arrangement of this group means it can orient itself either coplanar (all atoms lie within the same geometric plane) or orthogonal (methoxy group is at 90°) compared to the aromatic ring and to be more easily accommodated in the binding pocket, (see Figure 4) [335, 336]. These analogues are predicted to decrease the calculated LogP value to within the desired range of <5 at 4.88.

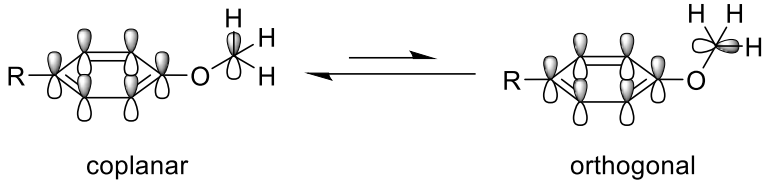

Figure 28- *Coplanar vs orthogonal conformations of methoxyphenyl [333, 336].*

The inclusion of naphthalenes in **40n**/**o** results in a large increase in molecular weight to explore binding pocket tolerability. It is notable that these ligands fall outside the Lipinski's rule of five, with both a molecular weight and cLogP outside of the desired values of <500 and <5 respectively [235]. As a result, these ligands are predicted to have high lipophilicity, poor absorption/permeation and display poor drug-likeness. Additionally, these analogues display the lowest predicted LogS value (-8.07) of the series which may result in aqueous solubility issues during preparation of the pharmacological characterization assays. The extension of the alkyl chain in the phenyl ethyl ester **40p** increases the number of rotatable bonds and the conformational flexibility of our ligand potentially improving binding affinity [238]. The predicted aqueous solubility and lipophilicity of **40p** remains unchanged compared to lead **25h**.

Finally, development of a series of phenols **40k**-**m**, which are weakly acidic (pK_a = 9.8) and can act as hydrogen bond donors, would enable the formation of interactions with any NH/OH species in the amino acids of the binding pocket (eg. Gln, Ser and Tyr) [337, 338]. Furthermore, aqueous solubility is predicted to improve with an increase in the LogS to -5.92 and decrease in the LogP value to 4.85 compared to **25h**.

***Table 9**-Series 2 compound library structures including their calculated molecular weight, Nº of H-bond donors/acceptors, LogP, LogS, Nº of rotatable bonds and total polar surface area (calculated using Marvinsketch version 25.1.75 by Chemaxon). Compounds in red were designed but not synthesized due to time constraints.*

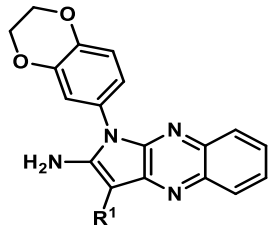

Compound Nº	R^1	Molecular weight	Nº H-bond acceptors	Nº H-bond donors	cLogP	cLogS	Rotatable bonds	Total polar surface area (Å²)
40a	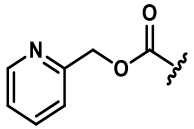	453.46	9	1	3.97	-5.35	6	114.4
40b	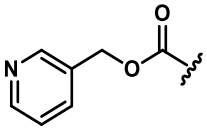	453.46	9	1	3.82	-5.22	6	114.4
40c	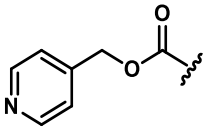	453.46	9	1	3.82	-5.22	6	114.4
40d	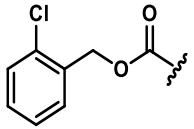	486.91	8	1	5.65	-7.01	7	101.5

40e	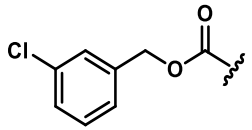	486.91	8	1	5.65	-7.01	7	101.5
40f	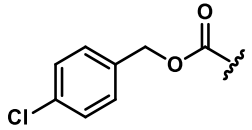	486.91	8	1	5.65	-7.01	7	101.5
40g	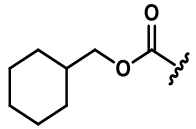	458.52	8	1	5.25	-7.15	6	101.5
40h	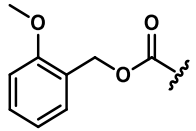	482.50	9	1	4.88	-6.30	8	110.7
40i	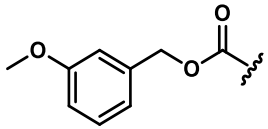	482.50	9	1	4.88	-6.30	8	110.7
40j	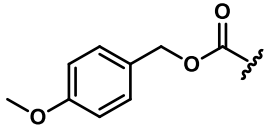	482.50	9	1	4.88	-6.30	8	110.7
40k	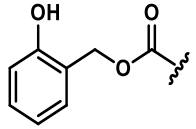	468.47	9	2	4.85	-5.92	7	121.7

40l	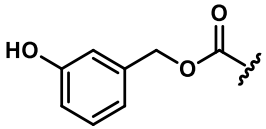	468.47	9	2	4.85	-5.92	7	121.7
40m	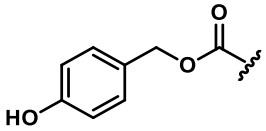	468.47	9	2	4.85	-5.92	7	121.7
40n	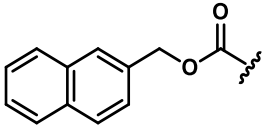	502.53	8	1	6.13	-8.07	6	101.5
40o	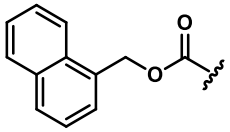	502.53	8	1	6.13	-8.07	6	101.5
40p	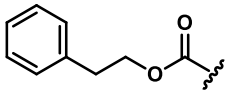	466.50	8	1	5.38	-6.38	7	101.5
40q	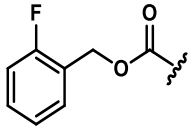	470.46	8	1	5.27	-6.62	7	101.5
40r	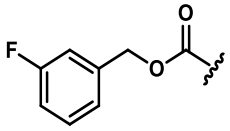	470.46	8	1	5.27	-6.62	7	101.5

40s	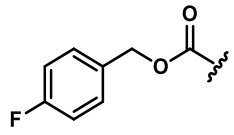	470.46	8	1	5.27	-6.62	7	101.5

4.2 Synthesis of analogues 40a-j and 40n-t.

The non-convergent synthetic route developed for series 1, inserting the ester moieties within the first reaction step, was employed for the synthesis of series 2 (see Scheme 6). University of Nottingham, School of Pharmacy students Sam Robinson, Ng Yu Yang and Bulbul Singh contributed to this work [339-341].

Scheme 6- *Non-convergent synthetic route to analogues* ***40a, c-j*** *&* ***n-s*** *[245, 246, 263].*

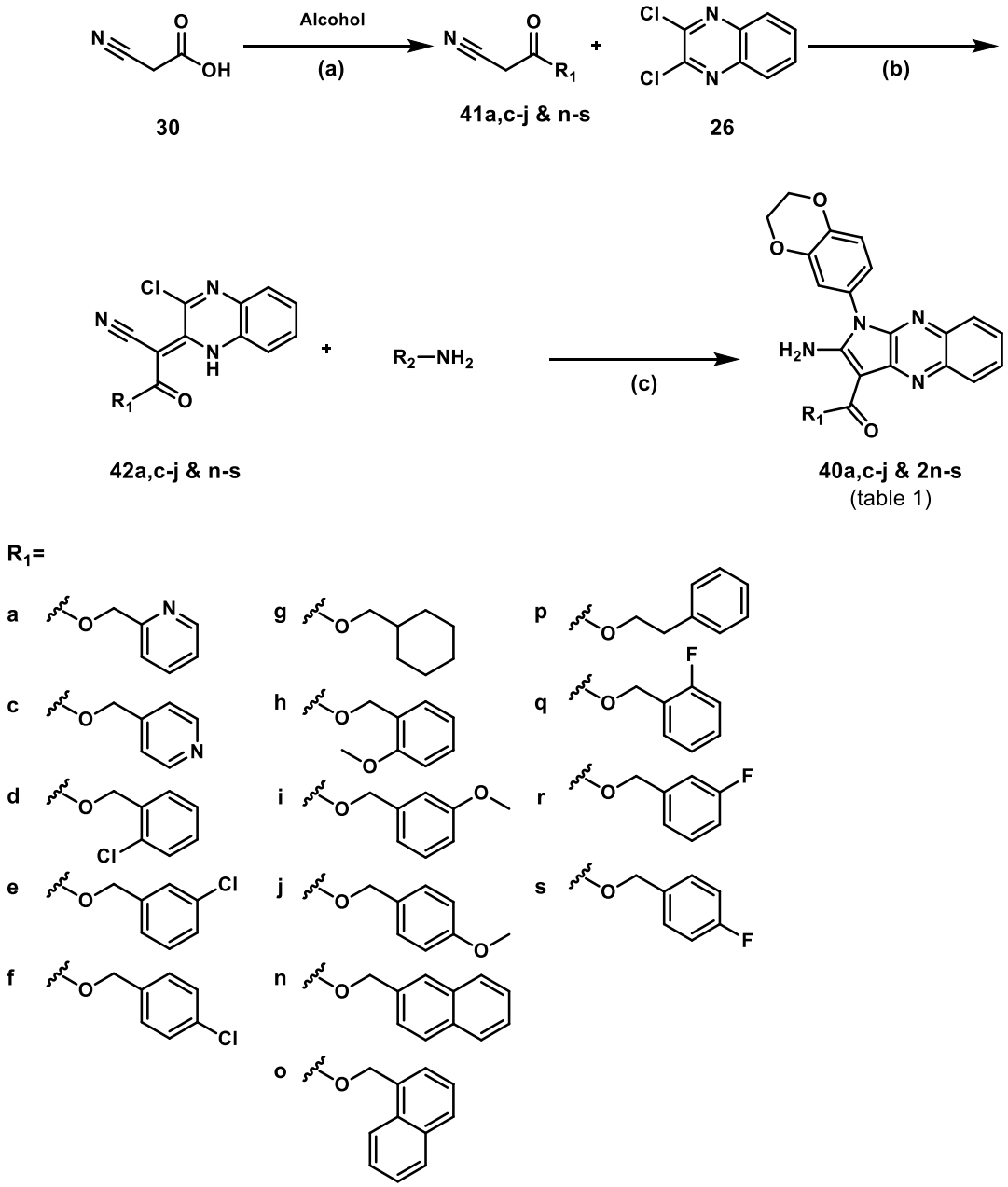

Reagents and conditions- *a) Alcohol, DCC, DMAP, DCM, 0 °C, rt, 24 h, 17-77 %. b) 2,3-Dichloroquinoxaline, Cs_2CO_3, DMF, rt, 24 h, 37-90 %. c) Amine, EtOHl/THF (3:1), 80 °C, 24 h, 12-91 %.*

This route employs a 'Steglich esterification' with 2-cyanoacetic acid (**30**) and the desired alcohol using DCC and DMAP coupling conditions [263]. The resulting esters (**41b**-**j** & **n**-**s**) then react via S_NAr with **26** to yield **42b**-**j** & **n**-**s** followed by cyclisation with the desired amine to yield the desired analogues [245, 246]. Final compounds were isolated in mg quantities and at suitable purities (>95 % by LCMS and NMR) to be carried forward into pharmacological characterisation.

Scheme 7*- Three-step one pot synthetic route to analogue* ***40b*** *[245, 246, 263].*

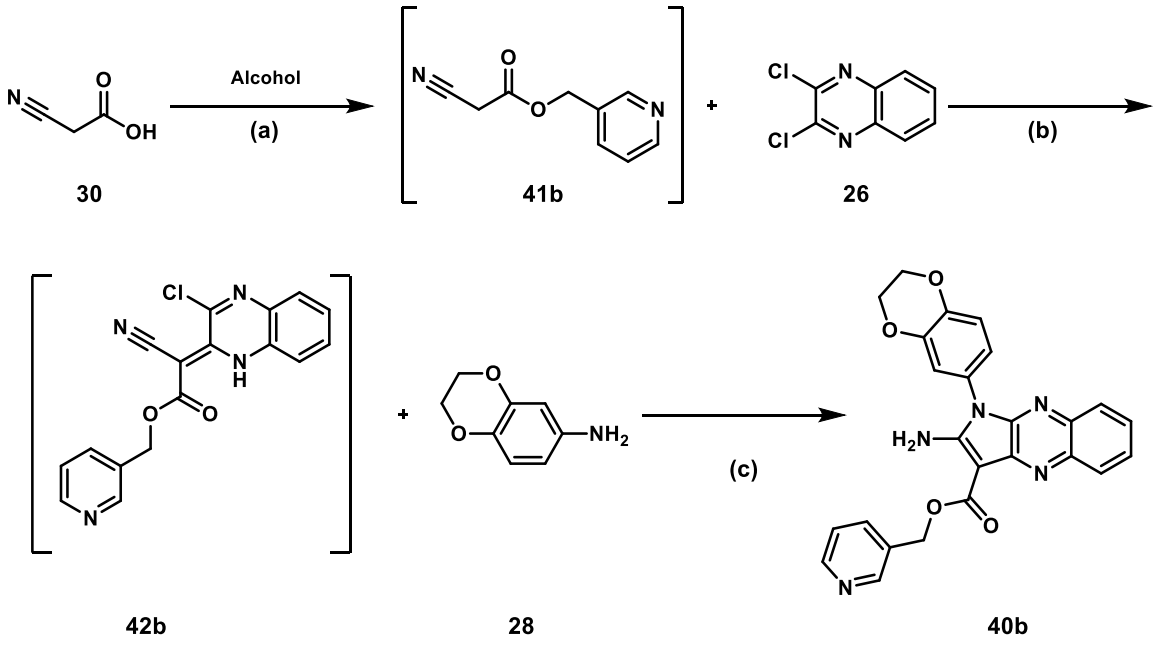

Reagents and conditions*- a) Alcohol, DCC, DMAP, DCM, 0 °C- rt, 24 h. b) 2,3-Dichloroquinoxaline, Cs_2CO_3, DMF, rt, 72 h, c) Amine, EtOH: THF (3:1), 80 oC, 24 h, 35 %.*

The synthesis of meta-pyridine **40b** was conducted in a three-step one pot reaction procedure, (see Scheme 7). This method involves a filtration and aqueous work-up for crude intermediate **41b** to remove the coupling reagents DCC and DMAP. The solvent DCM was also removed under vacuum at room temperature before the crude material underwent the S_NAr reaction with dichloroquinoxaline (**26**). Additionally, after the formation of intermediate **42b** DMF was removed under vacuum at room temperature, dry acetonitrile was then added and the crude material sonicated and filtered to remove the Cs_2CO_3. This crude material was carried forward into the final cyclisation reaction step to produce a white solid which crashed out upon cooling and was be recrystalized

in 3:1 EtOH: THF to yield the **40b** in mg quantities and appropriate purity (>95 % by LCMS and NMR).

This route was developed due to the tendency of the ester intermediate **41b** to undergo transformation from a pale pink solid to a dark pink/purple by-product upon attempted work-up/purification procedures. Additionally, upon isolation of intermediate pyridin-3-ylmethyl 2-cyanoacetate a colour and composition change from a pale pink solid running as a single spot by thin-layer chromatography (TLC) to a dark pink/purple oil with multiple spots on TLC occurred after drying in a vacuum oven overnight. This significant colour/composition change is likely the result of compound decomposition and as a result no heat was used in the first two reaction steps. Furthermore, an attempt was made to isolate **42b**, synthesized with the above reaction conditions, but was proved unsuccessful. A second nucleophilic aromatic substitution occurred at the chloro- position with methanol during the work-up/purification procedure and was identified by NMR and LCMS.

Alternative solvent conditions were trialled for the one-pot three step reaction following esterification to eliminate removal of Cs_2CO_3 and the use of DMF- a high boiling point and difficult to remove solvent. Similar polar aprotic solvents *N*-methylpyrrolidone (NMP) and 1,4-dioxane were trialled and formed intermediate **42b** confirmed by TLC and LCMS [342]. However, neither solvent yielded final compound **40b** upon reaction with amine **28** despite an increase in reaction temperature from 80 °C to 100 °C. Therefore, the original conditions in scheme 4 were employed with the described work-up procedures at each crude intermediate to yield **40b**.

4.3 Synthesis of phenols 40k-m.

Due to time constrains phenols **40k-m** were not successfully synthesized however significant synthetic effort was conducted attempting to produce these analogues. Since methoxy benzene **40h-j** analogues had already been synthesized as part of this series numerous demethylation reactions were trialled. Demethylation attempts using

reagents boron tribromide or pyridine hydrochloride in the microwave both resulted in hydrolysis of the ester to form the corresponding carboxylic acid by-product, therefore, an alternative approach to synthesise the phenols was required [343, 344]. This work was undertaken by student Bulbul Singh [340].

Due to the presence of two nucleophilic alcohols on the ortho/meta or para substituted -(hydroxymethyl)phenol starting material, the attachment of a protecting group to the phenol is essential in preventing unwanted side reactions and by-products. For example, during the esterification and nucleophilic aromatic substitution reactions. A reaction screen was conducted on 4-(hydroxymethyl)phenol to identify protecting groups that are selective for the phenyl alcohol and stable under basic conditions (see Table 10). Any successful protecting group strategies identified in this screen could then be used to produce the remaining ortho- and meta- substituted phenols.

***Table 10**- Reaction condition screen inserting a selective protection group on the para substituted phenol [345-349]*.

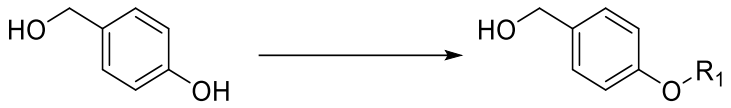

43 **44**

Experiment	Protecting Group R_1	Reagents	Reaction conditions	Outcome	Notes
1	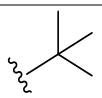	t-butyl chloride (excess) zinc dust (1eq.)	Rt, 24 h.	No product formation by NMR.	Reaction mixture plum coloured.
2		t-butyl chloride (1 eq.) K_2CO_3 (1.2 eq,) DMF	80 °C 48 h.	No desired product formation by LCMS.	Additional 0.5 eq. of both t-butyl chloride and K_2CO_3 at 24 h.
3	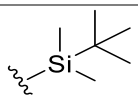	Tert-butyldimethylsilyl chloride (TBDMS-Cl, 1 eq.) 1,8-Diazabicyclo[5.4.0]undec-7-ene (DBU, 1.2 eq.) Acetonitrile	-10 °C -> rt, 24 hr,	23 % yield of desired product as a colourless oil.	Product unstable under mild basic conditions (Cs_2CO_3). Not suitable for second reaction step.

4	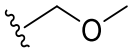	Chloromethyl methyl ether (MOM, 1 eq.) DIPEA (1.2 eq.) DCM	0 °C -> rt, 48 hr,	No desired product formation by LCMS.	At 12 hours an additional 0.5 eq. of DIPEA and MOM was added.
5	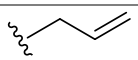	Allyl bromide (1 eq.) K_2CO_3 (1.2 eq.) DMF	80 °C 24 h.	39 % yield colourless oil.	Suitable protecting group to take forward.

The results of our screen identified the formation of an allyl ether **44** as a suitable protection strategy, scheme 8. This protected phenol could then undergo the 'Steglich esterification' with 2-cyanoacetic acid (**30**), followed by subsequent nucleophilic aromatic substitution and cyclisation to yield **22** [263]. A final deprotection reaction would theoretically generate desired phenol **40m**. Compound **22** was identified as a suitable analogue for pharmacological characterisation containing the same core structure as lead **25h** and a novel phenyl substituent with a hydrogen bond donor oxygen.

Scheme 8*- Unsuccessful Synthetic route to generate analogue* ***2m*** *involving protection of the phenol with an allyl ether prior to esterification and unsuccessful deprotection in the final reaction step using various conditions [245, 246, 263, 349]. Intermediate* ***40u*** *was isolated in mg amounts and appropriate purity for pharmacological characterisation.*

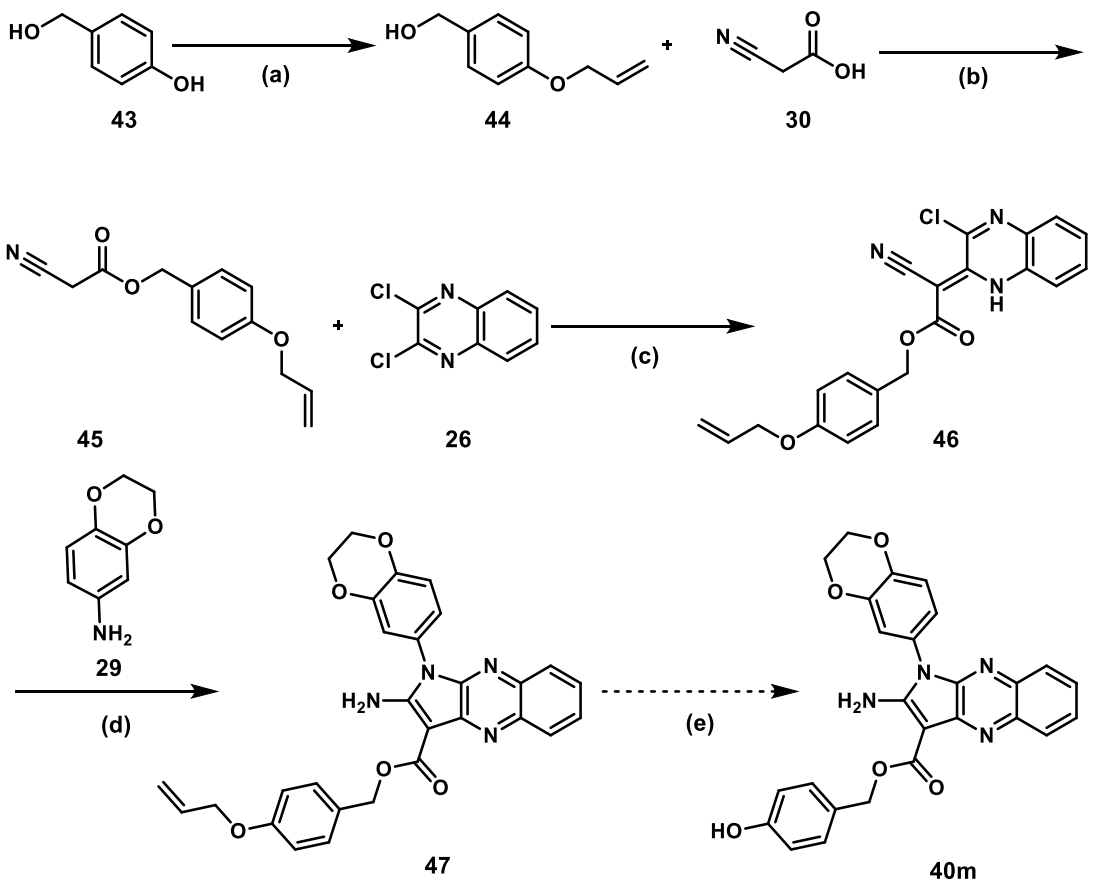

Reagents and conditions*- a) Alcohol, allyl bromide,* K_2CO_3*, DMF, 80 °C, 24 h, 39 %. b) 2-cyanoacetic acid, DCC, DMAP, DCM, 0 °C- rt, 24 h, 68%. c) 2,3-Dichloroquinoxaline,* Cs_2CO_3*, DMF, rt, 72 h, d) Amine, EtOH/THF (3:1), 80 °C, 24 h, 53%.*

A screen of reaction conditions for the deprotection of **47** was conducted but proved unsuccessful; either no reaction occurred, or the ester was hydrolysed to the carboxylic acid, (see Table 11).

***Table 11**- Reaction condition screen for the deprotection of allyl ether protected phenol [349-353].*

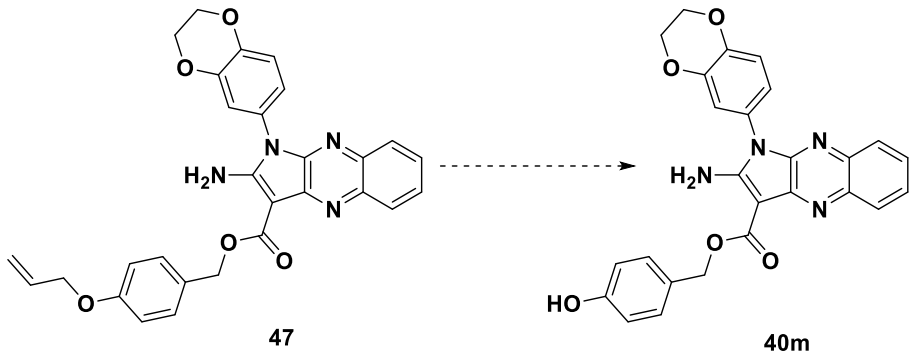

Experiment	Reagents	Reaction conditions	Outcome- monitored by LCMS	Notes
1	1mol% $Pd(PPh_3)_4$, K_2CO_3 (3 eq.) MeOH (degassed)	Rt, 36 h	Incomplete reaction- Majority **47** present with small amount of hydrolysed ester present.	
2	^{t}BuLi (1.1 eq.), pentane	Rt, 24 h.	No reaction- only starting material present	This is likely a solubility issue of **47** in pentane.
3	1. ^{t}BuOK (6 eq.), DMSO 2. HCl (6.6 eq.)	1. 120 °C, 16 h 2. Rt, 24 h	No formation of desired product, complete conversion to hydrolysed ester.	Due to the mg scale of this scope reaction adding 0.5 eq. of reagents was not viable.
4	10 % Pd/C 10 % KOH in MeOH	Rt, 30 hr,	No desired product formation by LCMS. Majority **47** with small amount of hydrolysed ester.	
5	BBr_3 (0.33 eq.) BCl_3 (0.33 eq.) DCM	-78 °C -> rt, 24 h.	Complete conversion to carboxylic acid by-product by ester hydrolysis.	

Future work for the synthesis of phenol's **40k**-**m** could explore the use of the Dakin reaction from the corresponding aromatic aldehyde using dihydrogen peroxide and a

base [354]. This reaction is a two-step one pot process involving a Baeyer-Villiger oxidation of the aryl aldehyde with a peroxide source to form an aryl formate ester which can be saponified to yield the desired phenol [355, 356]. Additionally, insertion of a nucleophilic flavin catalyst and a Hantzsch ester to the reaction could eliminate the need for dihydrogen peroxide in this reaction and can be conducted under mild basic conditions [357]. Palladium or copper catalysed reactions such as Buchwald-Hartwig etherification and an Ullmann reaction respectively, can also be employed to introduce oxygen to the phenyl ring [358, 359]. These reactions involve the coupling of an aryl halide with an oxygen source, such as water or hydroxide salt, and a catalyst. For the Ullman reaction a catalyst stabilising ligand such as *N*,*N*-dimethyl glycine is often employed [360]. Furthermore, the development of an amide series of analogues would mean the allyl ether protecting group strategy may be a viable approach for phenol synthesis. Amides are significantly more stable to demethylation conditions than their ester counterpart. This is a result of resonance stabilisation from the nitrogen lone pair resulting in a less electrophilic carbonyl and leading to resistance towards hydrolysis in typical acidic or basic conditions [361].

4.4 Synthesis of series 2 conclusion

In conclusion, the previously developed non-convergent synthetic route was successfully employed to synthesize 16 novel analogues of lead compound **25h**. A variety of functionality was inserted onto the benzyl ester phenyl ring attempting to vary physiochemical properties and add new moieties for the formation of new intermolecular interactions with the intracellular prostaglandin EP_2 binding pocket. Synthesis of the ortho-, meta- and para- analogues were conducted for each phenyl substituent to explore ligand toleration at this binding site. The synthesis of meta-pyridine **40b** required the modification of scheme 6 to produce a three-step one pot reaction (see Scheme 7) eliminating the need for purification of unstable intermediates.

Development of phenols **40k**-**m** would insert an additional hydrogen bond donor and was predicted to modify aqueous solubility and lipophilicity [337, 338]. Significant synthetic effort was conducted to yield these analogues but, due to time restraints, these phenols were not isolated. Firstly, demethylation of the methoxy benzene analogues **40h**-**j** proved unsuccessful. The ester, a better electrophile, is more reactive towards nucleophilic attack than the relatively stable methyl groups. Therefore, as expected a carboxylic acid by-product was observed under all screened demethylation conditions. An alternative approach called for the installation of a phenol protecting group prior to the initial 'Steglich esterification'. This would ensure selective ester coupling with the primary alcohol and prevent unwanted nucleophilic aromatic substitution upon reacting with the 2,3-dichloroquinoxaline. From a reaction screen allyl ether protection was identified as a suitable approach and carried through the synthesis route to yield **47**; identified as a suitable analogue to carry forward for pharmacological testing. However, deprotection strategies proved challenging with either no formation of the desired phenol, or with ester hydrolysis occurring. The development of an amide series which is stable to acid or base hydrolysis would circumvent issues relating to allyl ether deprotection and may provide a suitable strategy to yield a series of phenol analogues. Alternatively, future work could explore alternative synthetic approaches to install phenols at the phenyl ring. Some examples include the Dakin reaction, Buchwald-Hartwig etherification or the Ullmann reaction [354, 358, 359].

Additional future work involves conducting IAM analysis to experimentally predict and compare the membrane permeability and lipophilicity of each analogue [311]. IAM columns contain a monolayer of phospholipids covalently bonded to an inert silica support which mimic fluid cell membranes. The retention time of each compound through the columns are measured and converted into the solute capacity factor $\log K_{(IAM)}$ which correlates well with solute equilibrium partition coefficients $\log(K_m)$ measured in fluid liposome systems [311]. These experiments were not conducted due to project time constraints but would produce valuable data for future lead optimization strategies.

Chapter 5- Pharmacological assessment of series 2 analogues as EP_2 negative allosteric modulators

5.1 Aims of pharmacological characterization of series 2

Pharmacological characterisation of series 1 identified the benzyl ester analogue **25h** as the lead compound for further optimisation, as it displayed both the highest functional potency and binding affinity at the *h*EP_2 receptor in series 1. Seventeen novel analogues of **25h** were designed and synthesised with modifications focused on the ester phenyl ring, to yield the series 2 compound library. The aim of this series was to vary the physiochemical properties of the ligands and explore the formation of new intramolecular interactions with the intracellular EP_2 binding pocket to improve ligand functional potency and binding affinity. Series 2 underwent pharmacological characterization using the previously described NanoBRET™ competition binding assay utilizing the fluorescent probe TMR-Gαs19cha18 to assess and rank our ligand binding affinities for the intracellular allosteric $G\alpha_s$ binding pocket in EP_2. Next, the NanoBiT™ complementation assay measuring β-arrestin2 recruitment to EP_2 in the presence of the EC_{80} concentration of PGE_2 was utilized to determine ligand properties as functional antagonists of the pro-inflammatory target prostanoid receptor *h*EP_2 in cell-based assays (see Chapter 3.3). This assay was additionally employed to conduct selectivity studies at the closely related receptor *h*EP_4.

From the literature it was identified that the extent of NAM **25a**'s potency and efficacy for the reduction of cAMP production in C6 glioma cells was dependent on the agonist employed.[179] Therefore, the NanoBiT™ complementation assay measuring β-arrestin2 recruitment in the presence of the EC_{80} concentration of the partial agonist evatanepag (see Chapter 3.3.2) was conducted in HEK293 cells stably overexpressing either *h*EP_2 or *h*EP_4 whole cells to allow for direct comparison of our NAM's functional potency upon receptor activation by agonists with different intrinsic efficacy at the EP_2 receptor [362]. Furthermore, Schild style concentration response curve analysis employing the agonists PGE_2 and evatanepag in the presence and absence of different concentrations

of antagonist in whole cell NanoBiT complementation assays were conducted with the aim of providing further insight into the mode of action of our ligands. For competitive, reversible antagonists we would expect to see surmountable antagonism with no change in the maximum agonist response (R_{max}) but a rightward curve shift indicative of higher agonist EC_{50} values. In this instance the affinity of the antagonist could be calculated from this by a Schild plot/ Gaddum equation: [363-366]

$$concentration\ ratio\ (CR) = \frac{\log\ (agonist\ EC_{50}\ in\ presence\ of\ antagonist)}{Log(agonist\ EC_{50}\ in\ control)}$$

$$antagonist\ K_D = \frac{[antagonist]}{(CR - 1)}$$

In contrast for non-competitive (allosteric) or non-reversible antagonism a reduction in agonist R_{max} can be observed in the presence of the antagonist. Allosteric ligands may exhibit a ceiling effect with the extent of the curve shift saturating at higher concentrations of the modulator.

5.2 Determination of the EP_2 binding affinity of series 2 compounds through NanoBRET™ competition binding assay.

The previously described NanoBRET™ competition binding assay conducted at EP_2-*ts*NLuc HEK293 cell membranes, utilizing the fluorescently tagged G-protein mimetic TMR-Gαs19cha18, was used to calculate the binding affinities (reported as pK_i values) of our unlabelled ligands for the intracellular *h*EP_2 pocket (see section Chapter 1-5.3, Chapter 3-1.2) [219, 289].

All seventeen ligands in series 2 successfully displaced fluorescent tracer TMR-Gαs19cha18 with pK_i values within the range 6.53-7.59 (see Figure 29, Table 12). The series 1 lead compound **25h** was used as a reference control and re-characterised in these NanoBRET assays to account for any variations caused by utilising a new batch of membranes (produced from a later cell passage number) and to enable direct comparison to data produced in series 1. The p*K*i values in this series were lower than

previously reported; lead NAM **25h** had a calculated pK_i of 7.05 ±0.16 when assayed in tandem with series 2 compounds (see Figure 29A), compared to a previously determined pK_i of 7.84 ±0.18 when determined in series 1 data (see Figure 23, Table 5).

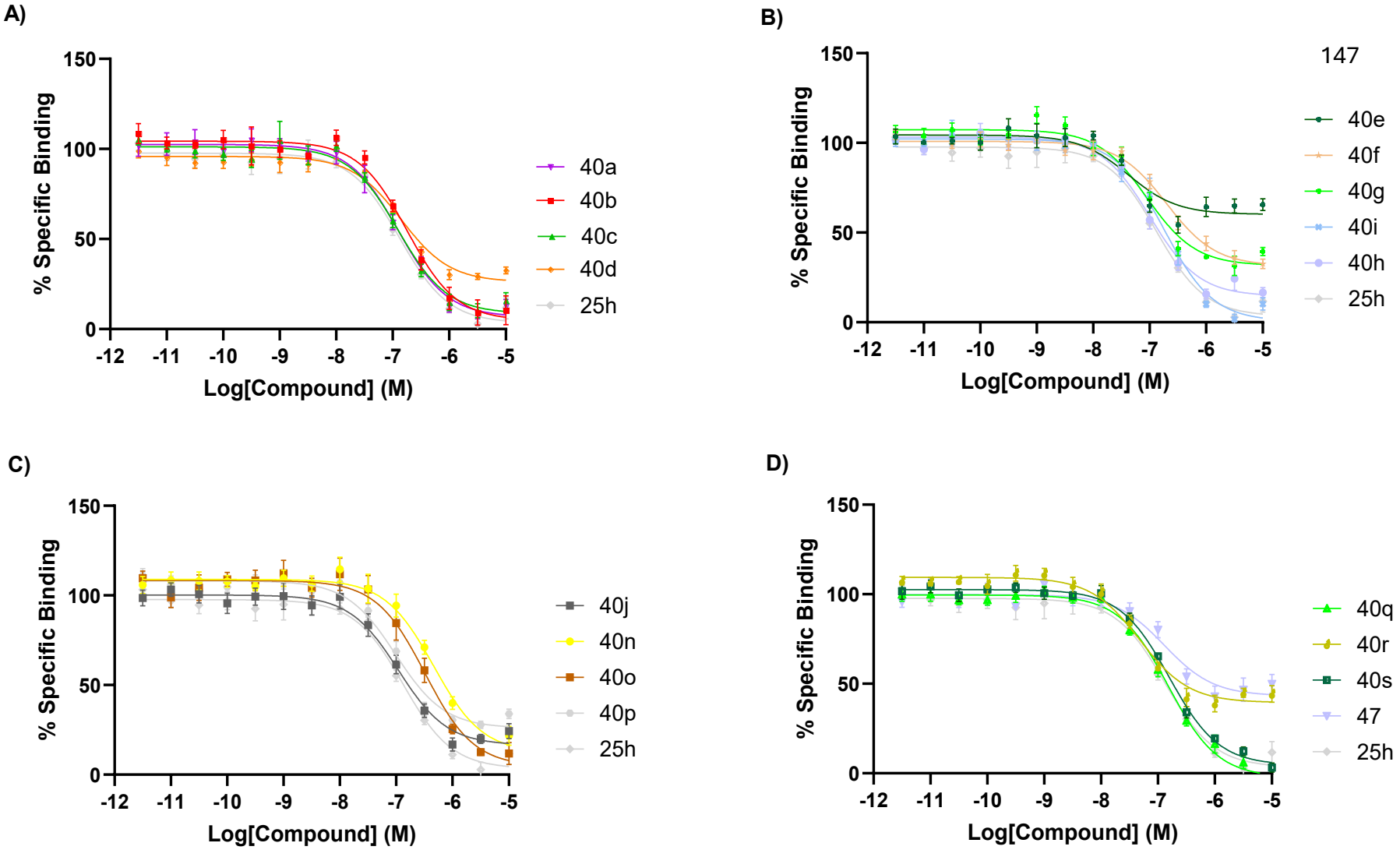

Figure 29-A-D) *NanoBRET® competition binding data for series 2 compounds shown as % specific binding against increasing concentrations of the competing ligand. The specific binding data shown was normalised and pooled from five independent experiments, with non-specific binding determined by addition of 10 µM of* ***25b****. Assay was performed using 1 µM TMR-Gαs19cha18 tracer in a low sodium buffer + 0.2 % bovine serum albumin, 1/960 Furimazine, 10 µM* PGE_2 *and varied concentrations of competing ligands, incubated at 37 °C for 1 h. [219, 289]*

Table 12- *Mean pK_i values of series 2 unlabelled competing ligands normalised and pooled from five independent NanoBRET competition binding experiments including the standard error of the mean (SEM), % reduction in specific binding, fold increase in pK_i from* ***25h*** *and compound structures. One way ANOVA followed by Dunnett's post test conducted for pK_i and % reduction in specific binding comparing to* ***25h*** *reference compound reported as *P<0.05, ** P<0.01 and ***P<0.001.*

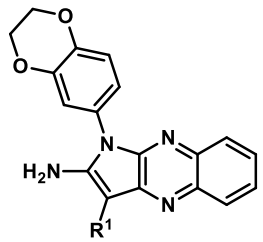

Compound	Structure	Mean pK_i ± SEM	Mean K_i (nM)	Fold change in K_i compared to 25h	% reduction in specific binding (mean ± SEM)
25h	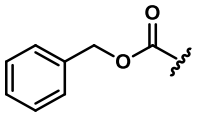	7.05 ± 0.16	89	1.00	94.7 ± 8.0
40a	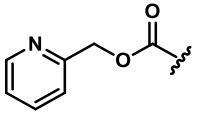	7.09 ± 0.12	81	1.10	95.9 ± 17.0
40b	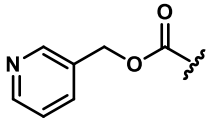	6.92 ± 0.01	120	-	99.7 ± 23.2
40c	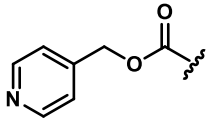	7.10 ± 0.18	79	1.13	92.9 ± 8.2

40d	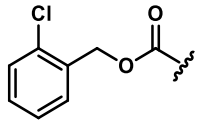	7.04 ± 0.09	91	-	69.7 ± 7.5*
40e	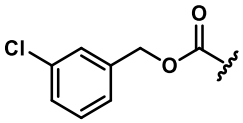	7.59 ± 0.18***	26	3.42	44.4 ± 9.9***
40f	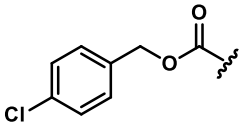	6.90 ± 0.23	126	-	70.0 ± 8.0*
40g	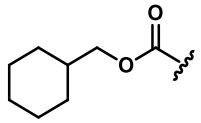	7.25 ± 0.18	56	1.59	76.0 ± 7.3
40h	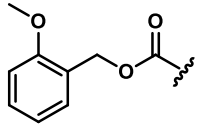	7.18 ± 0.18	66	1.35	89.1 ± 4.9
40i	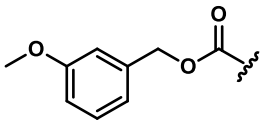	6.95 ± 0.21	112	-	102.2 ± 12.5
40j	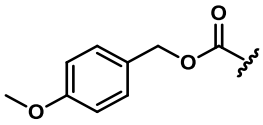	7.15 ± 0.17	71	1.25	83.9 ± 5.7
40n	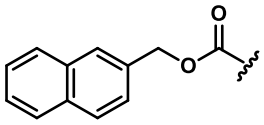	6.53 ± 0.15***	295	-	97.0 ± 9.4

40o	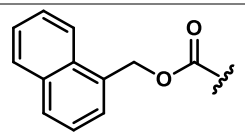	6.70 ± 0.26*	200	-	105.1 ± 17.1
40p	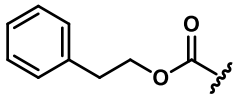	7.20 ± 0.09	63	1.41	82.3 ± 8.3
40q	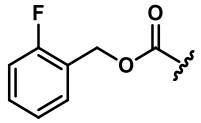	7.01 ± 0.17	98	-	102.3 ± 7.3
40r	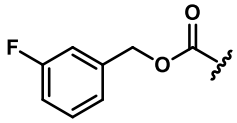	7.51 ± 0.11**	31	2.87	70.0 ± 8.8*
40s	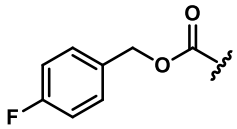	6.99 ± 0.15	102	-	98.6 ± 9.4
47	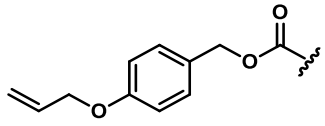	7.08 ± 0.16	83	1.07	56.7 ± 11.5

Series 2 analogues showed only modest differences in SAR in relation to the pK_i values, with no analogue showing more than a 3-fold increase or decrease in binding affinity compared to the representative **25h** (see Table 12). Nine analogues demonstrated an improved binding affinity for the Gs intracellular binding pocket compared to the lead compound from series 1, **25h**. Both meta- substituted halogens (**40e**/**r**) report the highest binding affinities for EP_2 with pK_i values of 7.59 and 7.51 for chloro- and fluoro-substituents respectively. This suggests the possible formation of a new halogen-π intermolecular interaction with the intracellular binding pocket [328, 329]. The sharp decrease in pK_i values for the corresponding ortho- and para- substituted halogens suggests that only meta- substituted halogens are positioned in the correct orientation and conformation for halogen-π bonding to occur with an amino acid in the Gs binding pocket. The naphthalene analogues **40n**/**o** have the lowest reported p*K*i values of this series at 6.53 and 6.70 respectively. This is likely a result of the bulkier naphthalene group not being sterically tolerated within the confines of the binding pocket. Large molecules often require an unfavourable energetic cost to the protein, by forcing conformational changes in amino acids of the binding pocket, leading to a high energetic barrier to binding and are therefore not tolerated [367, 368].

However, an additional characteristic of the data was that six ligands in series 2 had a % reduction in specific binding of <80 %, with **40e** having the lowest at 44.4%. Two hypotheses can be put forward to consider the incomplete competition. Firstly, these ligands are not fully displacing the probe either through binding in different conformations, driven by the addition of new phenyl substituents, or these ligands are binding to a different, but overlapping, site on the EP_2 intracellular pocket [369]. Mutagenesis studies, systematically altering amino acids within the EP_2 intracellular binding pocket between TM 2-6, would identify key residues essential for ligand and/or fluorescent tracer TMR-Gαs19cha18 binding [160, 179, 370]. This would enable identification of the extent of binding pocket overlap and the amino acid residues involved.

Alternatively, due to poor solubility, our ligands could be reaching a saturated solution at the higher concentrations, which then provides a ceiling to the free concentration of the unlabelled ligand in the assay, even if the input of concentration is higher (for example, at greater than 300 nM for ligand **40e**, see Figure 29B).[371] However, based on the calculated physiochemical property measures cLogP and cLogS (see Chapter 4.1, Table 9) the naphthalene analogues **40n**/**o** are predicted to have both the highest lipophilicity and poorest aqueous solubility but have ~ 100 % reduction in specific binding in our assays. Therefore, incomplete displacement of the fluorescent probe is a more likely contributor to this observed change in the % reduction of specific binding for some analogues. Thermodynamic solubility experiments, such as the shake-flask method, can be used to determine the equilibrium saturation solubility of a compound; state of equilibrium where no more solid compound will dissolve into the solution.[372] The shake-flask method involves the manual shaking of an excess amount of solid with a solvent at constant temperature until equilibrium is achieved. The compound concentration in the resulting saturated solution is then measured by ultraviolet (UV) spectroscopy and high-performance liquid chromatography (HPLC) [372, 373]. For both explanations, some caution should be applied to the pK_i calculations from analogues which showed incomplete competition. This is due to the Cheng-Prusoff correction, which calculates a K_i estimate for unlabelled competitors from the IC_{50} values in competition experiments, assuming completely competitive and reversible behaviour with the probe (i.e. 100 % maximum competition) and that the free concentration of the ligand in the assay is as calculated [374].

Overall, from this NanoBRET™ competition binding assay the meta-fluoro substituted benzyl ester **40r** can be identified as the ligand with the highest binding affinity to the Gs EP_2 binding pocket, with K_i decreased by 2.88-fold compared to lead **25h**, while **40r** retains near maximal displacement of the probe at 70.0 ± 8.8 %.

5.3 Determination of the EP_2 functional potency of series 2 compounds through NanoBiT™ complementation assay.

5.3.1 NanoBiT complementation assay for series two ligands at hEP_2 and hEP_4 in whole cells.

All ligands in series 2 demonstrating binding affinity for the Gs intracellular binding pocket of *h*EP_2 in NanoBRET™ competition binding assays were selected for further functional studies. Their functional potencies were first assessed as pIC_{50} measurements using a NanoBiT™ arrestin complementation assay conducted in EP_2-LgBiT, β-arrestin2-SmBiT tagged stably transfected HEK293 whole cells, and using a single EC_{80} concentration of the EP_2 agonist PGE_2 (see Figure 30A/B and Table 13) [222, 286]. The series 2 analogues displaying the highest functional potency for the *h*EP_2 receptor were then carried forward into selectivity studies using the equivalent NanoBiT™ β-arrestin2 complementation assays for EP_4 receptors stably transfected in Hek293 whole cells (see Figure 30c/d and Table 13). Lead compound **25h** was re-characterized as a reference ligand in these NanoBiT complementation assays to account for any variations in the cell line passages and enable direct comparison to data produced in series 1.

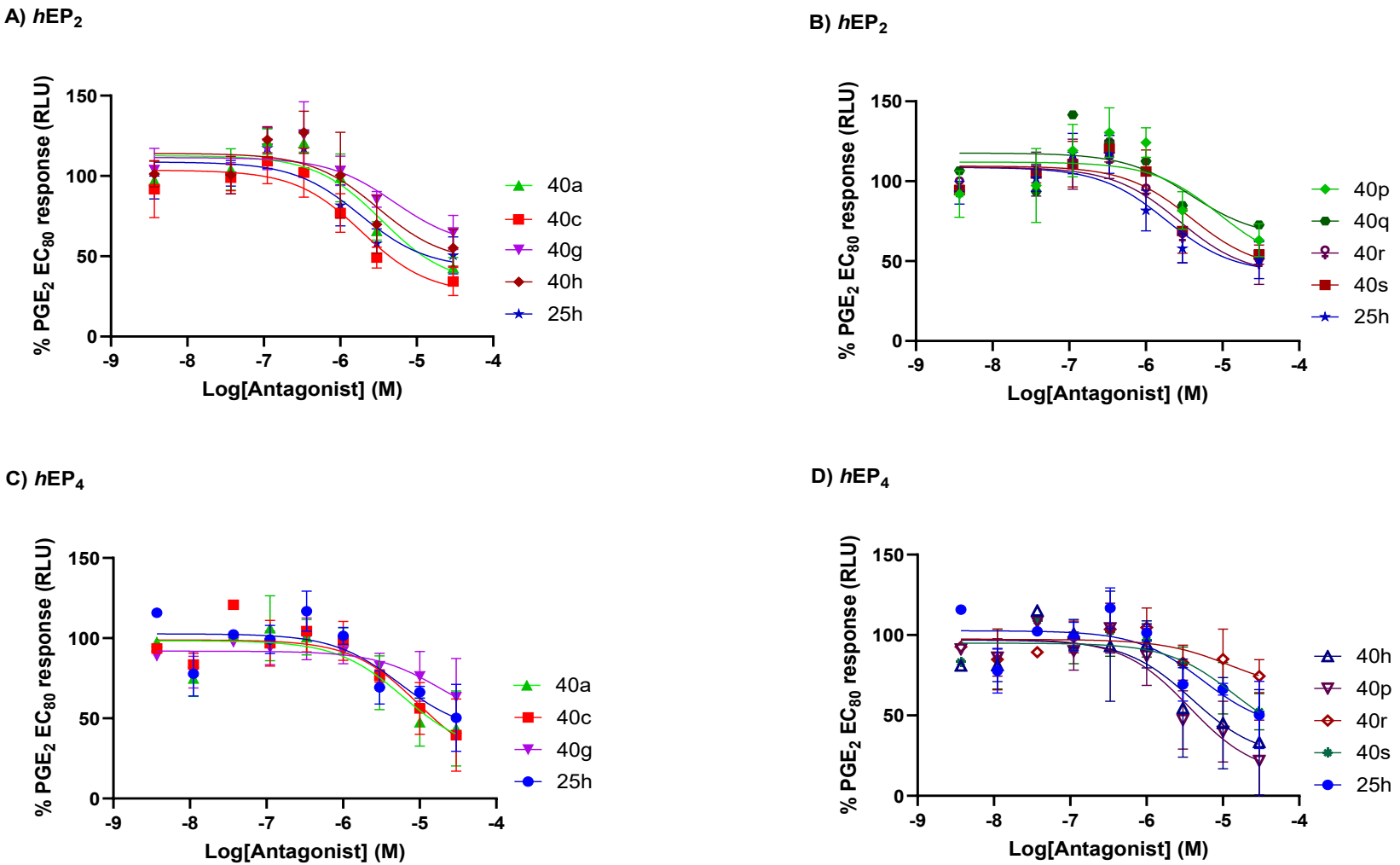

Figure 30*- NanoBiT complementation assay data in* ***A/B)*** *EP_2-LgBiT, β-arrestin2-SmBiT or* ***C/D)*** *EP_4-LgBiT, β-arrestin2-SmBiT tagged stably transfected HEK293 cells shown as % PGE_2 EC_{80} luminescence against increasing concentrations of competing ligand. Compounds were preincubated with cells for 30 min prior to PGE_2 addition at approximately EC_{80} concentration (164 nM EP_2; 1.25 nM EP_4). Response data 30- min post PGE_2 addition are shown as % PGE_2 EC_{80} luminescence against increasing concentrations of competing ligand (60 min total incubation). 1x HEPES buffer + 0.1 % BSA, incubated at 37 °C, 1:750 furimazine, 164 nM PGE_2 EC_{80}. The functional data shown were normalised and pooled from either five (****A/B****) or three (****C/D****) independent experiments.[222]*

.

Table 13- *Mean pIC_{50} values of series 2 unlabelled competing ligands normalised and pooled from five independent NanoBiT™ complementation experiments in hEP_2-LgBiT, β-arrestin2-SmBiT and hEP_4-LgBiT, β-arrestin2-SmBiT tagged stably transfected Hek293 whole cells including the standard error of the mean (SEM), fold selectivity and compound structures. Square brackets around EP_4 pIC_{50} values indicated these came from extrapolations to the curve fit beyond the top concentration of compound tested in the assay. Note- Analogue* ***40q*** *was not pharmacologically characterized at the hEP_4 receptor subtype due to time constraints. One way ANOVA followed by Dunnett's post test conducted for pIC_{50} and % inhibition comparing to* ***25h*** *reference compound at both hEP_2 and hEP_4 reported as *P<0.05, ** P<0.01 and ***P<0.001.*

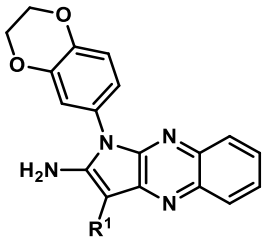

Compound	Structure	Mean *h*EP$_2$ pIC$_{50}$ ± SEM	Mean *h*EP$_4$ pIC$_{50}$ ± SEM	Fold selectivity IC$_{50}$ *h*EP$_4$ v *h*EP$_2$	% inhibition at top concentration (30 µM) from vehicle control for EP$_2$ ± SEM	% inhibition at top concentration (30 µM) from vehicle control for EP$_4$ ± SEM
25h	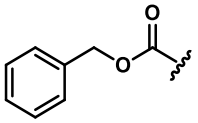	5.70 ± 0.03	4.62 ± 0.13	12.0	49.4 ± 5.8	49.6 ± 10.5
40a	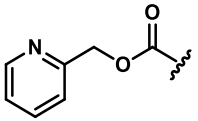	5.45 ± 0.07	4.80 ± 0.12	4.5	57.2 ± 2.9	55.9 ± 9.2
40c	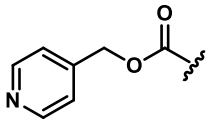	5.71 ± 0.03	4.86 ± 0.18	7.1	65.7 ± 3.9*	60.4 ± 9.2

40g	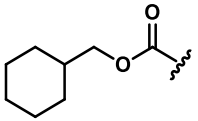	5.20 ± 0.19*	[4.34 ± 0.12]	7.2	35.2 ± 4.8	36.9 ± 9.9
40h	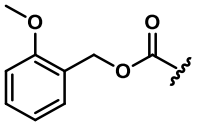	5.40 ± 0.12	5.05 ± 0.28	2.2	43.8 ± 4.1	63.2 ± 11.8
40p	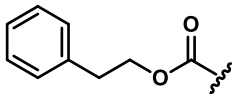	5.12 ± 0.09**	5.31 ± 0.16	-	37.2 ± 2.5	74.4 ± 7.2
40q	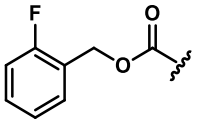	5.28 ± 0.07	-	-	27.7 ± 1.2**	-
40r	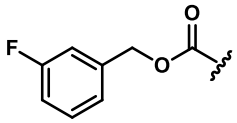	5.52 ± 0.04	[4.02 ± 0.15]	31.6	49.4 ± 4.8	25.6 ± 4.2
40s	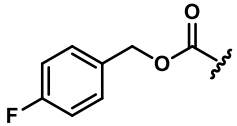	5.24 ± 0.14*	4.78 ± 0.07	2.9	45.6 ± 2.4	47.6 ± 4.6

The *h*EP_2 NanoBiT™ complementation assay demonstrated that all ligands that demonstrated known affinity for the Gαs allosteric binding pocket in the NanoBRET competition assay also displayed functional inhibition of β-arrestin2 recruitment at the *h*EP_2 receptor with pIC_{50} values ranging between 5.12-5.71 (1.9-7.6 μM). Of all the compounds in this series only the para pyridine analogue **40c** demonstrated comparable functional potency to series 1 lead **25h** with pIC_{50} values of 5.71 and 5.70 respectively. However, analogue **40c** saw a modest drop in fold selectivity between target receptor *h*EP_2 and closely related receptor *h*EP_4 when compared to **25h** (7.1 and 12.0 respectively; see Table 13) Comparatively, the 3-fluorobenzyl ester containing compound **40r**, displayed the largest fold selectivity difference between the two receptor subtypes at 31.6- fold change whilst maintaining a relatively high functional potency, pIC_{50} of 5.52 for the EP_2 receptor. The maximal inhibition, reduction in NanoBiT™ luminescent response from EC_{80} PGE_2 control response at *h*EP_2, by the highest concentration of compound was para pyridine **40c** at 66.2 % followed by ortho pyridine **40a** at 57.2 %. In comparison series 1 lead benzyl ester **25h** and 3-fluoro benzyl ester **40r** had similar maximal inhibition at 49.4 % and 45.6 % respectively for *h*EP_2. Additionally, analogue **40r** had the lowest reported maximal inhibition at *h*EP_4 at 25.6 %.

Almost all NAMs assayed by NanoBiT complementation demonstrated selectivity for target *h*EP_2 over the *h*EP_4 receptor, lower functional potency is reported at *h*EP_4 with pK_i values in the range of 4.02-4.86. An exception to this was the phenylethyl ester **40p** which had approximately similar functional potencies for both receptor types, which did not differ significantly (p= 0.3384 Student's unpaired t test). Furthermore, **40p** also had the largest reported maximal inhibition at *h*EP_4 at 74.4 %. Theoretically, the similar functional potency may be a result of the increased conformational flexibility of the molecule resulting in similar binding affinities to both the *h*EP_2 and *h*EP_4 receptors intracellular binding pockets.

5.3.2 PGE_2 concentration response curves in the absence and presence of series 2 ligands at hEP_2 in whole cells.

Additionally, PGE_2 CRCs in the absence and presence of two set concentrations (1 μM and 30 μM) of our modulators were conducted (see Figure 31) and the pEC_{50} and R_{max} values were calculated to provide more information on their mode of action (see Table 3) [197, 375].

.

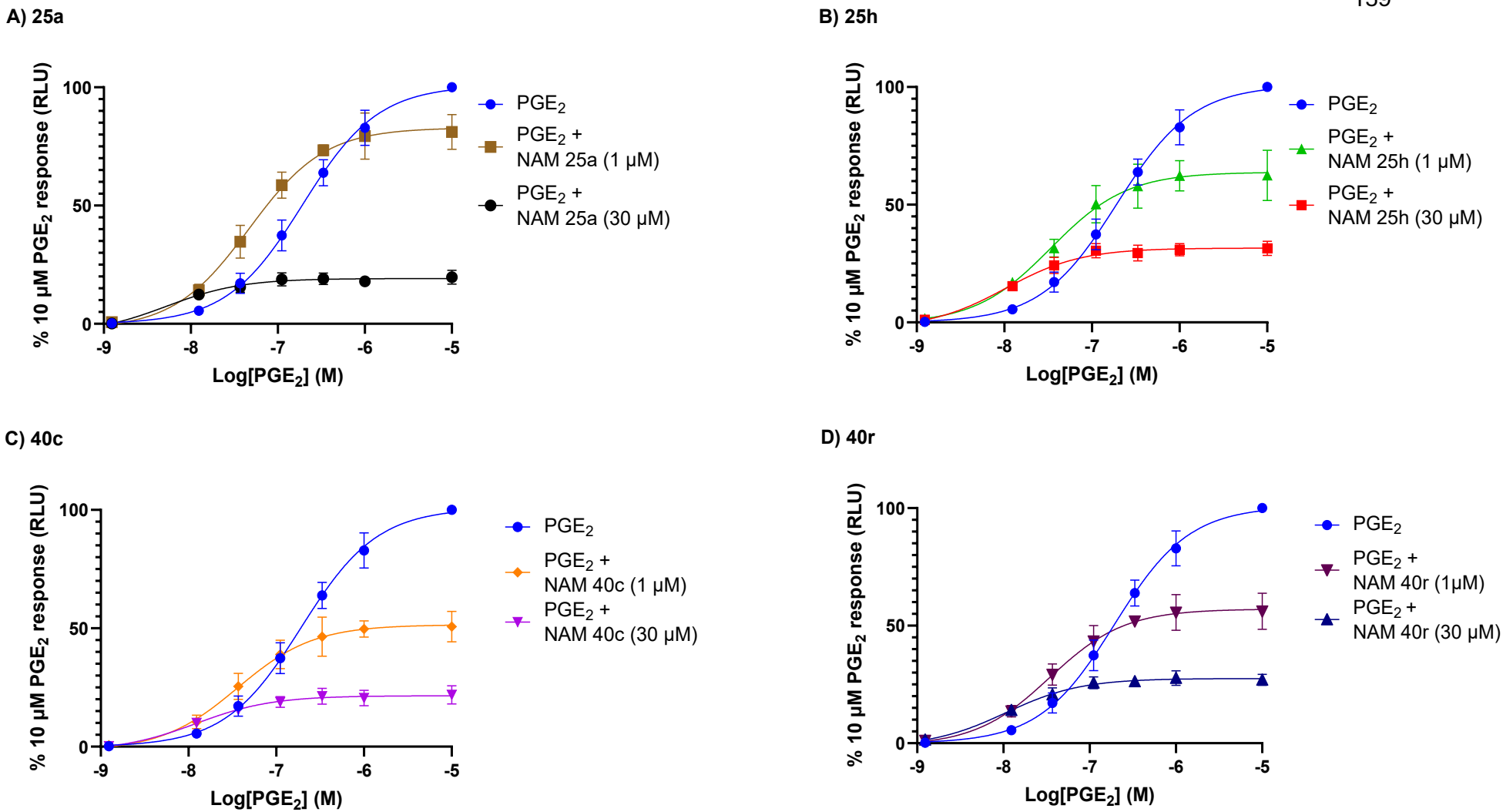

***Figure 31**- Effect of compounds on PGE_2 concentration response curves in the EP_2 receptor NanoBiT arresin complementation assay. Experiments were performed in EP_2-LgBiT, β-arrestin2-SmBiT tagged stably transfected HEK293 cells against increasing concentrations of agonist PGE_2 in the presence or absence of NAM ligands (1 µM or 30 µM). Compounds were preincubated with cells for 30 min prior to PGE_2 addition at approximately EC_{80} concentration (164 nM EP_2). Response data 30- min post PGE_2 addition are shown as % PGE_2 EC_{80} luminescence against increasing concentrations of competing ligand (60 min total incubation). 1x HEPES buffer + 0.1 % BSA, incubated at 37 °C, 1:750 furimazine. The functional data shown were normalised and pooled from five independent experiments [222].*

Table 14- *Mean pEC_{50} values of PGE_2 with/without addition of 1 μM or 30 μM NAMs* ***25a/h*** *or* ***40c/r****. Data were normalised and pooled from five independent NanoBiT complementation experiments in hEP_2-LgBiT, β-arrestin2-SmBiT tagged stably transfected HEK293 whole cells including the standard error of the mean (SEM), % R_{max} values, fold change in PGE_2 pEC_{50} from control and compound structures. One way ANOVA followed by Dunnett's post test conducted for pEC_{50} and % R_{max} comparing to PGE_2 control reported as *P<0.05, ** P<0.01 and ***P<0.001.*

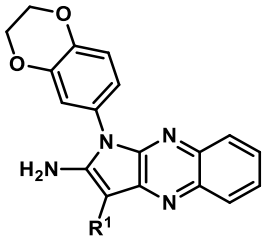

Compound	Structure	[Antagonist] (μM)	Mean *h*EP_2 pEC_{50} Mean ± SEM	Mean EC_{50} (nM)	% R_{max} mean ± SEM	Fold increase in PGE_2 EC_{50} from control
PGE_2 control		N/A	6.70 ± 0.06	200	100	N/A
25a	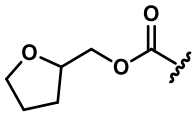	1	7.33 ± 0.06***	47	85.5 ± 2.7	4.3
		30	8.3 ± 0.06***	5	24.1 ± 1.8***	40.0
25h	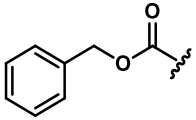	1	7.47 ± 0.06***	34	64.6 ± 4.2***	5.9
		30	8.00 ± 0.06***	10	34.5 ± 1.1***	20.0
40c	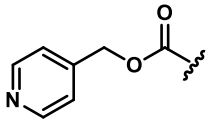	1	7.43 ± 0.04***	37	53.4 ± 2.7***	5.4
		30	7.92 ± 0.05***	12	23.5 ± 1.2***	16.7

40r	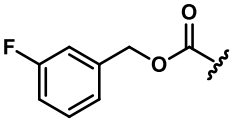	1	7.49 ± 0.04***	32	59.6 ± 2.8***	6.3
		30	7.97 ± 0.03***	11	29.2 ± 1.3***	18.2

All four analogues assayed displayed insurmountable antagonism with a significant reduction in the R_{max} value increasing with higher concentrations of our ligands [376]. At 30 μM **25a**, **25h**, **40c** and **40r** all demonstrated equivalent reduction in PGE_2 R_{max} values of 65-75 % inhibition (see Table 14). At the lower concentration of 1 μM **40c** produced the greatest inhibition (whilst submaximal compared to the effect at 30 μM), followed by **40r** and **25h**, and then **25a** with the lowest effect at 1 μM (see Table 14). Based on the extent of insurmountability, this suggests that **40c** may have greater functional potency than **40r**, **25h** and then **25a**- a difference that was not revealed by the measurement of IC_{50} only at a single agonist concentration in the same assay (see Figure 30, Table 13). Given the analogues were broadly equivalent in affinity, as determined by the NanoBRET binding assay (see Table 12), this may indicate some differences in negative allosteric efficacy (β co-operativity factor) within the series SAR, leading to greater functional inhibition at lower concentration by **40c** compared to **25a** [146, 147].

Additionally, there was an observed leftward shift of the curves upon addition of our NAMs and a resulting significant increase in the PGE_2 pEC_{50} values compared to the control (One way ANOVA followed by Dunnett's post test $p < 0.001$ for all NAM at both concentrations). This increase in PGE_2 functional potency at the *h*EP_2 receptor was in proportion to the increasing concentrations of our NAMs. This trend is indicative of an agonist dependent mechanism of action with positive affinity cooperativity (α) between allosteric and orthosteric ligand binding. This data supports the theory that our modulators preferentially bind and stabilise the active conformation of the *h*EP_2 receptor for which PGE_2 has the highest affinity [377, 378]. Leftward shifts in PGE_2 CRC in the presence of 30 μM ligands were 17-40-fold as determined by comparison of the EC_{50} values (see Table 3). Apart from NAM **25a** at 30 μM the shift in PGE_2 potency upon addition of 30 μM modulator is similar across the compounds assayed. This trend is supported by the flat SAR dataset produced in the NanoBRET competition binding assay which reported all ligands have a similar binding affinity to the *h*EP_2 receptor in membranes (performed in the presence of saturating concentrations of PGE_2) and therefore stabilise its active conformation to the same extent.

5.4 NanoBiT complementation assays using agonist evatanepag.

The literature reported that the extent of NAM **25a**'s potency and efficacy for the reduction of cAMP production in C6 glioma cells was dependent on the agonist employed (see Chapter 1.3.4)[179]. Six EP_2 agonists, in the presence of **25a**, were compared in the literature including PGE_2 (**10**), butaprost (**26**), evatanepag (**27**), taprenepag (**28**), ONO-AE1-259 (**29**) and ONO-4960073 (**30**) all changing the R_{max} and EC_{50} values to varying extents [179]. To explore whether the effects of the synthesised ligands were also orthosteric agonist dependent, the EP_2-β-arrestin2 NanoBiT complementation assays above were repeated using the partial agonist evatanepag for a selection of lead analogues from series 1 and 2 (see Chapter 3.3.1).

Firstly, concentration inhibition curves of our ligands were determined against the EC_{80} concentration of evatanepag (**27**, 950 nM) conducted in EP_2-LgBiT, β-arrestin2-SmBiT stably transfected HEK293 whole cells (see Figure 32). The pIC_{50} values have been reported (see Table 15).

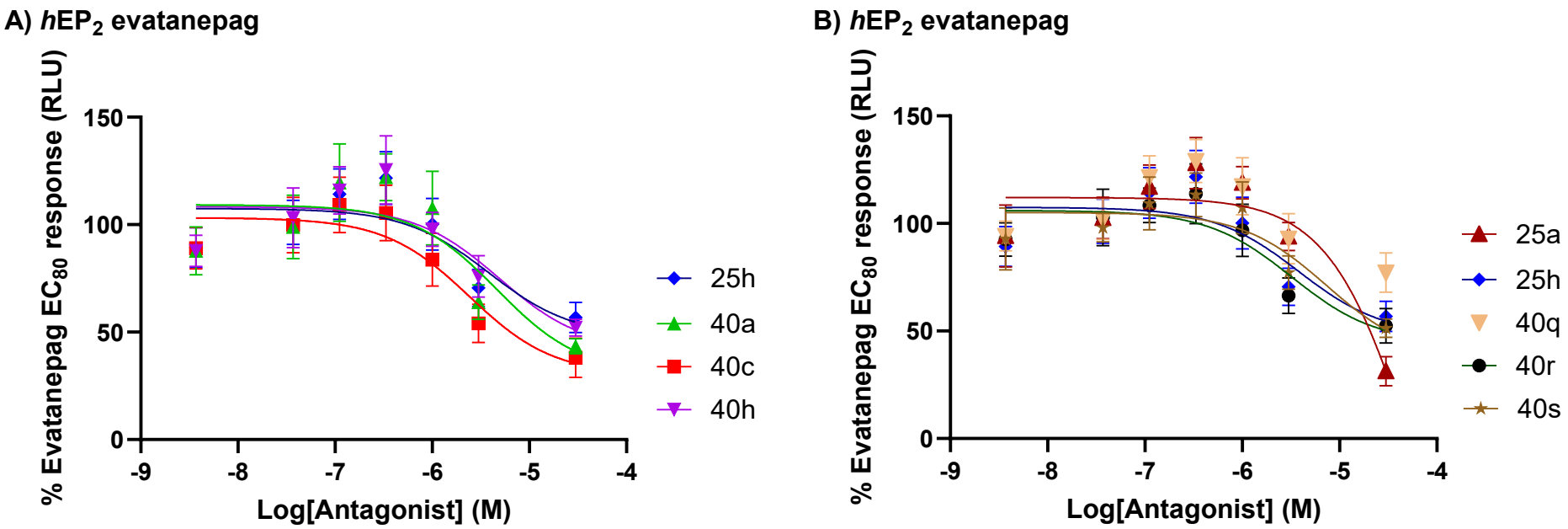

***Figure 32**- NanoBiT complementation assay data in EP_2-LgBiT, β-arrestin2-SmBiT tagged stably transfected HEK293 cells shown as % evatanepag EC_{80} luminescence against increasing concentrations of competing ligand. Compounds were preincubated with cells for 30 min prior to Evatanepag addition at approximately EC_{80} concentration (950 nM EP_2). Response data 30- min post PGE_2 addition are shown as % Evatanepag EC_{80} luminescence against increasing concentrations of competing ligand (60 min total incubation). 1x HEPES buffer + 0.1 % BSA, incubated at 37 °C, 1:750 furimazine, 950 nM evatanepag EC_{80}. The functional data shown were normalised and pooled from five independent experiments [222].*

Table 15- *Mean pIC_{50} values of lead NAMs from series 1 and 2 normalised and pooled from five independent NanoBiT complementation experiments using agonist evatanepag in hEP_2-LgBiT, β-arrestin2-SmBiT tagged stably transfected HEK293 whole cells including the standard error of the mean (SEM) and compound structures. One way ANOVA followed by Dunnett's post test conducted for pIC_{50} and % inhibition comparing to* ***25a*** *reference compound reported as *P<0.05, ** P<0.01 and ***P<0.001*.

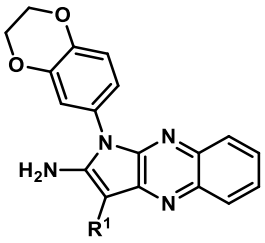

Compound	Structure	Mean *h*EP_2 pIC_{50} ± SEM evatanepag	% inhibition at top concentration (30 µM) from vehicle control for EP_2 ± SEM
25a	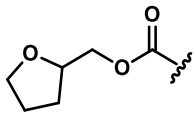	4.47 ± 0.11	69.3 ± 3.3
25h	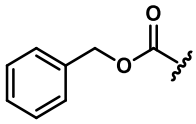	5.40 ± 0.09***	43.4 ± 3.2***
40a	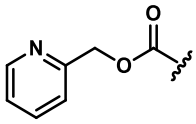	5.34 ± 0.04***	56.6 ± 1.6***
40c	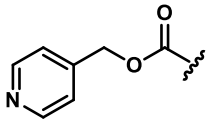	5.62 ± 0.02***	61.9 ± 4.1***
40h	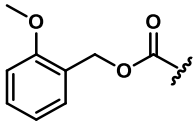	5.28 ± 0.09***	47.9 ± 1.8***
40q	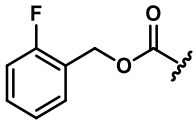	5.06 ± 0.15***	22.8 ± 4.1***
40r	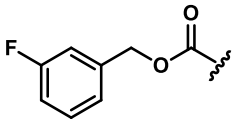	5.48 ± 0.07***	47.5 ± 3.6***

40s	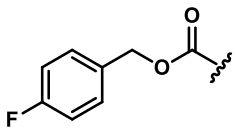	5.21 ± 0.08***	48.7 ± 1.9***

The NanoBiT™ complementation assay demonstrated functional inhibition of β-arrestin2 recruitment by our unlabelled ligands when using agonist evatanepag. The calculated pIC_{50} values for agonist evatanepag were not significantly different to the previously described PGE_2 pIC_{50} values for all compounds tested except for **40c** (Student t-test $p > 0.05$ except **40c** with $p < 0.05$ at 0.04). Both assays demonstrate a flat SAR dataset with generally similar analogue functional potency; analogues **40c**, **40r** and **25h** have the highest reported pIC_{50} values of 5.62, 5.48 and 5.40 respectively. The same trends in maximal inhibition, reduction in NanoBiT™ luminescent response from the EC_{80} evatanepag control response, was observed for our NAMs when employing partial agonist evatanepag compared to endogenous agonist PGE_2 in *h*EP_2 whole cells. The tetrahydrofuran ester **25a** from the literature has the highest % inhibition at 69.3 % followed by para-pyridine **40c** and ortho-pyridine **40a** at 61.9 % and 56.6 % respectively. For both pyridine analogues (**40a/c**) the % inhibition values were similar to those reported for the NanoBiT complementation assays employing agonist PGE_2. Additionally, no change in maximal inhibition for the 3-fluorobenzyl ester **40r** is observed between the two agonists employed; maximal inhibition reported at 47.5 ± 3.6 % for evatanepag and 45.6 ± 2.4 % for PGE_2.

Evatanepag concentration response curves in the absence and presence of two set concentrations (1 μM and 30 μM) of our lead modulators were also conducted (see Figure 33) and the pEC_{50} and R_{max} values were calculated (see Table 16) [197, 375] .

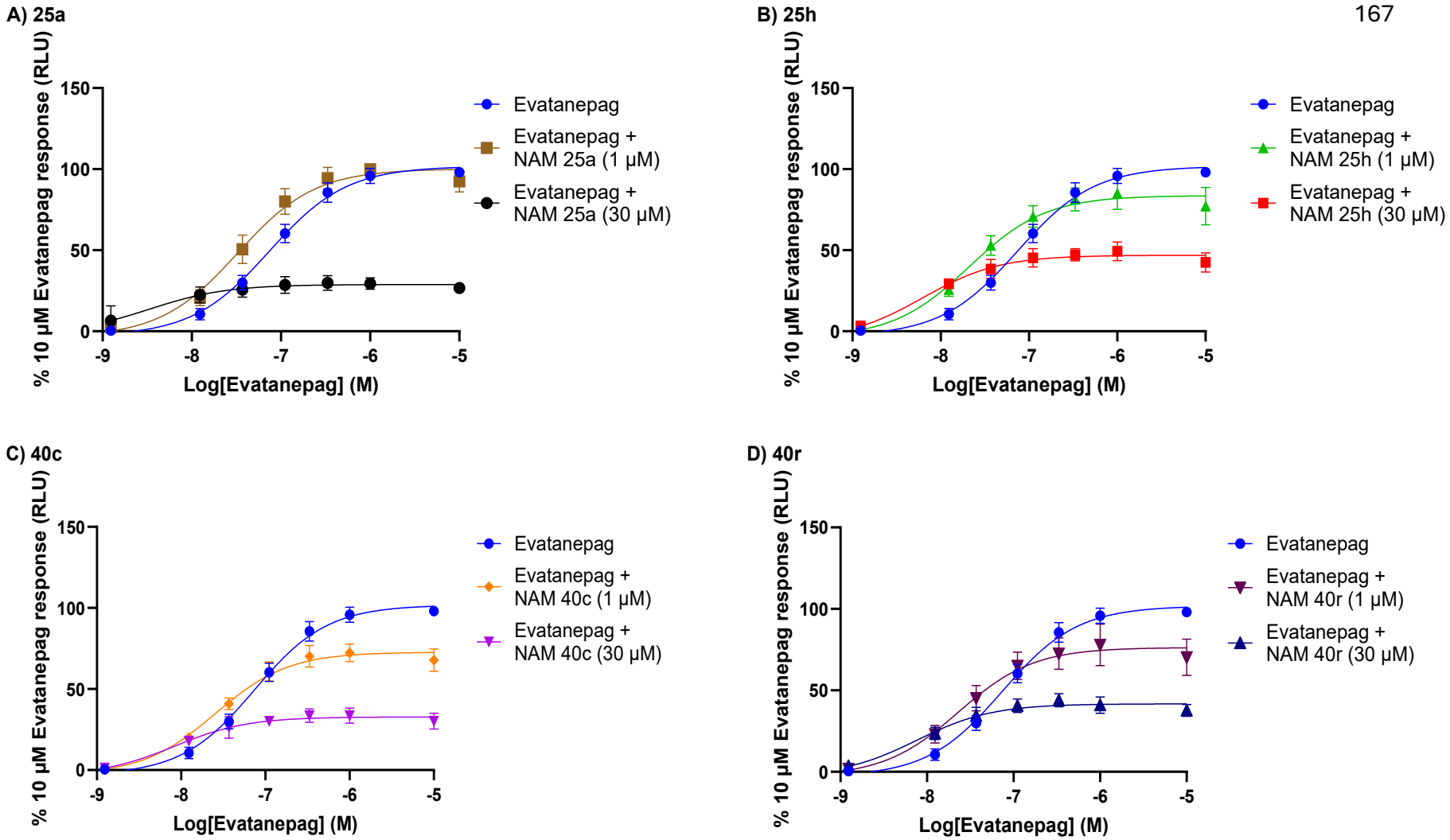

***Figure 33**- NanoBiT complementation assay data in EP_2-LgBiT, β-arrestin2-SmBiT tagged stably transfected HEK293 cells shown as % evatanepag response against increasing concentrations of agonist evatanepag in the presence or absence of NAM ligands (1 µM or 30 µM). Compounds were preincubated with cells for 30 min prior to Evatanepaf addition at approximately EC_{80} concentration (960 nM EP_2). Response data 30- min post PGE_2 addition are shown as % PGE_2 EC_{80} luminescence against increasing concentrations of competing ligand (60 min total incubation). 1x HEPES buffer + 0.1 % BSA, incubated at 37 °C, 1:750 furimazine. The functional data shown was normalised and pooled from five independent experiments [222].*

Table 16- *Mean pEC_{50} values of evatanepag with/without addition of 1 μM or 30 μM NAMs* ***25a/h*** *or* ***40c/r****. Data was normalised and pooled from five independent NanoBiT complementation experiments in hEP_2-LgBiT, β-arrestin2-SmBiT tagged stably transfected HEK293 whole cells including the standard error of the mean (SEM), % R_{max} values, fold change in evatanepag pEC_{50} from control and compound structures. One way ANOVA followed by Dunnett's post test conducted for pEC_{50} and % R_{max} comparing to evatanepag control reported as *P<0.05, ** P<0.01 and ***P<0.001.*

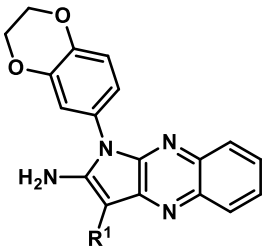

Compound	Structure	[Antagonist] (μM)	Mean *h*EP_2 pEC_{50} Mean ± SEM	Mean EC_{50} (nM)	% R_{max} Mean ± SEM	Fold change in evatanepag EC_{50} from control
Evatanepag control		N/A	7.17 ± 0.05	68	100	N/A
25a	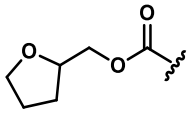	1	7.48 ± 0.04***	33	97.1 ± 1.3	2.0
		30	8.49 ± 0.04***	3	30.6 ± 4.4***	20.9
25h	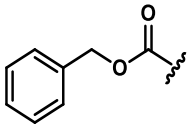	1	7.68 ± 0.04***	21	87.9 ± 4.5	3.2
		30	8.21 ± 0.07***	6	52.9 ± 2.2***	11.0
40c	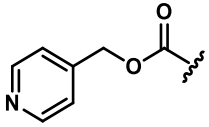	1	7.59 ± 0.01***	26	75.6 ± 2.4*	2.6
		30	8.08 ± 0.05***	8	36.3 ± 1.8***	8.1

40r	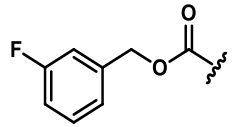	1	7.64 ± 0.02***	23	79.3 ± 4.4	3.0
		30	8.12 ± 0.03***	7	44.6 ± 1.0***	8.9

All four analogues assayed in the NanoBiT™ complementation assay using agonist evatanepag displayed insurmountable antagonism with a significant reduction in the evatanepag R_{max} value proportional to higher concentrations of our ligands. The maximal reduction in evatanepag R_{max} observed with 30 μM ligand was lower than that observed for PGE_2 inhibition. This may simply be a consequence of the NanoBiT response to the high efficacy agonist PGE_2 compared to partial agonist evatanepag (see Chapter 3-3.1). Despite evatanepag acting orthosterically at the same extracellular binding pocket as PGE_2, the agonist-EP_2 complex adopts a lower-level active conformation with a lower binding affinity of β-arrestin2 for the target resulting in the observed partial agonism [379]. Therefore, β-arrestin2 recruitment and its corresponding inhibition by our NAMs may vary between agonists [380].

The same overall trends in functional potency of our NAMs (comparing effects at two concentrations 1 μM and 30 μM) were observed when considering evatanepag concentration response curves (see Figure 33) compared to PGE_2 (see Figure 31). At 30 μM, all four analogues showed 50-70 % inhibition of the evatanepag response, whilst at 1 μM **40c**, **40r** and **25h** showed greater inhibition than **25a**. As for PGE_2 there was an observed leftward shift of the curves upon addition of our NAMs and a resulting increase in the evatanepag pEC_{50} values compared to the control. This increase in evatanepag functional potency of 8-20-fold at the *h*EP_2 receptor was in proportion to the increasing concentrations of our NAMs.

This data demonstrated positive co-operativity of our NAMs with both PGE_2 and evatanepag as orthosteric agonists, with a potentially greater effect on potency with the more efficacious agonist PGE_2. This would be consistent with our NAMs stabilising an active conformation of *h*EP_2 where the functional potency of PGE_2 is increased to a greater extent than for agonist evatanepag. However, as the binding of our NAMs inhibit the recruitment of β-arrestin2 to the *h*EP_2 receptor, overall, negative functional cooperativity is observed with regards to both the evatanepag and PGE_2 response.

5.5 Series 2 pharmacology conclusions

In summary, the NanoBRET™ competition assay of series 2, utilising fluorescently tagged G-protein mimetic TMR-Gαs19cha18, identified NAM **40r** as having the highest reported binding (pK_i= 7.51, 31 nM) affinity for the intracellular binding pocket fully displacing the probe [219, 289]. The data is indicative of a new halogen-π intermolecular interaction with the fluoro- substituent of **40r** and the receptor Gs binding pocket which is only conformationally viable at the meta position on the phenyl ring [326, 328, 329].

Additionally, the NanoBiT™ complementation assays determined fluorophenyl **40r** had the best fold selectivity (31.6) for the target *h*EP_2 receptor compared to closely related receptor subtype *h*EP_4 and maintained the third highest reported pIC_{50} value at 5.52, (3.02 μM), inhibiting β-arrestin2 recruitment, across the two series.

Lead modulators **25a**/**h** and **40c**/**r** all display classical allosteric insurmountable antagonism for both orthosteric agonists PGE_2 and evatanepag which is as expected for allosteric modulators binding to the intracellular binding site.[376] The Schild analysis determined that **40c** demonstrated the greatest insurmountability (reduction in R_{max}) at the lower concentration tested (1 μM) closely followed by **40r**, **25h** and **25a**. A clear use dependent mechanism was observed for both PGE_2 and evatanepag with the othosteric agonist potency (EC_{50}) increasing the in the presence of our antagonists. For agonist PGE_2 NAM **25a** at 30 μM has the largest shift in functional potency, 40-fold change vs control, with a PGE_2 pEC_{50} value of 8.30 ±0.08. This supports a NAM mechanism with positive affinity co-operativity (alpha) with the orthosteric agonist, but negative efficacy cooperativity (beta) as the ligand binding sterically inhibits effector coupling. The differences between the modulator action on PGE_2 and evatanepag responses were not sufficient to confirm dependence on the orthosteric ligand. However, a potentially higher degree of positive effect on potency was observed for PGE_2 compared to the lower efficacy ligand evatanepag. This can be rationalised by the modulator preferentially binding to the active EP_2 receptor conformation, which is stabilised more by higher efficacy orthosteric agonists.

In conclusion these data allow us to identify the 3-fluorophenyl NAM **40r** as a promising lead candidate for future optimisation and pharmacological exploration. Ligand **40r** demonstrated the highest reported binding affinity for the Gs intracellular binding pocket and maintained one of the highest functional potencies in all NanoBiT™ complementation assays from both compound libraries. The high selectivity of **40r** for *h*EP_2 over *h*EP_4 will minimise off target interactions, reducing potential negative side effects *in vivo* compared to literature compound **25a**.

Future work could involve the experimental identification of key amino acid residues for NAM binding using mutagenesis studies [381]. The resulting binding affinity data of our ligands, produced by NanoBRET competition binding assays, at these modified receptors can be compared and amino acid residues forming essential intermolecular interactions with our ligands can be identified [370]. The elucidation of the intracellular binding pocket can drive future lead optimisation work by exploiting new interactions between our NAMs and amino acids in close vicinity to our key residues.

In addition to monitoring β-arrestin2 recruitment at the EP_2 receptor, it would be beneficial to investigate the effect of our ligands on G-protein activity. As a result, we would be able to quantify any differences in the degree of modulation of our NAMs between β-arrestin2 and G-protein effector signalling. For example, a pharmacological characterisation experiment investigating the functional potency of our ligands on mini-Gαs protein recruitment can be conducted. This would utilise a NanoBiT™ complementation binding assay in EP_2-LgBiT, mGαs-SmBiT tagged stably transfected Hek293 whole cells with agonist PGE_2 to monitor G_s protein recruitment [223, 286]. Mini-Gα proteins are engineered GTPase domains of Gα subunits which preserve the GPCR receptor-G protein binding interface and have been applied to the NanoBiT system to measure interactions between GPCRs and their effector proteins [222, 223]. Alternatively, BRET Gαβγ biosensors, such as TRUPATH, could be used to monitor G protein-coupled receptor activity through measurement of heterotrimeric Gα and Gβγ dissociation in the presence or absence of our NAMs [382, 383]. For both assays' trends in pIC_{50}, R_{max} and agonist pEC_{50} data can be directly compared between recruitment

proteins. Furthermore, measurement of second messenger cAMP accumulation utilising cAMP biosensors (e.g. FRET-, luciferase-, or BRET-based cAMP sensors) would also provide EP_2 G-protein signalling functional data [384].

Additionally, further selectivity studies, utilising the NanoBiT™ complementation assays, at alternate Gαs coupled prostaglandin receptors should be conducted. For example, extended family members of prostanoid receptors DP_1 and IP have 44 % and 40 % structural homology (amino acid identity) to the *h*EP_2 receptor respectively, compared with 31 % for *h*EP_4 [116, 385]. The DP_1 and IP receptors are primarily responsible for inhibiting platelet aggregation and relaxation of myometrium and smooth muscles [386, 387]. As a result, inhibition of both receptors is associated with a reduction in vasodilation causing hypertension in patients and increasing the risk of myocardial infarction, stroke and kidney disease [388, 389]. DP_1 inhibition has also been linked to modulation of allergic responses, resulting from decreased histamine release, and disruption of sleep regulation [61, 390]. Therefore, selectivity of our NAMs for prostanoid receptor EP_2 over DP_1 and IP receptors is necessary to minimise the risk of off-target adverse effects. In order to trial these NAMs for the treatment of chronic inflammatory associated diseases in the clinic their activity at additional safety targets, such as the hERG potassium channel, adrenergic receptors (α and β), angiotensin receptors and opioid receptors, should be assessed to evaluate the potential for life-threatening off target toxicity [116, 385, 391, 392].

Chapter 6- Homology modelling of the NAM-*h*EP_2 receptor complex

6.1 An introduction to homology modelling

6.1.1 Development of a homology model

The aim of this project, as previously described, involves the development of intracellular allosteric antagonists for the inhibition of prostanoid receptor EP_2 and the treatment of chronic inflammation in numerous disease states. Structural elucidation and visualisation of three-dimensional ligand-receptor complexes has proved an essential tool in the drug development process. By revealing ligand binding sites and their interactions with the target receptor, researchers can tailor drug molecules to optimally bind to the desired pocket and yield highly efficacious and selective ligands [393-395]. To date, X-ray crystallography is the most comprehensive and leading method for determining the atomic-scale structure of crystalline materials including proteins, DNA and drugs [396]. A purified sample of the desired protein is crystallised before being exposed to an X ray beam. The resulting diffraction patterns are processed and a map of electron density calculated and used for structural determination.[396] However, the application of X-ray crystallography to study GPCRs faces several challenges. Firstly, as GPCRs are membrane proteins their hydrophobic and amphipathic nature means they are insoluble and unstable in the detergents required for purification processes [397, 398]. Additionally, GPCRs are highly flexible and dynamic which is essential to their function but makes them inherently difficult to crystalise; as a result elucidated structures often do not provide the whole picture of how G proteins/ligands couple to receptors [50, 397]. GPCRs possess multiple conformation states but to date only 74 and 64 GPCRs have been structurally elucidated in their active and inactive states respectively and only 36 GPCRs have experimental structures in both [399]. The development of high-resolution structure determination by cryo-EM has led to a rapid emergence of previously inaccessible membrane protein structures available to the scientific community [400]. Cryo-EM involves imaging radiation-sensitive specimens in a transmission electron microscope

under cryogenic conditions [401]. Despite the relative ease of structural elucidation of membrane proteins with cryo-EM structures, they are typically produced at a lower resolution than X-ray crystallography and are not suitable for proteins below 60 kDa in size. The coupling GPCRs in their active state with their heterotrimeric G protein is a technique used to counteract these limitations [397].

Where neither X-ray crystal or cryo-EM structures are available of the target receptor bound to the ligands of interest, the development of an alternative accurate three-dimensional (3D) representation is essential to understand ligand function and drive lead optimisation. Accessible computational structure predicting methods such as homology models, are the most reliable and accurate alternative to date [402, 403]. Homology models are developed based on the observation that protein 3D structures are determined by their amino acid sequences and evolutionally related proteins with similar sequences (homologous proteins) have a very similar structural conformation. Minor changes in amino acid sequences typically result in little variation of the 3D structure as protein structural conformation is more highly conserved [402]. Comparatively, very low structural similarity can be observed between proteins with low sequence homology <20 %) [404]. Other traditional protein structure prediction methods include threading, *de novo* and *ab initio* methods, with many modelling strategies using a combination of all four methods to model protein structures [403]. Threading methods assign the target amino acid sequence to templates which are not evolutionarily related but have known folds of similar architecture. Each trial template has the optimal sequence-to-structure alignment evaluated by a set of scoring functions based on physical parameters [405]. However, this method is limited to a search of known folds and is unable to predict a target structure which adopts novel folding. Both *de novo* and *ab initio* are free-modelling methods which do not require a template but are based on the amino acid sequence's thermodynamic and physiochemical properties. *De novo* methods utilise knowledge-based force fields as scoring functions, from experimentally determined structures, to find the in-silico conformation at the minimum potential energy through scanning of the energy landscape [403, 406]. In contrast, the *ab initio* method uses force fields based on first

principles, calculations and theories from fundamental established laws and principles, without reference to solved structures [403].

An example artificial intelligence (AI) system utilising a combination of the aforementioned methods is AlphaFold developed by DeepMind and EMBL's European Bioinformatic Institute (EMBL-EBI) [407, 408]. AlphaFold predicts the 3D structure of a protein from its amino acid sequence with atomic accuracy (near experimental accuracy in the majority of cases) and speed, the structures are freely available for the scientific community from a public database (AlphaFold Protein Structure Database) [407, 408]. The neural network AlphaFold that was developed was entered and determined vastly more accurate than competing methods by CASP14 assessment; the gold standard assessment for the accuracy of structure prediction comparing with recently released PDB structures. CASP14 determined AlphaFold structures had a median backbone accuracy of 0.96 Å and an all atom accuracy of 1.5 Å, the next best performing method 2.8 Å backbone accuracy and 3.5 Å all atom accuracy (for comparison the width of carbon atom is 1.4 Å) [408-410]. This improvement in accuracy of structure prediction is due to its incorporation of novel neural network architectures and training procedures based on the evolutionary, physical and geometric constrains of protein structures [408].

The development of a homology model was conducted for the *h*EP_2 receptor to evaluate the binding of our intracellular allosteric NAMs. Homology modelling involves multiple sequential steps: template selection, sequence alignment, model building, refinement and evaluation [403]. Template selection is the most important process of the model building stage. The best templates are identified by aligning the sequence of the target with template sequences of proteins with known structures. The Protein Database (PDB), a publicly accessible collection of protein information, is first utilised to obtain the target sequence of the desired protein [411]. The Basic Local Alignment Search Tool (BLAST) is then employed to generate sequence-sequence alignment between the target sequence and existing PDB sequences with known structures [412]. A single or multiple templates are chosen based on the extent of sequency similarity between

target and template, typically sequence homology needs to be >25 % to be successfully employed for homology modelling [413]. Other factors also requiring consideration during template selection include: resolution of the experimental structure (high-resolution templates, > 3 Å, provide a more accurate template foundation), phylogenetic similarity, environmental factors (pH, solvent type) and existence of a bound ligand within the structure [228, 413]. For the purpose of ligand docking, a template containing a ligand crystalized in a similar/the same pocket as the target ligand would be ideal. The development of multiple templates is conducted to improve model accuracy when the template-target sequence identity is below 40%, however, most modelling software does not support homology model development using multiple templates [228, 414]. Modelling software (e.g. SWISS-MODEL) can then align the amino acid sequences of the target to the chosen template and generate a structural model of the target protein. Most errors in homology model generation are the result of poor template selection, the better the target-template sequence alignment the higher the quality homology model [228]. Template dependent model building can be achieved through three methods. Firstly, assembly of rigid bodies method consists of building a model framework from sections of the target structure that align with the template sequence, de novo methods are then used to model fragments which do not align with the template [228]. Segment matching or coordinate reconstruction involves dividing the target structure into short segments which are matched against a database of known structures selected based on sequence identity, geometrical and energetic considerations. These segments are then placed upon the guiding template to produce the homology model [228]. Thirdly, the spatial restraint method is built by fulfilling restraints, such as bond angles and lengths, derived from the template structure [228]. Refinement of the homology model, by de novo molecular dynamics and energy minimisation procedures, is an important step to acquire the correct orientation of amino acid side chains and to add structure to the evolutionary diverse loop regions [403]. Both amino acids side chains and loop regions play crucial roles in protein function but typically do not have homologous regions in the template. Finally, the quality of the homology model must be evaluated for its agreement with known target

information [403]. Structural features of a model can be evaluated by generating a Ramachandra plot and by calculating clash scores for steric overlap using software such as PROCHECK, WHATCHECK or MolProbity [415-417]. Homology models can also be compared with experimental data from the literature including both mutagenesis studies and docking with known ligand binders, from an SAR dataset, in the binding site of the model [403].

6.1.2 Homology modelling of EP_2 docked with 25a in the literature

A *h*EP_2 receptor homology model docked with **25a** was included in the original publication [179]. This model was developed using the crystal structure of *h*EP_4 in complex with its antagonist ONO-AE3-208 and an inhibitory antibody Fab (PDB 5YWY) as a template, 3.2 Å resolution [179, 418]. UCSF Chimera, an interactive molecular visualization and analysis programme, was utilized to conduct molecular docking of **25a** and the highest score model was reported [179, 419]. The top three docking sites of this model predict ligand binding to occur at an intracellular allosteric binding pocket between TM2,3,5 &6 on the *h*EP_2 receptor (see Chapter 1, 3.4)[179]. The binding pose of **25a** was reported to have the tetrahydrofuran-2-yl methyl ester pointing up into the deepest region of the binding pocket between TM2,3 & 6 of the *h*EP_2 receptor. The 2,3-dihydrobenzo[*b*][1,4]dioxine moiety, identified as the key driver of ligand binding affinity, sits perpendicular to the receptor between TM5&6 and the quinoxaline ring system is solvent exposed oriented into the cell cytoplasm [179].

The presence of this proposed intracellular allosteric binding pocket is supported by the recent crystal structures of GPCRs β2AR, CCR2, CXCR2 and CCR9 all bound to intracellular allosteric modulators [157, 158, 183, 184]. Various mechanisms of inhibition is theorised for this intracellular allosteric site observed in numerous class A GPCRs. 'Compound 15' a NAM of β2AR reportedly binds to an intracellular pocket formed primarily by the cytoplasmic ends of TM1,2,6 &7 as well as ICL1 and helix 8.[158] The allosteric antagonists CCR2-RA-[*R*], CXCR2-00767013 (Navarixin analogue) and Vercirnon all bind to an intracellular allosteric pocket on receptors CCR2, CXCR2 and CCR9 respectively between TM1-3 & TM6-8 [157, 183, 184]. The binding pocket of

the above antagonists spatially overlaps the G-protein binding site of their receptors. Inhibition of β2AR, CCR2, CXCR2 and CCR9 by their NAMs is non-competitive and mechanistically blocks activation-associated conformational changes, through stabilisation of the inactive conformation, and inhibits the formation of the G-protein/β-arrestin-binding interface [158, 183, 184]. Due to the similarity in location between the intracellular allosteric binding pocket reported by the *h*EP_2 homology model compared with NAM binding sites observed at other family A GPCRs, the mechanism of EP_2 inhibition is predicted to be the same. However, this mechanism of action is not supported by our pharmacological data produced in chapters 3 and 5. Instead our NAMs are theorised to stabilise the active conformation of *h*EP_2, supported by the increased agonist affinity for the NAM-EP_2 complex, but sterically block the recruitment of the heterotrimeric G-proteins and β-arrestin2 resulting in the functional inhibition of *h*EP_2.

The use of the *h*EP_4 receptor as a template is not ideal for computational modelling due to poor sequence homology between these receptors (30 %) resulting in a lower quality model; the respective amino acids and their conformations lining the predicted binding pocket may not be conserved across receptors [228]. In 2021 a cryo-EM structure of the PGE_2-bound *h*EP_2-Gs complex (PDB 7CX2) with a 2.8 Å resolution was reported [160]. Therefore, development of a new homology model using the cryo-EM structure of *h*EP_2 as a template and evaluating the models against our SAR dataset for all NAMs in series 1 & 2 would produce a model which more accurately represents the 3D structure of *h*EP_2. This model would provide further insight into the size, shape and amino acid conformation at the NAM intracellular binding pocket of *h*EP_2, identify the conformation of our bound ligands including any essential ligand-receptor interactions, improve understanding of the mechanism of receptor inhibition and act as a guide for future lead optimisation studies [395, 420].

6.2 Generation of a new *h*EP_2 computational model

The cryo-EM structure of the PGE_2-bound EP_2-$G\alpha_s$ complex (PDB 7CX2) was identified as a suitable template for the development of a new homology model to perform docking of our compound library [160]. Two pre-established homology models of EP_2 in either its active or inactive conformation were obtained from GPCRdb, developed from the template EP_2 cryo-EM complex using multistate prediction protocol in AlphaFold2 [399]. AlphaFold2 uses a machine learning method to predict protein structures; these methods use both neural network models, that have learned how to deduce relationships between residues based on co-evolutionary couplings, and high-resolution structure generation modules trained on known experimental structures [399]. The molecular docking of our compound library into both models was performed using Maestro from the Schrödinger suite [421]. Firstly, both models underwent Schrödinger's protein preparation workflow which employs numerous tools to increase structural accuracy [422]. For example, protein preparation optimizes the protein's hydrogen bond network, adds missing hydrogen atoms and can correct potentially transposed heavy atoms in Asn, Gln and His side chains [422]. A SiteMap algorithm was then applied to identify all potential binding pockets on the receptor in an unbiased manner [423, 424]. Sitemap identifies potential binding sites by linking together 'site points' that are most likely to contribute to tight protein-protein or protein-ligand interactions. Site points are evaluated by how close they are to the protein surface and how sheltered they are from the solvent. When multiple site points are sufficiently close and could plausibly be bridged in solvent-exposed regions by ligand atoms they are merged and a binding pocket is identified [424]. For both models, only one allosteric binding pocket, located intracellularly between TM α-helices 2-4, was identified as large enough to accommodate the ligands in our compound library (see Figure 34a/b). The computational model of EP_2 in its inactive conformation had an intracellular allosteric binding pocket that was measured at approximately 16.31 Å by 8.08 Å, a sufficient size to accommodate various conformations of literature NAM **25a** (measured at approximately 17.37 Å by 9.92 Å, see Figure 34c).

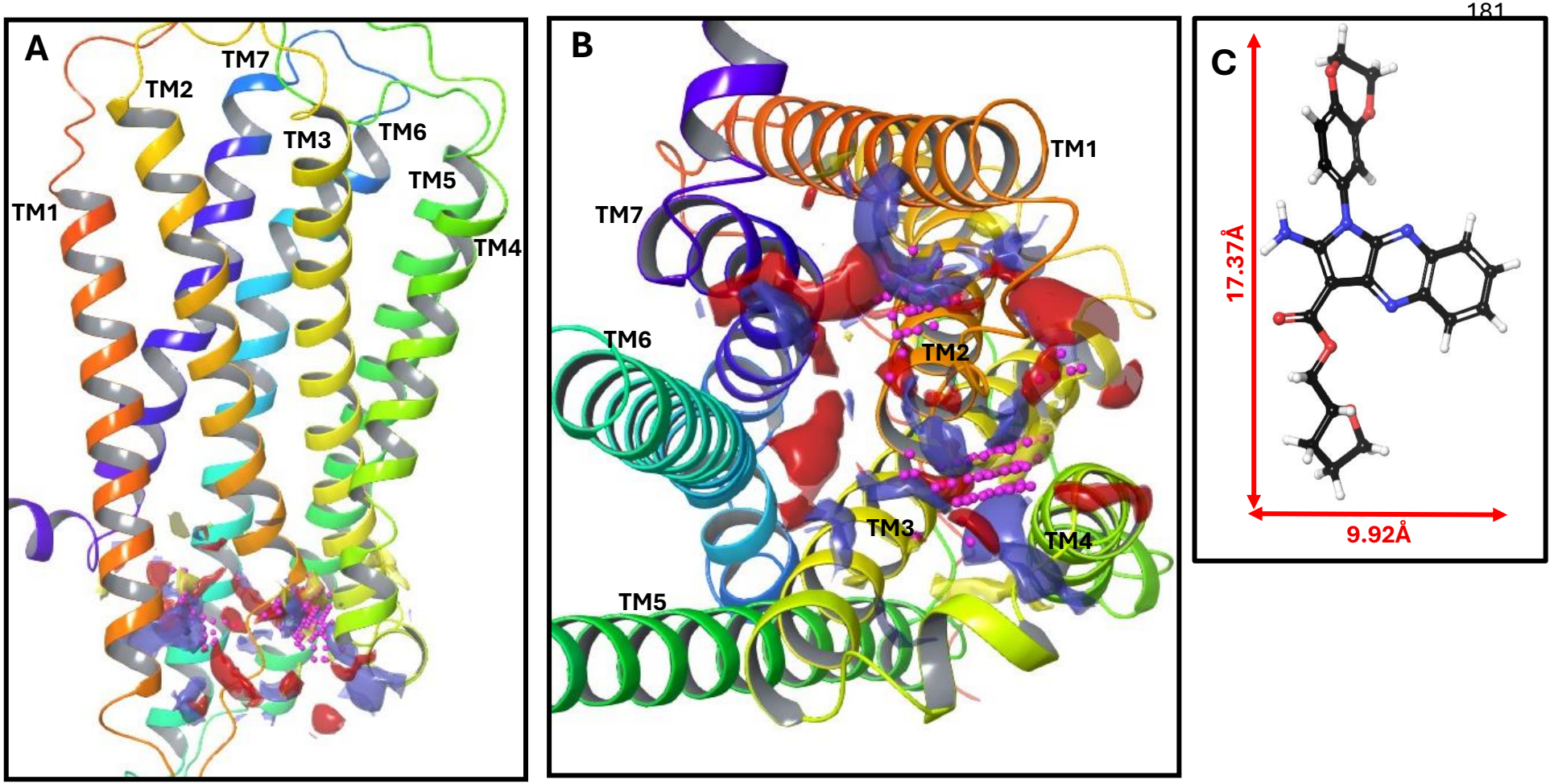

Figure 34*- *A*)** *A side on view of the EP_2 receptor inactive conformation computational model following protein preparation and site map identification with transmembrane labelling TM 1-7.* ***B*)** *Bottom-up view of the EP_2 receptor inactive conformation computational model following protein preparation and site map identification.* ***C*)** *Structure of* ***25a *with dimensions. The models display the intracellular allosteric site generated by sitemap (pink dots), hydrogen bond acceptor regions (red), hydrogen bond donor region (purple) and hydrophobic regions (yellow). Images taken directly from Maestro Schrödinger suite.*

Induced docking fit (IDF) using a combination of known binding and non-binding ligands from our SAR dataset was then conducted for both the inactive and active conformational models at the identified binding pocket [425-427]. IDF considers the flexibilities of both the ligand and the amino acid side chains in the receptor binding site as both change in their conformations to form a minimum energy and optimal-fit complex [428]. Upon analysing the generated IDF results only the inactive conformation model of EP_2 had consistent poses for all ligands with known binding affinity; the majority of known non-binding compounds did not dock into the corresponding pose. Therefore, based on this observed trend all additional docking work was undertaken using the EP_2 inactive conformation computational model.

Using a combination of predicted docking scores and key interactions observed in selected poses, the IDF results for the SAR dataset of ligands were evaluated, and a suitable model based on the IDF of **25b** was identified [425-427]. The chosen computational model produced a single high scoring ligand pose for all known active analogues. The 2,3-dihydrobenzo[*b*][1,4]dioxine moiety, previously identified as essential for ligand binding, is nestled in a novel EP_2 receptor pocket between TM 2 and 4 formed by five amino acids Ser149 (Ballesteros-Weinstein position 4.38), Arg150 (4.39), Gly153 (4.42), Leu154 (4.43) and Leu157 (4.46) (see Figure 36a-d). Three key hydrogen bonding interactions are predicted to be present in this model, the first between Arg150 (4.39) and the hydrogen bond acceptor oxygen within the dioxane, a second between Gln145 (34.54) and the nitrogen hydrogen bond donor in the quinoxaline ring and finally between Arg61 (loop not fixed) and the carbonyl of the ester. This hydrogen bonding interaction with the ester is experimentally supported by our SAR data as the removal of this moiety results in a significant loss in binding affinity. Furthermore, the ligand binding pose in this model displays the functionality attached to the ester oriented away from the receptor being solvent exposed. This supports the hypothesis that modifications in this region will have no effect on binding affinity but due to its flexibility may impact functionality by sterically blocking β-arrestin2 recruitment.

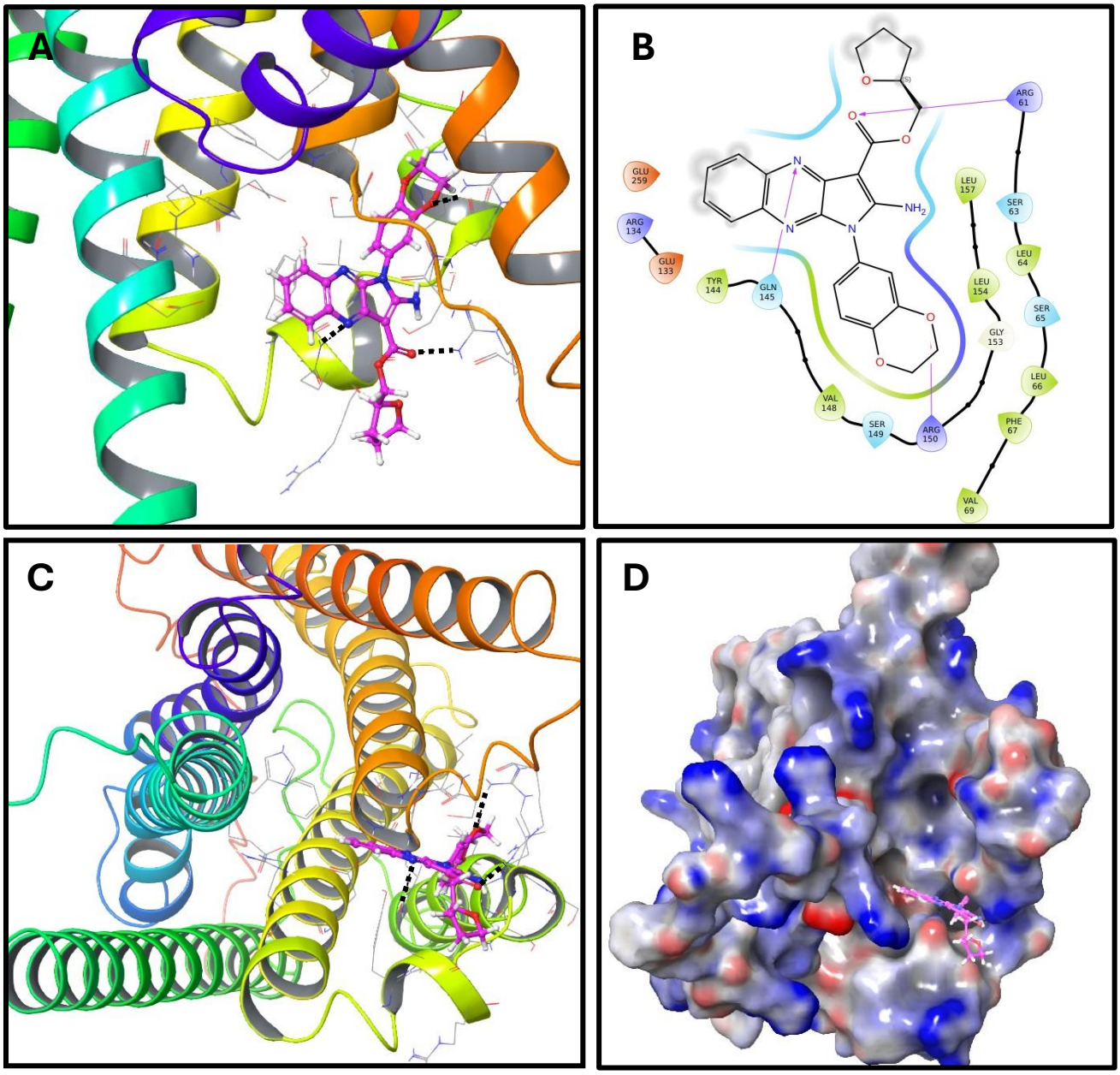

Figure 36 *- **A**) Side on view of the EP_2 inactive conformation computational model with compound **25a** docked (pink) including key hydrogen bonding interactions. S enantiomer shown as a representation. **B**) Ligand interaction diagram of **25a** with the predicted binding pocket and hydrogen bonding interactions to their corresponding amino acids. Image generated with Maestro from the Schrödinger suite. **C**) Bottom-up view of the EP_2 inactive conformation computational model with compound **25a** docked and key hydrogen bonding interaction. **D**) Bottom-up view of the EP_2 inactive conformation computational model with compound **25a** docked with added surface coloured as relative electrostatic potential.*

Docking of ligands containing a benzyl ester (e.g. **25h**, **40a**-**s**) into the computational model predicted the formation of a new aromatic hydrogen bonding interaction between Arg61(loop not fixed) and the π-system (see Figure 37a/b). This interaction supports the higher experimentally determined binding affinity and functional potency of benzyl ester containing analogues. Analysis of predicted binding for the phenols, which were designed but not successfully synthesized, highlighted the potential formation of a novel hydrogen bond between the alcohol and Val148 (34.57) for the meta-substituted phenol **40k**, (see Figure 37b/c). Therefore, future development of these phenol analogues should be prioritized; any resulting improvements in ligand binding affinity would support the accuracy of allosteric ligand binding at this EP_2 receptor computational model. Furthermore, docking of para-chlorobenzyl ester analogue **40f** into the computational model predicted the formation of a halogen bond with Arg61(loop not fixed) (see Figure 37d/e), however, this interaction was not observed for the remaining halogen-substituted benzyl esters including lead analogue **40r**.

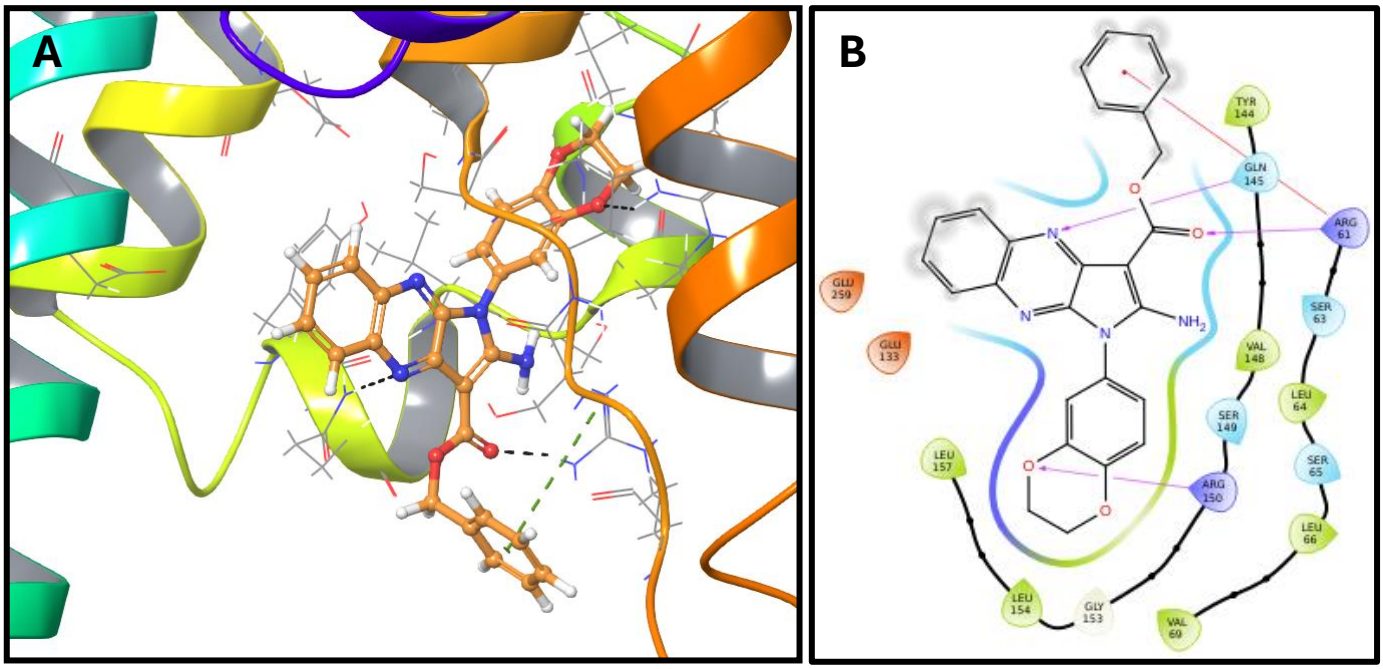

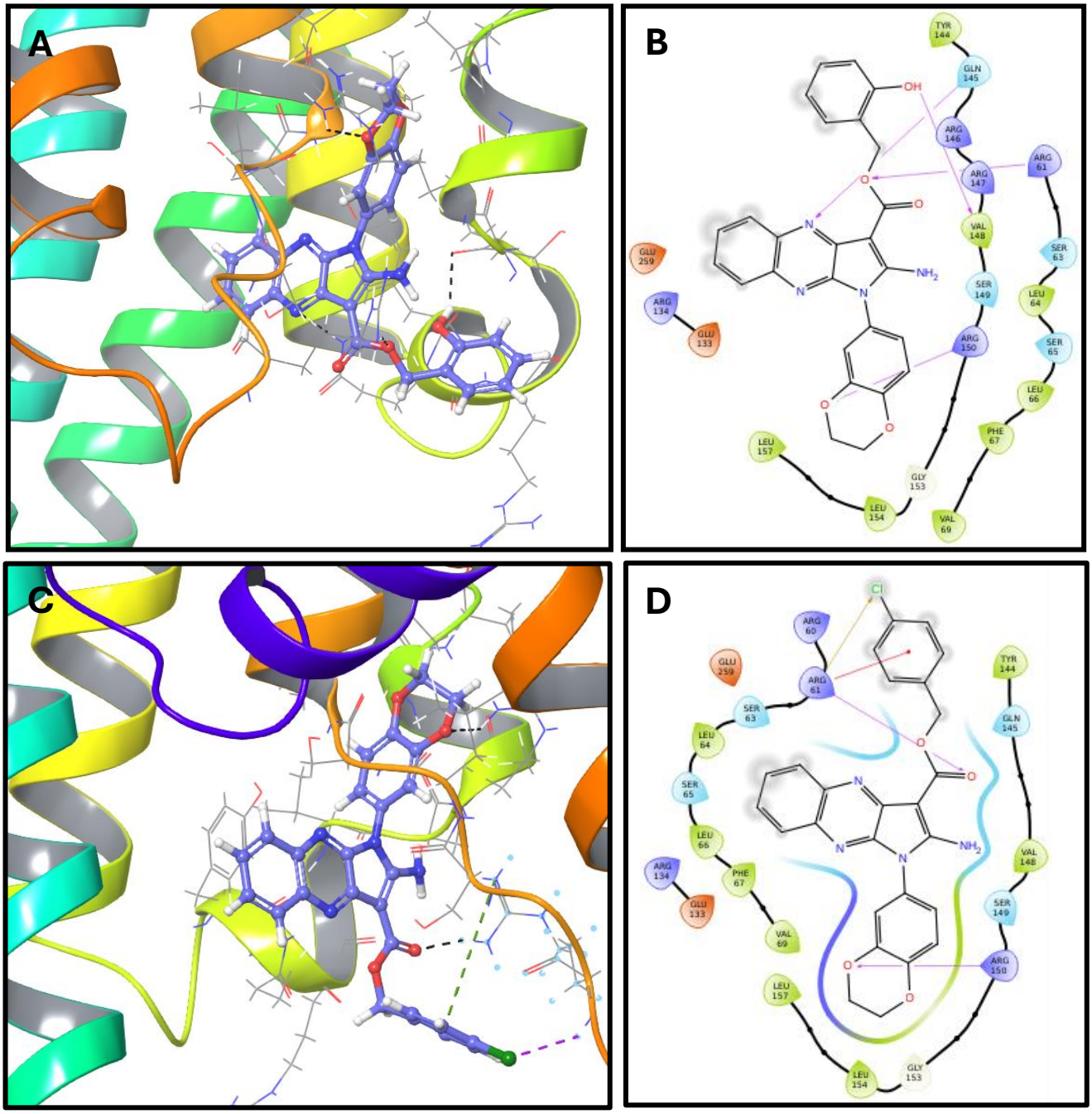

Figure 37*- Side on view of ligands* ***40k*** *and* ***40f*** *docked into the EP₂ computational model (****A*** *&****C*** *respectively) and their ligand interaction diagrams (****B*** *&* ***D*** *respectively).*

For this model 55 % of known non-binding ligands failed to dock or generated very low docking scores; higher docking scores indicate a more stable protein-ligand complex typically correlating qualitatively with ligands relative binding affinities [429]. The remaining non-binding controls (**25j-m**, **25w** & **25y**), all contained a hydrogen bond acceptor oxygen, in place of the 1,4-dioxane moiety, forming an interaction with Arg150

(4.39) believed to be the main driver of docking. Therefore, the presence of this interaction does not completely align with the experimental SAR data, and two theories have been generated for rationalisation. Firstly, it is theorised that replacement of the dioxane region with a less rigid hydrogen bond donor moiety, e.g. methoxy substituent, may have unfavourable entropic consequences when binding into this pocket (the freedom of rotation for these flexible bonds is impeded). Alternatively, ligand binding could be primarily driven by the presence of the ethylene bridge, not present in docked negative controls, forming key van-der Waals interactions with this binding pocket.

6.3 Comparison of NAM docking at the *h*EP_2 computational model against crystal structures of CXCR2-00767013 bound to CXCR2 and 'Compound 15' bound to β2AR.

Our generated computational model docked with literature compound **25a** was overlayed with X-ray crystal structures of CXCR2-00767013 (Navarixin analogue) bound CXCR2 receptor (PDB 6LFL) and 'Compound 15' bound β2AR (PDB 5X7D) using PyMOL (see Figure 38a/b) [157, 158]. Both ligands for the CXCR2 and β2AR occupy a known intracellular allosteric binding pocket between TM 1-3 and 6-8. Upon comparison, this overlay demonstrates that NAM **25a** and its analogues occupy a novel intracellular binding site, between TM2-4, not previously reported in the literature. Upon inclusion of the bound heterotrimeric $G\alpha_s$ protein we can identify a likely spatial overlap between the quinoxaline ring of docked ligand **25a** and the key binding region of the Gαs protein. This model supports the theory that our NAMs functionally inhibit the EP_2 by sterically blocking Gαs protein recruitment.

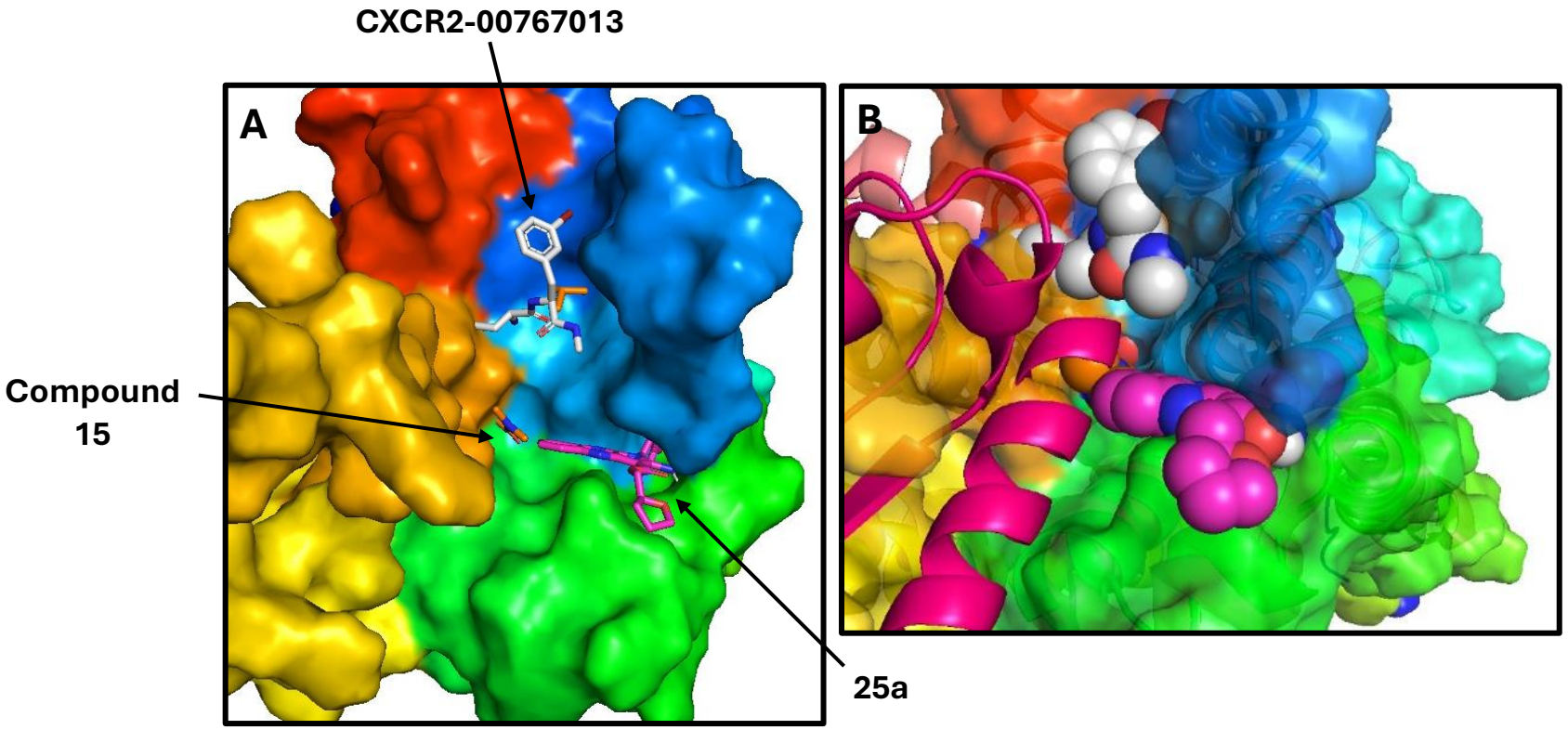

***Figure 38**- **A**) Bottom-up view of overlayed ligand **25a** (pink) bound EP_2 inactive conformation computational model with CXCR2-00767013 (orange) bound CXCR2 X-ray crystal structure and 'Compound 15' (grey) bound β2AR X-ray crystal structure. **B**) Bottom-up view of overlayed EP_2 inactive conformation computational model with the bound heterotrimeric Gαs protein (pink ribbon) and predicted docking of **25a** (shown in space-filling representation) against the CXCR2 and β2AR X-ray crystal structures with their respective allosteric ligands [157, 158].*

Sequence alignment for EP_2, CXCR2 and β2AR was then conducted using GPCRdb sequence alignment tool [430, 431]. The corresponding amino acids within a 4 Å distance of bound ligand **25a** (see Table 17) and CXCR2-00767013/'Compound 15' (see Table 18) were compared to identify differences in the allosteric binding pockets across receptors [158, 160, 183].

***Table 17**- Comparison of sequence aligned amino acids 4 Å from NAM **25a** docked into the EP_2 receptor computational model with CXCR2 and β2AR. For CXCR2 and β2AR amino acids in green are identical to the EP_2 pocket, orange indicates an amino acid in the same sub-group characterised by properties of their unique R-group (e.g. hydrophobic, polar and charged +/-) and red denotes an amino acid in a different sub-group. A blank section represents no corresponding amino acid within 4 Å of the bound ligand. Amino acids are reported as their three-letter code.*

GPCRdb position	EP_2 amino acid	CXCR2 amino acid	β2AR amino acid	Note
2.37	Ser65	Ser81	Thr66	
2.38	Leu66	Val82	Val67	CXCR2 orientation blocking binding of quinoxaline ring.
2.39	Phe67	-	-	
2.41	Val69	Val85	Tyr70	
3.49	Glu133	-	-	
3.5	Arg134	Arg144	Arg131	
34.51 (ICL-3)	-	-	Phe139	Loop region between TM3-4. β2AR amino acid blocks binding of the ester region.
34.53	Tyr144	Thr154	Tyr141	
34.54	Gln145	Leu155	Gln142	β2AR amino acid blocks quinoxaline region.
34.55	-	Thr156	Ser143	
34.56	-	-	Leu144	
34.57	Val148	Lys158	Leu145	

34.58	-	Arg159	-	CXCR2 main amino acid blocking the dioxane pocket
4.38	Ser149	-	Thr146	
4.39	Arg150	-	Lys147	β2AR main amino acid blocking the dioxane pocket
4.42	Gly153	Val162	Ala150	
4.43	Leu154	Lys176	Arg151	

***Table 18**- Comparison of sequence aligned amino acids 4 Å from NAM CXCR2-00767013/'Compound 15' docked into CXCR2 and β2AR computational model with EP_2. For EP_2 amino acids in green are identical to the those in CXCR2 or β2AR, orange indicates an amino acid in the same sub-group characterised by properties of their unique R-group (e.g. hydrophobic, polar and charged +/-) and red denotes an amino acid in a different sub-group. A blank section represents no corresponding amino acid within 4 Å of the bound ligand.*

GPCRdb position	CXCR2 amino acid	β2AR amino acid	EP_2 amino acid	Note
1.53	-	Val54	-	
1.56	Val72	-	Leu45	
1.57	Ile73	-	Leu46	
1.6	Ser76	Phe61	Arg49	
Loop not fixed			Trp50	
Loop not fixed			Leu64	

12.49 (ICL1)		Arg63	-	
12.5	Gly79	Leu64	-	
12.51	Arg80	Gln65	-	
2.37	Ser81	-	Ser65	
2.39	Thr83	Thr68	Phe67	EP_2 amino acid blocking the CXR2 and β2AR pocket.
2.40	Asp84	Asn69	His68	
2.43	Leu87	Ile72	Val71	
3.49	-	-	Glu133	
3.5	Arg144	Arg131	Arg134	
6.29	-	-	Gly258	
6.33	Glu249	Ala271	His262	EP_2 amino acid blocking the CXR2 and β2AR pocket. Glu249 is a mutation.
6.36	Val252	-	Leu265	
6.37	Ile253	Ile275	-	
7.53	Tyr314	Tyr326	Phe315	
8.47	Gly318	Ser329	Arg319	
8.49	Lys320	-	-	
8.5	Phe321	Phe322	Val322	

When comparing the EP_2 allosteric binding pocket with corresponding amino acids in CXCR2 and β2AR we can identify numerous sequence differences which sterically prevent ligand binding to this region in the latter receptors. For CXCR2 the presence of Arg159 (34.58) (loop between TM3-4) sterically blocks the 2,3-dihydrobenzo[*b*][1,4]dioxine binding pocket reported on the **25a** docked EP_2 computational model. Furthermore, the orientation of the R group in Val82 (2.38) on TM2, in place of EP_2 Leu66 (2.38), sterically blocks the quinoxaline ring. At β2AR amino acid Lys147 (4.39) on TM4, in place of Arg150 (4.39) on EP_2, occupies the 2,3-dihydrobenzo[*b*][1,4]dioxine binding pocket. Additionally, the loop region between TM3-4 contains Phe139 (34.51), which sterically hinders binding of the ester moiety and eliminates the hydrogen bonding formed by the ester carbonyl, and Gln142 (34.54) whose orientation has the potential to block the ligand quinoxaline region binding. Therefore, from this sequence alignment data, we can conclude that there is no corresponding intracellular pocket present at both CXCR2 and β2AR for the binding of NAM **25a** and analogues. As a result, we can predict our NAMs will demonstrate selectivity for EP_2 over CXCR2 and β2AR.

In comparison, sequence alignment data investigating the CXCR2-00767013/'Compound 15' binding pocket indicated this site is not present within the EP_2 receptor due to two key amino acid changes. Firstly, a change from Thr83/68 (2.39) in CXCR2 and B2AR respectively to a Phe67 (2.39) is reported for EP_2. Secondly a change from Ala271 (6.33) in β2AR (mutation present for CXCR2 at this position) to a His262 (6.33) is observed in EP_2. In both cases the amino acids present in EP_2 contain significantly larger side chains spatially blocking the corresponding binding site. As a result, it is predicted that NAMs 'Compound 15' and CXCR2-00767013 will not inhibit the EP_2 receptor.

6.4 Conclusions of computational modelling.

In conclusion, a new computational model based on the recently reported cryo-EM structure of EP_2, in an inactive conformation, has been generated which successfully docks known active compounds from our SAR dataset in a consistent pose with reasonable interactions into a novel intracellular allosteric binding pocket [160]. The binding pose of our ligands differs from the reported homology model in the literature with the essential 2,3-dihydrobenzo[*b*][1,4]dioxine moiety interacting with a novel pocket between TM2&4 forming a hydrogen bonding interaction with Arg150 (4.39). Comparatively, the literature reported that the tetrahydrofuran-2-yl methyl ester occupies this pocket. The new EP_2 computational model predicts the quinoxaline ring sits perpendicular to the EP_2 receptor, forming a hydrogen bond with Gln145 (34.54), and the ester moiety is solvent exposed with the ester carbonyl hydrogen bonding to Arg61 (loop not fixed). This binding pose is supported by our pharmacological data, with the presence of the ester improving ligand binding affinity but modifications to the attached moiety having little impact. Validation of this model was shown through most known inactive compounds failing to bind or producing low docking scores. Additional refinement of the 2,3-dihydrobenzo[*b*][1,4]dioxine pocket may be needed to rationally eliminate the docking of all remaining inactive ligands, however this is currently beyond the scope of the project.

Sequence alignment of the EP_2 receptor computational model with crystal structures of CXCR2 and β2AR bound to their intracellular allosteric modulators (TM1-3 & 6-8) highlighted that our NAMs bind to a novel pocket between TM2-4 not previously reported in the literature [158, 183]. The comparison of amino acid sequences at both binding sites identified that the CXCR2 and β2AR intracellular binding pocket is not present at EP_2 with amino acids Phe67 (2.39) and His262 (6.33) sterically blocking this site. The equivalent is also true in relation to the EP_2 binding pocket with amino acids Arg159 (34.58)/Val82 (2.38) at CXCR2 and Lys147 (4.39)/Phe139 (34.51)/Gln142 (34.54) at β2AR sterically hindering any ligand binding between TM2-4 [158, 160, 183]. Inclusion of the bound heterotrimeric $G\alpha_s$ protein with our NAM-bound EP_2 receptor model gives

an insight into the mechanism of functional inhibition; the quinoxaline ring of our NAMs overlaps the Gαs protein binding site and sterically blocks its recruitment to the receptor. Conducting a NanoBiT™ complementation assay in EP_2-LgBiT, m$G\alpha_s$-SmBiT tagged stably transfected Hek293 whole cells would quantify the functional inhibition of our NAMs on heterotrimeric $G\alpha_s$ protein recruitment and validate this proposed mechanism of action.

Based on both the predicted binding pose of our analogues and their overlap with the bound heterotrimeric $G\alpha_s$ protein it would be beneficial for future work to explore modifications at the pyrroloquinoxaline ring. Increasing the size of this core structure, for example through the addition of various substituents at the 6/7-pyrroloquinoxaline position, would both improve the overlap with the heterotrimeric $G\alpha_s$ protein binding pocket and enable the formation of new ligand-receptor interactions. Thus, potentially improving ligand binding affinity and functional potency. Furthermore, modifications at this moiety have the potential to produce biased inhibitors which can selectively inhibit certain signalling pathways and have the potential to optimize drug efficacy and improve safety profiles [167, 432]. For example, replacement of this core structure with a smaller ring system may remove the ability of our ligand to inhibit heterotrimeric $G\alpha_s$ protein recruitment, no overlap of the binding pockets, whilst still inhibiting β-arrestin signalling.

Chapter 7- General conclusions and future work

7.1 Thesis summary and conclusions

Prostaglandin EP_2 is a GPCR identified as an emerging pro-inflammatory target in chronic inflammatory disease. Chronic inflammation occurs when an inflammatory response continues past the point of healing or begins when there is no infection/injury and damages healthy cells, tissues and organs over time [3-6]. It plays an essential role in promoting the expression of pro-inflammatory cytokines at leukocytes, such as macrophages and lymphocytes, and is reported to modulate Th17 cell function to recruit/expand myeloid cells. Conversely, in the tumour micro-environment, EP_2 activity appears immune-suppressive, allowing cancer cells to escape the immune system, and may also have other tumour supporting actions including the stimulation of tumour angiogenesis and direct effects on proliferation and survival [18, 71, 73, 108, 110]. EP_2 receptors are also upregulated in chronic inflammation and EP_2 expression is linked to an exacerbation of a variety of diseases including cancer and chronic inflammatory neurodegenerative diseases such as Alzheimer's and Parkinson's disease [51, 72, 99, 118, 119, 131]. Despite NSAIDs (COX inhibitors) regularly being used to alleviate inflammation in rheumatoid arthritis and acute fever, they are not FDA approved for the treatment of cancer or neurodegenerative diseases due to numerous adverse effects associated with long-term use, which may arise from on target side effects (for example in the GI tract), and general elevation of prostanoid signalling through the nine different prostanoid receptor subtypes [27, 35, 40-42, 44]. Long-term NSAID therapy has been found to induce renal dysfunction, GI complications and increase the risk of cardiovascular events [35, 40-42, 44]. Therefore, the development of small molecule antagonist for the EP_2 receptor, downstream of the COX pathway, is an attractive therapeutic approach to modulate chronic inflammation whilst minimizing potential toxic side effects. This thesis details the design, synthesis and pharmacological characterisation of NAMs for prostaglandin EP_2, expanding on the first reported NAM **25a**, published in 2020 by C. Jiang, *et al* (see Figure 10) [179]. As the limited literature SAR data highlighted the 2,3-dihydrobenzo[*b*][1,4]dioxine motif as an essential driver of

NAM function, the development of our compound library was focused on expanding the SAR around the tetrahydrofuran-2-yl methyl ester [179]. The pharmacological characterisation of this compound library, utilizing NanoBRET competition binding and NanoBiT complementation assays, aimed to identify NAMs demonstrating improved binding affinites and functional potencies as well as providing further insights into potential mechanisms of action.

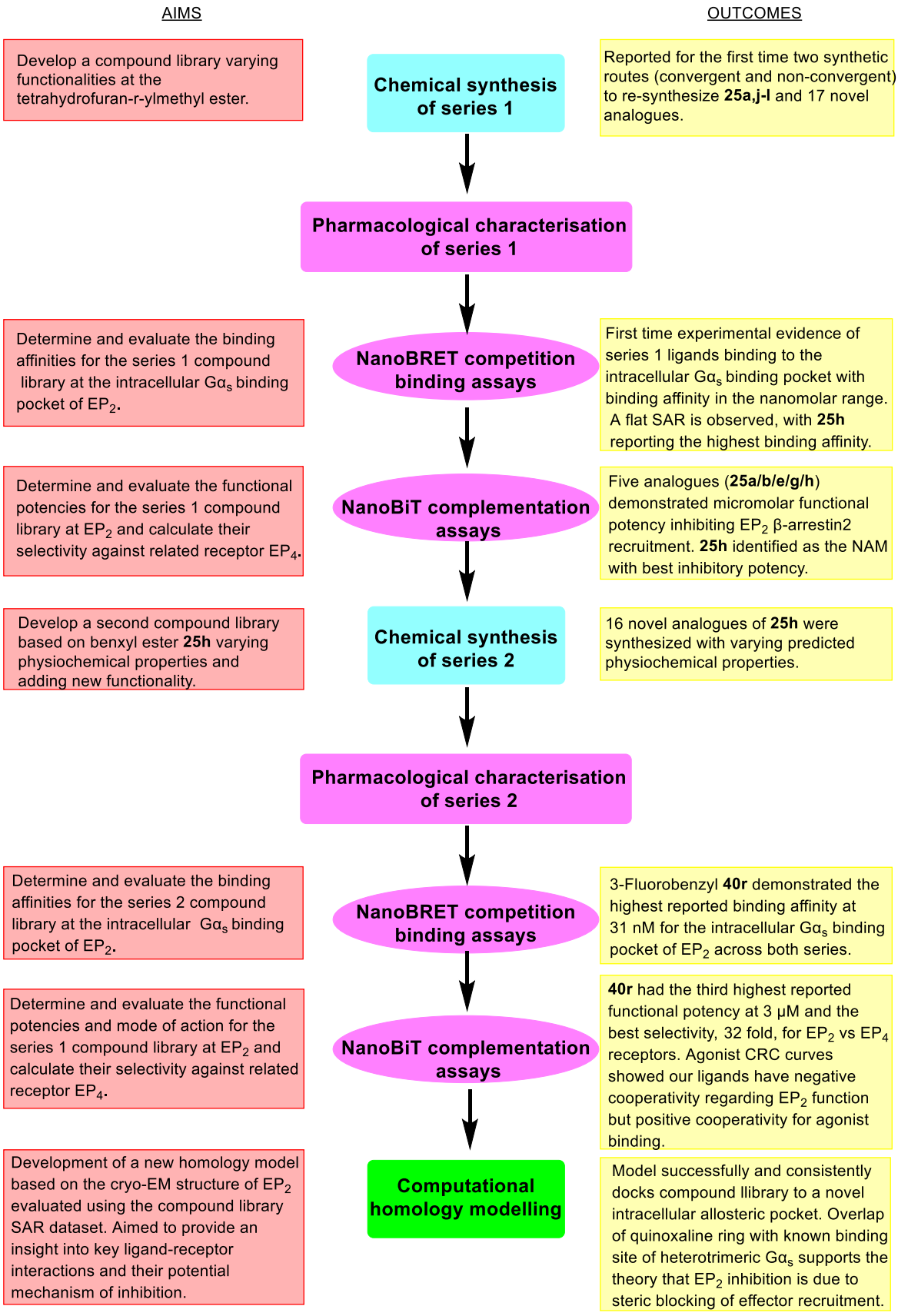

Figure 39- *A project workflow including a summarisation of the main aims and outcomes reported in this thesis.*

As no synthetic route to **25a** was provided in the literature, chapter 2 reports, for the first time, the development of both a convergent and non-convergent synthetic approach to resynthesize **25a** and produce the series 1 compound library. Series 1 was designed to insert new functionalities at the ester moiety with the aim of modifying physiochemical properties, with proposed variations in compound solubility and lipophilicity, and exploring potential new ligand-target interactions. In addition to the resynthesis of **25a** and three negative controls from the literature **25j-l** (containing modifications at the 2,3-dihydrobenzo[*b*][1,4]dioxine motif) a total of 17 novel analogues were isolated with a purity >95 % for pharmacological characterisation [179].

The pharmacological characterisation of series 1, presented in chapter 3, experimentally demonstrated that our ligands bind to an intracellular allosteric binding pocket, predicted to be the site of heterotrimeric $G\alpha_s$-receptor interaction, by competing with the G-protein mimetic fluorescent probe TMR-Gαs19cha18 in a NanoBRET competition binding assay for EP_2. Additionally, NanoBiT complementation assays were employed to determine our ligands act as functional antagonists inhibiting β-arrestin2 recruitment in cell-based assays at both the target *h*EP_2 receptors and closely homologous receptor *h*EP_4 for selectivity studies [219]. From this SAR of series 1, benzyl ester **25h** was identified as the allosteric antagonist of the *h*EP_2 receptor with the highest binding affinity (pK_I = 7.05 ± 0.16, 89 nM, highest functional potency (pIC_{50} = 5.70 ± 0.03, 2.0 μM) and best selectivity (12- fold) for EP_2 over EP_4 in series 1 (*note- data taken from Chapter 2 series 2 data to enable comparison between series*).

A second compound library was designed and synthesize based upon this lead compound **25h** with modifications focused on the phenyl ring disclosed in chapter 4. The aim of this series was to vary physiochemical properties predicting good cell membrane permeability and good bioavailability through their proposed reduction in lipophilicity. Insertion of new hydrogen bond donor/acceptor regions was also explored to exploit any additional interactions within the receptor binding pocket. In total, the non-convergent synthetic route was successfully employed to yield a further 16 novel analogues of **25a**.

The pharmacological characterisation of series 2, presented in chapter 5, identified 3-fluorobenzyl analogue **40r** as a promising lead compound (from both series) with the highest reported EP_2 binding affinity for the intracellular $G\alpha_s$ binding pocket (pK_I = 7.51 ± 0.11, 31 nM), third highest reported functional potency (pIC_{50} = 5.52 ± 0.04, 3.0 μM) inhibiting β-arrestin2 recruitment, and best fold selectivity (32) for the target *h*EP_2 receptor compared to closely related receptor subtype *h*EP_4. Despite the proposed theory of an allosteric mode of action improving EP_2 selectivity, when evaluating the selectivity reported for **40r** compared to selective orthosteric antagonists reported in the literature a 32-fold selectivity is low; TG4-155, TG6-129 and PF-04418948 all demonstrating >443-fold selectivity for EP_2 over EP_4 in functional cAMP assays (see Chapter 1-3.3) [115]. Additionally, **40r** has a lower EP_2 binding affinity (by 2-3 fold) than the best in class orthosteric antagonists TG4-155 (EP_2 K_i= 9.9 nM) and PF-04418948 (EP_2 K_i= 16 nM) [115]. A higher affinity would be desirable (<10 nM) to optimise further for in vivo studies, pharmacokinetics and ultimately candidate selection. Additionally, our NAMs, at two set concentrations, displayed classical allosteric insurmountable antagonism in PGE_2 CRC curves. A reduction in the R_{max} of the curves proportional to the increasing concentrations of the modulators is observed, indicative of negative cooperativity of our ligands with PGE_2 efficacy (EP_2 function). However, positive co-operativity between allosteric and orthosteric ligand binding is observed with a leftward curve shift and increase in functional potency of PGE_2 proportional to addition of our modulators. Therefore, it is proposed that our NAMs stabilise the active conformation of *h*EP_2 but functionally inhibit downstream signalling through sterically blocking effector recruitment. Furthermore, this pharmacological characterization verified the 'use dependent' property of our NAMs meaning compound binding and resulting EP_2 inhibition will be highest in the presence of high levels of PGE_2 in the tissues. For example, inhibition of EP_2 will be localised to sites of inflammation or the tumour microenvironment where high levels of PGE_2 are released. Conversely, tissues producing lower levels of PGE_2 will have a reduced level of EP_2 inhibition theoretically reducing the risk of on target side effects e.g. hypertension, increased ocular hypertension and renal dysfunction [115]. The non-surmountable inhibition, reduction

in R_{max} regardless of PGE_2 concentration, resulting from the allosteric action of our ligands would also prove beneficial in vivo with effective antagonism being achieved even in high PGE_2 concentrations. In comparison standard competitive, reversible orthosteric antagonists demonstrate surmountable antagonism and pose a risk that high inflammatory levels of PGE_2 would outcompete these antagonists and limit the extent of EP_2 inhibition lowering their therapeutic effect. Furthermore, as previously discussed allosteric antagonists have the potential to demonstrate a ceiling effect, reaching a maximal inhibitory effect even with increased NAM concentrations, which can titrate the magnitude of their effect and prevent overdose. However, our pharmacological data provides no evidence to indicate that this titration could be achieved in vitro, as the highest ligand concentrations in Schild analysis fully inhibited PGE_2, potentially a direct result of our NAMs competing with the effector protein β-arrestin2.

As part of this work a new computational model based on the recently reported cryo-EM structure of EP_2 in its inactive conformation was developed and reported in chapter 6. This model successfully docks known active compounds from our SAR dataset in consistent poses with reasonable interactions into a novel intracellular allosteric pocket not previously identified in the literature. Additionally, the model provides an insight into the mode of action of our NAMs. The quinoxaline ring of our receptor-bound ligands overlaps with the known binding site of the heterotrimeric $G\alpha_s$; thus, further supporting the theory that the NAMs inhibit EP_2 through steric blocking of effector recruitment. However, the computational model produced was based upon the inactive conformation of EP_2 when our pharmacological data strongly indicates our NAMs bind best to the active conformation of EP_2 based on the need for PGE_2 in the binding assays and use dependence in the functional assays. Therefore, further work should be conducted to model the active EP_2 conformation, despite IDF not producing consistent docking poses for ligands with known binding affinity, to explore whether receptor state differences in compound binding can be rationalised by comparing the docking scores and poses between the two. This information could help inform further refinements to the models and resultant in silico SAR.

In conclusion this work produced a well characterised novel lead NAM 3-fluorobenzyl analogue **40r**, selective for the prostaglandin EP_2 GPCR (over the closely related receptor EP_4) with the potential to treat chronic inflammation in numerous disease states whilst circumventing adverse effects commonly associated with current NSAID therapy. For the first time we have reported a successful synthetic route to yield these novel EP_2 NAMs and provided experimental evidence, from both EP_2 ligand binding and functional assays, supporting their intracellular allosteric mode of action. As this project is still in the early stages of the drug discovery process significant future work could be conducted to further elucidate the mechanism of action for these NAMs as well as improve drug pharmacodynamics and explore their pharmacokinetics.

7.2 Future work

The data reported in this thesis could be used to guide additional lead optimisation strategies and produce a third series of ligands to further expand our compound library with the objective to further increase binding affinity, functional potency, selectivity and metabolic stability (see Figure 40). Firstly, the proposed compounds designed for series 3 should be docked into the EP_2 computational model reported in this thesis; evaluating the binding poses, receptor-ligand interactions and docking scores produced could further justify or eliminate the synthesis of these ligands.

Amides:

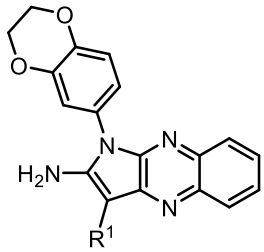

R^1=

48a

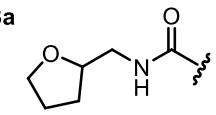

48b

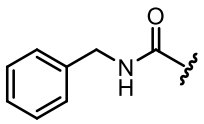

48c

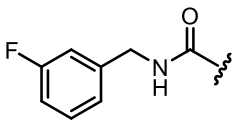

3d

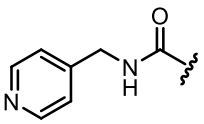

Pyrroloquinoxaline modifications:

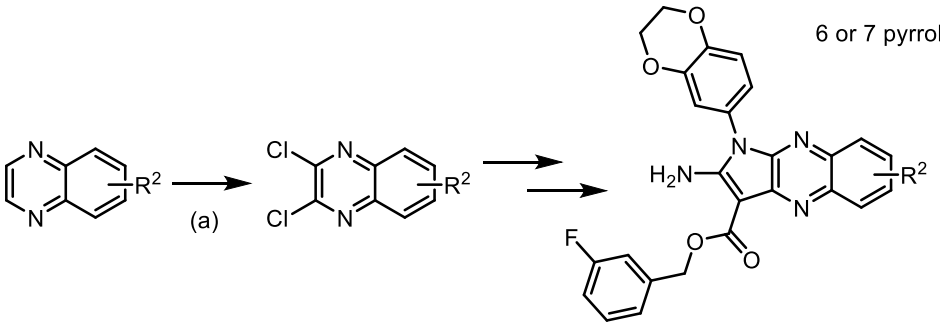

6 or 7 pyrroloquinoxaline substituents R^2=

48e/f —F **48m/n** —OMe

48g/h —Cl **48o/p** —NO_2

48i/j —Br **48q/r** —Me

48k/l —CF_3 **48s/t**

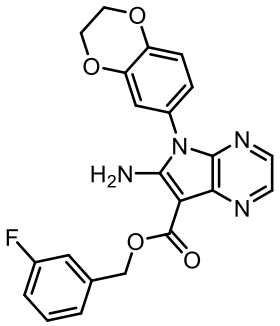

48u

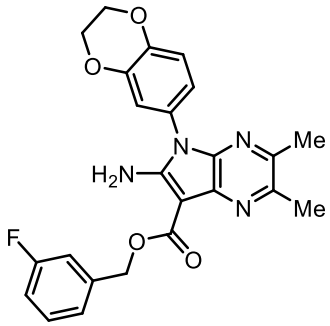

48v

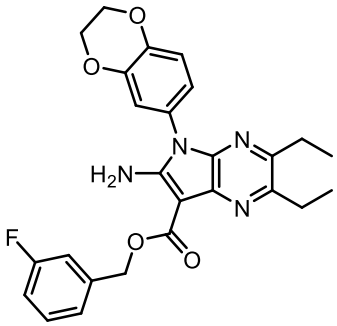

48w

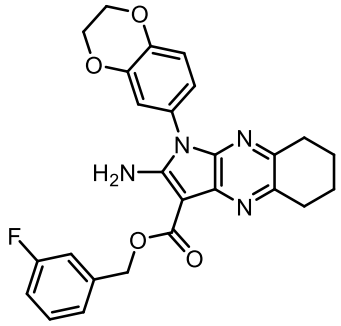

48x

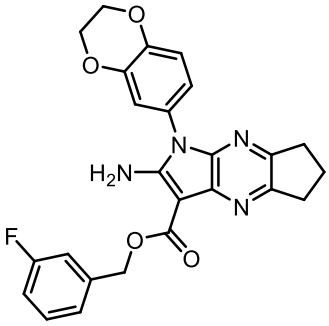

48y

Figure 40- *Proposed compounds for series 3 exploring the replacement of ester moiety with amides, addition of substituents to the 6/7 position of the pyrroloquinoxaline ring and replacement with an alternative ring system.* ***Reagents and conditions-*** *(a) 1. 30 % aq. H_2O_2 (10 eq.), acetic acid (excess), 50 °C, 24 h. 2. $POCl_3$ (5 eq.), reflux ,24 h. [433, 434] Subsequent synthesis to desired analogues is the same as reported in Chapter 4-2.*

Future work could focus on the development of an amide series (**48a-d**) replacing the ester functionality in lead NAMs **25a/h** and **40c/r** reported in this thesis. Not only do these analogues introduce a moiety with dual hydrogen-bonding capabilities, acting as both a HBD and HBA, but they would be expected to demonstrate improved metabolic stability compared to their ester counterparts [231]. Amides are less susceptible to hydrolysis (both chemically and enzymatically) and therefore, could provide synthetic access to the desired phenol analogues. As previously reported in chapter 4, deprotection of phenol **40m** from the corresponding protected allyl ether proved unviable due to the occurrence of an ester hydrolysis side reaction. Synthesis and subsequent pharmacological characterisation of these phenols would allow for further evaluation of our EP_2 computational model as docking studies indicated the presence of a new hydrogen bonding interaction of ortho substituted phenol **40k** with ICL2 amino acid Val148 (34.57) (detailed in chapter 6-2).

Based on proposed by docking of the NAMs into the EP_2 computational model it is theorised that addition of substituents at the 6/7-pyrroloquinoxaline position in **48e-t** would increase the overlap of our bound ligands with the $G\alpha_s$ protein intracellular binding pocket on EP_2 (see Chapter 6.3). As a result, these ligands may sterically hinder $G\alpha_s$ protein recruitment to EP_2 to a greater extent, resulting in improve functional potency for these NAMs. The generation of a biased antagonist toolkit would enable exploration of the EP_2 specific G protein versus β-arrestin signalling pathways involved in the chronic inflammatory immune response of cancer, AD and PD leading to disease progression. If one signalling pathway was identified as therapeutically relevant and the other linked to the production of side effects this would provide evidence for strategic development of biased EP_2 antagonists [435-437].

The inclusion of halogens (**48e**-**j**) at the 6/7-pyrroloquinoxaline position would enable the formation of halogen- π bonding between the ligand and EP_2 receptor potentially

improving NAM binding affinity and receptor selectivity.[326-331] Similarly, the insertion of a trifluoromethyl group (**48k/l**) can also introduce halogen- π bonding as well as weak hydrogen bonding interactions with the receptor protein backbone with fluorine acting as the acceptor. The trifluoromethyl group is also reported to increase metabolic stability and lipophilicity [438].

Furthermore, the introduction of the methoxy group (**48m**/**n**) could enable either new hydrogen bonding with oxygen (partial negative charge) as the acceptor and Van der Waals interactions with the methyl group (partial positive charge) as well as decreasing lipophilicity (see Chapter 4.1) [333]. Incorporation of a strong electron withdrawing nitro-group (**48o**/**p**) at the 6/7-pyrroloquinoxaline position introduces a new hydrogen bond acceptor and can also exhibit π -hole interactions, a positive electrostatic potential (positive charge) on the nitrogen can form a non-covalent bond with lone pairs on O/S atoms in the receptor binding site, in addition to decreasing lipophilicity and increasing aqueous solubility [439]. Additionally, this nitro-group can be reduced to an aniline which is amenable to further functionalisation. Finally, the methyl (**48q**/**r**) and isopropyl (**48s**/**t**) are bulky hydrophobic substituents aiming to fill the $G\alpha_s$ protein intracellular binding pocket and increase lipophilicity [440].

In contrast, replacement of the pyrroloquinoxaline ring system with a smaller ring system, e.g. the 5*H*-pyrrolo[2,3-*b*]pyrazine in **48u**, the 5,6-dimethyl-1*H*-indol-2-amine in **48v**, and the 5,6-diethyl-1*H*-indol-2-amine in **48w**, could lead to development of a biased inhibitor further validate our EP_2 computational model. In theory the binding pose of **48u-w**, bound to the intracellular allosteric binding pocket of EP_2, would not overlap with $G\alpha_s$ protein due to the lack of a third ring in the core (see Chapter 6.3). Therefore, it is predicted that **48u-w** would not inhibit heterotrimeric $G\alpha_s$ protein recruitment but could maintain steric inhibition of β-arrestin2 recruitment and its signalling. The replacement with 5,6,7,8-tetrahydro-1*H*-pyrrolo[2,3-*b*]quinoxaline-2-amine in **48x** and 1,5,6,7- tetrahydrocyclopenta[*b*]pyrrolo[2,3-*e*]pyrazin-2-amine in **48y** would remove aromaticity, lower lipophilicity and reduce the planarity of these

compounds whilst still having the potential to sterically hinder G-protein recruitment at the EP_2 $G\alpha_s$ protein binding site [441].

Additional pharmacological characterisation experiments to establish the effect of our NAMs on G-protein effector signalling at EP_2 could also be conducted, e.g. investigating the functional potency of our ligands on mini-Gαs protein recruitment, the dissociation of G-proteins through BRET Gαβγ biosensor TRUPATH or second messenger cAMP accumulation via cAMP biosensors. (see Chapter 5.5) [223, 286, 382-384]. This would quantify any differences in the degree of modulation of our NAMs on G-protein and β-arrestin2 signalling helping to guide the development of ligands which display signalling bias and further elucidate understanding of EP_2 signalling pathways. Expanding our NAM selectivity studies utilising NanoBiT complementation assays at closely related-prostanoid receptors DP_1 and IP, which share 44 % and 40 % total structural homology respectively and couple with $G\alpha_s$-proteins, would provide further experimental evidence that our NAMs have good selectivity against other prostanoid receptors.[116, 385] A screening of our ligands against additional safety targets (e.g. hERG potassium channel, adrenergic receptors (α and β), angiotensin receptors and opioid receptors) would assess the potential for life-threatening off target toxicity by our NAMs prior to in vivo studies [116, 385, 391, 392].

It would also be beneficial to evaluate the effects of our NAMs in suitable phenotypic assays for example measuring the effect of EP_2 inhibition on PGE_2 stimulated cytokine release in primary human immune cells [442, 443]. Studies evaluating the efficacy of EP_2-specific antagonists to protect conventional type 2 DCs (cDC2s) from suppressive effects (inhibit immunosuppressive IL-10 production and expansion of regulatory T cells) of tumour-derived PGE_2 in different tumour models can also be conducted [444].

Conducting mutagenesis studies to identify the key amino acid residues required for NAM binding [381]. Mutations at Arg61 (loop not fixed), Arg150 (4.39) and Gln145 (34.54), identified as essential hydrogen bonding amino acids at the intracellular allosteric binding pocket in our docking studies, could produce experimental evidence

to further validate our computational model. This data could also support the development of a computational model of EP_2 in its active conformation.

Furthermore, Immobilised artificial membrane analysis would enable the experimental quantification and ranking of the membrane permeability and lipophilicity of our compound library (detailed in chapter 4-4). This would provide suitable evidence to determine if ligand permeability is influencing the SAR functional potency data by limiting ligand ability to access the intracellular site and could guide compound optimisation for a drug-like profile.

Finally, initial drug metabolism and pharmacokinetics (DMPK) in vitro assessments should also be conducted to predict our ligands absorption, distribution, metabolism and excretion properties for potential in vivo application. Examples include conducting liver microsomal and hepatocyte stability assays to measure the rate of metabolism, calculate intrinsic clearance and identify potentially toxic metabolites using LC-MS [445-447].

Chapter 8- Experimental

8.1 Chemistry experimental

8.1.1 Materials and general methods

Chromatography- Normal phase flash column chromatography was conducted using flash silica gel 60 (particle size 40-63 µm) purchased from Sigma-Aldrich Company Ltd (England) and performed on Biotage HPFC SP4 system with UV detection at 254 nm. Reverse phase flash column chromatography was conducted on Interchim puriflash 4100 system with UV detection at 254 nm. The solvent systems used for purification are specified for each compound. Thin layer chromatography (TLC) was performed on aluminium sheet silica gel plates, 0.2 mm thick silica gel 60, using the stated mobile phase and reported as R_f values (the distance travelled by the component/distance travelled by the solvent). Visualisation of TLC plates was accomplished with UV-light (254 and 366 nm), $KMnO_4$, ninhydrin and bromocresol green staining. LCMS was performed using a Phenomenex GeminiNX C18 110A column (50 mm x 2 mm x 3 µm) at a flow rate 0.5 mL/min over a 5- or 15-minute period (gradient method of 5%-95% solvent B; solvent A= 0.01 % formic acid in H_2O, solvent B= 0.01% formic acid in CH_3CN). Spectra were recorded on a Shimadzu UFLCXR system coupled to an Applied Biosystems API2000 and visualised at 254 nm. Values given as retention time (t_R) and MS [$M+H^+$] *m/z*. The purity of final compounds was determined using area under the curve method on the UV trace recorded at a wavelength of 254 nm and NMR analysis found to be >95 % for all pharmacologically characterized compounds.

Equipment and materials- Solvents and chemicals were purchased from standard suppliers and used without further purification. Reactions were carried out at ambient temperature unless stated and monitored by TLC or LCMS.

NMR spectra- ^1H, ^{13}C and ^{19}F NMR was performed using Bruker-AV(III) HD 400 NMR equipped with a 5 mm $BBFO^+$ probe [400.25 MHz (^1H), 100.66 MHz (^{13}C), 377 MHz (^{19}F)]. Deuterated solvents used for NMR detection included $CDCl_3$, DMSO-d_6 or MeOD-d_4,

purchased from Sigma-Aldrich. Chemical shifts (δ) are reported as parts per million (ppm) and referenced against the residual proton or carbon references of the >99 % deuterated solvents as internal standards. Coupling constants (*J*) are reported as hertz (*Hz*). Data is reported in the following format: chemical shift, multiplicity (s= singlet, d=doublet, t=triplet, q= quartet, m=multiplet, dd= doublet of doublet, dt= doublet of triplets), coupling constants, integration and assignment. Spectra were assigned in combination with correlated spectroscopy (COSY) and heteronuclear single quantum coherence (HSQC). NMR were evaluated using MestReNova 14.0 (Mestrelab research).

High resolution mass spectra (HRMS)-HRMS was recorded on a Bruker microTOF mass spectrometer using electrospray ionization (ESI-TOF) operating in positive or negative ion mode.

General procedure 1: Nucleophilic aromatic substitution of 2,3-dichloroquinoxaline (26) with desired ester or malonitrile. The appropriate ester or malonitrile (1 eq.) is dissolved in DMF or DMSO before addition of Cs_2CO_3 (1.7-5 eq.) and 2,3- dichloroquinoxaline (**26**). The reaction mixture was either a) left to stir at rt for 16 hours or b) refluxed at 100 °C for 1 h. TLC (conditions reported for each compound) was used to monitor the reaction before further purification was undertaken.

General procedure 2: Cyclisation reactions with aniline and 2-substituted-3-chloroquinoxalin compounds. To a suspension of 2-substituted-3-chloroquinoxalin (1 eq.) in EtOH/THF (3:1, 3-75 mL: 1-25 mL) was added the desired amine (1.3 eq.). The reaction was heated under reflux at 80 °C with stirring for 16 h. TLC (conditions reported for each compound) was used to determine reaction completion before solvent was removed under reduced pressure to give a crude material for further purification.

General procedure 3: Acid-catalysed esterification of 2-amino-1-(2,3-dihydrobenzo[*b*][1,4]dioxin-6-yl)-1*H*-pyrrolo[2,3-*b*]quinoxaline-3-carboxylic acid (25c) with primary alcohols. Amino-1-(2,3-dihydrobenzo[*b*][1,4]dioxin-6-yl)-1*H*-pyrrolo[2,3-*b*]quinoxaline-3-carboxylic acid (**25c**) (1 eq.) was added to concentrated

H_2SO_4 (2.5 eq.) in the appropriate alcohol (1-9 mL). The reaction mixture was heated under reflux with stirring for 1 week. TLC (conditions reported for each compound) and LCMS used to determine reaction completion before solvent was removed under reduced pressure. The crude material was extracted into EtOAc (100 mL) and washed with $NaHCO_3$ (100 mL) and distilled water (100 mL). The organic layer was dried with $MgSO_4$ before being filtered and concentrated under reduced pressure. The crude material was then purified by column chromatography (conditions reported for each compound).

General procedure 4: Esterification of 2-cyanoacetic acid (31) with desired alcohol. To a solution of 2-cyanoacetic acid (**31**) (1 eq.) and alcohol (1 eq.) in DCM at 0°C was added a solution of DMAP (0.1 eq.), DCC (1 eq.) in DCM. The reaction mixture was stirred and allowed to warm to room temperature over 16 h. TLC (conditions reported for each compound) and LCMS was used to determine reaction completion. The reaction mixture was filtered to remove the white solid urea by-product washing with cold DCM. The resulting filtrate was washed with distilled water (100 mL) before being dried over $MgSO_4$, filtered, and concentrated under reduced pressure. The crude material then underwent further purification using column chromatography (conditions reported for each compound).

8.1.2 Series 1 experimental

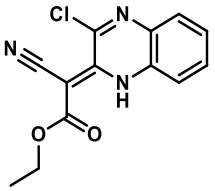

Ethyl (*Z*)-2-(3-chloroquinoxalin-2(1*H*)-ylidene)-2-cyanoacetate (28). Ethylcyanoacetate (**27**) (0.55 mL, 584 mg, 5 mmol, 2.0 eq.) was added dropwise with stirring to a suspension of NaH (60 % in mineral oil, 208 mg, 5.2 mmol, 2.0 eq.) in dimethoxyethane (DME, 10 mL). The reaction mixture was left stirring at rt for 30 minutes before addition of 2,3-dichloroquinoxaline (**26**) (500 mg, 2.5 mmol, 1 eq.) The reaction mixture was stirred at rt for 2 hr before addition of a further 20 mL DME increasing to reflux (80 °C) for 1h. Monitoring by TLC confirmed reaction completion (1:5 EtOAc:cyclohexane). The solvent was removed under reduced pressure before the crude material was treated with cold aqueous 2M

HCl (100 mL) to give a yellow solid that was filtered under vacuum and washed with cold water. The resulting solid was then recrystalised in EtOAc and filtered under vacuum to give the title compound as a yellow solid (425 mg, 62 %). R_f= 0.41 (1:5 EtOAc: cyclohexane). LC/MS *m/z* calculated for $C_{13}H_{11}ClN_3O_2$ $[M+H]^+$:276.1, found: 276.0, t_R 2.8 min. **^{1}H NMR (400 Hz, $CDCl_3$)**- δ 14.50 (s, 1H, quinoxaline-1-N***H***), 7.80 (d, *J*= 8.1 Hz, 1H, quinoxaline-5-C***H***), 7.62 (t, *J*= 7.6 Hz, 1H, quinoxaline-6-C***H***), 7.46 (t, *J*= 7.9 Hz, 1H, quinoxaline-7-C***H***), 7.39 (d, *J*= 7.1 Hz, 1H, quinoxaline-8-C***H***), 4.38 (q, *J*= 7.1, 2H, $CH_3C\boldsymbol{H}_2O$), 1.41 (t, *J*= 7.1 Hz, 3H, $C\boldsymbol{H}_3$).**^{13}C NMR (101 Hz, $CDCl_3$)**- δ 171.1 (***C***=O), 146.4 (cyanoacetate-2-***C***), 143.9 (quinoxaline-3-***C***), 134.5 (quinoxaline-8a-***C***), 132.5 (quinoxaline-4a-***C***), 128.9 (quinoxaline-7-***C***H), 128.5 (quinoxaline-6-***C***H), 126.8 (quinoxaline-5-***C***H), 116.8 (nitrile-***C***N), 116.7 (quinoxaline-8-***C***H), 69.6 (cyanoacetate-2-***C***), 62.4 ($CH_3\boldsymbol{C}H_2O$), 14.4 (***C***H_3).

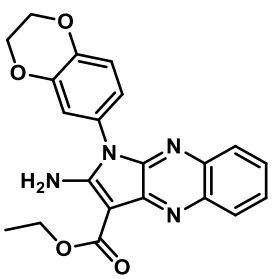

Ethyl 2-amino-1-(2,3-dihydrobenzo[*b*][1,4]dioxin-6-yl)-1H-pyrrolo[2,3-b]quinoxaline-3-carboxylate (25b). 2,3-Dihydrobenzo(1,4)dioxin-6-amine (**29**) (356 mg, 2.36 mmol, 1.4 eq.) was reacted with ethyl 2-(3-chloroquinoxalin-2-yl)-2-cyanoacetate (**28**) (508 mg, 1.81 mmol, 1.0 eq.) according to general procedure in EtOH (20 mL) and THF (7 mL). The reaction was monitored by TLC using conditions 1:1 EtOAc: cyclohexane. The crude material was recrystallised in hot EtOH to produce the title compound (656 mg, 91 %). R_f= 0.22 (1:1 EtOAc: cyclohexane). LC/MS *m/z* calculated for $C_{21}H_{19}N_4O_4$ $[M+H]^+$:391.1, found: 391.1, t_R 2.59 min. HRMS (TOF ES$^+$) calculated: 391.1401, found: 391.1395. **^{1}H NMR (400 Hz, DMSO-d_6)**- δ 7.94 (m, 3H, N***H***$_2$, pyrroloquinoxaline-5-C***H***), 7.76 (dd, *J*= 8.2, 1.5 Hz, 1H, pyrroloquinoxaline-8-C***H***), 7.56 (t, *J*= 7.8 Hz, 1H, pyrroloquinoxaline-6-C***H***), 7.48 (t, *J*= 7.6 Hz, 1H, pyrroloquinoxaline-7-C***H***), 7.12 (m, 2H, benzodioxane-7-C***H***, benzodioxane-5-C***H***), 7.02 (dd, *J*= 8.6, 2.4 Hz, 1H, benzodioxane-8-C***H***), 4.36 (m, 6H, benzodioxane-2-C***H***$_2$, benzodioxane-3-C***H***$_2$, $CH_3C\boldsymbol{H}_2O$), 3.33 (s, 3H, $C\boldsymbol{H}_3$). **^{13}C NMR (101 Hz, DMSO-d_6)**- δ 165.4 (***C***=O), 160.6 (pyrroloquinoxaline-8a-***C***), 144.9 (benzodioxane-8a-***C***), 144.4 (benzodioxane-4a-***C***), 143.7 (pyrroloquinoxaline-9a-***C***), 141.9 (pyrroloquinoxaline-3a-

C), 141.1 (pyrroloquinoxaline-4a-***C***), 137.4 (benzodioxane-6-***C***), 128.0 (pyrroloquinoxaline-5-***C***H), 127.9 (pyrroloquinoxaline-8-***C***H), 126.9 (pyrroloquinoxaline-6-***C***H), 126.0 (pyrroloquinoxaline-7-***C***H), 125.3 (pyrroloquinocaline-2-***C***), 122.4 (benzodioxane-8-***C***H), 118.44 (benzodioxane-7-***C***H), 118.40 (benzodioxane-5-***C***H), 81.3 (pyrroloquinoxaline-3-***C***), 64.7 (benzodioxane-3-***C***H_2), 64.6 (benzodioxane-2-***C***H_2), 59.2 (CH_3***C***H_2O), 15.3 (***C***H_3).

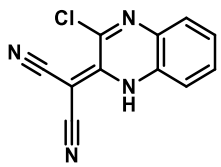

2-(3-Chloroquinoxalin-2(1*H*)-ylidene)malononitrile (30). [245] Malonitrile (732 mg, 0.011 mol, 1.1 eq.), DMSO (30 mL), Cs_2CO_3 (5.56 g, 0.017 mol, 1.7 eq.) and 2,3-dichloroquinoxaline (**26**) (2.00 g, 0.01 mol, 1.0 eq.) were reacted according to general procedure 1(a). A colour change from colourless to orange was observed. TLC analysis (EtOAc/cyclohexane 2:8) confirmed reaction completion through disappearance of 2,3-dichloroquinoaxline (**26**) (product R_f= 0, on baseline). The reaction mixture was diluted with distilled water (300 mL) and 2 M HCl (10 mL) before the product was back extracted into EtOAc (2 x 200 mL). The phases were separated, and the resulting organic phases were combined, dried over $MgSO_4$, filtered and concentrated under reduced pressure to yield an orange powder. DMSO found to be present and was removed by addition of cold distilled water (30 mL) allowing to stir for 5 minutes to form a suspension. The material was filtered and dried under vacuum filtration to produce the title compound as an orange solid (2.041 g, 89 %). LC/MS *m/z* calculated for $C_{11}H_6ClN_4$ $[M+H]^+$:229.0, found: 229.0, t_R 2.62 min. **^{1}H NMR (400 Hz, DMSO-d_6)**- δ 7.81 (dd, *J*= 8.4, 1.3 Hz, 1H, quinoxaline-8-C***H***), 7.74 (dd, *J*= 8.2, 1.4 Hz, 1H, quinoxaline-5-C***H***), 7.65 (ddd, *J*= 8.5, 7.2, 1.5 Hz, 1H, quinoxaline-7-C***H***), 7.45 (ddd, *J*= 8.3, 7.1, 1.3 Hz, 1H, quinoxaline-6-C***H***).**^{13}C NMR (101 Hz, DMSO-d_6)**- δ 149.0 (quinoxaline-2-***C***), 142.2 (quinoxaline-3-***C***), 134.8 (quinoxaline-8a-***C***), 133.4 (quinoxaline-4a-***C***l), 131.6 (quinoxaline-5-***C***H), 127.7 (quinoxaline-7-***C***H), 125.8 (quinoxaline-6-***C***H), 119.3 (2x nitrile-***C***N), 117.9 (quinoxaline-8-***C***H), 46.9 (malonitrile-1-***C***).

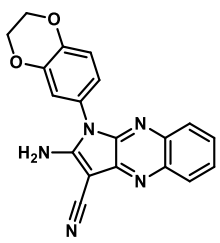

2 Amino-1-(2,3-dihydrobenzo[*b*][1,4]dioxin-6-yl)-1*H*-pyrrolo[2,3-*b*]quinoxaline-3-carbonitrile (25d). The title compound was obtained by reacting 2-(3-Chloroquinoxalin-2(1*H*)-ylidene)malononitrile (**30**) (3.961 g, 0.0173 mol, 1.0 eq.) with 2,3-dihydrobenzo(1,4)dioxin-6-amine (**29**) (3.405 g, 0.0225 mol, 1.3 eq.) according to general procedure 2 in EtOH (75 mL) and THF (25 mL). The reaction was monitored using TLC conditions 1:1 EtOAc: cyclohexane. The crude material was recrystalised using the minimum amount of EtOH before being filtered and dried under vacuum filtration. The title compound was isolated as red solid (**25d**) (5.778 g, 97%), R_f= 0.22 (1:1 EtOAc: cyclohexane). LC/MS *m/z* calculated for $C_{19}H_{14}N_5O_2$ $[M+H]^+$:344.1, found: 344.1, t_R 2.68 min. HRMS (TOF ES$^+$) calculated: 344.1142, found: 344.1137.**^{1}H NMR (400 Hz, DMSO-*d*$_6$)**- *δ* 8.32 (s, 2H, amine-N***H***$_2$), 7.93 (dd, *J*= 8.2, 1.4 Hz, 1H, pyrroloquinoxaline-5-C***H***), 7.78 (dd, *J*= 8.2, 1.5 Hz, 1H, pyrroloquinoxaline-8-C***H***), 7.59 (ddd, *J*= 8.3, 6.8, 1.5 Hz, 1H, pyrroloquinoxaline-6-C***H***), 7.50 (ddd, *J*= 8.3, 6.9, 1.5 Hz, 1H, pyrroloquinoxaline-7-C***H***), 7.14-7.06 (m, 2H, benzodioxane-5-C***H***, benzodioxane-7-C***H***), 7.00 (dd, *J*= 8.5, 2.4 Hz, 1H, benzodioxane-8-C***H***), 4.34 (t, *J*= 3.6 Hz, 4H, benzodioxane-2-C***H***$_2$, benzodioxane-3-C***H***$_2$).**^{13}C NMR (101 Hz, DMSO-*d*$_6$)**-*δ* 160.6 (pyrroloquinoxaline- 8a-***C***), 145.0 (benzodioxane-8a-***C***), 144.4 (benzodioxane-4a-***C***), 144.2 (pyrroloquinoxaline-9a-***C***), 143.5 (pyrroloquinoxaline-3a-***C***), 140.9 (pyrroloquinoxaline-4a-***C***), 137.7 (benzodioxane-6-***C***), 128.1 (pyrroloquinoxaline-8-C***H***), 127.5 (pyrroloquinoxaline-5-***C***H), 127.2 (pyrroloquinoxaline-2-***C***),126.1 (pyrroloquinoxaline-6-***C***H), 125.1 (pyrroloquinoxaline-7-***C***H), 122.5 (benzodioxane-8-***C***H), 118.5 (benzodioxane-7-***C***H), 118.43 (benzodioxane-5-***C***H), 115.73 (nitrile-***C***N), 64.7 (benzodioxane-3-***C***H$_2$), 60.8 (benzodioxane-2-***C***H$_2$), 54.9 (pyrroloquinoxaline-3-***C***CN)

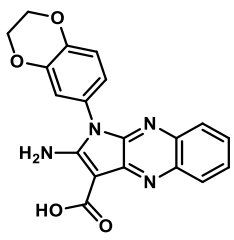

2-Amino-1-(2,3-dihydrobenzo[*b*][1,4]dioxin-6-yl)-1*H*-pyrrolo[2,3-*b*]quinoxaline-3-carboxylic acid (25c). Six batches of 2-amino-1-(2,3-dihydrobenzo[*b*][1,4]dioxin-6-yl)-1*H*-pyrrolo[2,3-*b*]quinoxaline-3-carbonitrile (**25d**) (500 mg, 1.46 mmol, 1.0 eq.) were suspended in

1,4-dioxane (6 mL) in a microwave vial before addition of 10 M NaOH (6 mL). The reaction mixture was shaken before placing in a microwave for 8 h at 120 °C, with high stirring. An LCMS at this timepoint showed approximately 3:1 ratio of product: starting material. The batches were combined before being concentrated under reduced pressure to remove the 1,4-dioxane. Distilled water (100 mL) was added, and the reaction mixture acidified to pH 5 before being back extracted with EtOAc (4 x 100 mL); large amounts of orange solid precipitated out of solution and collected by filtration. The organic phase was separated, dried over $MgSO_4$, filtered, and concentrated under reduced pressure to give a yellow solid. LCMS determined both batches of solid contained a mixture of product and starting material. The two were combined before being recrystalised in hot ethanol to give an orange solid of the title compound (**25c**) (466 mg, 15 %) over 3 batches, R_f= 0.27 (3:1 EtOAc: cyclohexane). A batch of crude material (703 mg) containing a 1:1 ratio of product: starting material by LCMS proved difficult to further recrystalize (starting material R_f= 0.6 in 3:1 EtOAc: cyclohexane). LC/MS *m/z* calculated for $C_{19}H_{15}N_4O_4$: $[M+H]^+$:362.1, found: 362.1, t_R 2.75 min. HRMS (TOF ES^+) calculated: 362.1244 ,found: 362.1239.**^{1}H NMR (400 Hz, DMSO-*d*$_6$)**- *δ* 8.03 (s, 1H, carboxylicacid-O***H***), 7.92 (dd, *J*= 8.2, 1.4 Hz, 1H, pyrroloquinoxaline-5-C***H***), 7.81-7.72 (m, 2H, pyrroloquinoxaline-8-C***H***, 1x amine-N***H***), 7.56 (ddd, *J*= 8.4, 6.9, 1.5 Hz, 1H, pyrroloquinoxaline-6-C***H***), 7.46 (ddd, *J*= 8.3m 6.9, 1.5 Hz, 1H, pyrroloquinoxaline-7-C***H***), 7.32 (s, 1H, 1x amine-N***H***), 7.15-7.07 (m, 2H, 1 x benzodioxane-5-C***H***, 1 x benzodioxane-7-C***H***), 7.01 (dd, *J*= 8.5, 2.4 Hz, 1H, benzodioxane-8-C***H***), 4.43 (s, 4H, benzodiocane-2-C***H***$_2$, benzodioxane-3- C***H***$_2$).**^{13}C NMR (101 Hz, DMSO-*d*$_6$)**-*δ* 167.2 (***C***=O), 159.8 (pyrroloquinoxaline-8a-***C***), 144.8 (benzodioxane-4a-***C***), 144.3 (benzodioxane-8a-***C***), 144.2 (pyrroloquinoxaline-9a-***C***), 142.0 (pyrroloquinoxaline-3a-***C***), 140.0 (pyrroloquinoxaline-4a-***C***), 137.3 (benzodioxane-6-***C***), 128.1 (pyrroloquinoxaline-8-***C***H), 127.3 (pyrroloquinoxaline-5-***C***H), 127.1 (pyrroloquinoxaline-6-***C***H), 125.6 (pyrroloquinoxaline-7-***C***H), 125.2 (pyrroloquinoxaline-2-***C***), 122.2 (benzodioxane-8-***C***H), 118.4 (benzodioxane-7-***C***H), 118.2 (benzodioxane-5-***C***H), 82.9 (pyrroloquinoxaline-3-***C***) 64.7 (benzodiocane-3-***C***H_2) , 64.6 (benzodioxane-2-***C***H_2).

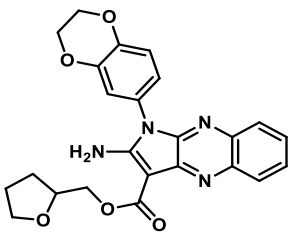

(Tetrahydrofuran-2-yl)methyl 2-amino-1-(2,3-dihydrobenzo[*b*][1,4]dioxin-6-yl)-1*H*-pyrrolo[2,3-*b*]quinoxaline-3-carboxylate (25a).[179] The title compound was obtained by reacting 2-amino-1-(2,3-dihydrobenzo[*b*][1,4]dioxin-6-yl)-1*H*-pyrrolo[2,3-*b*]quinoxaline-3-carboxylic acid (**25c**) (111 mg, 0.307 mmol, 1.0 eq.) with tetrahydrofurfuryl alcohol (9 mL) according to general procedure 3. The reaction was monitored by TLC conditions 3:1 EtOAc: cyclohexane. Column chromatography was conducted using a 12 g flash silica gel 60 column at a flow rate 15 mL/min, using the following gradients: A (50 %)/ B (50 %) for 3 column volumes (CV) to A (75 %)/B (25 %) for 8 CVs (A = EtOAc; B = cyclohexane). Fractions containing product were combined and concentrated under reduced pressure to give 51 mg of yellow solid (NMR determined impurities present). Crude material dissolved in minimum amount of methanol before addition of distilled water resulting in a white solid precipitating out; this was filtered and dried to yield the title compound as a pale-yellow solid (29 mg, 21 %). R_f= 0.33 (3:1 EtOAc: cyclohexane). LC/MS *m/z* calculated for $C_{24}H_{23}N_4O_5$: $[M+H]^+$: 447.2, found; 447.2, t_R 2.61 min. HRMS (TOF ES^+) calculated: 447.1663, found: 447.1657.**^{1}H NMR (400 Hz, $CDCl_3$)-** δ 8.14 (dd, *J*= 8.4, 1.5 Hz, 1H, pyrroloquinoxaline-5-C***H***), 7.88 (dd, *J*= 8.3, 1.5 Hz, 1H, pyrroloquinoxaline-8-C***H***), 7.58 (ddd, *J*= 8.4, 6.9, 1.6 Hz, 1H, pyrroloquinoxaline-6-C***H***), 7.50 (ddd, *J*= 8.3, 6.9, 1.5 Hz, 1H, pyrroloquinoxaline-7-C***H***), 7.10 (d, *J*= 8.5 Hz, 1H, benzodioxane-5-C***H***), 7.03 (d, *J*= 2.4 Hz, 1H, benzodioxane-7-C***H***), 6.97 (dd, *J*= 8.5, 2.5 Hz, 1H, benzodioxane-8-C***H***), 4.57 (m, 1H, tetrahydrofuran-2-C***H***), 4.43-4.31 (m, 6H, $CO_2C\boldsymbol{H}_2$ benzodioxane-3-$C\boldsymbol{H}_2$, benzodioxane-2-$C\boldsymbol{H}_2$), 4.10-4.01 (m, 1H, 1x tetrahydrofuran-5-$C\boldsymbol{H}_2$), 3.86 (dt, *J*= 8.0, 6.5 Hz, 1H, 1x tetrahydrofuran-5-$C\boldsymbol{H}_2$), 2.19-2.07 (m, 2H, tetrahydrofuran-4-$C\boldsymbol{H}_2$), 2.02-1.91 (m, 2H, tetrahydrofuran-3-$C\boldsymbol{H}_2$).**^{13}C NMR (101 Hz, (DMSO-d_6)-** δ 165.1 (***C***=O), 160.6 (pyrroloquinoxaline-8a-***C***), 144.9 (benzodioxane-4a-***C***), 144.4 (benzodioxane-8a-***C***), 143.7 (pyrroloquinoxaline-9a-***C***), 142.0 (pyrroloquinoxaline-3a-***C***), 141.2 (pyrroloquinoxaline-4a-***C***), 137.4 (benzodioxane-6-***C***), 128.0 (pyrroloquinoxaline-5-***C***H), 127.9 (pyrroloquinoxaline-8-***C***H), 126.9 (pyrroloquinoxaline-6-***C***H), 126.0 (pyrroloquinoxaline-7-***C***H), 125.3

(benzodioxane-8-***C***H), 122.4 (pyrroloquinoxaline-2-***C***), 118.5 (benzodioxane-7-***C***H), 118.4 (benzodioxane-5-***C***H), 81.2 (pyrroloquinoxaline-3-***C***), 76.7 (tetrahydrofuran-2-***C***), 68.2 (tetrahydrofuran-5-***C***H_2), 65.4 (CO_2***C***H_2), 64.7 (benzodioxane-3-***C***H_2), 64.6 (benzodioxane-2-***C***H_2), 27.9 (tetrahydrofuran-3-***C***H_2), 25.9 (tetrahydrofuran-4-***C***H_2).

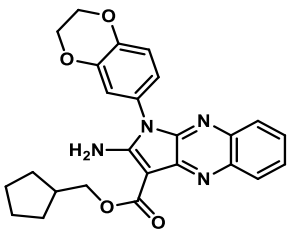

Cyclopentylmethyl 2-amino-1-(2,3-dihydrobenzo[*b*][1,4]dioxin-6-yl)-1*H*-pyrrolo[2,3-*b*]quinoxaline-3-carboxylate (25e). The title compound was obtained by reacting 2-amino-1-(2,3-dihydrobenzo[*b*][1,4]dioxin-6-yl)-1*H*-pyrrolo[2,3-*b*]quinoxaline-3-carboxylic acid (**25c**) (90 mg, 0.25 mmol, 1.0 eq.) with cyclopentanemethanol (1 mL) according to general procedure 3. The reaction was monitored using TLC conditions 0.5 % MeOH in DCM. Reverse phase column chromatography was conducted using a C18 110A column at a flow rate 15 mL/min, using the following gradients: A (95 %)/ B (5 %) to A (5 %)/B (95 %) over 15 CVs (A = H2O containing HCOOH: 0.1 %; B = ACN). Fractions containing product were combined and concentrated under reduced pressure to give the title compound as a cream solid (8.7 mg, 7 %). R_f= 0.29 (0.5 % MeOH in DCM). LC/MS *m/z* calculated for $C_{25}H_{25}N_4O_4$: $[M+H]^+$: 445.2, found: 445.1, t_R 2.85 min. HRMS (TOF ES^+) calculated: 445.1870 , found: 445.1854.**^{1}H NMR (400 Hz, DMSO-*d*$_6$)**- *δ* 7.93-7.84 (m, 3H, 1 x pyrroloquinoxaline-5-C***H***, 2 amine-N***H***$_2$), 7.75 (d, *J* = 8.2 Hz, 1H, pyrroloquinoxaline-8-C***H***), 7.56 (t, *J* = 6.8 Hz, 1H, pyrroloquinoxaline-6-C***H***), 7.47 (t, *J* = 7.6 Hz, 1H, pyrroloquinoxaline-7-C***H***), 7.15-7.07 (m, 2H, benzodiocane-5-C***H***, benzodioxane-7-C***H***), 7.01 (dd, *J* = 8.2, 2.4 Hz, 1H, benzodioxane-8-C***H***), 4.35 (s, 4H, benzodioxane-3-C***H***$_2$ benzodioxane-2-C***H***$_2$), 4.21 (d, *J* = 6.5 Hz, 2H, CO_2C***H***$_2$), 2.36 (m,1H, cyclopentane-1-C***H***), 1.85- 1.66 (m, 4H, cyclopentane-2-C***H***$_2$, cyclopentane-5-C***H***$_2$), 1.61-1.42 (m, 4H, cyclopentane-3-C***H***$_2$, cyclopentane-4-C***H***$_2$). **^{13}C NMR (101 Hz, DMSO-*d*$_6$)**- *δ* 165.5 (***C***=O), 160.5 (pyrroloquinocaline-8a-***C***), 144.9 (benzodioxane-4a-***C***), 144.4 (benzodioxane-8a-***C***), 143.7 (pyrroloquinoxaline-9a-***C***), 142.1 (pyrroloquinoxaline-3a-***C***), 141.2 (pyrroloquinoxaline-4a-***C***), 137.4 (benzodioxane-6-***C***), 128.1 (pyrroloquinoxaline-5-***C***H), 127.9 (pyrroloquinoxaline-8-***C***H), 126.8

(pyrroloquinoxaline-6-***C***H), 125.9 (pyrroloquinoxaline-7-***C***H), 125.3 (pyrroloquinoxaline-2-***C***), 122.4 (benzodioxane-8-***C***H), 118.4 (benzodioxane-7-***C***H), 118.3 (benzodioxane-5-***C***H), 81.3 (pyrroloquinoxaline-3-***C***), 66.7 (CO_2***C***H_2), 64.7 (benzodioxane-3-***C***H_2), 64.6 (benzodiocane-3-***C***H_2), 48.8 (cyclopentane-1-***C***H), 29.2 (cyclopentane-2-***C***H_2, cyclopentane-5-***C***H_2), 25.3 (cyclopentane-3- ***C***H_2, cyclopentane-4-***C***H_2).

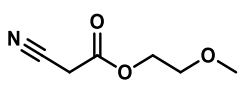

2-Methoxyethyl 2-cyanoacetate (32f). 2-Cyanoacetic acid (**31**) (150 mg, 1.76 mmol, 1.0 eq.) was reacted with 2-methoxyethan-1-ol (0.139 mL, 134 mg, 1.76 mmol, 1.0 eq.), DCC (362 mg, 1.76 mmol, 1.0 eq.), DMAP (22 mg, 0.18 mmol, 0.1 eq) in 5 mL DCM according to general procedure 4. The reaction was monitored using TLC conditions 3:7 EtOAc: cyclohexane. The crude material was purified by column chromatography on 12 g silica, 0-20 % EtOAc in cyclohexane increased in 5 % increments with 3 CVs solvent each time. Desired fractions were combined and concentrated under reduced pressure to yield the title compound as a colourless oil (144 mg, 57%). R_f = 0.22 (3:7, EtOAC: Cyclohexane). LC/MS *m/z* calculated for $C_6H_{10}NO_3$: $[M+H]^+$: 144.1, found: 143.0, t_R 2.74 min. **^{1}H NMR (400 Hz, $CDCl_3$)**- δ 4.38-4.31 (m, 2H, CO_2C***H***$_2$), 3.61 (t, *J*= Hz, 2H, C***H***$_2OCH_3$), 3.50 (s, 2H, cyanoacetate-2-C***H***$_2$), 3.37 (s, 3H, C***H***$_3$).**^{13}C NMR (101 Hz, $CDCl_3$)**- δ 163.1 (***C***=O), 112.9 (nitrile-***C***N), 69.8 (***C***H_2OCH_3), 65.7 (CO_2***C***H_2), 59.0 (***C***H_3), 24.7 (cyanoacetate-2-***C***H_2).

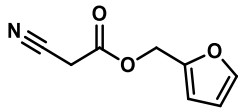

Furan-2-ylmethyl 2-cyanoacetate (32g). 2-Cyanoacetic acid (**31**) (150 mg, 1.76 mmol, 1.0 eq.) was reacted with furan-2-yl methanol (0.152 mL, 173 mg, 1.76 mmol, 1.0 eq.), DCC (364 mg, 1.76 mmol, 1.0 eq.) and DMAP (22 mg, 0.18 mmol, 0.1 eq.) in DCM 5 mL according to general procedure 4. The reaction was monitored using TLC conditions 3:7 EtOAc: cyclohexane. The crude material was purified by column chromatography on 30 g silica 0-40 % EtOAc in Cyclohexane increased in 5 % increments with 3 CVs solvent each time. Desired fractions combined and concentrated under reduced pressure to obtain the title compound as a yellow oil (191 mg, 66 %). R_f = 0.5 (3:7 EtOAc:Cyclohexane). No LCMS data obtained.**^{1}H NMR (400 Hz, $CDCl_3$)**- δ 7.44 (m, 1H, furan-5-C***H***), 6.48 (d, *J*= 3.30 Hz, 1H, furan-4-C***H***), 6.39 (m, 1H, furan-3-C***H***), 5.91 (s, 2H, CO_2C***H***$_2$), 3.48 (s, 2H,

cyanoacetate-2-C***H***$_2$).**^{13}C NMR (101 Hz, CDCl$_3$)**- *δ* 162.5 (***C***=O), 147.7 (furan-2-***C***), 143.6 (furan-5-***C***H), 112.6 (nitrile-***C***N), 111.7 (furan-4-***C***H), 110.6 (furan-3-***C***H), 59.8 (CO_2***C***H_2), 24.5 (cyanoacetate-2-***C***H_2).

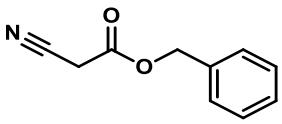

Benzyl 2-cyanoacetate (32h). 2-Cyanoacetic acid (**31**) (200 mg, 2.35 mmol, 1 eq.) was reacted with benzyl alcohol (0.243 mL, 485 mg, 2.35 mmol, 1 eq.), DCC (485 mg, 2.35 mmol, 1 eq.) and DMAP (29 mg, 0.34 mmol, 0.1 eq.) in DCM 3 mL according to general procedure 4. The reaction was monitored using TLC conditions 1:4 EtAOc: cyclohexane. The resulting crude material was purified by column chromatography on 24 g silica 5 CV 10% EtOAc in Cyclohexane followed by 10 CVs 20 % EtOAc in Cyclohexane. The desired fractions were combined and concentrated under reduced pressure to yield a colourless oil of the title compound (264 mg, 64 %). R_f= 0.34 (2:8, EtOAc: cyclohexane). LC/MS *m/z* calculated for $C_{10}H_{10}NO_2$: $[M+H]^+$: 176.1, no ion found but UV peak at t_R 2.58 min.**^{1}H NMR (400 Hz, CDCl$_3$)**- *δ* 7.38 (s, 5H, benzyl-***H***), 5.23 (s, 2H, CO_2C***H***$_2$), 3.47 (s, 2H, cyanoacetate-2-C***H***$_2$).**^{13}C NMR (101 Hz, CDCl$_3$)**- *δ* 162.9 (***C***=O), 134.4 (benzyl-1-***C***), 128.9 (benzyl-3-***C***H, benzyl-5-***C***H), 128.8 (benzyl-4-***C***H), 128.6 (benzyl-2-***C***H, benzyl-6-***C***H), 113.0 (nitrile-***C***N), 68.5 (CO_2***C***H_2), 24.8 (cyanoacetate-2-***C***H_2).

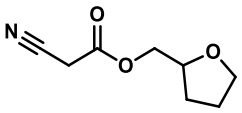

(Tetrahydrofuran-2-yl)methyl 2-cyanoacetate (32n). 2-Cyanoacetic acid (**32**) (153 mg, 1.76 mmol, 1.0 eq.) was reacted with tetrahydrofuran-2-yl methanol (0.17 mL, 1.76 mmol, 1.0 eq.), DCC (370 mg, 1.76 mmol, 1.0 eq.) and DMAP (22 mg, 0.76 mmol, 0.1 eq.) in DCM 5 mL according to general procedure 4. The reaction was monitored by TLC conditions 1:1 EtOAc: cyclohexane. The crude material was purified by column chromatography on 12 g silica, 30-70 % EtOAc in cyclohexane over 12CV. The desired fractions were combined and concentrated under reduced pressure to yield a colourless oil of the title compound (94 mg, 32 %). R_f = 0.29 (50% EtOAc in cyclohexane).**^{1}H NMR (400 Hz, CDCl$_3$)**- *δ* 4.27 (q, *j*= 6.6 Hz, 1H, tetrahydrofuran-2-C***H***), 4.15 (m, 2H, CO_2C***H***$_2$), 3.89 (q, *j*= 7.4 Hz, 1H, 1x tetrahydrofuran-5-C***H***$_2$), 3.81 (q, *j*= 6.8 Hz, 1H, 1x tetrahydrofuran-5-C***H***$_2$), 2.10-1.84 (m, 3H, tetrahydrofuran-4-C***H***$_2$, 1x tetrahydrofuran-3-C***H***$_2$), 1.71-1.57 (m, 1H, 1x

tetrahydrofuran-3-C***H***$_2$).**^{13}C NMR (101 Hz, CDCl$_3$)**- *δ* 163.4 (***C***=O), 113.3 (nitrile-***C***N), 76.4 (tetrahydrofuran-2-***C***H), 69.0 (CO_2***C***H_2), 68.7 (tetrahydrofuran—5-***C***H_2), 28.3 (tetrahydrofuran-3-***C***H_2), 26.1 (tetrahydrofuran-4-***C***H_2), 25.2 (cyanoacetate-2-***C***H_2).

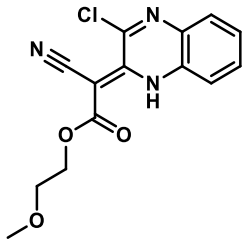

2-Methoxyethyl (*Z*)-2-(3-chloroquinoxalin-2(1*H*)-ylidene)-2-cyanoacetate (33f). 2,3-Dichloroquinoxaline (**26**) (195 mg, 0.98 mmol, 1.0 eq.) was reacted with 2-methoxyethyl 2-cyanoacetate **32a** (140 mg, 0.98 mmol, 1.0 eq.) and Cs_2CO_3 (1.591 g, 4.89 mmol, 5.0 eq.) in DMF (5 mL) according to general procedure 1(a). The reaction was monitored by LCMS. The crude material was dissolved into EtOAc (100 mL) and washed with 1M HCL (aq) 200 mL, The Aqueous phase was then back extracted with EtOAC (100 mL) until the aqueous phase was colourless (yellow organic phase). The organic phases were combined, dried over $MgSO_4$, filtered and concentrated under reduced pressure. The crude material underwent recrystallization in EtOAc being placed in the freezer overnight for crystal formation before being filtered to yield the title compound as orange crystals (155 mg, 52 %). LC/MS *m/z* calculated for $C_{14}H_{13}ClN_3O_3$: $[M+H]^+$: 306.1, found: 306.0, t_R 2.76 min. **^{1}H NMR (400 Hz, CDCl$_3$)**- *δ* 14.44 (s, 1H, quinoxaline-1-N***H***), 7.81 (d, *J*= 8.17 Hz, 1H, quinoxaline-8-C***H***), 7.63 (t, *J*= 7.28 Hz, 1H, quinoxaline-7-C***H***), 7.47 (t, *J*= 7.48 Hz, 1H, quinoxaline-6-C***H***), 7.39 (d, *J*= 8.20 Hz, 1H, quinoxaline-5-C***H***), 4.48 (t, *J*= 4.17 Hz, 2H, CO_2C***H***$_2$), 3.75 (t, *J*= 4.03 Hz, 2H, C***H***$_2OCH_3$), 3.44 (s, 3H, C***H***$_3$). **^{13}C NMR (101 Hz, CDCl$_3$)**- *δ* 170.8 (***C***=O), 146.3 (quinoxaline-2-***C***), 143.8 (quinoxaline-3-***C***), 134.4 (quinoxaline-8a-***C***), 132.4 (quinoxaline-4a-***C***), 128.8 (quinoxaline-5-***C***H), 128.3 (quinoxaline-6-***C***H), 126.8 (quinoxaline-7-***C***H), 116.6 (nitrile-***C***N), 116.5 (quinoxaline-5-***C***H), 70.3 (***C***H_2OCH_3), 69.3 (cyanoacetate-2-***C***), 64.9 (CO_2***C***H_2), 59.4 (***C***H_3).

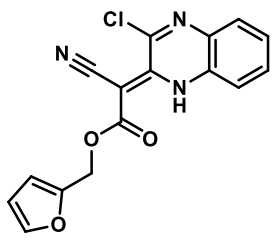

Furan-2-ylmethyl (*Z*)-2-(3-chloroquinoxalin-2(1*H*)-ylidene)-2-cyanoacetate (33g). 2,3-Dichloroquinoxaline (**26**) (229 mg, 1.15 mmol, 1.0 eq.) was reacted with furan-2-ylmethyl 2-cyanoacetate (**32b**) (191 mg, 1.15 mmol, 1.0 eq.), Cs_2CO_3 (1.881g, 5.75 mmol, 5.0 eq.) in DMF (5 mL) according to general procedure 1(a). The

reaction was monitored by TLC conditions 2:3 EtOAc: cyclohexane. The crude material was extracted into EtOAc (150 mL) washing with 2 M HCl (150 mL), all orange colour present in the organic phase. The organic phase was separated, dried over $MgSO_4$, filtered and concentrated under reduced pressure. The resulting crude material was purified by column chromatography on 25 g silica 3 CVs at 20 % EtOAc in cyclohexane increased from 20-40 % over 5 CVs, 40 % for 5 CVs, 60 % for 3 CVs, 80 % for 3 CVs and finally 100 % for 6 CVs. The desired fractions were combined and concentrated under reduced pressure to yield the title compound as a red solid (190 mg, 50 %). R_f= 0.375 (2:3 EtOAc: cyclohexane). LC/MS *m/z* calculated for $C_{16}H_{11}ClN_3O_3$: $[M+H]^+$: 328.0, found: 328.1, t_R 2.82 min. **^{1}H NMR (400 Hz, DMSO-*d*$_6$)**- δ 14.04 (s, 1H, quinoxaline-1-N***H***), 7.90 (d, *J*= 8.3 Hz, 1H, quinoxaline-8-C***H***), 7.83 (d, *J*= 8.1, 1H, quinoxaline-5-C***H***), 7.79-7.68 (m, 2H, quinoxaline-7-C***H***, furan-5-C***H***), 7.56 (t, *J*= 7.7 Hz, 1H, quinoxaline-6-C***H***), 6.63 (d, *J*= 3.3 Hz, 1H, furan-4-C***H***), 6.51 (m, 1H, furan-3-C***H***), 5.32 (s, 2H, CO_2CH_2). **^{13}C NMR (101 Hz, DMSO-*d*$_6$)**- δ 169.6 (***C***=O), 149.5 (quinoxaline-2-***C***, furan-2-***C***), 144.5 (quinoxaline-3-***C***, furan-5-***C***H), 134.6 (quinoxaline-8a-***C***), 132.9 (quinoxaline-4a-***C***), 128.3 (quinoxaline-5-***C***H, quinoxaline-6-***C***H), 127.4 (quinoxaline-7-***C***H), 118.5 (quinoxaline-8-***C***H), 111.8 (nitrile-***C***N), 111.3 (furan-3***C***H, fuan-4-***C***H), 58.9 (CO_2CH_2).

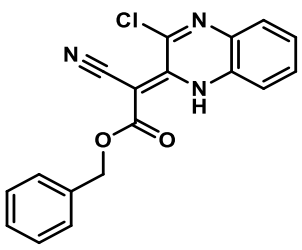

Benzyl (*Z*)-2-(3-chloroquinoxalin-2(1*H*)-ylidene)-2-cyanoacetate (33h). 2,3-Dichloroquinoxaline (**26**) (298 mg, 1.5 mmol, 1.0 eq.) was reacted with benzyl 2-cyanoacetate (**32c**) (264 mg, 1.5 mmol, 1.0 eq.), CS_2CO_3 (2.44 g, 7.5 mmol, 5.0 eq.) in 10 mL DMF in accordance with general procedure 1(b), a colour change to red was observed. The reaction was monitored by TLC conditions 1:4 EtOAc: cyclohexane. The crude material was extracted into EtOAc (100 mL) and washed with 2 M HCl (100 mL) and distilled water (100 mL), the red colouring remained in the organic phase. The phases were separated and the organic dried over $MgSO_4$ before filtering and concentrating under reduced pressure. The crude material underwent column chromatography on 40 g silica at 20 % EtOAc in cyclohexane over 10 CVs. The resulting fractions were combined and concentrated under reduced pressure

to yield the title compound as sparkly yellow crystals (433 mg, 85 %). R_f= 0.38 (1:4 EtOAc: cyclohexane). LC/MS *m/z* calculated for $C_{18}H_{13}ClN_3O$: $[M+H]^+$: 338.1, found: 338.0, t_R 3.05 min. **^{1}H NMR (400 Hz, $CDCl_3$)**- δ 7.80 (d, *J*= 8.2 Hz, 1H, quinoxaline-8-C***H***), 7.70 (t, *J*= 7.8 Hz, 1H, quinoxaline-7-C***H***), 7.63 (d, *j*= 8.4 Hz, 1H, quinoxaline-5-C***H***), 7.53 (t, *j*= 8.1 Hz, 1H, quinoxaline-6-C***H***), 7.47 (d, *j*= 7.5 Hz, 2H, benzyl-2-C***H***, benzyl-6-C***H***) , 7.38 (t, *j*= 7.6 Hz, 2H, benzyl-3-C***H***, benzyl-5-C***H***), 7.33 (m, 1H, benzyl-4-C***H***), 5.36 (s, 2H, CO_2***C***H_2). **^{13}C NMR (101 Hz, $CDCl_3$)**- δ 153.8 (***C***=O), 147.1 (quinoxaline-2-***C***), 142.7 (quinoxaline-3-***C***), 135.4 (benzyl-1-***C***), 134.4 (quinoxaline-8a-***C***), 132.4 (quinoxaline-4a-***C***), 128.8 (quinoxaline-5-***C***H), 128.7 (benzyl-4-***C***H), 128.6 (benzyl-3-***C***H, benzyl-5-***C***H), 128.4 (quinoxaline-6-***C***H), 127.7 (benzyl-2-***C***H, benzyl-3-***C***H), 126.8 (quinoxaline-7-***C***H), 116.5 (nitrile-***C***N, quinoxaline-8-***C***H), 77.4 (cyanoacetate-2-***C***), 67.3 (CO_2***C***H_2).

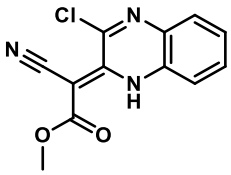

Methyl (*Z*)-2-(3-chloroquinoxalin-2(1*H*)-ylidene)-2-cyanoacetate (33i). 2,3-Dichloroquinoxaline (**26**) (100 mg, 0.5 mmol, 1.0 eq.), was reacted with methyl cyanoacetate (**32i**) (66.8 µL, 75 mg, 0. 76 mmol, 1.5 eq.), Cs_2CO_3 (821 mg, 2.5 mmol, 5.0 eq.) in DMF (5 mL) according to general procedure 1(b). The reaction was monitored by TLC conditions 1:5 EtOAc: cyclohexane. The crude material was extracted into EtOAc (100 mL) and washed with 2 M HCl (50 mL) and distilled water (150 mL). The aqueous phase was back extracted with an additional 100 mL EtOAc before the phases were separated and the organic combined, dried over $MgSO_4$, filtered and concentrated under reduced pressure. A 12 g silica column chromatography was conducted 20 %-30 % EtOAc in cyclohexane over 10 CVs, increased from 30-50 % over 9 CVs, then 50 -100 % over an additional 9 CVs. The desired fractions were combined and concentrated under reduced pressure to give the title compound as a yellow solid (119 mg, 91 %). R_f= 0.22 (1:5 EtOAc: cyclohexane). LC/MS m/z calculated for $C_{18}H_{13}ClN_3O_2$: $[M+H]^+$: 262.0, found: 262.1, t_R 2.73 min. **^{1}H NMR (400 Hz, $CDCl_3$)**- δ 14.45 (s, 1H, quinoxaline-1-N***H***), 7.82 (d, J= 8.17 Hz, 1H, quinoxaline-8-C***H***), 7.63 (t, J= 7.74 Hz, 1H, quinoxaline-6-C***H***), 7.47 (t, J= 8.26, 1H, quinoxaline-7-C***H***), 7.40 (d, J= 8.93 Hz, 1H, quinoxaline-5-C***H***), 3.93 (s, 3H, C***H***$_3$). **^{13}C NMR (101 Hz, $CDCl_3$)**- δ 169.5 (***C***=O), 145.9 (quinoxaline-2-***C***), 142.7 (quinoxaline-3-***C***),

133.6 (quinoxaline-8a-***C***), 131.9 (quinoxaline-4a-***C***), 128.1 (quinoxaline-5-***C***H), 127.4 (quinoxaline-7-***C***H), 126.4 (quinoxaline-6-***C***H), 117.42 (nitrile-***C***N), 116.6 (quinoxaline-8-***C***H), 66.8 (cyanoacetate-2-***C***), 52.1 (***C***H_3).

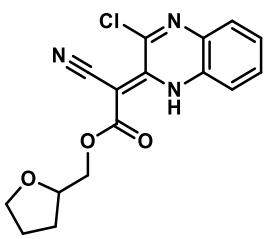

(Tetrahydrofuran-2-yl)methyl (*Z*)-2-(3-chloroquinoxalin-2(1*H*)-ylidene)-2-cyanoacetate (33n). 2,3-Dichloroquinoxaline (**26**) (103 mg, 0.52 mmol, 1.0 eq.) was reacted with tetrahydrofuran-2-yl)methyl 2-cyanoacetate (**32n**) (88 mg, 0.52 mmol, 1.0 eq.), CS_2CO_3 (876m g, 2.69 mmol, 5.2 eq.) in 6 mL DMF in accordance with general procedure 1(a). The reaction was monitored using TLC conditions 1:1 EtOAc: cyclohexane. The DMF was removed under high vacuum before the crude material was extracted into EtOAc (200 mL) washing with distilled water (200 mL), 2 M HCl (50 mL) and brine (20 mL). The phases were separated, dried over $MgSO_4$, filtered and concentrated under reduced pressure. The crude material was purified by column chromatography on 12g silica column 30-70 % EtOAc in cyclohexane over 12 CV. The desired fractions were combined and concentrated under reduced pressure to yield the title compound as a yellow solid (109 mg, 63 %). R_f= 0.26 (1:1 EtOAc: cyclohexane). LC/MS *m/z* calculated for $C_{16}H_{15}ClN_3O_3$: $[M+H]^+$: 332.1, found: 332.1, t_R 2.97 min. **^{1}H NMR (400 Hz, $CDCl_3$)**- *δ* 14.43 (broad s, 1H, quinoxaline-1-N***H***), 7.81 (d, *j*= 8.1 Hz, 1H, quinoxaline-8-C***H***), 7.62 (t, *j*= 7.7 Hz, 1H, quinoxaline-7-C***H***), 7.47 (t, *j*= 7.7 Hz, 1H, quinoxaline-6-C***H***), 7.39 (d, *j*= 8.2 Hz, 1H, quinoxaline-5-C***H***), 4.40 (dd, *j*= 11.2, 4.0 Hz, 1H, tetrahydrofuran-2-C***H***), 4.35-4.21 (m, 2H, CO_2C***H***$_2$), 3.96 (q, *j*= 6.3 Hz, 1H, 1x tetrahydrofuran-5-C***H***$_2$), 3.81 (q, *j*= 7.1 Hz, 1H, 1x tetrahydrofuran-5-C***H***$_2$) 2.13-1.81 (m, 4H, tetrahydrofuran-4-C***H***$_2$, tetrahydrofuran-3-C***H***$_2$). **^{13}C NMR (101 Hz, $CDCl_3$)**- *δ* 170.9 (***C***=O), 146.3 (quinoxaline-2-***C***), 143.9 (quinoxaline-3-***C***), 134.6 (quinoxaline-8a-***C***), 132.5 (quinoxaline-4a-***C***), 128.9 (quinoxaline-5-***C***H), 128.4 (quinoxaline-7-***C***H), 126.9 (quinoxaline-6-***C***H), 116.7 (nitrile-***C***N), 116.5 (quinoxaline-8-***C***H), 76.4 (tetrahydrofuran-2-***C***H), 69.5 (cyanoacetate-2-***C***H_2), 69.0 (CO_2***C***H_2), 67.5 (tetrahydrofuran-5-***C***H_2), 28.1 (tetrahydrofuran-3-***C***H_2), 26.0 (tetrahydrofuran-4-***C***H_2).

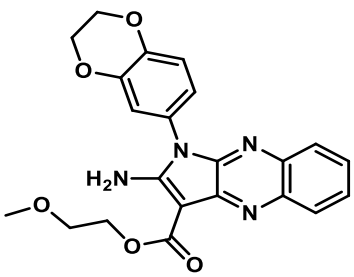

2-Methoxyethyl 2-amino-1-(2,3-dihydrobenzo[*b*][1,4]dioxin-6-yl)-1*H*-pyrrolo[2,3-*b*]quinoxaline-3-carboxylate (25f). 2,3-Dihydrobenzo(1,4)dioxane-6-amine (**29**) (100 mg, 0.65 mmol, 1.3 eq.) was reacted with 2-methoxyethyl 2-(3-chloroquinoxalin-2-yl)-2-cyanoacetate (**33a**) (155 mg, 0.5 mmol, 1.0 eq.) in accordance with general procedure 2 in EtOH (7.5 mL) and THF (2.5 mL). The reaction was monitored by TLC conditions 1% MeOH in DCM. The resulting crude material was first placed on a 25 g silica column chromatography 0-5 % MeOH in DCM over 13 CVs followed by 5-10 % MeOH over 5 CVs. The resulting desired fractions were combined and concentrated under reduced pressure- NMR determined impurities still present. The crude material was further purified by reverse phase column chromatography using a C18 110A column at a flow rate 15 mL/min, using the following gradients: A (95 %)/ B (5 %) to A (5 %)/B (95 %) over 15 CVs (A = H_2O containing HCOOH: 0.1 %; B = ACN). The desired fractions were combined and concentrated under reduced pressure to yield the title compound as a cream solid (25 mg, 12 %). R_f= 0.15 (1 % MeOH in DCM). LC/MS *m/z* calculated for $C_{22}H_{20}N_4O_5$: $[M+H]^+$: 421.1, found: 421.1, t_R 3.83 min (long run). HRMS (TOF ES^+) calculated: 421.1506 , found: 421.1504 **^{1}H NMR (400 Hz, DMSO-d_6)**- δ 7.90 (m, 3H, amine-N***H***$_2$, pyrroloquinoxaline-5-C***H***), 7.75 (d, *J*= 8.25 Hz, 1H, pyrroloquinoxaline-8-C***H***), 7.56 (t, *J*= 6.85 Hz, 1H, pyrroloquinoxaline-6-C***H***), 7.47 (t, *J*= 7.45, 1H, pyrroloquinoxaline-7-C***H***), 7.12 (m, 2H, enzodioxane-5-C***H***, benzodioxane-7-C***H***), 7.01 (dd, *J*= 8.53 Hz, 2.40 Hz, 1H, benzodioxane-8-C***H***), 4.42 (t, *J*= 4.72, 2H, CO_2C***H***$_2$), 4.35 (m, 4H, benzodioxane-2-C***H***$_2$ benzodioxane-3-C***H***$_2$), 3.70 (t, *J*= 3.97 Hz, 2H, C***H***$_2OCH_3$), 3.40 (s, 3H, C***H***$_3$). **^{13}C NMR (101 Hz, DMSO-d_6)**- δ 164.4 (***C***=O), 160.1 (pyrroloquinoxaline-8a-***C***), 144.4 (benzodioxane-4a-***C***), 143.9 (benzodioxane-8a-***C***), 143.3 (pyrroloquinoxaline-9a-***C***), 141.6 (pyrroloquinoxaline-3a-***C***), 140.6 (pyrroloquinoxaline-4a-***C***), 136.9 (benzodioxane-6-***C***), 127.6 (pyrroloquinoxaline-5-***C***H), 127.4 (pyrroloquinoxaline-8-***C***H), 126.4 (pyrroloquinoxaline-6-***C***H), 125.5 (pyrroloquinoxaline-7-***C***H), 124.8 (pyrroloquinoxaline-2-***C***), 121.9 (benzodioxane-8-***C***H), 118.46 (benzodioxane-7-***C***H), 118.41 (benzodioxane-5-***C***H), 80.7

(pyrroloquinoxaline-3-***C***), 70.3 (CO_2***C***H_2), 64.2 (benzodioxane-3-***C***H_2), 64.1 (benzodioxane-2-***C***H_2), 62.1 (***C***H_2OCH_3), 58.4 (***C***H_3).

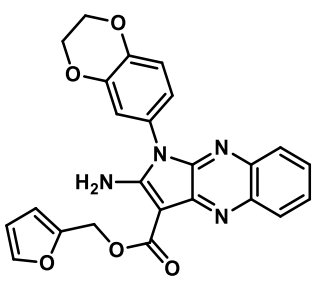

Furan-2-ylmethyl 2-amino-1-(2,3-dihydrobenzo[*b*][1,4]dioxin-6-yl)-1*H*-pyrrolo[2,3-*b*]quinoxaline-3-carboxylate (25g). 2,3-Dihydrobenzo(1,4)dioxin-6-amine (**29**) (114 mg, 0.76 mmol, 1.3 eq.) was reacted with furan-2-ylmethyl 2-(3-chloroquinoxalin-2-yl)-2-cyanoacetate (**33b**) (190 mg, 0.58 mmol, 1 eq.) according to general procedure 2 in EtOH (7.5 mL) and THF (2.5 mL). The reaction was monitored by TLC conditions 1:1 EtOAc: cyclohexane. A white solid precipitated out in the reaction mixture which was filtered under vacuum washing with cold MeOH to give a brown solid- NMR identified impurities present. The crude material was purified by reverse phase chromatography conducted using a C18 110A column at a flow rate 15 mL/min, using the following gradients: A (95 %)/ B (5 %) to A (5 %)/B (95 %) over 15 column volumes (A = H_2O containing HCOOH: 0.1 %; B = ACN). The desired fractions were combined and concentrated under reduced pressure to yield the title compound as a cream solid (82 mg, 32 %). R_f= 0.25 (1:1 EtOAc: cyclohexane). LC/MS *m/z* calculated for $C_{24}H_{19}N_4O_5$: $[M+H]^+$: 443.1, found: 443.1, t_R 2.55 min. HRMS (TOF ES^+) calculated: 443.1350, found: 443.1346. **^{1}H NMR (400 Hz, DMSO-d_6)**- δ 7.93 (m, 3H, amine-N***H***$_2$, pyrroloquinoxaline-5-C***H***), 7.74 (d, *J*= 8.14 Hz, 1H, pyrroloquinoxaline-8-C***H***), 7.69 (m, 1H, furan-5-C***H***), 7.55 (t, *J*= 7.45 Hz, 1H, pyrroloquinoxaline-6-C***H***), 7.47 (t, *J*= 7.98 Hz, 1H, pyrroloquinoxaline-7-C***H***), 7.10 (m, 2H, benzodioxane-7-C***H***, benzodioxane-5-C***H***), 7.00 (m, 1H, benzodioxane-8-C***H***), 6.60 (d, *J*= 3.31 Hz, 1H, furan-3-C***H***), 6.50 (m, 1H, furan-4-C***H***), 5.36 (s, 2H, CO_2C***H***$_2$), 4.11 (m, 4H, benzodioxane-3-C***H***$_2$, benzodioxane-2-C***H***$_2$). **^{13}C NMR (101 Hz, DMSO-d_6)**- δ 164.1 (***C***=O), 160.1 (pyrroloquinoxaline-8a-***C***), 150.4 (furan-2-***C***), 144.2 (benzodioxane-8a-***C***), 143.7 (benzodioxane-4a-***C***), 143.1 (furan-5-***C***H), 143.0 (pyrroloquinoxaline-9a-***C***), 141.2 (pyrroloquinoxaline-3a-***C***), 140.4 (pyrroloquinoxaline-4a-***C***), 136.7 (benzodioxane-6-***C***), 127.4 (pyrroloquinoxaline-5-***C***H), 127.2 (pyrroloquinoxaline-8-***C***H), 126.2 (pyrroloquinoxaline-6-***C***H), 125.4

(pyrroloquinoxaline-7-***C***H), 124.5 (pyrroloquinoxaline-2-***C***), 121.7 (benzodioxane-8-***C***H), 117.8 (benzodioxane-7-***C***H), 117.7 (benzodioxane-5-***C***H), 110.5 (furan-3-***C***H), 110.1 (furan-4-***C***H), 80.1 (pyrroloquinoxaline-3-***C***), 64.0 (benzodioxane-3-***C***H_2), 63.9 (benzodioxane-2-***C***H_2), 56.0 (CO_2***C***H_2).

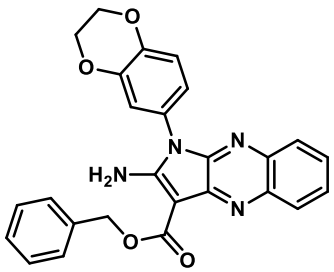

Benzyl 2-amino-1-(2,3-dihydrobenzo[*b*][1,4]dioxin-6-yl)-1*H*-pyrrolo[2,3-*b*]quinoxaline-3-carboxylate (25h). 2,3-Dihydrobenzo(1,4)dioxin-6-amine (**29**) (252 mg, 1.67 mmol, 1.3 eq.) was reacted with benzyl 2-(3-chloroquinoxalin-2-yl)-2-cyanoacetate (**33c**) (433 mg, 1.28 mmol, 1.0 eq.) in accordance with general procedure 2 in EtOH (15 mL) and THF (5 mL). The reaction was monitored by LCMS. White precipitate was formed in the reaction mixture which was filtered under vacuum and washed with cold MeOH, drying under vacuum overnight. A fluffy pale-yellow solid of the title compound (269 mg, 46 %) was obtained. LC/MS *m/z* calculated for $C_{26}H_{21}N_4O_4$: $[M+H]^+$: 453.2, found: 453.1, t_R 2.71 min. HRMS (TOF ES^+) calculated: 453.1557, found: 453.1554. **^{1}H NMR (400 Hz, DMSO-*d*$_6$)**- *δ* 7.95 (m, 3H, N***H***$_2$, pyrroloquinoxaline-5-C***H***), 7.76 (d, *J*= 7.36 Hz, 1H, pyrroloquinoxaline-8-C***H***), 7.62 (d, *J*= 7.13 Hz, 2H, benzyl-2-C***H***, benzyl-6-C***H***), 7.57 (t, *J*= 7.73 Hz, 1H, pyrroloquinoxaline-6-C***H***), 7.48 (t, *J*= 8.27 Hz, 1H, pyrroloquinoxaline-7-C***H***), 7.42 (t, *J*= 7.61 Hz, 2H, benzyl-3-C***H***, benzyl-5-C***H***), 7.32 (t, *J*= 7.39 Hz, 1H, benzyl-4-C***H***), 7.12 (m, 2H, benzodioxane-7-C***H***, benzodioxane-5-C***H***), 7.02 (d, *J*= 8.6, 1H, benzodioxane-8-C***H***), 5.43 (s, 2H, CO_2***C***H_2), 4.35 (m, 4H, benzodioxane-2-C***H***$_2$, benzodioxane-3-C***H***$_2$). **^{13}C NMR (101 Hz, DMSO-*d*$_6$)**- *δ* 164.6 (***C***=O), 160.3 (pyrroloquinoxaline-8a-***C***), 144.5 (benzodioxane-8a-***C***), 143.9 (benzodioxane-4a-***C***), 143.4 (pyrroloquinoxaline-9a-***C***), 141.6 (pyrroloquinoxaline-3a-***C***), 140.7 (pyrroloquinoxaline-4a-***C***), 137.6 (benzodioxane-6-***C***), 136.9 (benzyl-1-***C***), 128.3 (benzyl-2-***C***H, benzyl-6-***C***H), 127.7 (pyrroloquinoxaline-5-***C***H) , 127.48 (benzyl-4-***C***H) , 127.45 (pyrroloquinoxaline-8-***C***H) , 127.2 (benzyl-3-***C***H, benzyl-5-***C***H), 126.5 (pyrroloquinoxaline-6-***C***H) , 125.6 (pyrroloquinoxaline-7-***C***H), 124.8 (pyrroloquinoxaline-2-***C***), 121.9 (benzodioxane-8-***C***H), 118.0 (benzodioxane-7-***C***H), 117.9 (benzodioxane-5-***C***H), 80.7

(pyrroloquinoxaline-3-***C***), 64.2 (benzodioxane-3-***C***H_2), 64.1 (benzodioxane-2-***C***H_2), 63.9 (CO_2***C***H_2).

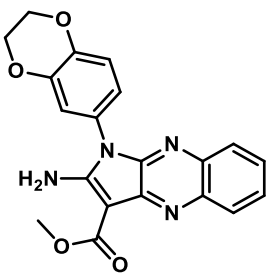

Methyl 2-amino-1-(2,3-dihydrobenzo[*b*][1,4]dioxin-6-yl)-1*H*-pyrrolo[2,3-*b*]quinoxaline-3-carboxylate (25i). 2,3-Dichlorobenzo(1,4)dioxin-6-amine (**29**) (90 mg, 0.59 mmol, 1.3 eq.) was reacted with methyl 2-(3-chloroquinoxalin-2-yl)-2-cyanoacetate (**33d**) (119 mg, 0.45 mmol, 1.0 eq.) in accordance with general procedure 2 in EtOH (13.5 mL) and THF (4.5 mL). The reaction was monitored by TLC conditions 0.5 % MeOH in DCM. To the crude material was added 5 mL MeOH which was sonicated and formed a cream precipitate which was filtered under vacuum and washed with cold MeOH (5 mL). A cream solid of the title compound (102 mg, 60%) was yielded. R_f= 0.3 (0.5 % MeOH in DCM). LC/MS *m/z* calculated for $C_{20}H_{16}N_4O_4$: $[M+H]^+$: 377.1, found: 377.1, t_R 3.54 (long run). HRMS (TOF ES^+) calculated: 377.1244, found: 377.1241. **^{1}H NMR (400 Hz, DMSO-*d*$_6$)**- δ 7.94 (m, 3H, amine-N***H***$_2$, pyrroloquinoxaline-5-C***H***), 7.75 (d, *J*= 8.16 Hz, 1H, pyrroloquinoxaline-8-C***H***), 7.56 (t, *J*= 7.52 Hz, 1H, pyrroloquinoxaline-6-C***H***), 7.47 (t, *J*= 7.89 Hz, 1H, pyrroloquinoxaline-7-C***H***), 7.11 (m, 2H, benzodioxane-7-C***H***, benzodioxane-5-C***H***), 7.01 (dd, *J*= 8.54, 2.39 Hz, 1H, benzodioxane-8-C***H***), 4.35 (m, 4H, benzodioxane-3-C***H***$_2$,benzodioxane-2-C***H***$_2$), 3.84 (s, 3H, C***H***$_3$). **^{13}C NMR (101 Hz, DMSO-*d*$_6$)**- δ 165.3 (***C***=O), 160.2 (pyrroloquinoxaline-8a-***C***), 144.4 (benzodioxane-8a-***C***), 143.9 (benzodioxane-4-***C***), 143.3 (pyrroloquinoxaline-9a-***C***), 141.4 (pyrroloquinoxaline-3a-***C***), 140.6 (pyrroloquinoxaline-4a-***C***), 136.9 (benzodioxane-6-***C***), 127.5 (pyrroloquinoxaline-5-***C***H), 127.4 (pyrroloquinoxaline-8-***C***H), 126.4 (pyrroloquinoxaline-6-***C***H), 125.5 (pyrroloquinoxaline-7-***C***H), 124.8 (pyrroloquinoxaline-2-***C***), 121.9 (benzodioxane-8-***C***H), 118.0 (benzodioxane-7-***C***H), 117.9 (benzodioxane-5-***C***H), 80.7 (pyrroloquinoxaline-3-***C***), 64.2 (benzodioxane-3-***C***H_2), 64.1 (benzodioxane-2-***C***H_2), 50.5 (***C***H_3).

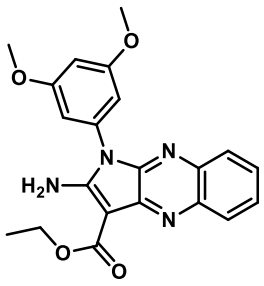

Ethyl 2-amino-1-(3,5-dimethoxyphenyl)-1*H*-pyrrolo[2,3-*b*]quinoxaline-3-carboxylate (25j). 3,5-Dimethoxyaniline (72 mg, 0.47 mmol, 1.3 eq.) was reacted with ethyl 2-(3-chloroquinoxalin-2-yl)-2-cyanoacetate (**28**) (100 mg, 0.3 mmol, 1.0 eq.) in accordance with general procedure 2 in EtOH (7.5 mL) and THF (2.5 mL). The reaction was monitored by TLC conditions 3:7 EtOAc: cyclohexane. The crude material was first purified on a 12 g silica column 0-5 % MeOH in DCM increasing in 1% increments for 4 CV each. Fractions combined and concentrated under reduced pressure, amine starting material was still present by NMR. The crude material was split onto two thin layer chromatography plates (silica gel, 20x20 cm, 2000 micron, Miles Scientific) and ran 3 times at 40 % EtOAc in cyclohexane, leaving the plate to dry between each run. The baseline band (5) silica was scraped and extracted using EtOAc before being filtered and concentrated under reduced pressure to give a pale-yellow solid of the title compound (47 mg, 33 %). R_f= 0.2 (3:7 EtOAc:cyclohexane). LC/MS *m/z* calculated for $C_{21}H_{21}N_4O_4$: $[M+H]^+$: 393.2, found: 393.1, t_R 4.18 min (long run). HRMS (TOF ES^+) calculated: 393.1557, found: 393.1550. **^{1}H NMR (400 Hz, DMSO-*d*$_6$)**- *δ* 7.95 (m, 3H, amine-N***H***$_2$, pyrroloquinoxaline-5-C***H***), 7.77 (d, *J*= 8.19, 1H, pyrroloquinoxaline-8-C***H***), 7.56 (t, *J*= 7.19 Hz, 1H, pyrroloquinoxaline-6-C***H***), 7.48 (t, *J*= 8.10, 1H, pyrroloquinoxaline-7-C***H***), 6.75 (m, 3H, phenyl-2-C***H***, phenyl-6-C***H***, phenyl-4-C***H***), 4.37 (q, *J*= 7.05, 2H, $CO_2C\boldsymbol{H}_2$), 3.81 (s, 6H, 3-OC***H***$_3$, 5-OC***H***$_3$), 1.36 (t, *J*= 7.02, 3H, C***H***$_3$). **^{13}C NMR (101 Hz, DMSO-*d*$_6$)**- *δ* 164.9 (***C***=O), 161.1 (pyrroloquinoxaline-8a-***C***), 159.8 (phenyl-3-***C***, phenyl-5-***C***), 142.9 (pyrroloquinoxaline-9a-***C***), 141.5 (pyrroloquinoxaline-3a-***C***), 140.6 (pyrroloquinoxaline-4a-***C***), 136.9 (phenyl-1-***C***), 133.7 (pyrroloquinoxaline-2-***C***), 127.6 (pyrroloquinoxaline-5-***C***H), 127.5 (pyrroloquinoxaline-8-***C***H), 126.5 (pyrroloquinoxaline-6-***C***H), 125.5 (pyrroloquinoxaline-7-***C***H), 107.1 (phenyl-2***C***H, phenyl-6-***C***H), 101.5 (phenyl-4-***C***H), 81.0 (pyrroloquinoxaline-3-***C***), 58.8 ($CO_2\boldsymbol{C}H_2$), 55.6 (3-O***C***H$_3$, 5-O***C***H$_3$) , 14.8 (***C***H$_3$).

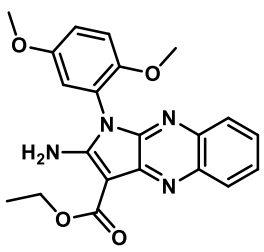

Ethyl 2-amino-1-(2,5-dimethoxyphenyl)-1*H*-pyrrolo[2,3-*b*]quinoxaline-3-carboxylate (25k). 2,5-Dimethoxyaniline (72 mg, 0.47 mmol, 1.3 eq.) was reacted with ethyl 2-(3-chloroquinoxalin-2-yl)-2-cyanoacetate (**28**) (100 mg, 0.3 mmol, 1.0 eq.) according to general procedure 2 in EtOH (7.5 mL) and THF (2.5 mL). The reaction was monitored using TLC conditions 1:1 EtOAc: cyclohexane. The crude material was purified on thin layer chromatography plates (silica gel, 20x20 cm, 2000 micron, Miles Scientific) and ran twice at 50 % EtOAc in cyclohexane, leaving the plate to dry between each run. The baseline band was scraped, and material extracted into EtOAc before filtering and concentrating under reduced pressure. This material then underwent MeOH recrystallization to produce a dark yellow solid of the title compound (50.5 mg, 35 %). R_F= 0.19 (1:1 EtOAc: cyclohexane). LC/MS *m/z* calculated for $C_{21}H_{21}N_4O_4$: $[M+H]^+$: 393.2, found: 393.1, t_R 3.89 min (long run). HRMS (TOF ES^+) calculated: 393.1557, found: 393.1555.**^{1}H NMR (400 Hz, DMSO-*d*$_6$)**- δ 7.93 (m, 3H, amine-N***H***$_2$, pyrroloquinoxaline-5-C***H***), 7.74 (d, *J*= 7.97, 1H, pyrroloquinoxaline-8-C***H***), 7.55 (t, *J*= 7.29 Hz, 1H, pyrroloquinoxaline-6-C***H***), 7.46 (t, *J*= 7.85, 1H, pyrroloquinoxaline-7-C***H***), 7.25 (d, *J*= 8.80 Hz, 1H, phenyl-3-C***H***), 7.18 (m, 2H, phenyl-4-C***H***, phenyl-6-C***H***), 4.36 (q, *J*= 7.03 Hz, 2H, $CO_2C\boldsymbol{H}_2$), 3.77 (s, 3H, 2-OC***H***$_3$), 3.66 (s, 3H, 5-OC***H***$_3$), 1.36 (t, *J*= 7.02 Hz, 3H, C***H***$_3$). **^{13}C NMR (101 Hz,(DMSO-*d*$_6$)**- δ 164.9 (***C***=O), 160.2 (pyrroloquinoxaline-8a-***C***), 153.4 (phenyl-5-***C***), 150.2 (phenyl-2-***C***), 143.1 (pyrroloquinoxaline-9a-***C***), 141.6 (pyrroloquinoxaline-3a-***C***), 140.6 (pyrroloquinoxaline-4a-***C***), 136.9 (phenyl-1-***C***), 127.6 (pyrroloquinoxaline-5-***C***H), 127.4 (pyrroloquinoxaline-8-***C***H), 126.4 (pyrroloquinoxaline-6-***C***H), 125.5 (pyrroloquinoxaline-7-***C***H), 120.6 (pyrroloquinoxaline-2-***C***), 116.7 (phenyl-6-***C***H), 116.5 (phenyl-4-***C***H), 114.0 (phenyl-3-***C***H), 80.9 (pyrroloquinoxaline-3-***C***), 58.8 ($CO_2\boldsymbol{C}H_2$), 56.2 (5-O***C***H_3), 55.7 (2-O***C***H_3), 14.9 (***C***H_3).

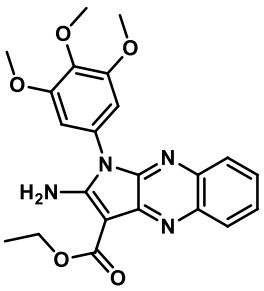

Ethyl 2-amino-1-(3,4,5-trimethoxyphenyl)-1*H*-pyrrolo[2,3-*b*]quinoxaline-3-carboxylate (25l). 3,4,4-Trimethoxyaniline (86 mg, 0.47 mmol, 1.3 eq.) was reacted with ethyl 2-(3-chloroquinoxalin-2-yl)-2-cyanoacetate (**28**) (100 mg, 0.3 mmol, 1.0 eq.) in accordance with general procedure 2 in EtOH (7.5 mL) and THF (2.5 mL). The reaction was monitored by LCMS. A cream solid precipitated upon cooling of the reaction mixture, this was filtered under vacuum washing with cold 3:1 EtOH:THF mixture to yield a pale-yellow solid of the title compound (110 mg, 72 %). LC/MS *m/z* calculated for $C_{22}H_{23}N_4O_5$: $[M+H]^+$: 423.2, found: 423.2, t_R 3.92 min (long run). HRMS (TOF ES^+) calculated: 423.1663, found: 423.1661. **^{1}H NMR (400 Hz, DMSO-d_6)**- δ 8.55 (s, 2H, amine-N***H***$_2$), 8.16 (d, *J*= 8.31 Hz, 1H, pyrroloquinoxaline-5-C***H***), 7.88 (d, *J*= 8.17 Hz, 1H, pyrroloquinoxaline-8-C***H***), 7.67 (t, *J*= 7.66 Hz, 1H, pyrroloquinoxaline-6-C***H***), 7.57 (t, *J*= 7.61 Hz, 1H, pyrroloquinoxaline-7-C***H***), 6.94 (s, 2H, phenyl-2-C***H***, phenyl-6-C***H***), 4.44 (q, *J*= 7.03, 2H, CO_2C***H***$_2$), 3.8 (s, 9H, 3-OC***H***$_3$, 4-OC***H***$_3$, -5-OC***H***$_3$), 1.38 (t, *J*= 7.01 Hz, 3H, C***H***$_3$). **^{13}C NMR (101 Hz, DMSO-d_6)**- δ 163.2 (***C***=O), 160.7 (pyrroloquinoxaline-8a-***C***), 153.7 (phenyl-3-***C***, phenyl-5-***C***), 146.1 (pyrroloquinoxaline-9a-***C***, pyrroloquinoxaline-3a-***C***), 138.5 (phenyl-4-***C***, pyrroloquinoxaline-4a-***C***), 135.0 (phenyl-1-***C***), 128.3 (pyrroloquinoxaline-6-***C***H), 127.0 (pyrroloquinoxaline-8-***C***H), 126.5 (pyrroloquinoxaline-7-***C***H), 122.4 (pyrroloquinoxaline-5-***C***, pyrroloquinoxaline-2-***C***), 106.8 (phenyl-2-***C***H, phenyl-6-***C***H), 82.5 (pyrroloquinoxaline-3-***C***), 60.6 (4-O***C***H_3), 59.8 (CO_2***C***H_2), 56.2 (3-O***C***H_3, 5-O***C***H_3), 14.8 (***C***H_3).

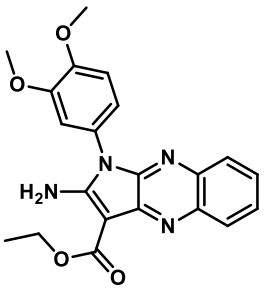

Ethyl 2-amino-1-(3,4-dimethoxyphenyl)-1*H*-pyrrolo[2,3-*b*]quinoxaline-3-carboxylate (25m). 3,4-Dimethoxyaniline (72 mg, 0.47 mmol, 1.3 eq.) is reacted with ethyl 2-(3-chloroquinoxalin-2-yl)-2-cyanoacetate (**28**) (100 mg, 0.3 mmol, 1.0 eq.) in accordance with general procedure 2 in EtOH (7.5 mL) and THF (2.5 mL). The reaction was monitored by LCMS. Upon cooling the reaction mixture contained a white solid suspension crashed out which was filtered

under vacuum washing with a cold 3:1 EtOH:THF mixture to yield a white solid of the title compound (36 mg, 25 %). LC/MS *m/z* calculated for $C_{21}H_{21}N_4O_4$: $[M+H]^+$: 393.2, found: 393.1, t_R 3.63 min (long run). HRMS (TOF ES^+) calculated: 393.1557, found: 393.1551. **^{1}H NMR (400 Hz, DMSO-*d*$_6$)**- δ 7.93 (m, 3H, amine-N***H***$_2$, pyrroloquinoxaline-5-C***H***), 7.74 (d, *J*= 8.20, 1H, pyrroloquinoxaline-8-C***H***), 7.56 (t, *J*= 7.02 Hz, 1H, pyrroloquinoxaline-6-C***H***), 7.47 (t, *J*= 7.72 Hz, 1H, pyrroloquinoxaline-7-C***H***), 7.19 (m, 2H, phenyl-5-C***H***, phenyl-2-C***H***), 7.10 (d, *J*= 8.3 Hz, 1H, phenyl-6-C***H***), 4.37 (q, *J*= 7.04 Hz, 2H, CO_2C***H***$_2$), 3.88 (s, 3H, 3-OC***H***$_3$), 3.78 (s, 3H, 4-OC***H***$_3$), 1.36 (t, *J*= 7.00 Hz, 3H, C***H***$_3$). **^{13}C NMR (101 Hz, DMSO-*d*$_6$)**- δ 164.9 (***C***=O), 160.2 (pyrroloquinoxaline-8a-***C***), 149.6 (phenyl-3-***C***), 149.4 (phenyl-4-***C***), 143.3 (pyrroloquinoxaline-9a-***C***), 141.5 (pyrroloquinoxaline-3a-***C***), 140.6 (pyrroloquinoxaline-4a-***C***), 136.9 (phenyl-1-***C***), 127.6 (pyrroloquinoxaline-5-***C***H), 127.5 (pyrroloquinoxaline-8-***C***H), 126.4 (pyrroloquinoxaline-6-***C***H), 125.5 (pyrroloquinoxaline-7-***C***H), 124.4 (pyrroloquinoxaline-2-***C***), 121.4 (phenyl-6-***C***H), 112.5 (phenyl-5-***C***H), 112.2 (phenyl-2-***C***H), 80.3 (pyrroloquinoxaline-3-***C***), 58.8 (CO_2***C***H_2), 55.7 (3-O***C***H_3, 4-O***C***H_3), 14.9 (***C***H_3).

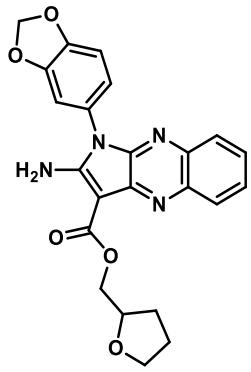

Tetrahydrofuran-2-yl)methyl 2-amino-1-(benzo[*d*][1,3]dioxol-5-yl)-1*H*-pyrrolo[2,3-*b*]quinoxaline-3-carboxylate (25n). 3,4-(Methylenedioxy)aniline (61 mg, 0.44 mmol, 1.3 eq.) was reacted with (tetrahydrofuran-2-yl)methyl (*Z*)-2-(3-chloroquinoxalin-2(1*H*)-ylidene)-2-cyanoacetate (**33n**) (109 mg, 0.33 mmol, 1.0 eq.) in 9 mL EtOH and 3 mL THF in accordance with general procedure 2. The reaction was monitored by TLC conditions 3:7 EtOAc: cyclohexane. The solvent was removed under reduced pressure before the crude material was purified on a 12 g silica column 20-100 % EtOAc in cyclohexane over 10 CV. Fractions were combined and concentrated under reduced pressure to produce impure material as a pale pink solid. This was further purified by reverse phase column chromatography on 12 g C18 column 5-95 % Acetonitrile in water over 12 CV. The desired fractions were combined and concentrated under reduced pressure to yield a white solid of the title compound (22 mg, 15 %). R_f= 0.37 (3:7 EtOAc: cyclohexane).

LC/MS *m/z* calculated for $C_{23}H_{21}N_4O_5$: $[M+H]^+$: 433.1, found: 433.0, t_R 4.48 min. HRMS (TOF ES^+) calculated: 433.1506, found: 433.1501.**^{1}H NMR (400 Hz, $CDCl_3$)**- *δ* 7.90 (m, 3H, amine-N***H***$_2$, pyrroloquinoxaline-5-C***H***), 7.76 (d, *j*= 7.9 Hz, 1H, pyrroloquinoxaline-8-C***H***), 7.56 (t, *j*= 7.1 Hz, 1H, pyrroloquinoxaline-6-C***H***), 7.48 (t, *j*= 7.7 Hz, 1H, pyrroloquinoxaline-7-C***H***), 7.19 (s, 1H, benzodioxane-4-C***H***), 7.15 (d, *j*= 8.1 Hz, 1H, benzodioxane-6-C***H***), 7.04 (d, *j*= 8.3 Hz, 1H, benzodioxane-7-C***H***), 6.19 (s, 2H, benzodioxane-2-C***H***$_2$), 4.36-4.18 (m, 3H, CO_2C***H***$_2$, tetrahydrofuran-2-C***H***), 3.95 (q, *j*= 7.0 Hz, 1H, 1x tetrahydrofuran-5-C***H***$_2$), 3.70 (q, *j*= 7.0 Hz, 1H, 1x tetrahydrofuran-5-C***H***$_2$), 2.20-1.78 (m, 4H, tetrahydrofuran-4-C***H***$_2$, tetrahydrofuran-3-C***H***$_2$). **^{13}C NMR (101 Hz, $CDCl_3$)**- *δ* 163.9 (***C***=O), 159.6 (pyrroloquinoxaline-8a-***C***), 147.6 (benzodioxane-7a-***C***), 147.5 (benzodioxane-3a-***C***), 142.7 (pyrroloquinoxaline-9a-***C***), 141.0 (pyrroloquinoxaline-3a-***C***), 140.1 (pyrroloquinoxaline-4a-***C***), 136.3 (benzodioxane-5-***C***), 126.9 (pyrroloquinoxaline-5-***C***H), 126.8 (pyrroloquinoxaline-8-***C***H), 125.8 (pyrroloquinoxaline-6-***C***H), 124.9 (pyrroloquinoxaline-7-***C***H), 124.8 (pyrroloquinoxaline-2-***C***), 122.4 (benzodioxane-7-***C***H), 109.3 (benzodioxane-6-***C***H), 108.3 (benzodioxane-4-***C***H), 101.4 (benzodioxane-2-***C***H_2), 80.1 (pyrroloquinoxaline-3-***C***), 75.6 (tetrahydrofuran-2-***C***H), 67.1 (tetrahydrofuran-5-***C***H_2), 64.3 (CO_2***C***H_2), 26.9 (tetrahydrofuran-3-***C***H_2), 24.9 (tetrahydrofuran-4-***C***H_2).

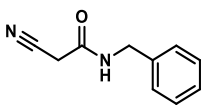

***N*-Benzyl-2-cyanoacetamide (35). Conducted by student Fook Looeng Lai. Method a)** To a solution of 2-cyanoacetic acid (**31**) (100 mg, 1.18 mmol, 1.0 eq.) and benzyl amine (**34**) (151 mg, 1.41 mmol, 1.2 eq.) in DCM (2 mL), was added a solution of DMAP (14 mg, 0.18 mmol, 0.1 eq.) and EDC (200 mg, 1.29 mmol, 1.1 eq.) in DCM (2 mL). The reaction mixture was left to stir at rt for 48 h, colour change to pale yellow, before TLC confirmed reaction completion staining with $KMnO_4$, R_f= 0.39 in MeOH/DCM 2:98. Additional DCM (28 mL) was added before washing with 2 M aqueous HCl (30 mL) and distilled water (3 x 20 mL). The organic was separated, dried over $MgSO_4$, filtered and concentrated under reduced pressure. The crude material was then purified by column chromatography on a 25 g flash silica gel 60 column at a flow rate 15 mL/min, using the following gradients: A (30 %)/ B (70 %) to A

(50 %)/ B (50 %) over 5 CVs, followed by A (50 %)/B (50 %) for 8 CVs before increasing to A (80 %)/B (20 %) over 2 CVs. (A= EtOAc, B= Cyclohexane). The fractions containing product were combined and concentrated under reduced pressure to yield **35** as a cream solid (47 mg, 23 %). R_F= 0.4 (1:1 EtOAc: cyclohexane). **Method b)** Methylcyanoacetate (**32d**) (200 mg, 2.06 mmol, 1.0 eq.) and benzyl amine (**34**) (242 mg, 2.26 mmol, 1.0 eq.) were stirred for 3 h to form a cloudy yellow solid. The solid was filtered and dried under vacuum washing with cold diethyl ether to remove excess amine. The resulting solid was recrystallised using hot EtOAc and filtered to yield white solid of **35** (125 mg, 35 %). LC/MS *m/z* calculated for $C_{10}H_{11}N_2O$: $[M+H]^+$: 175.1, found: 175.0, t_R 2.15 min. **^{1}H NMR (400 Hz, DMSO-*d*$_6$)**- *δ* 8.71 (s, 1H, amide-N***H***), δ 7.38-7.22 (m, 5H, benzyl-2-C***H***, benzyl-3-C***H***, benzyl-4-C***H***, benzyl-5-C***H***, benzyl-6-C***H***), δ 4.29 (d, *J*= 5.8 Hz, 2H, benzyl-C***H***$_2$), δ 3.70 (s, 2H, cyanoacetamide-2-C***H***$_2$). **^{13}C NMR (101 Hz, DMSO-*d*$_6$)-** *δ* 161.9 (***C***=O), 138.4 (benzyl-1-***C***), 128.2 (benzyl-3-***C***H, benzyl-5-***C***H), 127.2 (benzyl-2-***C***H, benzyl-6-***C***H), 126.8 (benzyl-4-***C***H), 115.9 (nitrile-***C***N), 42.4 (N***C***H$_2$), 25.1 (cyanoacetamide-2-***C***H$_2$).

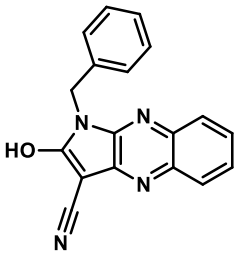

1-Benzyl-2-hydroxy-1*H*-pyrrolo[2,3-*b*]quinoxaline-3-carbonitrile (37). Conducted by student Fook Looeng Lai. The title compound was obtained by reacting 2,3-dichloroquinoxaline (**26**) (18 mg, 0.09 mmol, 1.0 eq.) with *N*-benzyl-2-cyanoacetamide (**35**) (20 mg, 0.11 mmol, 1.5 eq.) according to general procedure 1. The reaction was monitored by LCMS. The resulting material was purified using prep TLC plate in 1 M MeOH-NH_3/DCM 1:99 ran three times (R_f=0.52). The band of silica containing product was removed and extracted using MeOH/ DCM 5:95 before filtering yielded cream solid **37** (12 mg, 42 %). LC/MS *m/z* calculated for $C_{18}H_{13}N_4O$: $[M+H]^+$: 301.1, found: 301.0, t_R 2.84 min. HRMS (TOF ES$^+$) calculated: 301.1084, found: 301.1077.**^{1}H NMR (400 Hz, DMSO-*d*$_6$)**- *δ* 10.64 (s, 1H, alcohol-O***H***), 7.94 (d, *J* = 8.2 Hz, 1H, pyrroloquinoxaline-8-C***H***), 7.88 (d, *J* = 8.1 Hz, 1H, pyrroloquinoxaline-5-C***H***), 7.73-7.64 (t, *J* = 7.84 Hz, 1H, pyrroloquinoxaline-7-C***H***), 7.60 (t, *J* = 7.6 Hz, 1H, pyrroloquinoxaline-6-C***H***), 7.49-7.37 (m, 4 H, benzyl-2-C***H***, benzyl-6-C***H***, benzyl-3-C***H***, benzyl-5-C***H***), 7.33 (dd, *J* = 8.3, 6.1

Hz, 1H, benzyl-4-C***H***), 4.78 (s, 2H, benzyl-CH_2).**^{13}C NMR (101 Hz, DMSO-*d*$_6$)**- *δ* 166.8 (pyrroloquinoxaline-2-***C***), 151.3 (pyrroloquinoxaline-8a-***C***), 145.1 (pyrroloquinoxaline-9a-***C***), 141.8 (pyrroloquinoxaline-3a-***C***), 137.5 (pyrroloquinoxaline-4a-***C***), 136.8 (benzyl-1-***C***), 129.2 (pyrroloquinoxaline-5-***C***H), 128.8 (pyrroloquinoxaline-8-***C***H), 128.5 (pyrroloquinoxaline-6-***C***H), 128.2 (pyrroloquinoxaline-7-***C***H), 128.1 (benzyl-3-***C***H, benzyl-5-***C***H), 127.5 (benzyl-2-***C***H, benzyl-6-***C***H), 127.1 (benzyl-4-***C***H), 114.2 (nitrile-***C***N), 64.3 (pyrroloquinoxaline-3-***C***), 46.5 (N***C***H_2).

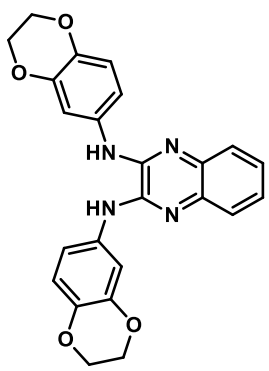

N*^{2},*N*^{3}-Bis(2,3-dihydrobenzo[*b*][1,4]dioxin-6-yl)quinoxaline-2,3-diamine (39). Conducted by student Fook Looeng Lai.** To a microwave vial was added 2,3-dichloroquinoxaline (**26**) (100mg, 0.51 mmol, 1.0 eq.) and 2,3-dihydrobenzo(1,4)dioxin-6-amine (**29**) (114 mg, 0.758 mmol, 1.5 eq.) in EtOH (3.5 mL) and ran in the microwave for 2 h at 100 °C with high stirring. TLC confirmed starting material was still present so the reaction was put back on for an additional 1 h at 110 °C with high stirring. TLC confirmed reaction completion with formation of a yellow precipitate (R_f= 0.56, 2:8 EtOAc: cyclohexane). The resulting solid was isolated and dried by vacuum filtration washing with cold acetone (100 mL) to give a pale-yellow solid of **39** (50 mg, 23 %). LC/MS *m/z* calculated for $C_{24}H_{21}N_4O_4$: $[M+H]^+$: 429.2, found: 429.0, t_R 6.30 min (long run). HRMS (TOF ES$^+$) calculated: 429.1557, found: 429.1545. **^{1}H NMR (400 Hz, DMSO-*d*$_6$)**- *δ* 9.12 (s, 2H, 2x amine-NH***), 7.58 (s, 2H, 2x benzodioxane-7-C***H***), 7.49 (dd, J = 6.1, 3.5 Hz, 2H, quinoxaline-5-C***H***, quinoxaline-8-C***H***), 7.33-7.22 (m, 4H, 2x benzodioxane-8-C***H***, 2x benzodioxane-5-C***H***), 6.89 (d, J = 8.8 Hz, 2H, quinoxaline-7-C***H***, quinoxaline-6-C***H***), 4.26 (td, J = 5.3, 2.7 Hz, 8H, 2x benzodioxane-2-CH_2, 2x benzodioxane-3-CH_2). **^{13}C NMR (101 Hz, DMSO-*d*$_6$)**- *δ* 164.0 (quinoxaline-2-***C***, quinoxaline-3-***C***), 143.2 (2x benzodioxane-4a-***C***), 141.5 (2x benzodioxane-8a-***C***), 140.4 (2x benzodioxane-6-***C***), 131.9 (quinoxaline-4a-***C***, quinoxaline-8a-***C***), 125.6 (quinoxaline-5-***C***H, quinoxaline-8-***C***H, quinoxaline-6-***C***H, quinoxaline-7-***C***H), 117.1 (2x benzodioxane-7-***C***H), 115.4 (2x benzodioxane-8-***C***H),

111.2 (2x benzodioxane-5-***C***H), 64.2 (2x benzodioxane-3-***C***H_2), 64.1 (2x benzodioxane-2-***C***H_2).

8.1.3 Series 2 experimental

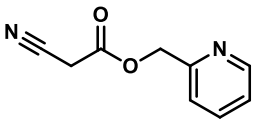

Pyridin-2-ylmethyl 2-cyanoacetate (41a). Conducted by student Sam Robinson. 2-Cyanoacetic acid (**31**) (200 mg, 2.35 mmol, 1.0 eq.) was reacted with pyridin-2-ylmethanol (257 mg, 2.35 mmol, 1.0 eq.), DCC (485 mg, 12.35 mmol, 1.0 eq.) and DMAP (29 mg, 0.24 mmol, 0.1 eq.) in DCM 4 mL according to general procedure 4. The reaction mixture was monitored using TLC conditions 3:1 EtOAc: cyclohexane. The crude material was purified by column chromatography on a 25 g silica column using solvent conditions 50-75 % EtOAc in cyclohexane over 10 CVs. The desired fractions were combined and concentrated under reduced pressure to yield the title compounds as a white solid (178 mg, 43 %). R_f = 0.43 (3:1 EtOAc: cyclohexane). **^{1}H NMR (400 Hz, $CDCl_3$)**- δ 8.61 (d, *J*= 4.83, 1H, pyridine-6-C***H***), 7.74 (t, *J*= 7.68, 1H, pyridine-4-C***H***), 7.39 (d, *J*= 7.79, 1H, pyridine-3-C***H***), 7.28 (m, 1H, pyridine-5-C***H***), 5.34 (s, 2H, CO_2C***H***$_2$), 3.58 (s, 2H, cyanoacetate-2-C***H***$_2$). **^{13}C NMR (101 Hz, $CDCl_3$)**- δ 162.8 (***C***=O), 154.2 (pyridine-2-***C***), 149.8 (pyridine-6-***C***H), 137.1 (pyridine-4-***C***H), 123.5 (pyridine-3-***C***H), 122.2 (pyridine-5-***C***H), 112.9 (nitrile-***C***N), 68.8 (CO_2***C***H_2), 24.9 (cyanoacetate-2-***C***H_2).

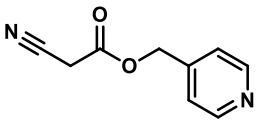

Pyridin-4-ylmethyl 2-cyanoacetate (41c). 2-Cyanoacetic acid (**31**) (150 mg, 1.76 mmol, 1.0 eq.) was reacted with pyridin-4-ylmethanol (211 mg, 1.93 mmol, 1.1 eq.), DCC (364 mg, 1.76 mmol, 1.0 eq.) and DMAP (22 mg, 0.18 mmol, 0.1 eq.) in DCM 5 mL according to general procedure 4. The reaction mixture was monitored by TLC using solvent conditions 3:97 MeOH:DCM. A colour change from colourless to light brown was observed and a white precipitate formed. The crude material was purified by column chromatography using a 12 g silica column and solvent system 1-5 % MeOH in DCM over 12 CVs. The desired fractions were combined and concentrated under reduced pressure to give the title compound as a white solid (113 mg, 36 %). R_f = 0.36 (3:97 MeOH: DCM). LC/MS *m/z* calculated for $C_9H_9N_2O_2$ $[M+H]^+$:177.1, found: 176.9, t_R 0.35 min. **^{1}H NMR (400 Hz,**

$CDCl_3$)- *δ* 8.64 (m, 2H, pyridine-2-C***H***, pyridine-6-C***H***), 7.27 (m, 2H, 2x pyridine-3-C***H***, pyridine-5-C***H***), 5.24 (s, 2H, CO_2CH_2), 3.56 (s, 2H, cyanoacetate-2-CH_2). **^{13}C NMR (101 Hz, $CDCl_3$)**- *δ* 163.0 (***C***=O), 150.8 (pyridine-2-***C***H, pyridine-6-C***H***), 143.5 (pyridine-4-***C***), 122.4 (pyridine-3-***C***H, pyridine-5-***C***H), 112. 9 (nitrile-***C***N), 66.8 (CO_2CH_2), 25.1 (cyanoacetate-2-CH_2).

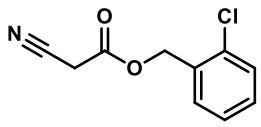

2-Chlorobenzyl 2-cyanoacetate (41d). Conducted by student Ng Yu Yang. 2-Cyanoacetic acid (**31**) (200 mg, 2.35 mmol, 1.0 eq.) was reacted with 2-chlorobenzyl alcohol (335 mg, 2.35 mmol, 1.0 eq.), DCC (485 mg, 2.35 mmol, 1.0 eq.) and DMAP (29 mg, 0.24 mmol, 0.1 eq.) in DCM 4 mL according to general procedure 4. The reaction was monitored using TLC conditions 99:1 chloroform: cyclohexane). The crude material was purified by column chromatography on a 40 g silica column using solvent conditions 99:1 chloroform: cyclohexane over 8 CV. The desired fractions were combined and concentrated under reduced pressure to yield the title compound as a colourless oil (258 mg, 52 %). R_f = 0.31 (99:1 chloroform: cyclohexane). **^{1}H NMR (400 Hz, $CDCl_3$)**- *δ* 7.43 (m, 2H, benzyl-3-C***H***, benzyl-4-C***H***), 7.31 (m, 2H, benzyl-5-C***H***, benzyl-6-C***H***), 5.34 (s, 2H, CO_2CH_2), 3.53 (s, 2H, cyanoacete-2-CH_2). **^{13}C NMR (101 Hz, $CDCl_3$)**- *δ* 162.8 (***C***=O), 134.2 (benzyl-1-***C***), 132.2 (benzyl-2-***C***), 130.5 (benzyl-3-***C***H), 130.4 (benzyl-4-***C***H), 129.9 (benzyl-6-***C***H), 127.2 (benzyl-5-***C***H), 112.9 (nitrile-***C***N), 66.0 (CO_2CH_2), 24.8 (cyanoacetate-2-CH_2).

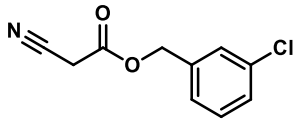

3-Chlorobenzyl 2-cyanoacetate (41e). Conducted by student Ng Yu Yang. 2-Cyanoacetic acid (**31**) (200 mg, 2.35 mmol, 1.0 eq.) was reacted with 3-chlorobenzyl alcohol (335 mg, 2.35 mmol, 1.0 eq.), DCC (485 mg, 2.35 mmol, 1.0 eq.) and DMAP (29 mg, 0.24 mmol, 0.1 eq.) in DCM 4 mL according to general procedure 4. The reaction was monitored by TLC conditions 99:1 chloroform: cyclohexane. The crude material was purified by column chromatography on a 40 g silica column using solvent conditions 99:1 chloroform: cyclohexane over 8 CV. The desired fractions were combined and concentrated under reduced pressure to yield the title compound as a colourless oil (274 mg, 56 %). R_f = 0.30 (99:1 chloroform: cyclohexane). **^{1}H NMR (400 Hz, $CDCl_3$)**- *δ* 7.37-7.24 (m, 4H,

benzyl-2-C***H***, benzyl-4-C***H***, benzyl-5-C***H***, benzyl-6-C***H***), 5.20 (s, 2H, $CO_2C\boldsymbol{H}_2$), 3.51 (s, 2H, cyanoacetate-2-$C\boldsymbol{H}_2$). **^{13}C NMR (101 Hz, $CDCl_3$)**- *δ* 163.1 (***C***=O), 136.7 (benzyl-3-***C***), 130.6 (benzyl-5-***C***H), 129.6 (benzyl-4-***C***H), 129.0 (benzyl-2-***C***H), 127.0 (benzyl-6-***C***H), 113.1 (nitrile-***C***N), 68.0 ($CO_2\boldsymbol{C}H_2$), 25.2 (cyanoacetate-2-$\boldsymbol{C}H_2$).

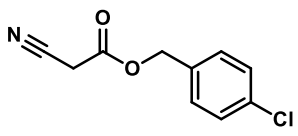

4-Chlorobenzyl 2-cyanoacetate (41f). Conducted by student Bulbul Singh. 2-Cyanoacetic acid (**31**) (250 mg, 2.94 mmol, 1.0 eq.) was reacted with 4-chlorobenzyl alcohol (455 mg, 2.94 mmol, 1.0 eq.), DCC (598 mg, 2.94 mmol, 1.0 eq.) and DMAP (35 mg, 0.29 mmol, 0.1 eq.) in DCM 5 mL according to general procedure 4. The reaction was monitored using TLC conditions 1:4 diethyl ether: cyclohexane. The crude material was purified by column chromatography on a 40 g silica column using solvent conditions 20 % diethyl ether in cyclohexane over 10 CV. The desired fractions were combined and concentrated under reduced pressure to give the title compound as a colourless oil (299 mg, 48 %). R_f = 0.35 (1:4 diethyl ether: cyclohexane). LC/MS *m/z* calculated for $C_{10}H_9ClNO_2$ $[M+H]^+$:209.0, found: 100.9 (fragment $C_4H_4NO_2$), t_R 3.09 min. **^{1}H NMR (400 Hz, $CDCl_3$)**- *δ* 7.36 (d, *j*= 8.2 Hz, 2H, benzyl-3-C***H***, Benzyl-5-C***H***), 7.31 (d, *j*= 8.4 Hz, 2H, benzyl-2-C***H***, benzyl-6-C***H***), 5.20 (s, 2H, $CO_2C\boldsymbol{H}_2$), 3.49 (s, 2H, cyanoacetate-2-$C\boldsymbol{H}_2$). **^{13}C NMR (101 Hz, $CDCl_3$)**- *δ* 167.5 (***C***=O), 132.3 (benzyl-1-***C***), 130.75 (benzyl-4-***C***), 129.0 (benzyl-3-**C**H, benzyl-5-***C***H), 128.7 (benzyl-2-***C***H, benzyl-6-***C***H), 116.4 (nitrile-***C***N), 66.3 ($CO_2\boldsymbol{C}H_2$), 29.1 (cyanoacetate-2-$\boldsymbol{C}H_2$).

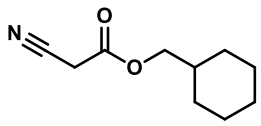

Cyclohexylmethyl 2-cyanoacetate (41g). 2-Cyanoacetic acid (**31**) (165 mg, 1.94 mmol, 1.1 eq.) was reacted with cyclohexylmethanol (201 mg, 1.76 mmol, 1.0 eq.), DCC (364 mg, 1.76 mmol, 1.0 eq.) and DMAP (22 mg, 0.17 mmol, 0.1 eq.) in DCM 5 mL according to general procedure 4. The reaction was monitored using TLC conditions 1:4 EtOAc: cyclohexane staining with bromocresol green and phosphomolybdic acid (PMA). The resulting crude material was purified by column chromatography on a 12 g silica column using solvent conditions 0-30 % EtOAc in cyclohexane over 13 CV. The desired fractions were combined and concentrated under reduced pressure to give a colourless oil of the title compound (100

mg, 31 %). R_f = 0.33 (1:4 EtOAc: cyclohexane). **^{1}H NMR (400 Hz, $CDCl_3$)**- δ 4.02 (d, *j*= 6.3 Hz, 2H, CO_2CH_2), 3.45 (s, 2H, cyanoacetate-2-CH_2), 1.81-1.62 (m, 6H, cyclohexane-3-CH_2, cyclohexane-5-CH_2, cyclohexane-4-CH_2), 1.34-1.10 (m, 3H, cyclohexane-1-C***H***, 1 x cyclohexane-2-CH_2, 1x cyclohexane-9-CH_2) 1.06-0.91 (m, 2H, 1 x cyclohexane-2-CH_2, 1x cyclohexane-9-CH_2) **^{13}C NMR (101 Hz, $CDCl_3$)**- δ 163.4 (***C***=O), 113.5 (nitrile-***C***N), 72.4 (CO_2***C***H_2), 37.3 (cyclohexane-1-***C***H), 29.9 (cyclohexane-2-***C***H_2, cyclohexane-6-***C***H_2), 26.7 (cyclohexane-4-***C***H_2), 26.0 (cyclohexane-3-***C***H_2,cyclohexane-5-***C***H_2), 25.2 (cyanoacetate-2-***C***H_2).

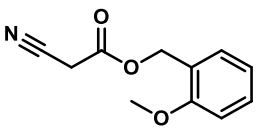

2-Methoxybenzyl 2-cyanoacetate (41h). Conducted by student Bulbul Singh. 2-Cyanoacetic acid (**31**) (500 mg, 5.8 mmol, 1.0 eq.) was reacted with 3-methoxybenzylalcohol (736 mg, 5.8 mmol, 1.0 eq.), DCC (1.213 g, 5.8 mmol, 1.0 eq.) and DMAP (72 mg, 0.58 mmol, 0.1 eq.) in DCM 5 mL according to general procedure 4. The reaction was monitored using TLC solvent conditions 100 % chloroform. The crude material was purified by column chromatography on a 80 g silica column using solvent conditions 100 % chloroform over 10 CV. The desired fractions were combined and concentrated under reduced pressure to yield a colourless oil of the title compound (207 mg, 17 %). R_f = 0.20 (100 % chloroform). LC/MS *m/z* calculated for $C_{11}H_{12}NO_3$: $[M+H]^+$: 206.2, found: 206.4, t_R 2.77 min.**^{1}H NMR (400 Hz, $CDCl_3$)**- δ 7.39-7.30 (m, 2H, benzyl-5-C***H***, benzyl-6-***H***), 6.96 (t, *j*= 7.5 Hz, 1H, benzyl-4-C***H***), 6.91 (d, *j*= 8.2 Hz, 1H, benyl-3-C***H***), 5.28 (s, 2H, CO_2CH_2), 3.85 (s, 3H, OCH_3), 3.48 (s, 2H, cyanoacetate-2-CH_2).**^{13}C NMR (101 Hz, $CDCl_3$)**- δ 163.3 (***C***=O), 158.2 (benzyl-2-***C***), 130.9 (benzyl-6-***C***H, benzyl-3-***C***H), 123.1 (benzyl-4-***C***H), 121.0 (benzyl-1-***C***), 113.4 (nitrile-***C***N), 111.1 (benzyl-5-***C***H), 64.7 (CO_2***C***H_2), 55.9 (O***C***H_3), 25.3 (cyanoacetate-2-***C***H_2).

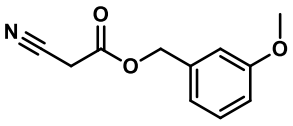

3-Methoxybenzyl 2-cyanoacetate (41i). Conducted by student Bulbul Singh. 2-Cyanoacetic acid (**31**) (500 mg, 5.8 mmol, 1.0 eq.) was reacted with 3-methoxybenzylalcohol (736 mg, 5.8 mmol, 1.0 eq.), DCC (1.213 g, 5.8 mmol, 1.0 eq.) and DMAP (72 mg, 0.58 mmol, 0.1 eq.) in DCM 5 mL according to general procedure 4. The reaction was monitored

using TLC conditions 1:4 EtOAc: cyclohexane). The crude material was purified by column chromatography on a 80 g silica column using solvent system 20 % EtOAc in cyclohexane over 10 CV. The desired fractions were combined and concentrated under reduced pressure to yield the title compound as a colourless oil (250 mg, 21 %). R_f = 0.29 (1:4 EtOAc: cyclohexane). LC/MS *m/z* calculated for $C_{11}H_{12}NO_3$: $[M+H]^+$: 206.2, found: 206.5, t_R 2.64 min. **^{1}H NMR (400 Hz, $CDCl_3$)**- δ 7.64 (m, 2H, benzyl-5-C***H***, benzyl-6-C***H***), 7.27 (m, 2H, benzyl-2-C***H***, benzyl-4-C***H***), 5.55 (s, 2H, $CO_2C\boldsymbol{H}_2$), 4.17 (s, 3H, $OC\boldsymbol{H}_3$), 3.84 (s, 2H, cyanoacetate-2-$C\boldsymbol{H}_2$). **^{13}C NMR (101 Hz, $CDCl_3$)**- δ 163.2 (***C***=O), 160.3 (benzyl-3-***C***), 136.2 (benzyl-1-***C***), 130.3 (benzyl-5-***C***H), 121.13 (benzyl-6-***C***H), 114.9 (benzyl-2-***C***H), 114.4 (benzyl-4-***C***H), 113.3 (nitrile-***C***N), 68.9 ($CO_2\boldsymbol{C}H_2$), 55.8 ($O\boldsymbol{C}H_3$), 25.3 (cyanoacetate-2-$\boldsymbol{C}H_2$).

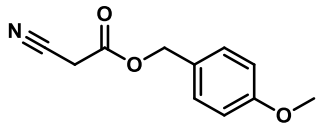

4-Methoxybenzyl 2-cyanoacetate (41j). Conducted by student Bulbul Singh. 2-Cyanoacetic acid (**31**) (500 mg, 5.8 mmol, 1.0 eq.) was reacted with 4-methoxybenzylalcohol (836 mg, 5.8 mmol, 1.1 eq.), DCC (1.213 g, 5.8 mmol, 1.0 eq.) and DMAP (72 mg, 0.58 mmol, 0.1 eq.) in DCM 5 mL according to general procedure 4. The reaction was monitored by TLC conditions 1:4 EtOAc: cyclohexane. The crude material was purified by column chromatography on a 80 g silica column using solvent conditions 20% EtOAc in cyclohexane over 12 CV. The desired fractions were combined and concentrated under reduced pressure to yield a colourless oil of the title compound (482 mg, 40 %). R_f = 0.26 (1:4 EtOAc: cyclohexane). LC/MS *m/z* calculated for $C_{11}H_{12}NO_3$: $[M+H]^+$: 206.2, found: 206.4, t_R 3.12 min. **^{1}H NMR (400 Hz, $CDCl_3$)**- δ 7.32 (d, *j*= 8.5 Hz, 2H, benzyl-2-C***H***, benzyl-6-C***H***), 6.90 (d, *j*= 8.6 Hz, 2H, benzyl-3-C***H***, benzyl-5-C***H***), 5.17 (s, 2H, $CO_2C\boldsymbol{H}_2$), 3.82 (s, 3H, $OC\boldsymbol{H}_3$), 3.46 (s, 2H, cyanoacetate-2-$C\boldsymbol{H}_2$). **^{13}C NMR (101 Hz, $CDCl_3$)**- δ 163.3 (***C***=O), 160.6 (benzyl-4-***C***), 131.1 (benzyl-2-***C***H, benzyl-6-***C***H), 126.9 (benzyl-1-***C***), 114.6 (benzyl-3-***C***H, benzyl-5-***C***H), 113.4 (nitrile-***C***N), 68.9 ($CO_2\boldsymbol{C}H_2$), 55.8 ($O\boldsymbol{C}H_3$), 25.3 (cyanoacetate-2-$\boldsymbol{C}H_2$).

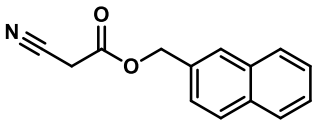

Naphthalen-2-ylmethyl 2-cyanoacetate (41n). 2-Cyanoacetic acid (**31**) (150 mg, 1.76 mmol, 1.0 eq.) was reacted with napthalen-2-yl methanol (280 mg, 1.76 mmol, 1.0 eq.), DCC (364 g, 1.76 mmol, 1.0 eq.) and DMAP (22 mg, 0.76 mmol, 0.1 eq.) in DCM 5 mL according to general procedure 4. The reaction was monitored by TLC conditions 1:4 EtOAc: cyclohexane. The crude material was purified by column chromatography on a 12 g silica column ran with solvent conditions 20% EtOAc in cyclohexane over 10 CV. The desired fractions were combined and concentrated under reduced pressure to yield a colourless oil of the title compound (226 mg, 57 %). R_f = 0.23 (1:4 EtOAc: cyclohexane). LC/MS *m/z* calculated for $C_{14}H_{12}NO_2$: $[M+H]^+$: 226.1, found: 225.1, t_R 3.04 min. **^{1}H NMR (400 Hz, $CDCl_3$)**- δ 7.90-7.81 (m, 4H, naphthalene-8-C***H***, naphthalene-3-C***H***, naphthalene-7-C***H***, naphthalene-4-C***H***), 7.56-7.43 (m, 3H, naphthalene-2-C***H***, naphthalene-5-C***H***, naphthalene-6-C***H***C), 5.40 (s, 2H, $CO_2C\boldsymbol{H}_2$), 3.41 (s, 2H, cyanoacetate-2-C$\boldsymbol{H}_2$). **^{13}C NMR (101 Hz, $CDCl_3$)**- δ 162.9 (***C***=O), 133.5 (naphthalene-1-***C***), 133.2 (naphthalene-7a-***C***), 131.8 (naphthalene-3a-***C***), 128.8 (naphthalene-2-***C***H), 128.3 (naphthalene-4-***C***H), 128.2 (naphthalene-7-***C***H), 127.9 (naphthalene-3-***C***H), 126.8 (naphthalene-8-***C***H), 126.7 (naphthalene-6-***C***H), 126.0 (naphthalene-5-***C***H), 113.0 (nitrile-***C***N), 68.9 ($CO_2\boldsymbol{C}H_2$), 25.0 (cyanoacetate-2-$\boldsymbol{C}H_2$).

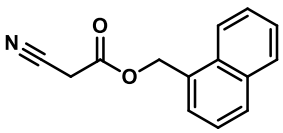

Naphthalen-1-ylmethyl 2-cyanoacetate (41o). 2-Cyanoacetic acid (**31**) (150 mg, 1.76 mmol, 1.0 eq.) was reacted with napthalen-1-yl methanol (280 mg, 1.76 mmol, 1.0 eq.), DCC (364 g, 1.76 mmol, 1.0 eq.) and DMAP (22 mg, 0.76 mmol, 0.1 eq.) in DCM 5 mL according to general procedure 4. The reaction was monitored by TLC conditions 100 % DCM. The crude material was purified by column chromatography on a 25 g silica column ran with solvent conditions 100% DCM over 6 CV. The desired fractions were combined and concentrated under reduced pressure to yield a colourless oil of the title compound (245 mg, 62 %). R_f = 0.24 (100% DCM). LC/MS *m/z* calculated for $C_{14}H_{12}NO_2$: $[M+H]^+$: 226.1, found: 225.2, t_R 3.50 min. **^{1}H NMR (400 Hz, $CDCl_3$)**- δ 8.00 (d, *j*= 8.1 Hz, 1H, naphthalene-8-C***H***), 7.88 (m, 2H, naphthalene-5-C***H***, naphthalene-4-C***H***), 7.57 (m, 3H, naphthalene-2-C***H***, naphthalene-3-C***H***, naphthalene-6-C***H***), 7.47 (t, *j*= 9.5 Hz, 1H,

naphthalene-7-C***H***), 5.71 (s, 2H, $CO_2C\boldsymbol{H}_2$), 3.48 (s, 2H, cyanoacetate-2-$C\boldsymbol{H}_2$). **^{13}C NMR (101 Hz, $CDCl_3$)**- *δ* 163.3 (***C***=O), 134.2 (naphthalene-8a-***C***), 132.0 (naphthalene-4a-***C***), 130.5 (naphthalene-2-***C***H), 130.3 (naphthalene-1-***C***), 129.3 (naphthalene-5-***C***H), 128.7 (naphthalene-4-***C***H), 127.4 (naphthalene-7-***C***H), 126.7 (naphthalene-6-***C***H), 125.7 (naphthalene-3-***C***H), 123.7 (naphthalene-8-***C***H), 113.2 (nitrile-***C***N), 67.3 ($CO_2\boldsymbol{C}H_2$), 25.3 (cyanoacetate-2-$\boldsymbol{C}H_2$).

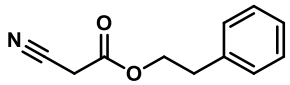

Phenethyl 2-cyanoacetate (41p). 2-Cyanoacetic acid (**31**) (160 mg, 1.88 mmol, 1.1 eq.) was reacted with 2-phenylethan-1-ol (215 mg, 1.76 mmol, 1.0 eq.), DCC (364 g, 1.76 mmol, 1.0 eq.) and DMAP (22 mg, 0.76 mmol, 0.1 eq.) in DCM 5 mL according to general procedure 4. The reaction was monitored by TLC conditions 3:7 EtOAc: cyclohexane. The crude material was purified using a silica plug washing with 200 mL 30% EtOAc in cyclohexane followed by 100 mL 50% EtOAc in cyclohexane. The resulting filtrate was concentrated under reduced pressure to yield a colourless oil of the title compound (257 mg, 77 %). R_f = 0.4 (3:7 EtOAc: cyclohexane).**^{1}H NMR (400 Hz, $CDCl_3$)**- *δ* 7.39-7.22 (m, 5H, phenyl-2-C***H***, phenyl-3-C***H***, phenyl-4-C***H***, phenyl-5-C***H***, phenyl-6-C***H***), 4.45 (t, *j*= 7.1 Hz, 2H, $CO_2C\boldsymbol{H}_2$), 3.45 (s, 2H, cyanoacetate-2-$C\boldsymbol{H}_2$), 3.02 (t, *j*= 7.0 Hz, 2H, $CO_2CH_2C\boldsymbol{H}_2$). **^{13}C NMR (101 Hz, $CDCl_3$)**- *δ* 162.8 (***C***=O), 136.9 (phenyl-1-***C***), 128.9 (2x phenyl-2-***C***H, phenyl-6-***C***H), 128.7 (phenyl-3-***C***H, phenyl-5-***C***H), 126.9 (phenyl-4-***C***H), 112.9 (nitrile-***C***N), 67.3 ($CO_2\boldsymbol{C}H_2$), 34.8 ($CO_2CH_2\boldsymbol{C}H_2$), 24.7 (cyanoacetate-2-$\boldsymbol{C}H_2$).

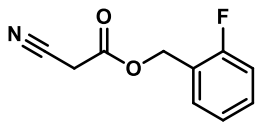

2-Fluorobenzyl 2-cyanoacetate (41q). Conducted by student Ng Yu Yang. 2-Cyanoacetic acid (**31**) (200 mg, 2.35 mmol, 1.0 eq.) was reacted with 2-fluorobenzyl alcohol (297 mg, 2.04 mmol, 1.0 eq.), DCC (521 g, 2.35 mmol, 1.1 eq.) and DMAP (29 mg, 0.24 mmol, 0.1 eq.) in DCM 4 mL according to general procedure 4. The reaction was monitored by TLC conditions 99:1 chloroform: cyclohexane. The crude material was purified by column chromatography on a 25 g silica column using solvent conditions 99:1 chloroform: cyclohexane over 10CV. The desired fractions were combined and concentrated under reduced pressure to yield a colourless oil of the title compound (269 mg, 59 %). R_f = 0.28 (99:1 chloroform:

cyclohexane). **^{1}H NMR (400 Hz, $CDCl_3$)**- *δ* 7.45-7.32 (m, 2H, phenyl-3-C***H***, phenyl-4-C***H***), 7.17 (t, *j*= 7.4 Hz, 1H, phenyl-6-C***H***), 7.10 (t, *j*= 9.3 Hz, 1H, phenyl-5-C***H***), 5.30 (s, 2H, $CO_2C\boldsymbol{H}_2$), 3.50 (s, 2H, cyanoacetate-2-C$\boldsymbol{H}_2$). **^{13}C NMR (101 Hz, $CDCl_3$)**- *δ* 163.2 (***C***=O), 160.3 (phenyl-2-***C***), 131.5 (phenyl-4-***C***H), 131.4 (phenyl-6-***C***H), 124.8 (phenyl-1-***C***), 122.0 (phenyl-5-***C***H), 116.3 (phenyl-3-***C***H), 113.2 (nitrile-***C***N), 62.9 ($CO_2\boldsymbol{C}H_2$), 25.2 (cyanoacetate-2-$\boldsymbol{C}H_2$).**^{19}F NMR (377 Hz, $CDCl_3$)**- δ – 117.5 (dt, *j*= 9.24, 6.15 Hz, 1F, C***F***).

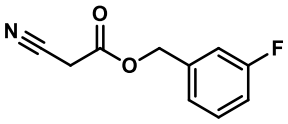

3-Fluorobenzyl 2-cyanoacetate (41r). Conducted by student Ng Yu Yang. 2-Cyanoacetic acid (**31**) (204 mg, 2.4 mmol, 1.0 eq.) was reacted with 3-fluorobenzyl alcohol (297 mg, 2.4 mmol, 1.0 eq.), DCC (478 g, 2.31 mmol, 1.0 eq.) and DMAP (32 mg, 0.26 mmol, 0.11 eq.) in DCM 4 mL according to general procedure 4. The reaction was monitored by TLC conditions 99:1 chloroform: cyclohexane. The crude material was purified by column chromatography on a 25 g silica column using solvent conditions 99:1 chloroform: cyclohexane over 10CV. The desired fractions were combined and concentrated under reduced pressure to yield a colourless oil of the title compound (149 mg, 33 %). R_f = 0.25 (99:1 chloroform: cyclohexane). **^{1}H NMR (400 Hz, $CDCl_3$)**- *δ* 7.35 (q, *j*= 7.0 Hz, 1H, phenyl-5-C***H***), 7.15 (d, *j*= 7.6 Hz, 1H, phenyl-6-C***H***), 7.07 (m, 2H, phenyl-2-C***H***, phenyl-4-C***H***), 5.22 (s, 2H, $CO_2C\boldsymbol{H}_2$), 3.50 (s, 2H, cyanoacetate-2-C$\boldsymbol{H}_2$). **^{13}C NMR (101 Hz, $CDCl_3$)**- δ 164.1 (***C***=O), 162.7 (phenyl-3-***C***), 136.7 (phenyl-1-***C***), 130.4 (phenyl-5-***C***H), 124.0 (phenyl-6-***C***H), 115.8 (phenyl-4-***C***H), 115.3 (phenyl-2-***C***H), 112.7 (nitrile-***C***N), 67.6 ($CO_2\boldsymbol{C}H_2$), 24.8 (cyanoacetate-2-$\boldsymbol{C}H_2$). **^{19}F NMR (377 Hz, $CDCl_3$)**- *δ* -112.2 (td, *j*= 9.0, 5.7 Hz, 1F, C***F***).

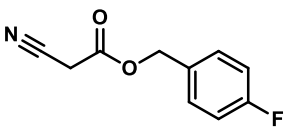

4-Fluorobenzyl 2-cyanoacetate (41s). Conducted by student Ng Yu Yang. 2-Cyanoacetic acid (**31**) (200 mg, 2.35 mmol, 1.2 eq.) was reacted with 4-fluorobenzyl alcohol (257 mg, 2.04 mmol, 1.0 eq.), DCC (485 g, 2.35 mmol, 1.2 eq.) and DMAP (29 mg, 0.24 mmol, 0.1 eq.) in DCM 4 mL according to general procedure 4. The reaction was monitored by TLC conditions 99:1 chloroform: cyclohexane. The crude material was purified by column chromatography on a 25 g silica column with solvent conditions 99:1 chloroform:

cyclohexane over 10CV. The desired fractions were combined and concentrated under reduced pressure to yield a colourless oil of the title compound (130 mg, 29 %). R_f = 0.29 (99:1 chloroform: cyclohexane).**^{1}H NMR (400 Hz, $CDCl_3$)**- *δ* 7.41-7.32 (m, 2H, phenyl-2-CH, phenyl-6-C***H***), 7.07 (t, *j*= 8.6 Hz, 2H, phenyl-3-C***H***, phenyl-5-C***H***), 5.20 (s, 2H, $CO_2C\boldsymbol{H}_2$), 3.48 (s, 2H, cyanoacetate-2-C$\boldsymbol{H}_2$).**^{13}C NMR (101 Hz, $CDCl_3$)**- *δ* 164.3 (***C***=O), 162.7 (phenyl-4-***C***), 130.7 (phenyl-2-***C***H, phenyl-6-***C***H), 130.2 (phenyl-1-***C***), 115.9 (phenyl-3-***C***H, phenyl-5-***C***H), 112.7 (nitrile-***C***N), 67.8 ($CO_2\boldsymbol{C}H_2$), 24.8 (cyanoacetate-2-***C***H_2).**^{19}F NMR (377 Hz, $CDCl_3$)**- δ -112.33 (ddd, *j*= 13.9, 8.8, 5.2 Hz, 1F, C***F***).

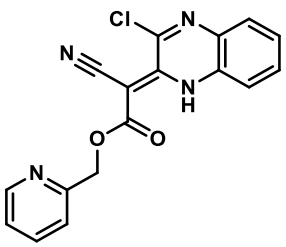

Pyridin-2-ylmethyl (Z)-2-(3-chloroquinoxalin-2(1H)-ylidene)-2-cyanoacetate (42a). Conducted by student Sam Robinson. 2,3-Dichloroquinoxaline (**26**) (201 mg, 1.0 mmol, 1.0 eq.) was reacted with 3-methoxybenzyl 2-cyanoacetate (**41a**) (178 mg, 1.01 mmol, 1.0 eq.), CS_2CO_3 (1.041 g, 3.2 mmol, 5.0 eq.) in 10 mL DMF in accordance with general procedure 1(b). The reaction was monitored by TLC conditions 1:1 EtOAc:cyclohexane. The DMF was removed under high vacuum before the crude material was extracted into EtOAc (200 mL) and washed with 2 M HCl (50 mL) and distilled water (200 mL). The phases were separated and the organic dried over $MgSO_4$ before filtering and concentrating under reduced pressure. The crude material was purified by column chromatography on a 12 g silica column using solvent conditions 30-70 % EtAOc in cyclohexane over 12 CVs. The resulting fractions were combined and concentrated under reduced pressure to yield the title compound as orange solid (90 mg, 26 %). R_f= 0.22 (1:1 EtOAc: cyclohexane). LC/MS *m/z* calculated for $C_{17}H_{12}ClN_4O_2$: $[M+H]^+$: 339.1, found: 339.5, t_R 2.52 min. **^{1}H NMR (400 Hz, $CDCl_3$)**- *δ* 14.41 (broad s, 1H, quinoxaline-1-N***H***), 8.60 (d, *j*= 4.86 Hz, 1H, pyridine-3-C***H***), 7.82 (d, *j*= 8.18 Hz, 1H, quinoxaline-8-C***H***), 7.76 (t, *j*= 7.61 Hz, 1H, quinoxaline-7-C***H***), 7.64 (t, *j*= 7.75 Hz, 1H, quinoxaline-6-C***H***), 7.56 (d, *j*= 7.9 Hz, 1H, quinoxaline-5-C***H***), 7.48 (t, *j*= 7.73 Hz, 1H, pyridine-5-C***H***), 7.41 (d, *j*= 8.19 Hz, 1H, pyridine-6-C***H***), 7.25 (m, 1H, pyridine-4-C***H***), 5.48 (s, 2H, $CO_2C\boldsymbol{H}_2$). **^{13}C NMR (101 Hz, $CDCl_3$)**- *δ* 170.9 (***C***=O), 155.9 (quinoxaline-2-***C***), 149.8 (pyridine-1-***C***), 146.7 (quinoxaline-3-***C***), 144.1 (pyridine-3-***C***H),

137.6 (quinoxaline-8a-***C***), 135.0 (quinoxaline-4a-***C***), 133.0 (pyridine-5-***C***H), 129.3 (quinoxaline-5-***C***H), 128.7 (quinoxaline-6-***C***H), 127.4 (quinoxaline-7-***C***H), 123.4 (pyridine-6-***C***H), 121.6 (pyridine-4-***C***H), 117.1 (quinoxaline-8-***C***H), 116.9 (nitrile-***C***N), 69.6 (cyanoacetate-2-***C***), 68.1 (CO_2***C***H_2).

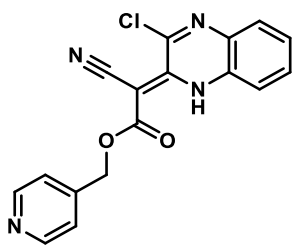

Pyridin-4-ylmethyl (*Z*)-2-(3-chloroquinoxalin-2(1*H*)-ylidene)-2-cyanoacetate (42c). 2,3-Dichloroquinoxaline (**26**) (127 mg, 0.64 mmol, 1.0 eq.) was reacted with pyridin-4-ylmethyl 2-cyanoacetate (**41c**) (113 mg, 0.64 mmol, 1.0 eq.), CS_2CO_3 (1.041 g, 3.2 mmol, 5.0 eq.) in 10 mL DMF in accordance with general procedure 1(b), a colour change to red from yellow was observed. The reaction was monitored by TLC conditions 3:97 MeOH: DCM. The DMF was removed under high vacuum before the crude material was extracted into EtOAc (200 mL) and washed with 2 M HCl (50 mL) and distilled water (200 mL). The phases were separated and the organic dried over $MgSO_4$ before filtering and concentrating under reduced pressure. LCMS determined the product remained in the aqueous phase, a small amount of water removed under pressure before an orange solid crashed out. The mixture was placed in the freezer for 1h before being filtered under vacuum. The crude material was purified by column chromatography on 12 g silica column using solvent conditions 1-10 % MeOH in DCM over 15 CVs. The resulting fractions were combined and concentrated under reduced pressure to yield the title compound as an orange solid (80 mg, 37 %). R_f= 0.65 (3 % MeOH in DCM). LC/MS *m/z* calculated for $C_{17}H_{12}ClN_4O_2$: $[M+H]^+$: 339.1, found: 339.1, t_R 2.65 min. **^{1}H NMR (400 Hz, $CDCl_3$)**- *δ* 13.89 (broad s, 1H, quinoxaline-1-N***H***), 8.62 (d, *j*= 5.0 Hz, 2H, pyridine-3-C***H***, pyridine-5-C***H***), 7.88 (d, *j*= 8.3 Hz, 1H, quinoxaline-8-C***H***), 7.84 (d, *j*= 8.2 Hz, 1H, quinoxaline-5-C***H***), 7.72 (t, *j*= 7.8 Hz, 1H, quinoxaline-7-C***H***), 7.55 (t, *j*= 7.7 Hz, 1H, quinoxaline-6-C***H***), 7.45 (d, *j*= 5.0 Hz, 2H, pyridine-2-C***H***, pyridine-6-C***H***), 5.39 (s, 2H, CO_2C***H***$_2$).**^{13}C NMR (101 Hz, $CDCl_3$)**- *δ* 169.2 (***C***=O), 153.4 (quinoxaline-2-***C***), 149.9 (quinoxaline-3-***C***, pyridine-3-***C***H, pyridine-5-***C***H), 146.7 (pyridine-1-***C***), 135.0 (quinoxaline-8a-***C***), 132.6 (quinoxaline-4a-***C***), 128.2 (quinoxaline-5-***C***H), 127.4 (quinoxaline-6-***C***H), 126.3 (quinoxaline-7-***C***H), 122.01

(pyridine-2-***C***H, pyridine-6-***C***H), 119.4 (pyridine-8-***C***H), 114.1 (nitrile-***C***N), 64.7 (cyanoacetate-2-***C***).

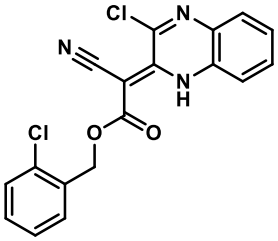

2-chlorobenzyl (*Z*)-2-(3-chloroquinoxalin-2(1*H*)-ylidene)-2-cyanoacetate (42d). Conducted by student Ng Yu Yang. 2,3-Dichloroquinoxaline (**26**) (245 mg, 1.23 mmol, 1.0 eq.) was reacted with 2-chlorobenzyl 2-cyanoacetate (**41d**) (258 mg, 1.23 mmol, 1.0 eq.), CS_2CO_3 (2 g, 6.15 mmol, 5.0 eq.) in 10 mL DMF in accordance with general procedure 1(b). The reaction was monitored by TLC conditions 1:4 EtOAc: cyclohexane. The DMF was removed under high vacuum before the crude material was extracted into EtOAc where a yellow precipitate crashed out. The resulting mixture was filtered under vacuum to give the title compound as a yellow solid (250 mg, 45 %). R_f= 0.25 (1:4 EtOAc: cyclohexane). LC/MS *m/z* calculated for $C_{18}H_{12}Cl_2N_3O_2$: $[M+H]^+$: 372.0, found: 372.1, t_R 3.19 min. **^{1}H NMR (400 Hz, $CDCl_3$)**- δ 14.42 (broad s, 1H, quinoxaline-1-N***H***), 7.83 (d, *j*= 8.18 Hz, 1H, quinoxaline-8-C***H***), 7.69-7.57 (m, 2H, benzyl-3-C***H***, quinoxaline-7-C***H***), 7.49 (t, *j*= 7.43 Hz, 1H, quinoxaline-6-C***H***), 7.44-7.38 (m, 2H, quinoxaline-5-C***H***, benzyl-4-C***H***), 7.36-7.27 (m, 2H, benzyl-5-C***H***, benzyl-6-C***H***), 5.47 (s, 2H, CO_2CH_2). **^{13}C NMR (101 Hz, $CDCl_3$)**- δ 170.6 (***C***=O), 146.7 (quinoxaline-2-***C***), 142.9 (quinoxaline-3-***C***), 135.0 (benzyl-1-***C***), 133.5 (quinoxaline-8a-***C***), 133.0 (quinoxaline-4a-***C***), 132.9 (benzyl-2-***C***), 129.9 (benzyl-3-***C***H), 129.8 (benzyl-4-***C***H), 129.3 (benzyl-6-***C***H), 129.1 (benzyl-5-***C***H), 128.7 (quinoxaline-5-***C***H), 127.7 (quinoxaline-7-***C***H), 127.4 (quinoxaline-6-***C***H), 117.1 (quinoxaline-8-***C***H), 116.8 (nitrile-***C***N), 69.6 (cyanoacetate-2-***C***), 64.9 (CO_2***C***H_2).

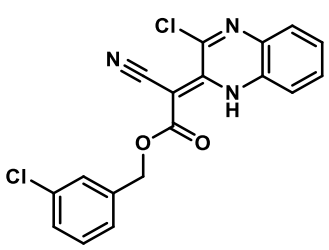

3-chlorobenzyl (*Z*)-2-(3-chloroquinoxalin-2(1*H*)-ylidene)-2-cyanoacetate (42e). 2,3-Dichloroquinoxaline (**26**) (261 mg, 1.31 mmol, 1.0 eq.) was reacted with 3-chlorobenzyl 2-cyanoacetate (**41e**) (274 mg, 1.31 mmol, 1.0 eq.), CS_2CO_3 (2.129 g, 6.54 mmol, 5.0 eq.) in 10 mL DMF in accordance with general procedure 1(b). The reaction was monitored by TLC conditions 3:7 EtOAc: cyclohexane. The DMF was removed under high vacuum before MeOH was added and

product crashed out as a orange precipitate. The resulting mixture was filtered under vacuum to give the title compound as a orange solid (135 mg, 28 %). R_f= 0.30 (3:7 EtOAc: cyclohexane). LC/MS *m/z* calculated for $C_{18}H_{12}Cl_2N_3O_2$: $[M+H]^+$: 372.0, found: 372.2, t_R 3.17 min. **^{1}H NMR (400 Hz, $CDCl_3$)**- δ 14.38 (broad s, 1H, quinoxaline-1-N***H***), 7.82 (d, *j*= 8.15 Hz, 1H, quinoxaline-8-C***H***), 7.63 (t, *j*= 7.74 Hz, 1H, quinoxaline-7-C***H***), 7.48 (t, *j*= 7.50 Hz, 1H, quinoxaline-6-C***H***), 7.45-7.38 (m, 2H, quinoxaline-5-C***H***, benzyl-2-C***H***), 7.38-7.28 (m, 3H, benzyl-4-C***H***, benzyl-5-C***H***, benzyl-6-C***H***), 5.33 (s, 2H, $CO_2C\boldsymbol{H}_2$). **^{13}C NMR (101 Hz, $CDCl_3$)**- δ 171.0 (***C***=O), 146.7 (quinoxaline-2-***C***), 144.1 (quinoxaline-3-***C***), 137.8 (quinoxaline-8a-***C***), 135.0 (quinoxaline-4a-***C***), 132.9 (benzyl-1-***C***), 130.5 (benzyl-3-***C***), 129.3 (benzyl-5-***C***H), 129.0 (benzyl-4-***C***H), 128.6 (benzyl-2-***C***H), 128.3 (quinoxaline-5-***C***H, benzyl-6-***C***H), 127.4 (quinoxaline-7-***C***H), 126.3 (quinoxaline-6-***C***H), 117.1 (quinoxaline-8-***C***H), 116.8 (nitrile-***C***N), 69.6 (cyanoacetate-2-***C***), 66.8 ($CO_2\boldsymbol{C}H_2$).

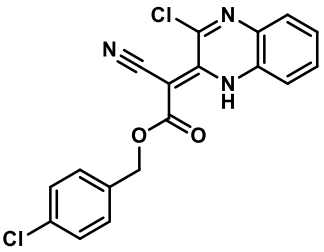

4-Chlorobenzyl (*Z*)-2-(3-chloroquinoxalin-2(1*H*)-ylidene)-2-cyanoacetate (42f). Conducted by student Bulbul Singh. 2,3-Dichloroquinoxaline (**26**) (171 mg, 0.85 mmol, 1.0 eq.) was reacted with 3-chlorobenzyl 2-cyanoacetate (**41f**) (179 mg, 0.85 mmol, 1.0 eq.), CS_2CO_3 (1.391 g, 4.25 mmol, 5.0 eq.) in 10 mL DMF in accordance with general procedure 1(b). The reaction was monitored by TLC conditions 100 % DCM. The DMF was removed under high vacuum before the crude material was extracted into EtOAc (60 mL) washing with water (70 mL) and saturated sodium bicarbonate (70 mL) and brine (50 mL). The phases were separated, organic dried over $MgSO_4$ and concentrated under reduced pressure. The resulting crude material was recrystalised in EtOH and filtered under vacuum to give the title compound as a red solid (87 mg, 28 %). R_f= 0.7 (100 % DCM). LC/MS *m/z* calculated for $C_{18}H_{12}Cl_2N_3O_2$: $[M+H]^+$: 372.0, found: 372.2, t_R 3.21 min.**^{1}H NMR (400 Hz, $CDCl_3$)**- δ 14.38 (broad s, 1H, quinoxaline-1-N***H***), 7.81 (d, *j*= 8.2 Hz, 1H, quinoxaline-8-C***H***), 7.63 (t, *j*= 8.1 Hz, 1H, quinoxaline-7-C***H***), 7.48 (t, *j*= 8.1 Hz, 1H, quinoxaline-6-C***H***), 7.44-7.33 (m, 5H, quinoxaline-5-C***H***, 2x benzyl-2-C***H***, benzyl-3-C***H***, benzyl-5-C***H***, benzyl-6-C***H***).**^{13}C NMR (101 Hz, $CDCl_3$)**- δ 167.9 (***C***=O), 146.4 (quinoxaline-2-***C***), 134.7 (quinoxaline-3-***C***),

134.5 (quinoxaline-8a-***C***), 134.0 (quinoxaline-4a-***C***), 132.6 (benzyl-1-***C***), 131.1 (benzyl-4-***C***), 129.3 (benzyl-2-***C***H, benzyl-6-***C***H), 129.0 (quinoxaline-5-***C***H), 128.3 (benzyl-3-***C***H, benzyl-5-***C***H), 128.3 (quinoxaline-7-***C***H), 127.1 (quinoxaline-8-***C***H), 116.7 (quinoxaline-8-***C***H, nitrile-***C***N), 66.7 (CO_2***C***H_2), 29.6 (cyanoacetate-2-***C***).

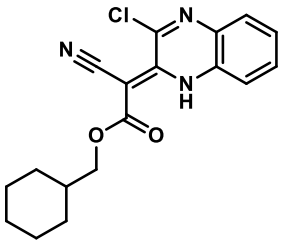

Cyclohexylmethyl (*Z*)-2-(3-chloroquinoxalin-2(1*H*)-ylidene)-2-cyanoacetate (42g). 2,3-Dichloroquinoxaline (**26**) (106 mg, 0.54 mmol, 1.0 eq.) was reacted with cyclohexylmethyl 2-cyanoacetate (**41g**) (97 mg, 0.54 mmol, 1.0 eq.), CS_2CO_3 (896 mg, 2.68 mmol, 5.0 eq.) in 10 mL DMF in accordance with general procedure 1(b). The reaction was monitored by TLC conditions 1:4 EtOAc: cyclohexane. The DMF was removed under high vacuum before the crude material was extracted into EtOAc (200 mL) washing with water (200 mL) and 2M HCl (50 mL). The phases were separated, and the aqueous phase was back extracted with 50 mL EtOAC. The organic phases were combined and dried over $MgSO_4$ and concentrated under reduced pressure. The crude material was purified by column chromatography on a 12g silica column using solvent conditions 0-50 % EtOAc in cyclohexane over 10 CV. The desired fractions were combined and concentrated under reduced pressure to yield the title compound as a yellow solid (102 mg, 55 %). R_f= 0.33 (20 % EtOAc in cyclohexane). LC/MS *m/z* calculated for $C_{18}H_{19}ClN_3O_2$: $[M+H]^+$: 344.1, found: 344.1, t_R 3.09 min.**^{1}H NMR (400 Hz, $CDCl_3$)**- *δ* 14.48 (broad s, 1H, quinoxaline-1-N***H***), 7.80 (d, *j*= 8.1 Hz, 1H, quinoxaline-8-C***H***), 7.61 (t, *j*= 7.7 Hz, 1H, quinoxaline-7-C***H***), 7.45 (t, *j*= 7.9 Hz, 1H, quinoxaline-6-C***H***), 7.38 (d, *j*= 8.1 Hz, 1H, quinoxaline-5-C***H***), 4.11 (d, *j*= 4.11 Hz, 2H, CO_2C***H***$_2$), 1.91-1.62 (m, 7H, cyclohexane-1-C***H***, 1x cyclohexane-2-C***H***$_2$, 1x cyclohenxane-3-C***H***$_2$, cyclohexane-4-C***H***$_2$, 1x cyclohexane-5-C***H***$_2$, 1x cyclohexane-6-C***H***$_2$), 1.38-1.12 (m, 4H, 1x cyclohexane-2-C***H***$_2$, cyclohenxane-3-C***H***$_2$, cyclohexane-5-C***H***$_2$, cyclohexane-6-C***H***$_2$).**^{13}C NMR (101 Hz, $CDCl_3$)**- *δ* 171.1 (***C***=O), 146.3 (quinoxaline-2-***C***), 143.9 (quinoxaline-3-***C***), 134.5 (quinoxaline-8a-***C***), 132.5 (quinoxaline-4a-***C***), 128.9 (quinoxaline-5-***C***H), 128.5 (quinoxaline-7-***C***H), 126.8 (quinoxaline-6-***C***H), 116.6 (quinoxaline-8-***C***H), 116.5 (nitrile-***C***N), 71.2 (CO_2***C***H_2), 69.7 (cyanoacetate-2-***C***), 37.2

(cyclohexane-1-***C***H), 29.6 (cyclohexane-2-***C***H_2, cyclohexane-6-***C***H_2), 26.4 (cyclohexane-4-***C***H_2), 25.8 (cyclohexane-3-CH_2, quinoxaline-5-***C***H_2).

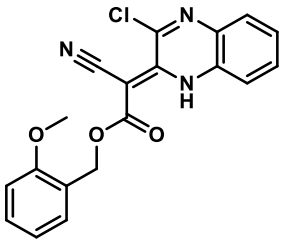

2-Methoxybenzyl (*Z*)-2-(3-chloroquinoxalin-2(1*H*)-ylidene)-2-cyanoacetate (42h). Conducted by student Bulbul Singh. 2,3-Dichloroquinoxaline (**26**) (98 mg, 0.5 mmol, 1.0 eq.) was reacted with of 2-methoxybenzyl 2-cyanoacetate (**41h**) (103 mg, 0.5 mmol, 1.0 eq.), CS_2CO_3 (809 mg, 2.48 mmol, 5.0 eq.) in 2 mL DMF in accordance with general procedure 1(a). The reaction was monitored by TLC conditions 3:7 EtOAc: cyclohexane. The DMF was removed under high vacuum before the crude material was extracted into EtOAc (60 mL) washing with water (120 mL) and brine (65 mL). The phases were separated and dried over $MgSO_4$ and concentrated under reduced pressure to yield a red solid of the title compound (148 mg, 80 %). R_f= 0.29 (3:7 EtOAc: cyclohexane). LC/MS *m/z* calculated for $C_{19}H_{15}ClN_3O_3$: $[M+H]^+$: 368.1, found: 368.0, t_R 3.15 min. **^{1}H NMR (400 Hz, $CDCl_3$)**- *δ* 14.48 (broad s, 1H, quinoxaline-1-N***H***), 7.81 (d, *j*= 8.2 Hz, 1H, quinoxaline-8-C***H***), 7.62 (t, *j*= 7.5 Hz, 1H, quinoxaline-7-C***H***), 7.46 (m, 2H, quinoxaline-6-C***H***, benzyl-6-C***H***), 7.38 (d, *j*= 8.2 Hz, 1H, quinoxaline-5-C***H***), 7.31 (t, *j*= 7.9 Hz, 1H, quinoxaline-5-C***H***), 6.99 (t, *j*= 7.5 Hz, 1H, quinoxaline-4-C***H***), 6.91 (d, *j*= 8.3 Hz, 1H, quinoxaline-3-C***H***), 5.42 (s, 2H, CO_2C***H***$_2$), 3.88 (s, 3H, OC***H***$_3$). **^{13}C NMR (101 Hz, $CDCl_3$)**- *δ* 171.2 (***C***=O), 157.5 (CH_3O***C***), 146.7 (quinoxaline-2-***C***), 144.3 (quinoxaline-3-***C***), 138.2 (quinoxaline-8a-***C***), 134.9 (quinoxaline-4a-***C***), 132.8 (benzyl-6-***C***H), 129.9 (benzyl-3-***C***H), 129.2 (benzyl-4-***C***H), 129.0 (quinoxaline-5-***C***H), 128.4 (benzyl-1-***C***), 127.2 (benzyl-5-***C***H), 124.2 (quinoxaline-7-***C***H), 121.1 (quinoxaline-6-***C***H), 117.0 (nitrile-***C***N), 110.9 (quinoxaline-8-***C***H), 70.0 (cyanoacetate-2-***C***), 63.5 (CO_2***C***H_2), 56.0 (O***C***H_3).

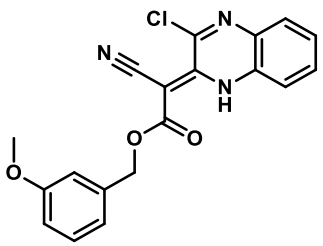

3-Methoxybenzyl (*Z*)-2-(3-chloroquinoxalin-2(1*H*)-ylidene)-2-cyanoacetate (42i). Conducted by student Bulbul Singh. 2,3-Dichloroquinoxaline (**26**) (243 mg, 1.22 mmol, 1.0 eq.) was reacted with cyclohexylmethyl 2-cyanoacetate (**41i**) (250 mg, 1.22 mmol, 1.0 eq.), CS_2CO_3 (1.985 g, 6.09 mmol, 5.0 eq.) in 2

mL DMF in accordance with general procedure 1(a). The reaction was monitored by TLC conditions 100 % DCM. The DMF was removed under high vacuum before the crude material was extracted into EtOAc (60 mL) washing with water (60 mL) and brine (60 mL). The phases were separated and dried over $MgSO_4$ and concentrated under reduced pressure. The crude material was purified by silica plug washing with EtOAc (200 mL) to yield the title compound as a red solid (208 mg, 47 %). R_f= 0.47 (100 % DCM). LC/MS *m/z* calculated for $C_{19}H_{15}ClN_3O_3$: $[M+H]^+$: 368.1, found: 368.0, t_R 3.00 min. **^{1}H NMR (400 Hz, $CDCl_3$)**- δ 14.4 (broad s, 1H, quinoxaline-1-N***H***), 7.81 (d, *j*= 8.2 Hz, 1H, quinoxaline-8-C***H***), 7.61 (t, *j*= 8.0 Hz, 1H, quinoxaline-7-C***H***), 7.47 (t, *j*= 7.8 Hz, 1H, quinoxaline-6-C***H***), 7.39 (d, *j*= 8.2 Hz, 1H, quinoxaline-5-C***H***), 7.30 (t, *j*= 7.9 Hz, 1H, benzyl-5-C***H***), 7.02 (m, 2H, benzyl-2-C***H***, benzyl-4-C***H***), 6.87 (d, j= 8.1 Hz, 1H, benzyl-6-C**H**), 5.34 (s, 2H, $CO_2C\boldsymbol{H}_2$), 3.83 (s, 3H, $OC\boldsymbol{H}_3$). **^{13}C NMR (101 Hz, $CDCl_3$)**- δ 170.7 (***C***=O), 160.0 (benzyl-3-***C***), 146.4 (quinoxaline-2-***C***), 142.8 (quinoxaline-3-***C***),137.1 (benzyl-1-***C***), 134.6 (quinoxaline-8a-***C***), 132.5 (quinoxaline-4a-***C***), 129.9 (benzyl-5-***C***H), 128.9 (quinoxaline-5-***C***H), 128.4 (quinoxaline-7-***C***H), 127.0 (quinoxaline-6-***C***H), 119.9 (benzyl-6-***C***H), 116.7 (quinoxaline-8-***C***H), 116.6 (nitrile-***C***N), 114.2 (benzyl-2-***C***H), 113.0 (benzyl-3-***C***H), 69.5 (cyanoacetate-2-***C***), 67.3 ($CO^2\boldsymbol{C}H_2$), 55.5 ($O\boldsymbol{C}H_3$).

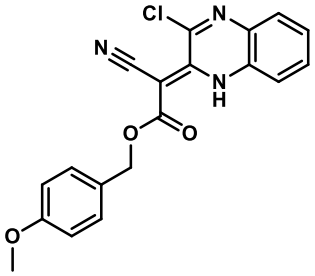

4-Methoxybenzyl (*Z*)-2-(3-chloroquinoxalin-2(1*H*)-ylidene)-2-cyanoacetate (42j). Conducted by student Bulbul Singh. 2,3-Dichloroquinoxaline (**26**) (243 mg, 1.22 mmol, 1.0 eq.) was reacted with of 4-methoxybenzyl 2-cyanoacetate (**41j**) (250 mg, 1.22 mmol, 1.0 eq.), CS_2CO_3 (1.985 g, 6.09 mmol, 5.0 eq.) in 3 mL DMF in accordance with general procedure 1(a). The reaction was monitored by TLC conditions 100 % DCM. The DMF was removed under high vacuum before the crude material was extracted into EtOAc (60 mL) washing with water (300 mL) and brine (60 mL). The phases were separated and dried over $MgSO_4$ and concentrated under reduced pressure to yield a red solid of the title compound (207 mg, 46 %). R_f= 0.44 (100 % DCM). LC/MS *m/z* calculated for $C_{19}H_{15}ClN_3O_3$: $[M+H]^+$: 368.1, found: 368.3, t_R 2.65 min. **^{1}H NMR (400 Hz, $CDCl_3$)**- δ 14.44 (broad s, 1H, quinoxaline-1-N***H***), 7.80 (d, *j*= 8.2 Hz, 1H, quinoxaline-8-C***H***), 7.62 (t, *j*= 7.7 Hz, 1H, quinoxaline-7-C***H***), 7.46 (t, *j*= 7.6 Hz, 1H,

quinoxaline-6-C***H***), 7.42- 7.37 (m, 3H, quinoxaline-5-C***H***, benzyl-2-C***H***, benzyl-6-C***H***), 6.91 (d, *j*= 8.4 Hz, 2H, benzyl-3-C***H***, benzyl-5-C***H***), 5.30 (s, 2H, OC***H***$_2$C), 3.81 (s, 3H, C***H***$_3$OC). **^{13}C NMR (101 Hz, CDCl$_3$)**- *δ* 170.9 (***C***=O), 159.9 (benzyl-2-***C***), 146.4 (quinoxaline-2-***C***), 143.9 (quinoxaline-3-***C***), 134.5 (quinoxaline-8a-***C***), 132.5 (quinoxaline-4a-***C***), 120.9 (benzyl-2-***C***H, benzyl-6-***C***H), 128.9 (benzyl-1-***C***), 128.4 (quinoxaline-5-***C***H), 127.6 (quinoxaline-7-***C***H), 126.9 (quinoxaline-6-***C***H), 116.7 (benzyl-2-***C***H, benzyl-6-***C***H), 116.65 (nitrile-***C***N), 114.2 (quinoxaline-8-***C***H), 69.6 (cyanoacetate-2-***C***), 67.4 (CO_2***C***H_2), 55.5 (O***C***H_3).

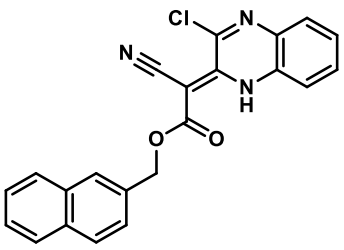

Naphthalen-2-ylmethyl (*Z*)-2-(3-chloroquinoxalin-2(1*H*)-ylidene)-2-cyanoacetate (42n). 2,3-Dichloroquinoxaline (**26**) (194 mg, 1.0 mmol, 1.0 eq.) was reacted with of naphthalen-2-ylmethyl 2-cyanoacetate (**41n**) (223 mg, 1.0 mmol, 1.0 eq.), CS_2CO_3 (1.597 g, 4.91 mmol, 4.9 eq.) in 7 mL DMF in accordance with general procedure 1(a). The reaction was monitored by TLC conditions1:4 EtOAc: cyclohexane. The DMF was removed under high vacuum before the crude material was extracted into EtOAc (100 mL) washing with water (100 mL), 2M HCl (100 mL) and brine (100 mL). The phases were separated, aqueous layer back extracted with DCM (100 mL) before the organic was combined and a yellow precipitate crashed out. The precipitate filtered under vacuum and washed with cold EtOAc (50 mL) to give a yellow solid. The filtered solid was recrystalized in hot EtOAc to yield the title compound (324 mg, 85 %). R_f= 0.0 (1:4 EtOAc: cyclohexane). LC/MS *m/z* calculated for $C_{22}H_{15}ClN_3O_2$: $[M+H]^+$: 388.8, found: 388.1, t_R 3.36 min. **^{1}H NMR (400 Hz, CDCl$_3$)**- *δ* 14.05 (broad s, 1H, quinoxaline-1-N***H***), 8.02-7.86 (m, 5H, naphthalene-3-C***H***, naphthalene-2-C***H***, naphthalene-4-C***H***, naphthanele-8-C***H***, naphthalene-7-C***H***), 7.83 (d, *j*= 8.1 Hz, 1H, quinoxaline-8-C***H***), 7.72 (t, *j*= 7.7 Hz, 1H, quinoxaline-7-C***H***), 7.61-7.49 (m, 4H, quinoxaline-5-C***H***, quinoxaline-6-C***H***, naphthalene-5-C***H***, naphthalene-6-C***H***), 5.52 (s, 2H, CO_2C***H***$_2$). **^{13}C NMR (101 Hz, CDCl$_3$)**- *δ* 169.8 (***C***=O), 146.9 (quinoxaline-2-***C***), 143.7 (quinoxaline-3-***C***), 134.6 (quinoxaline-8a-***C***), 134.0 (quinoxaline-4a-***C***), 133.2 (naphthanele-1-***C***), 133.1 (naphthalene-7a-***C***), 132.8 (naphthalene-3a-***C***), 128.7 (naphthanele-2-***C***H), 128.3 (naphthalene-7-***C***H, naphthalene-4-***C***H), 128.25

(naphthalene-8-***C***H), 128.1 (naphthalene-3-***C***H), 127.3 (quinoxaline-5-***C***H), 127.1 (naphthalene-6-***C***H), 127.0 (naphthalene-5-***C***H), 126.8 (quinoxaline-7-***C***H), 126.1 (quinoxaline-6-***C***H), 118.5 (nitrile-***C***N), 118.45 (quinoxaline-8-***C***H), 67.0 (cyanoacetate-2-***C***, CO_2***C***H_2).

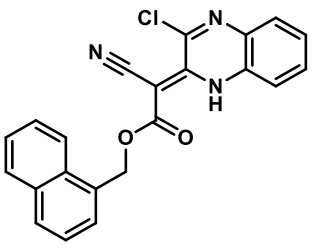

Naphthalen-1-ylmethyl (*Z*)-2-(3-chloroquinoxalin-2(1*H*)-ylidene)-2-cyanoacetate (42o). 2,3-Dichloroquinoxaline (**26**) (216 mg, 1.09 mmol, 1.0 eq.) was reacted with of naphthalen-1-ylmethyl 2-cyanoacetate (**41o**) (245 mg, 1.09 mmol, 1.0 eq.), CS_2CO_3 (1.763 g, 5.45 mmol, 4.9 eq.) in 6 mL DMF in accordance with general procedure 1(a). The reaction was monitored by TLC conditions 1:4 EtOAc: cyclohexane. The DMF was removed under high vacuum before the crude material was extracted into EtOAc (200 mL) washing with water (200 mL), 2M HCl (50 mL) and brine (70 mL). The Aqueous was back extracted with EtOAc (50 mL) before the phases were separated, dried over $MgSO_4$, filtered and concentrated under reduced pressure to give an orange solid. Recrystallisation of the crude material in EtOAc attempted but proved unsuccessful. The crude material was purified by reverse phase column chromatography on 12g C18 column using solvent conditions 10-90 % acetonitrile in water over 12 CV to yield the title compound as a yellow solid (90 mg, 21 %). R_f= 0.21 (1:4 EtOAc: cyclohexane). LC/MS *m/z* calculated for $C_{22}H_{15}ClN_3O_2$: $[M+H]^+$: 388.8, found: 185.3 fragment, t_R 3.34 min. **^{1}H NMR (400 Hz, $CDCl_3$)**- *δ* 13.49 (broad s, 1H, quinoxaline-1-N***H***), 8.10 (d, *j*= 8.4 Hz, 1H, naphthalene-4-C***H***), 7.98 (dd, *j*=14.1, 8.0 Hz, 2H, naphthalene-8-C***H***, naphthalene-5-C***H***), 7.82-7.68 (m, 2H, naphthalene-3-C***H***, naphthalene-6-C***H***), 7.68-7.38 (m, 6H, quinoxaline-5-C***H***, quinoxaline-6-C***H***, quinoxaline-7-C***H***, quinoxaline-8-C***H***, naphthalene-2-C***H***, naphthalene-7-C***H***), 5.81 (s, 2H, CO_2C***H***$_2$). **^{13}C NMR (101 Hz, $CDCl_3$)**- *δ* 169.1 (***C***=O), 152.8 (quinoxaline-2-***C***), 142.7 (quinoxaline-3-***C***), 133.3 (quinoxaline-8a-**C**), 133.0 (quinoxaline-4a-***C***), 131.5 (naphthalene-8a-***C***, naphthalene-4a-***C***), 130.9 (naphthalene-1-***C***), 129.0 (naphthalene-2-***C***H), 128.6 (naphthalene-5-***C***H), 128.1 (naphthalene-4-***C***H), 127.8 (quinoxaline-5-***C***H), 126.8 (naphthalene-7-***C***H), 126.7 (naphthalene-6-***C***H), 126.2 (naphthalene-3-***C***H),

126.1 (naphthalene-8-***C***H), 125.4 (quinoxaline-7-***C***H), 117.6 (nitrile-***C***N), 117.1 (quinoxaline-8-***C***H), 66.1 (cyanoacetate-2-***C***), 64.6 (CO_2***C***H_z).

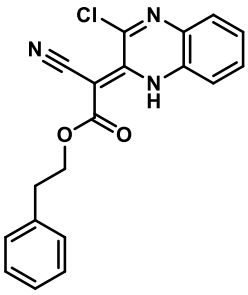

Phenethyl (*Z*)-2-(3-chloroquinoxalin-2(1*H*)-ylidene)-2-cyanoacetate (42p). 2,3-Dichloroquinoxaline (**26**) (265 mg, 1.32 mmol, 1.0 eq.) was reacted with of phenethyl 2-cyanoacetate (**41p**) (249 mg, 1.34 mmol, 1.0 eq.), CS_2CO_3 (2.150 g, 6.61 mmol, 5.0 eq.) in 10 mL DMF in accordance with general procedure 1(a). The reaction was monitored using TLC conditions 3:7 EtOAc: cyclohexane. The DMF was removed under high vacuum before the crude material was extracted into EtOAc (200 mL) washing with water (200 mL), 2M HCl (50 mL) and brine (50 mL). The aqueous was back extracted with EtOAc (50 mL) and the phases were separated, dried over $MgSO_4$, filtered and concentrated under reduced pressure to give an orange solid. The crude material was purified by column chromatography on 25g silica column using solvent conditions 0-60 % EtOAc in cyclohexane over 19 CV. The desired fractions were combined and concentrated under reduced pressure to yield the title compound as a yellow solid (180 mg, 38 %). R_f= 0.3 (3:7 EtOAc: cyclohexane). LC/MS *m/z* calculated for $C_{19}H_{15}ClN_3O_2$: $[M+H]^+$: 352.1, found: 352.0, t_R 3.20 min. **^{1}H NMR (400 Hz, $CDCl_3$)**- δ 14.43 (broad s, 1H, quinoxaline-1-N***H***), 7.80 (d, *j*= 8.1 Hz, 1H, quinoxaline-8-C***H***), 7.62 (t, *J*= 8.2 Hz, 1H, quinoxaline-7-C***H***), 7.46 (t, *j*= 8.0 Hz, 1H, quinoxaline-6-C***H***), 7.37 (d, *j*= 8.3 Hz, 1H, quinoxaline-5-C***H***), 7.35-7.3 (m, 5H, phenyl-2-C***H***, phenyl-3-C***H***, phenyl-4-C***H***, phenyl-5-C***H***, phenyl-6-C***H***), 4.48 (t, *j*= 7.1 Hz, 2H, CO_2C***H***$_2$), 3.09 (t, *j*= 7.1 Hz, 2H, CO_2CH_2C***H***$_2$). **^{13}C NMR (101 Hz, $CDCl_3$)**- δ 170.6 (***C***=O), 146.0 (quinoxaline-2-***C***), 143.6 (quinoxaline-3-***C***), 137.2 (quinoxaline-8a-***C***), 134.2 (quinoxaline-4a-***C***), 132.2 (phenyl-1-***C***), 129.0 (phenyl-3-***C***H, phenyl-5-***C***H), 128.6 (quinoxaline-5-***C***H), 128.4 (phenyl-2-***C***H, phenyl-6-***C***H), 128.1 (phenyl-4-***C***H), 126.59 (quinoxaline-7-***C***H), 126.54 (quinoxaline-6-***C***H), 117.0 (nitrile-***C***N, quinoxaline-8-***C***H), 69.2 (cyanoacetate-2-***C***), 66.5 (O***C***H_2), 35.0 (OCH_2***C***H_2).

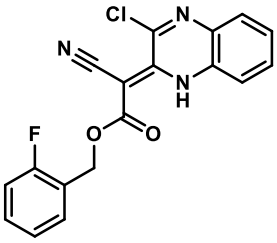

2-Fluorobenzyl (*Z*)-2-(3-chloroquinoxalin-2(1*H*)-ylidene)-2-cyanoacetate (42q). 2,3-Dichloroquinoxaline (**26**) (225 mg, 1.13 mmol, 1.2 eq.) was reacted with 2-fluorobenzyl 2-cyanoacetate (**41q**) (269 mg, 1.39 mmol, 1.0 eq.), CS_2CO_3 (2.243 g, 6.88 mmol, 5.0 eq.) in 10 mL DMF in accordance with general procedure 1(b). The reaction was monitored by TLC conditions 1:9 MeOH: DCM. The DMF was removed under high vacuum before the crude material was extracted into EtOAc (200 mL) washing with water (200 mL), 2M HCl (50 mL) and brine (50 mL). The phases were separated, dried over $MgSO_4$, filtered and concentrated under reduced pressure. The crude material was purified by column chromatography on a 25g silica column using solvent system 10 % cyclohexane in DCM over 13 CV. The desired fractions were combined and concentrated under reduced pressure to yield the title compound as a yellow solid (208 mg, 42 %). R_f= 0.37 (10 % MeOH in DCM). LC/MS *m/z* calculated for $C_{18}H_{12}ClFN_3O_2$: $[M+H]^+$: 356.1, found: 356.2, t_R 2.93 min. **^{1}H NMR (400 Hz, $CDCl_3$)**- δ 14.41 (broad s, 1H, quinoxaline-1-N***H***), 7.82 (d, *j*= 8.2 Hz, 1H, quinoxaline-8-C**H**), 7.63 (t, *j*= 7.4 Hz, 1H, quinoxaline-7-C***H***), 7.54 (t, *j*= 7.6 Hz, 1H, benzyl-4-C***H***), 7.48 (t, *j*= 7.4 Hz, 1H, quinoxaline-6-C***H***), 7.40 (d, *j*= 8.3 Hz, 1H, quinoxaline-5-C***H***), 7.33 (q, *j*= 7.0 Hz, 1H, benzyl-6-C***H***), 7.19 (t, *j*= 7.6 Hz, 1H, benzyl-3-C***H***), 7.09 (t, *j*= 9.8 Hz, 1H, benzyl-5-C***H***), 5.44 (s, 2H, CO_2CH_z). **^{13}C NMR (101 Hz, $CDCl_3$)**- δ 171.0 (***C***=O), 159.7 (benzyl-2-***C***), 146.7 (quinoxaline-2-***C***),144.2 (quinoxaline-3-***C***), 134.9 (quinoxaline-8a-***C***), 132.9 (quinoxaline-4a-***C***), 130.7 (benzyl-4-***C***H), 130.6 (benzyl-6-***C***H), 130.3 (benzyl-1-***C***), 129.3 (quinoxaline-5-***C***H), 128.7 (benzyl-5-***C***H), 127.3 (quinoxaline-7-***C***H), 125.0 (quinoxaline-6-***C***H), 117.1 (benzyl-3-***C***H), 116.8 (nitrile-***C***N), 116.0 (quinoxaline-8-***C***H), 69.7 (cyanoacetate-2-***C***), 61.6 (CO_2CH_2).**^{19}F NMR (377 Hz, $CDCl_3$)**- δ -118.05 (t, *j*= 11.4 Hz, 1F, C***F***).

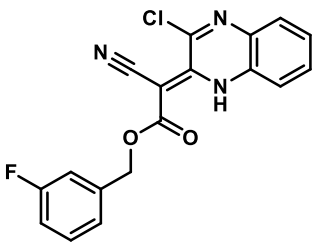

3-Fluorobenzyl (*Z*)-2-(3-chloroquinoxalin-2(1*H*)-ylidene)-2-cyanoacetate (42r). Conducted by student Ng Yu Yang. 2,3-Dichloroquinoxaline (**26**) (155 mg, 0.78 mmol, 1.0 eq.) was reacted with of 3-fluorobenzyl 2-cyanoacetate (**41r**) (149 mg, 0.77 mmol, 1.0 eq.), CS_2CO_3 (1.253 g, 3.85 mmol, 5.0 eq.) in 10

mL DMF in accordance with general procedure 1(b). The reaction was monitored by TLC conditions 1:9 cyclohexane: chloroform. The DMF was removed under high vacuum before the crude material was extracted into EtOAc (200 mL) washing with water (200 mL), 2M HCl (50 mL) and brine (50 mL). The phases were separated, dried over $MgSO_4$, filtered and concentrated under reduced pressure. The crude material was purified by column chromatography on a 25g silica column using solvent system 10 % cyclohexane in chloroform over 10 CV. The desired fractions were combined and concentrated under reduced pressure to yield the title compound as a yellow solid (97 mg, 35 %). R_f= 0.38 (1:9 cyclohexane: chloroform). **^{1}H NMR (400 Hz, $CDCl_3$)**- δ 14.39 (broad s, 1H, quinoxaline-1-N***H***), 7.82 (d, *j*= 8.2 Hz, 1H, quinoxaline-8-C***H***), 7.63 (t, *j*= 7.6 Hz, 1H, quinoxaline-7-C***H***), 7.48 (t, *j*= 7.8 Hz, 1H, quinoxaline-6-C***H***), 7.41 (d, *j*= 8.4 Hz, 1H, quinoxaline-5-C***H***), 7.39-7.32 (m, 1H, benzyl-5-C***H***), 7.24 (d, *j*= 8.2 Hz, 1H, benzyl-6-C***H***), 7.16 (d, *j*= 9.2 Hz, 1H, benzyl-4-C***H***), 7.03 (t, *j*= 8.5 Hz, 1H, benzyl-2-C***H***), 5.35 (s, 2H, $CO_2C\boldsymbol{H}_2$).**^{13}C NMR (101 Hz, $CDCl_3$)**- δ 164.6 (***C***=O), 162.1 (benzyl-3-***C***), 146.7 (quinoxaline-2-***C***), 144.2 (quinoxaline-3-***C***), 138.3 (benzyl-1-***C***), 135.0 (quinoxaline-8a-***C***), 132.9 (quinoxaline-4a-***C***), 130.8 (benzyl-5-***C***H), 129.3 (quinoxaline-5-***C***H), 128.6 (quinoxaline-7-***C***H), 127.4 (quinoxaline-6-***C***H), 123.6 (benzyl-6-***C***H), 117.8 (benzyl-4-***C***H), 116.8 (benzyl-2-***C***H), 115.8 (nitrile-***C***N), 115.2 (quinoxaline-8-***C***H), 69.6 (cyanoacetate-2-***C***), 66.9 ($CO_2\boldsymbol{C}H_2$). **^{19}F NMR (377 Hz, $CDCl_3$)**- δ -113.37 (td, *j*= 8.8, 4.4 Hz, 1F, C***F***).

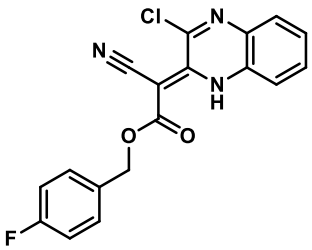

4-Fluorobenzyl (*Z*)-2-(3-chloroquinoxalin-2(1*H*)-ylidene)-2-cyanoacetate (42s). Conducted by student Ng Yu Yang. 2,3-Dichloroquinoxaline (**26**) (136 mg, 0.70 mmol, 1.0 eq.) was reacted with of 4-fluorobenzyl 2-cyanoacetate (**41s**) (130 mg, 0.67 mmol, 1.0 eq.), CS_2CO_3 (1.103 g, 3.39 mmol, 5.1 eq.) in 10 mL DMF in accordance with general procedure 1(b). The reaction was monitored by TLC conditions 1:9 MeOH: DCM. The DMF was removed under high vacuum before the crude material was extracted into EtOAc (200 mL) washing with water (200 mL), 2M HCl (50 mL) and brine (50 mL). The phases were separated, dried over $MgSO_4$, filtered and concentrated under reduced pressure. The crude material was purified by column

chromatography on a 25g silica column using solvent conditions 3-15 % MeOH in DCM over 16 CV. The desired fractions were combined and concentrated under reduced pressure to yield the title compound as a yellow solid (135 mg, 56 %). R_f= 0.84 (1:9 MeOH: DCM). **^{1}H NMR (400 Hz, $CDCl_3$)**- δ 14.40 (broad s, 1H, quinoxaline-1-N***H***), 7.82 (d, *j*= 8.1 Hz, 1H, quinoxaline-8-C***H***), 7.62 (t, *j*= 7.7 Hz, 1H, quinoxaline-7-C***H***), 7.50- 7.37 (m, 4H, quinoxaline-5-C***H***, quinoxaline-6-C***H***, benzyl-2-C***H***, benzyl-6-C***H***), 7.07 (t, *j*= 6.7 Hz, 2H, benzyl-3-C***H***, benzyl-5-C***H***), 5.30 (s, 2H, CO_2CH_2). **^{13}C NMR (101 Hz, $CDCl_3$)**- δ 164.4 (***C***=O), 162.0 (F***C***), 146.7 (quinoxaline-2-***C***), 144.1 (quinoxaline-3-***C***), 134.9 (quinoxaline-8a-***C***), 132.9 (quinoxaline-4a-***C***), 131.6 (benzyl-1-***C***), 123.4 (benzyl-2-***C***H, benzyl-6-***C***H), 129.3 (quinoxaline-5-***C***H), 128.6 (quinoxaline-7-***C***H), 127.3 (quinoxaline-6-***C***H), 117.0 (benzyl-5-***C***H, benzyl-3-***C***H), 116.9 (nitrile-***C***N), 116.2 (quinoxaline-8-***C***H), 69.7 (cyanoacetate-2-***C***), 67.1 (CO_2CH_2). **^{19}F NMR (377 Hz, $CDCl_3$)**- δ -113.37 (td, *j*= 8.8, 4.4 Hz, 1F, C***F***).

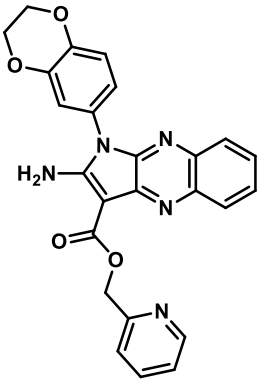

Pyridin-2-ylmethyl 2-amino-1-(2,3-dihydrobenzo[*b*][1,4]dioxin-6-yl)-1*H*-pyrrolo[2,3-*b*]quinoxaline-3-carboxylate (40a). Conducted by student Sam Robinson. 2,3-Dihydrobenzo[*b*][1,4]dioxin-6-amine (**29**) (58 mg, 0.38 mmol, 1.4 eq.) was reacted with pyridin-2-ylmethyl (*Z*)-2-(3-chloroquinoxalin-2(1*H*)-ylidene)-2-cyanoacetate (**42a**) (90 mg, 0.27 mmol, 1.0 eq.) in 9 mL EtOH and 3 mL THF in accordance with general procedure 2. The reaction was monitored by TLC conditions 1:99 MeOH: DCM. The solvent was removed under reduced pressure and the crude material purification was attempted using column chromatography on a 12g silica column with solvent conditions 0.5-3 % MeOH in DCM over 12 CV. The desired fractions were combined and concentrated under reduced pressure, NMR identified impurities present. A prep plate was ran first at 1% MeOH in DCM followed by 3% MeOH in DCM. The desired silica band was removed, sonicated in 10% MeOH in DCM then filtered and concentrated under reduced pressure to yield the title compound as a cream solid (43 mg, 36 %). R_f= 0.3 (1:99 MeOH: DCM). LC/MS *m/z* calculated for $C_{25}H_{20}N_5O_4$: $[M+H]^+$: 454.1, found: 454.2, t_R 3.91 min (long run). HRMS (TOF ES^+) calculated: 454.1510, found: 454.1505. **^{1}H NMR**

(400 Hz, $CDCl_3$)- δ 8.59 (d, *j*= 4.8 Hz, 1H, pyridine-3-C**H**), 8.15 (d, *j*= 8.3 Hz, 1H, pyridine-6-C***H***), 7.93 (d, *j*= 7.9 Hz, 1H, pyrroloquinoxaline-5-C***H***), 7.88 (d, *j*= 8.3 Hz, 1H, pyrroloquinoxaline-8-C***H***), 7.78 (t, *j*= 7.6 Hz, 1H, pyridine-5-C***H***), 7.58 (t, *j*= 5.6 Hz, 1H, pyrroloquinoxaline-6-C***H***), 7.50 (t, *j*= 7.6 Hz, 1H, pyrroloquinoxaline-7-C***H***), 7.23 (t, *j*= 6.3 Hz, 1H, pyridine-4-C***H***), 7.05 (m, 2H, benzodioxane-5-C***H***, benzodioxane-7-C***H***), 6.97 (d, *j*= 8.7 Hz, 1H, benzodioxane-8-C***H***), 5.62 (s, 2H, CO_2CH_2), 4.32 (s, 4H, benzodioxane-2-CH_2, benzodioxane-3-CH_2).**^{13}C NMR (101 Hz, $CDCl_3$)**- δ 159.3 (***C***=O), 157.1 (pyridine-1-***C***), 149.2 (pyridine-3-***C***H), 145.1 (pyrroloquinoxaline-8a-***C***), 144.8 (benzodioxane-8a-***C***, benzodioxane-4a-***C***), 143.1 (pyrroloquinoxaline-9a-***C***, pyrroloquinoxaline-3a-***C***), 141.5 (pyrroloquinoxaline-4a-***C***), 141.4 (benzodioxane-6-***C***), 137.8 (pyridine-5-***C***H), 137.0 (pyridine-6-***C***H), 128.6 (pyrroloquinoxaline-8-***C***H), 128.1 (pyrroloquinoxaline-6-***C***H), 127.0 (pyrroloquinoxaline-7-***C***H), 126.3 (pyrroloquinoxaline-3-***C***), 124.4 (pyrroloquinoxaline-2-***C***), 122.6 (pyridine-4-***C***H), 121.7 (benzodioxane-8-***C***H), 121.2 (pyrroloquinoxaline-5-***C***H), 119.0 (benzodioxane-7-***C***H), 117.4 (benzodioxane-5-***C***H). 65.9 (CO_2***C***H_2), 64.5 (benzodioxane-2-***C***H_2), 64.4 (benzodioxane-3-***C***H_2).

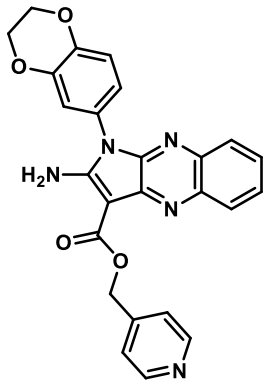

Pyridin-4-ylmethyl 2-amino-1-(2,3-dihydrobenzo[*b*][1,4]dioxin-6-yl)-1*H*-pyrrolo[2,3-*b*]quinoxaline-3-carboxylate (40c). 2,3-Dihydrobenzo[*b*][1,4]dioxin-6-amine (**29**) (63 mg, 0.42 mmol, 1.8 eq.) was reacted with pyridin-4-ylmethyl (*Z*)-2-(3-chloroquinoxalin-2(1*H*)-ylidene)-2-cyanoacetate (**42c**) (78 mg, 0.23 mmol, 1.0 eq.) in 9 mL EtOH and 3 mL THF in accordance with general procedure 2. The reaction was monitored by TLC conditions 3:97 MeOH: DCM. The solvent was removed under reduced pressure and the crude material was purified by column chromatography on a 12g silica column using solvent conditions 1-10 % MeOH in DCM over 12 CV. The desired fractions were combined and concentrated under reduced pressure to yield the title compound as a cream solid (47 mg, 45 %). R_f= 0.29 (3:97 MeOH: DCM). LC/MS *m/z* calculated for $C_{25}H_{20}N_5O_4$: $[M+H]^+$: 454.1, found: 454.1, t_R 4.51 min (long run). HRMS (TOF ES^+) calculated: 454.1510, found: 454.1500. **^{1}H**

NMR (400 Hz, DMSO-*d*$_6$)- *δ* 8.62 (d, *j*= 4.6 Hz, 2H, pyridine-3-C***H***, pyridine-5-C***H***), 8.02-7.94 (m, 3H, pyrroloquinoxaline-5-C***H***, amine-N***H***$_2$), 7.77 (d, *j*= 8.2 Hz, 1H, pyrroloquinoxaline-8-C***H***), 7.67 (d, *j*= 5.0 Hz, 2H, pyridine-2-C***H***, pyridine-6-C***H***), 7.59 (t, *j*= 7.1 Hz, 1H, pyrroloquinoxaline-6-C***H***), 7.50 (t, *j*= 7.6 Hz, 1H, pyrroloquinoxaline-7-C***H***), 7.17-7.07 (m, 2H, benzodioxane-5-C***H***, benzodioxane-7-C***H***), 7.03 (d, 8.5 Hz, 1H, benzodioxane-8-C***H***), 5.46 (s, 2H, CO_2C***H***$_2$), 4.35 (s, 4H, benzodioxane-2-C***H***$_2$, benzodioxane-3-C***H***$_2$). **^{13}C NMR (101 Hz, DMSO-*d*$_6$)**- *δ* 164.8 (***C***=O), 160.8 pyrroloquinoxaline-8a-***C***), 150.1 (pyridine-3-***C***H, pyridine-5-***C***H), 147.1 (pyridine-1-***C***), 144.9 (benzodioxane-8a-***C***), 144.4 (benzodioxane-4a-***C***), 143.9 (pyrroloquinoxaline-9a-***C***), 142.1 (pyrroloquinoxaline-3a-***C***), 141.2 (pyrroloquinoxaline-4a-***C***), 137.5 (benzodioxane-6-***C***), 128.2 (pyrroloquinoxaline-5-***C***H), 127.9 (pyrroloquinoxaline-8-***C***H), 127.0 (pyrroloquinoxaline-6-***C***H), 126.1 (pyrroloquinoxaline-7-***C***H), 125.2 (pyrroloquinoxaline-2-***C***), 122.4 (benzodioxane-8-***C***H), 121.9 (pyridine-2-***C***H, pyridine-6-***C***H), 118.5 (benzodioxane-7-***C***H), 118.4 (benzodioxane-5-***C***H), 81.0 (pyrroloquinoxaline-3-***C***), 64.7 (benzodioxane-2-***C***H$_2$), 64.6 (benzodioxane-3-***C***H$_2$), 63.0 (CO_2***C***H$_2$).

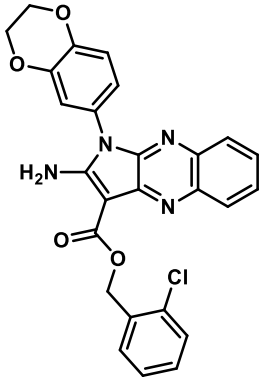

2-Chlorobenzyl 2-amino-1-(2,3-dihydrobenzo[*b*][1,4]dioxin-6-yl)-1*H*-pyrrolo[2,3-*b*]quinoxaline-3-carboxylate (40d). Conducted by student Ng Yu Yang. 2,3-Dihydrobenzo[*b*][1,4]dioxin-6-amine (**29**) (124 mg, 0.82 mmol, 1.5 eq.) was reacted with 2-chlorobenzyl (*Z*)-2-(3-chloroquinoxalin-2(1*H*)-ylidene)-2-cyanoacetate (**42d**) (205 mg, 0.55 mmol, 1.0 eq.) in 7.5 mL EtOH and 2.5 mL THF in accordance with general procedure 2. The reaction was monitored by LCMS. A white precipitate crashed out which was filtered under vacuum washing with cold MeOH (10 mL). The crude material was purified by reverse phase column chromatography on a 12g C18 column using solvent conditions 10-90 % acetonitrile in water over 12 CV. The desired fractions were combined and concentrated under reduced pressure to yield a white solid (116 mg, 80 %). LC/MS *m/z* calculated for $C_{26}H_{20}ClN_4O_4$:$[M+H]^+$: 487.1, found: 487.0, t_R 2.95 min. HRMS (TOF ES$^+$) calculated: 487.1168, found: 487.1183. **^{1}H NMR (400 Hz, DMSO-*d*$_6$)**- *δ* 8.10 (d, *j*= 7.7 Hz, 1H, benzyl-3-C***H***), 7.96 (m, 3H, amine-N***H***$_2$, pyrroloquinoxaline-5-C***H***),

7.77 (d, *j*= 8.4 Hz, 1H, pyrroloquinoxaline-8-C***H***), 7.59 (t, *j*= 7.1 Hz, 1H, pyrroloquinoxaline-6-C***H***), 7.55-7.47 (m, 3H, pyrroloquinoxaline-7-C***H***, benzyl-4-C***H***, benzyl-6-C***H***), 7.39 (t, *j*= 7.7 Hz, 1H, benzyl-5-C***H***), 7.17-7.07 (m, 2H, benzodioxane-5-C***H***, benzodioxane-7-C***H***), 7.03 (d, *j*= 8.6 Hz, 1H, benzodioxane-8-C***H***), 5.47 (s, 2H, $CO_2C\boldsymbol{H}_2$), 4.35 (s, 4H, benzodioxane-2-C$\boldsymbol{H}_2$, benzodioxane-3-C$\boldsymbol{H}_2$). **^{13}C NMR (101 Hz, DMSO-*d*$_6$)**- *δ* 164.6 (***C***=O), 160.8 (pyrroloquinoxaline-8a-***C***), 145.0 (benzodioxane-8a-***C***), 144.4 (benzodioxane-4a-***C***), 143.9 (pyrroloquinoxaline-9a-***C***), 142.1 (pyrroloquinoxaline-3a-***C***), 141.1 (pyrroloquinoxaline-4a-***C***), 137.5 (benzodioxane-6-***C***), 135.4 (benzyl-1-***C***), 131.7 (benzyl-2-***C***), 129.6 (benzyl-3-***C***H), 129.5 (benzyl-4-***C***H), 129.3 (benzyl-6-***C***H), 128.2 (pyrroloquinoxaline-5-***C***H), 128.0 (pyrroloquinoxaline-8-***C***H), 127.8 (benzyl-5-***C***H), 127.0 (pyrroloquinoxaline-6-***C***H), 126.2 (pyrroloquinoxaline-7-***C***H), 125.2 (pyrroloquinoxaline-2-***C***), 122.4 (benzodioxane-8-***C***H), 118.5 (benzodioxane-7-***C***H), 118.4 (benzodioxane-5-***C***H), 81.0 (pyrroloquinoxaline-3-***C***), 64.7 (benzodioxane-2-***C***H_2), 64.6 (benzodioxane-3-***C***H_2), 61.6 ($CO_2\boldsymbol{C}H_2$).

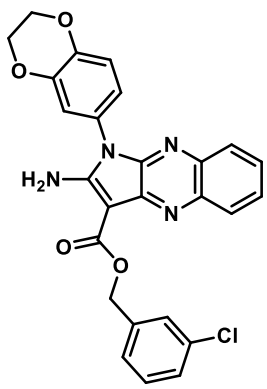

3-Chlorobenzyl 2-amino-1-(2,3-dihydrobenzo[*b*][1,4]dioxin-6-yl)-1*H*-pyrrolo[2,3-*b*]quinoxaline-3-carboxylate (40e). 2,3-Dihydrobenzo[*b*][1,4]dioxin-6-amine (**29**) (82 mg, 0.54 mmol, 1.5 eq.) was reacted with 3-chlorobenzyl (*Z*)-2-(3-chloroquinoxalin-2(1*H*)-ylidene)-2-cyanoacetate (**42e**) (135 mg, 0.36 mmol, 1.0 eq.) in 7.5 mL EtOH and 2.5 mL THF in accordance with general procedure 2. The reaction was monitored by LCMS. A white precipitate crashed out upon cooling which was filtered under vacuum washing with cold MeOH (10 mL) to yield a white solid (50 mg, 28 %). LC/MS *m/z* calculated for $C_{26}H_{20}ClN_4O_4$:$[M+H]^+$: 487.1, found: 487.2, t_R 6.03 min (long run). HRMS (TOF ES$^+$) calculated: 487.1168, found: 487.1173. **^{1}H NMR (400 Hz, DMSO-*d*$_6$)**- *δ* 8.15- 8.04 (m, 3H, amine-N$\boldsymbol{H}_2$, pyrroloquinoxaline-5-C***H***), 7.92 (s, 1H, benyl-2-C***H***), 7.79 (d, *j*= 8.2 Hz, 1H, pyrroloquinoxaline-8-C***H***), 7.65-7.36 (m, 5H, pyrroloquinoxaline-7-C***H***, pyrroloquinoxaline-6-C***H***, benzyl-4-C***H***, benzyl-5-C***H***, benzyl-6-C***H***), 7.17-7.07 (m, 2H, benzodioxane-5-C***H***, benzodioxane-7-C***H***), 7.03 (d, *j*= 8.8 Hz, 1H, benzodioxane-8-C***H***), 5.44 (s, 2H, $CO_2C\boldsymbol{H}_2$), 4.35 (s, 4H, benzodioxane-2-C$\boldsymbol{H}_2$, benzodioxane-3-C$\boldsymbol{H}_2$).**^{13}C NMR**

(101 Hz, DMSO-d_6)- δ 164.5 (***C***=O), 160.9 (pyrroloquinoxaline-8a-***C***), 145.1 (benzodioxane-8a-***C***, benzodioxane-4a-***C***), 144.4 (pyrroloquinoxaline-9a-***C***, pyrroloquinoxaline-3a-***C***), 140.5 (pyrroloquinoxaline-4a-***C***, benzyl-1-***C***), 137.3 (benzodioxane-6-***C***), 133.6 (benzyl-3-***C***), 130.7 (benzyl-5-***C***H), 128.1 (pyrroloquinoxaline-5-***C***H), 127.8 (pyrroloquinoxaline-8-***C***H, benzyl-4-***C***H), 127.5 (pyrroloquinoxaline-6-***C***H), 127.4 (benzyl-2-***C***H), 126.4 (benzyl-6-***C***H), 126.1 (pyrroloquinoxaline-7-***C***H), 125.0 (pyrroloquinoxaline-2-***C***), 122.4 (benzodioxane-8-***C***H), 118.5 (benzodioxane-7-***C***H), 118.4 (benzodioxane-5-***C***H), 81.4 (pyrroloquinoxaline-3-***C***), 64.7 (benzodioxane-2-***C***H_2), 64.6 (benzodioxane-3-***C***H_2), 63.8 (CO_2***C***H_2).

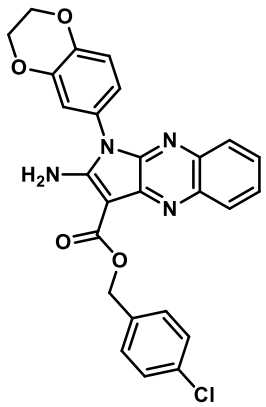

4-Chlorobenzyl 2-amino-1-(2,3-dihydrobenzo[*b*][1,4]dioxin-6-yl)-1*H*-pyrrolo[2,3-b]quinoxaline-3-carboxylate (40f). Conducted by student Bulbul Singh. 2,3-Dihydrobenzo[*b*][1,4]dioxin-6-amine (**29**) (27 mg, 0.17 mmol, 1.3 eq.) was reacted with 4-chlorobenzyl (*Z*)-2-(3-chloroquinoxalin-2(1*H*)-ylidene)-2-cyanoacetate (**42f**) (50 mg, 0.13 mmol, 1.0 eq.) in 7.5 mL EtOH and 2.5 mL THF in accordance with general procedure 2. The reaction was monitored by TLC conditions 1:1 EtOAc: cyclohexane. A white precipitate crashed out upon cooling which was filtered under vacuum washing with cold MeOH (10 mL) to yield a white solid. The crude material was purified by column chromatography on a 12g silica column using solvent conditions 30-70 % EtOAc in cyclohexane over 10 CV. The desired fractions were combined and concentrated under reduced pressure to yield a white solid of the title compound (28 mg, 44 %). R_f= 0.23 (1:1 EtOAc: cyclohexane). LC/MS *m/z* calculated for $C_{26}H_{20}ClN_4O_4$:$[M+H]^+$: 487.1, found: 487.1, t_R 6.19 min (long run). HRMS (TOF ES^+) calculated: 487.1168, found: 487.1165. **^{1}H NMR (400 Hz, DMSO-d_6)**- δ 8.00-7.92 (m, 3H, amine-N***H***$_2$, pyrroloquinoxaline-5-C***H***), 7.76 (d, *j*= 8.3 Hz, 1H, pyrroloquinoxaline-8-C***H***), 7.68 (d, *j*= 7.8 Hz, 2H, benzyl-3-C***H***, benzyl-5-C***H***), 7.58 (t, *j*= 6.9 Hz, 1H, pyrroloquinoxaline-6-C***H***), 7.50-7.46 (m, 3H, benzyl-2-C***H***, benzyl-6-C***H***, pyrroloquinoxaline-7-C***H***), 7.12 (m, 2H, benzodioxane-7-C***H***, benzodioxane-5-C***H***), 7.02

(d, *j*=8.6 Hz, 1H, benzodioxane-8-C***H***), 5.42 (s, 2H, CO_2C***H***), 4.35 (s, 4H, benzodioxane-3-C***H***$_2$, benzodioxane-2-C***H***$_2$). **^{13}C NMR (101 Hz, DMSO-*d*$_6$)**- *δ* 164.9 (***C***=O), 160.7 (pyrroloquinoxaline-8a-***C***), 144.9 (benzodioxane-8a-***C***), 144.4 (benzodioxane-4a-***C***), 143.8 (pyrroloquinoxaline-9a-***C***, pyrroloquinoxaline-3a-***C***), 142.0 (pyrroloquinoxaline-4a-***C***), 137.5 (benzodioxane-6-***C***), 137.1 (benzyl-1-***C***), 132.5 (benzyl-4-***C***), 129.5 (benzyl-2-***C***H, benzyl-6-***C***H), 128.8 (benzyl-3-***C***H, benzyl-5-***C***H), 128.2 (pyrroloquinoxaline-5-***C***H), 127.0 (pyrroloquinoxaline-8-***C***H), 126.1 (pyrroloquinoxaline-6-***C***H), 125.2 (pyrroloquinoxaline-7-***C***H), 123.9 (pyrroloquinoxaline-2-***C***), 122.4 (benzodioxane-8-***C***H), 118.5 (benzodioxane-7-***C***H), 118.4 (pyrroloquinoxaline-5-***C***H), 91.8 (pyrroloquinoxaline-3-***C***), 64.6 (benzodioxane-2-***C***H_2), 63.7 (benzodioxane-3-***C***H_2).

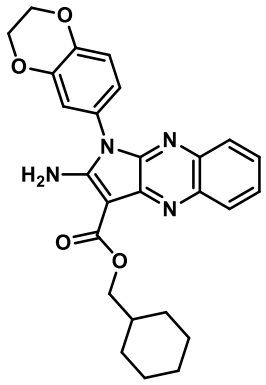

Cyclohexylmethyl 2-amino-1-(2,3-dihydrobenzo[*b*][1,4]dioxin-6-yl)-1*H*-pyrrolo[2,3-*b*]quinoxaline-3-carboxylate (40g). 2,3-Dihydrobenzo[*b*][1,4]dioxin-6-amine (**29**) (57 mg, 0.38 mmol, 1.4 eq.) was reacted with cyclohexylmethyl (*Z*)-2-(3-chloroquinoxalin-2(1*H*)-ylidene)-2-cyanoacetate (**42g**) (92 mg, 0.27 mmol, 1.0 eq.) in 7.5 mL EtOH and 2.5 mL THF in accordance with general procedure 2. The reaction was monitored by TLC using solvent conditions 1:4 EtOAc: cyclohexane. A white precipitate crashed out upon cooling which was filtered under vacuum washing with cold MeOH (10 mL) to yield a white solid of the title compound (44 mg, 36 %). R_f= 0.00 (20 % EtOAc in cyclohexane). LC/MS *m/z* calculated for $C_{26}H_{27}N_4O$: $[M+H]^+$: 459.2, found: 459.3, t_R 3.05 min. HRMS (TOF ES$^+$) calculated: 459.2027, found: 459.2038. **^{1}H NMR (400 Hz, $CDCl_3$)**- *δ* 8.11 (d, *j*= 8.5 Hz, 1H, pyrroloquinoxaline-5-C***H***), 7.88 (d, *j*= 8.5 Hz, 1H, pyrroloquinoxaline-8-C***H***), 7.58 (t, *j*= 7.0 Hz, 1H, pyrroloquinoxaline-6-C***H***), 7.49 (t, *j*= 8.2 Hz, 1H, pyrroloquinoxaline-7-C***H***), 7.13-7.01 (m, 2H, benzodioxane-7-C***H***, benzodioxane-5-C***H***), 7.00-6.94 (m, 1H, benzodioxane-8-C***H***), 4.34 (s, 4H, benzodioxane-2-C***H***$_2$, benzodioxane-3-C***H***$_2$), 4.27 (d, *j*= 6.4 Hz, 2H, CO_2C***H***$_2$), 2.06-1.67 (m, 6H, cyclohexane-1-C***H***, 1x cyclohexane-2-C***H***$_2$, 1x cyclohexane-3-C***H***$_2$, 1x cyclohexane-4-C***H***$_2$, 1x cyclohexane-5-C***H***$_2$, 1x cyclohexane-6-C***H***$_2$), 1.42-1.10 (m, 5H, 1x cyclohexane-2-C***H***$_2$, 1x cyclohexane-3-C***H***$_2$, 1x cyclohexane-

4-C***H***$_2$, 1x cyclohexane-5-C***H***$_2$, 1x cyclohexane-6-C***H***$_2$). **^{13}C NMR (101 Hz, CDCl$_3$)**- δ 166.1 (***C***=O), 158.9 (pyrroloquinoxaline-8a-***C***), 144.9 (benzodioxane-8a-***C***), 144.7 (benzodioxane-4a-***C***), 142.8 (pyrroloquinoxaline-9a-***C***), 141.5 (pyrroloquinoxaline-3a-***C***), 141.4 (pyrroloquinocaline-4a-***C***), 137.6 (benzodioxane-6-***C***), 128.7 (pyrroloquinoxaline-5-***C***H), 127.9 (pyrroloquinoxaline-8-***C***H), 126.7 (pyrroloquinoxaline-6-***C***H), 126.1 (pyrroloquinoxaline-7-***C***H), 124.4 (pyrroloquinoxaline-2-***C***), 121.0 (benzodioxane-8-***C***H), 118.9 (benzodioxane-7-***C***H), 117.2 (benzodioxane-5-***C***H), 82.9 (pyrroloquinoxaline-3-***C***), 69.0 (CO_2***C***H_2), 64.4 (benzodioxane-2-***C***H_2), 64.3 (benzodioxane-3-***C***H_2), 37.6 (cyclohexane-1-***C***H), 29.9 (cyclohexane-2-***C***H_2, cyclohexane-6-***C***H_2), 26.6 (cyclohexane-4-***C***H_2), 25.9 (cyclohexane-3-***C***H_2, cyclohexane-5-***C***H_2).

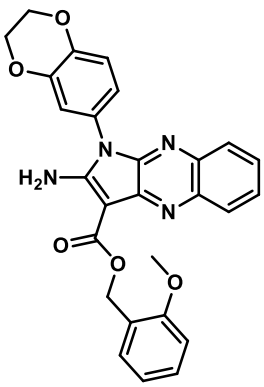

2-Methoxybenzyl 2-amino-1-(2,3-dihydrobenzo[*b*][1,4]dioxin-6-yl)-1*H*-pyrrolo[2,3-*b*]quinoxaline-3-carboxylate (40h). **Conducted by student Bulbul Singh.** 2,3-Dihydrobenzo[*b*][1,4]dioxin-6-amine (**29**) (79 mg, 0.5 mmol, 1.3 eq.) was reacted with 2-methoxybenzyl (*Z*)-2-(3-chloroquinoxalin-2(1*H*)-ylidene)-2-cyanoacetate (**42h**) (148 mg, 0.4 mmol, 1.0 eq.) in 2.5 mL EtOH and 2.5 mL THF in accordance with general procedure 2. The reaction was monitored by LCMS. The solvent was removed under reduced pressure and the crude material recrystalised in hot MeOH to yield the title compound as a light brown solid (67 mg, 35 %). LC/MS *m/z* calculated for $C_{27}H_{23}N_4O_5$: $[M+H]^+$: 483.2, found: 483.2, t_R 4.98 min. HRMS (TOF ES$^+$) calculated: 483.1663, found: 483.1660. **^{1}H NMR (400 Hz, DMSO-*d*$_6$)**- δ 7.94 (m, 3H, amine-N***H***$_2$, pyrroloquinoxaline-5-C***H***), 7.84 (d, *j*= 7.4 Hz, 1H, benzyl-6-C***H***), 7.77 (d, *j*= 8.2 Hz, 1H, pyrroloquinoxaline-8-C***H***), 7.58 (t, *j*= 7.0 Hz, 1H, pyrroloquinoxaline-6-C***H***), 7.49 (t, *j*= 7.6 Hz, 1H, pyrroloquinoxaline-7-C***H***), 7.33 (t, *j*= 7.8 Hz, 1H, benzyl-5-C***H***), 7.16-6.99 (m, 5H, benzodioxane-5-C***H***, benzodioxane-7-C***H***, benzodioxane-8-C***H***, benzyl-3-C***H***, benzyl-4-C***H***), 5.38 (s, 2H, CO_2C***H***$_2$), 4.35 (s, 4H, benzodioxane-2-C***H***$_2$, benzodioxane-3-C***H***$_2$), 3.87 (s, 3H, C***H***$_3$O).**^{13}C NMR (101 Hz, DMSO-*d*$_6$)**- δ 164.1 (***C***=O), 160.0 (benzyl-2-***C***),

156.1 (pyrroloquinoxaline-8a-***C***), 144.3 (benzodioxane-4a-***C***), 143.7 (benzodioxane-8a-***C***), 143.2 (pyrroloquinoxaline-9a-***C***, pyrroloquinoxaline-3a-***C***), 141.4 (pyrroloquinoxaline-4a-***C***), 136.8 (benzodioxane-6-***C***), 128.5 (benzyl-6-***C***H), 127.7 (benzyl-4-***C***H), 127.4 (pyrroloquinoxaline-5-***C***H), 127.3 (pyrroloquinoxaline-8-***C***H), 126.3 (pyrroloquinoxaline-7-***C***H, pyrroloquinoxaline-6-***C***H), 125.4 (benzyl-3-***C***H), 125.0 (benzyl-5-***C***H), 124.5 (pyrroloquinoxaline-2-***C***), 121.7 (benzyl-1-***C***), 120.1 (benzodioxane-8-***C***H), 117.8 (benzodioxane-7-***C***H), 117.7 (benzodioxane-5-***C***H), 80.6 (pyrroloquinoxaline-3-***C***), 64.0 (benzodioxande-3-***C***H_2), 63.9 (benzodioxane-2-***C***H_2), 59.6 (CO_2***C***H_2), 55.3 (***C***H_3O).

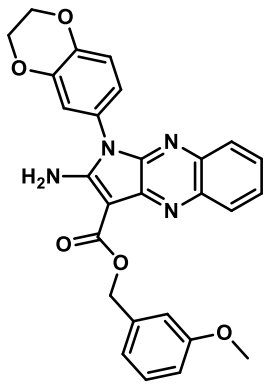

3-Methoxybenzyl 2-amino-1-(2,3-dihydrobenzo[*b*][1,4]dioxin-6-yl)-1*H*-pyrrolo[2,3-*b*]quinoxaline-3-carboxylate (40i). **Conducted by student Bulbul Singh.** 2,3-Dihydrobenzo[*b*][1,4]dioxin-6-amine (**29**) (102 mg, 0.67 mmol, 1.6 eq.) was reacted with 3-methoxybenzyl (*Z*)-2-(3-chloroquinoxalin-2(1*H*)-ylidene)-2-cyanoacetate (**42i**) (154 mg, 0.41 mmol, 1.0 eq.) in 2.5 mL EtOH and 2.5 mL THF in accordance with general procedure 2. The reaction was monitored by LCMS. A white precipitate crashed out upon cooling which was filtered under vacuum washing with cold MeOH (10 mL) to yield a white solid of the title compound (61 mg, 47 %). LC/MS *m/z* calculated for $C_{27}H_{23}N_4O_5$: $[M+H]^+$: 483.2, found: 483.2, t_R 2.75 min. HRMS (TOF ES^+) calculated: 483.1663, found: 483.1664. **^{1}H NMR (400 Hz, DMSO-*d*$_6$)**- *δ* 7.99-7.92 (m, 3H, N***H***$_2$, pyrroloquinoxaline-5-C***H***), 7.76 (d, *j*= 8.3 Hz, 1H, pyrroloquinoxaline-8-C***H***), 7.57 (t, *j*= 6.9 Hz, 1H, pyrroloquinoxaline-6-C***H***), 7.49 (t, *j*= 8.2 Hz, 1H, pyrroloquinoxaline-7-C***H***), 7.33 (t, *j*= 7.9 Hz, 1H, benzyl-5-C***H***), 7.26 (s, 1H, benzyl-6-C***H***), 7.17 (d, *j*= 7.5 Hz, 1H, benzyl-2-C***H***), 7.15-7.08 (m, 2H, benzodioxane-7-C***H***, benzodioxane-5-C***H***), 7.02 (d, *j*= 8.6 Hz, 1H, benzodioxane-8-C***H***), 6.89 (d, *j*= 8.3 Hz, 1H, benzyl-4-C***H***), 5.41 (s, 2H, CO_2C***H***$_2$), 4.35 (s, 4H, benzodioxane-2-C***H***$_2$, benzodioxane-3-C***H***$_2$), 3.83 (s, 3H, OC***H***$_3$). **^{13}C NMR (101 Hz, DMSO-*d*$_6$)**- *δ* 164.5 (***C***=O), 160.3 (pyrroloquinoxaline-8a-***C***), 159.4 (benzyl-3-***C***), 144.5 (benzodioxane-8a-***C***), 143.9 (benzodioxane-4a-***C***), 143.4 (pyrroloquinoxaline-9a-***C***),

141.6 (pyrroloquinoxaline-3a-***C***), 140.7 (pyrroloquinoxaline-4a-***C***), 139.1 (benzodioxane-6-***C***), 137.0 (benzyl-1-***C***), 129.4 (benzyl-5-***C***H), 127.6 (pyrroloquinoxaline-5-***C***H), 127.5 (pyrroloquinoxaline-8-***C***H), 126.5 (pyrroloquinoxaline-6-***C***H), 125.6 (pyrroloquinoxaline-7-***C***H), 124.8 (pyrroloquinoxaline-2-***C***), 121.9 (benzodioxane-8-***C***H), 119.1 (benzyl-6-***C***H), 118.0 (benzodioxane-7-***C***H), 117.9 (benzodioxane-5-***C***H), 112.8 (benzyl-2-***C***H), 112.7 (benzyl-4-***C***H), 80.7 (pyrroloquinocaline-3-***C***), 64.2 (benzodioxane-2-***C***H_2), 64.1 (benzodioxane-3-***C***H_2), 63.7 (CO_2***C***H_2), 55.1 (O***C***H_3).

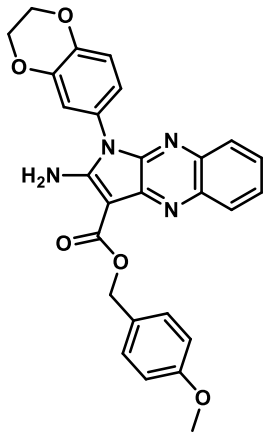

4-Methoxybenzyl 2-amino-1-(2,3-dihydrobenzo[*b*][1,4]dioxin-6-yl)-1*H*-pyrrolo[2,3-*b*]quinoxaline-3-carboxylate (40j).

Conducted by student Bulbul Singh. 2,3-Dihydrobenzo[*b*][1,4]dioxin-6-amine (**29**) (80 mg, 0.53 mmol, 1.3 eq.) was reacted with 4-methoxybenzyl (*Z*)-2-(3-chloroquinoxalin-2(1*H*)-ylidene)-2-cyanoacetate (**42j**) (150 mg, 0.4 mmol, 1.0 eq.) in 2.5 mL EtOH and 2.5 mL THF in accordance with general procedure 2. The reaction was monitored by LCMS. The solvent was removed under reduced pressure and the crude material recrystalised into methanol to give an impure cream solid. The crude material was purified by column chromatography on a 12g silica column using solvent conditions 0-5 % MeOH in DCM over 22 CVs. The desired fractions were combined and concentrated under reduced pressure to yield the title compound as a cream solid (89 mg, 45 %). LC/MS *m/z* calculated for $C_{27}H_{23}N_4O_5$: $[M+H]^+$: 483.2, found: 483.3, t_R 11.44 min (long run). HRMS (TOF ES^+) calculated: 483.1663, found: 483.1654. **^{1}H NMR (400 Hz, DMSO-*d*$_6$)**- δ 7.97-7.90 (m, 3H, pyrroloquinoxaline-5-C***H***, amine-N***H***$_2$), 7.76 (d, *j*= 8.1 Hz, 1H, pyrroloquinoxaline-8-C***H***), 7.60-7.51 (m, 3H, pyrroloquinoxaline-6-C***H***, benzyl-2-C***H***, benzyl-6-C***H***), 7.48 (t, *j*= 8.2 Hz, 1H, pyrroloquinoxaline-7-C***H***), 7.15-7.07 (m, 2H, benzodioxane-7-C***H***, benzodioxane-5-C***H***), 7.05-6.93 (m, 3H, benzyl-3-C***H***, benzyl-5-C***H***, benzodioxane-8-C***H***), 5.35 (s, 2H, CO_2C***H***$_2$), 4.35 (s, 4H, benzodioxane-2-C***H***$_2$, benzodioxane-3-C***H***$_2$), 3.76 (s, 3H, OC***H***$_3$). **^{13}C NMR (101 Hz, DMSO-*d*$_6$)**- δ 164.6 (***C***=O), 160.2 (benzyl-4-***C***), 158.8 (pyrroloquinoxaline-8a-***C***), 144.4 (benzodioxane-4a-***C***), 143.9

(benzodioxane-8a-***C***), 143.3 (pyrroloquinoxaline-9a-***C***), 141.5 (pyrroloquinoxaline-3a-***C***), 136.9 (pyrroloquinoxaline-4a-***C***), 136.8 (benzodioxane-6-***C***), 129.4 (benzyl-1-***C***), 129.2 (benzyl-2-***C***H, benzyl-6-***C***H), 127.6 (pyrroloquinoxaline-5-***C***H), 127.4 (pyrroloquinoxaline-8-***C***H), 126.4 (pyrroloquinoxaline-6-***C***H), 125.6 (pyrroloquinoxaline-7-***C***H), 124.8 (pyrroloquinoxaline-2-***C***), 121.9 (benzodioxane-8-***C***H), 118.0 (benzodioxane-7-***C***H), 117.9 (benzodioxane-5-***C***H), 113.7 (benzyl-3-***C***H, benzyl-5-***C***H), 80.8 (pyrroloquinoxaline-3-***C***), 64.2 (benzodioxane-2-***C***H_2), 64.1 (benzodioxane-2-***C***H_2), 63.7 (CO_2***C***H_2), 55.1 (***C***H_3O).

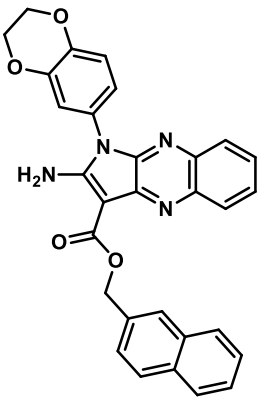

Naphthalen-2-ylmethyl 2-amino-1-(2,3-dihydrobenzo[*b*][1,4]dioxin-6-yl)-1*H*-pyrrolo[2,3-*b*]quinoxaline-3-carboxylate (40n). 2,3-Dihydrobenzo[*b*][1,4]dioxin-6-amine (**29**) (174 mg, 1.15 mmol, 1.4 eq.) was reacted with naphthalen-2-ylmethyl (*Z*)-2-(3-chloroquinoxalin-2(1*H*)-ylidene)-2-cyanoacetate (**42n**) (324 mg, 0.84 mmol, 1.0 eq.) in 7.5 mL EtOH and 2.5 mL THF in accordance with general procedure 2. The reaction was monitored by LCMS. A yellow solid precipitated out upon cooling of the reaction mixture and the solvent was removed under reduced pressure. The crude material was sonicated and heated in EtOAc (200 mL) before being filtered under vacuum to yield a yellow solid of the title compound (139 mg, 33 %). LC/MS *m/z* calculated for $C_{30}H_{23}N_4O_4$: $[M+H]^+$: 503.2, found: 503.2, t_R 8.04 min (long run). HRMS (TOF ES^+) calculated: 503.1714, found: 503.1707. **^{1}H NMR (400 Hz, DMSO-*d*$_6$)**- *δ* 8.38 (broad s, 2H, amine-N***H***$_2$), 8.17-8.08 (m, 2H, naphthalene-7-CH, naphthalene-4-C***H***), 8.00-7.90 (m, 3H, naphthalene-2-C***H***, naphthalene-3- C***H***, naphthalene-8-C***H***), 7.83 (d, *j*= 8.2 Hz, 1H, pyrroloquinoxaline-5-C***H***), 7.74 (d, *j*= 8.5 Hz, 1H, pyrroloquinoxaline-8-C***H***), 7.65 (t, *j*= 7.6 Hz, 1H, pyrroloquinoxaline-6-C***H***), 7.59-7.48 (m, 3H, pyrroloquinoxaline-7-C***H***, naphthanele-6-C***H***, naphthalene-5-C***H***), 7.16-7.09 (m, 2H, benzodioxane-7-C***H***, benzodioxane-5-C***H***), 7.03 (d, *j*= 8.6 Hz, 1H, benzodioxane-8-C***H***), 5.63 (s, 2H, CO_2C***H***$_2$), 4.35 (s, 4H, benzodioxane-2-C***H***$_2$, benzodioxane-3-C***H***$_2$).**^{13}C NMR (101 Hz, DMSO-*d*$_6$)**- *δ* 164.3 (***C***=O), 161.1 (pyrroloquinoxaline-8a-***C***), 145.2

(benzodioxane-4a-***C***), 144.5 (benzodioxane-8a-***C***), 141.7 (pyrroloquinoxaline-9a-***C***), 139.7 (pyrroloquinoxaline-3a-***C***), 137.0 (pyrroloquinoxaline-4a-***C***), 135.4 (benzodioxane-6-***C***, naphthalene-1-***C***), 133.2 (naphthalene-7a-***C***), 133.0 (naphthalene-3a-***C***), 128.5 (naphthalene-2-***C***H), 128.2 (naphthalene-7-***C***H, naphthalene-4-***C***H), 128.1 (naphthalene-8-***C***H, naphthalene-3-***C***H), 126.9 (naphthalene-6-***C***H, pyrroloquinoxaline-5-***C***H), 126.7 (pyrroloquinoxaline-8-***C***H), 126.6 (pyrroloquinoxaline-6-***C***H), 126.2 (pyrroloquinoxaline-7-***C***H, naphthalene-5-***C***H), 124.7 (pyrroloquinoxaline-2-***C***), 122.5 (benzodioxane-8-***C***H), 118.6 (benzodioxane-7-***C***H), 118.4 (benzodioxane-5-***C***H), 82.0 (pyrroloquinoxaline-3-***C***), 65.1 (CO_2***C***H_2), 64.7 (benzodioxane-2- ***C***H_2), 64.6 (benzodioxane-3-***C***H_2).

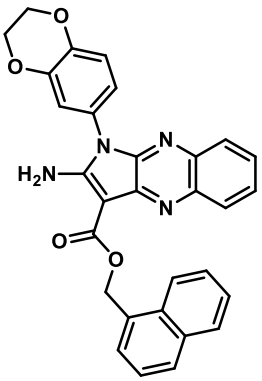

Naphthalen-1-ylmethyl 2-amino-1-(2,3-dihydrobenzo[*b*][1,4]dioxin-6-yl)-1*H*-pyrrolo[2,3-*b*]quinoxaline-3-carboxylate (40o). 2,3-Dihydrobenzo[*b*][1,4]dioxin-6-amine (**29**) (45 mg, 0.3 mmol, 1.3 eq.) was reacted with naphthalen-1-ylmethyl (*Z*)-2-(3-chloroquinoxalin-2(1*H*)-ylidene)-2-cyanoacetate (**42n**) (82 mg, 0.2 mmol, 1.0 eq.) in 3 mL EtOH and 1 mL THF in accordance with general procedure 2. The reaction was monitored by TLC conditions 1:1 EtOAc: cyclohexane. A yellow solid precipitated out upon cooling of the reaction mixture which was filtered under vacuum washing with cold MeOH (10 mL), LCMS confirmed the filtrate contained product. The filtrate was concentrated under reduced pressure before being extracted into EtOAc (100 mL), washed with 2 M HCl (50 mL), water (50 mL) and brine (20 mL). The phases were separated, and the organic was dried over $MgSO_4$, filtered and concentrated under reduced pressure. The crude material was purified by column chromatography on a 12 g silica column using solvent conditions 20-70 % EtOAc in cyclohexane over 12 CV. The desired fractions were combined and concentrated under reduced pressure to yield an impure orange solid. The material was triturated from methanol with sonication and the solid filtered under vacuum to give a white solid of the tile compound (5.3 mg, 5 %). R_f= 0.27 (1:1 EtOAc: cyclohexane). LC/MS *m/z* calculated for $C_{30}H_{23}N_4O_4$: $[M+H]^+$: 503.2, found:

503.2, t_R 7.42 min (long run). HRMS (TOF ES$^+$) calculated: 503.1714, found: 503.1708. **^{1}H NMR (400 Hz, DMSO-*d*$_6$)**- δ 8.38 (d, *j*= 8.5 Hz, 1H, naphthalene-8-C***H***), 8.19 (d, 8.2 Hz, 1H, naphthalene-5-C***H***), 8.01 (d, *j*= 7.1 Hz, 1H, naphthalene-4-C***H***), 7.89 (d, *j*= 8.2 Hz, 2H, pyrroloquinoxaline-8-C***H***, pyrroloquinoxaline-5-C***H***), 7.85 (d, *j*= 8.3 Hz, 1H, naphthalene-2-C***H***), 7.64-7.57 (m, 2H, pyrroloquinoxaline-6-C***H***, pyrroloquinoxaline-7-C***H***), 7.52 (q, *j*= 8.0 Hz, 3H, naphthalene-3-C***H***, naphthalene-7-C***H***, naphthalene-6-C***H***), 7.07 (d, *j*= 8.6 Hz, 1H, benzodioxane-7-C***H***), 7.01 (s, 1H, benzodioxane-5-C***H***), 6.95 (d, *j*= 8.5 Hz, 1H, benzodioxane-8-C***H***), 6.00 (s, 2H, $CO_2C\boldsymbol{H}_2$), 4.33 (s, 4H, benzodioxane-2-C$\boldsymbol{H}_2$, benzodioxane-3-C$\boldsymbol{H}_2$). **^{13}C NMR (101 Hz, DMSO-*d*$_6$)**- δ 165.7 (***C***=O), 160.1 (pyrroloquinoxaline-8a-***C***), 145.4 (benzodioxane-8a-***C***), 145.2 (benzodioxane-4a-***C***), 143.3 (pyrroloquinoxaline-9a-***C***), 142.0 (pyrroloquinoxaline-3a-***C***), 138.2 (pyrroloquinoxaline-4a-***C***), 136.4 (benzodioxane-6-***C***), 134.2 (naphthalene-8a-***C***, naphthalene-4a-***C***), 132.9 (naphthalene-1-***C***), 131.8 (naphthalene-2-***C***H), 129.2 (naphthalene-5-***C***H), 129.1 (pyrroloquinoxaline-5-***C***H, naphthalene-4-***C***H), 128.4 (pyrroloquinoxaline-8-***C***H), 127.3 (pyrroloquinoxaline-6-***C***H), 126.8 (pyrroloquinoxaline-7-***C***H), 126.6 (naphthalene-7-***C***H), 126.3 (naphthalene-6-***C***H), 126.0 (naphthalene-3-***C***H), 124.7 (pyrroloquinoxaline-2-***C***), 124.4 (naphthalene-8-***C***H), 121.5 (benzodioxane-8-***C***H), 119.3 (benzodioxane-7-***C***H), 117.7 (benzodioxane-5-***C***H), 77.7 (pyrroloquinoxaline-3-***C***), 64.8 (benzodioxane-2-***C***H_2), 64.7 (benzodioxane-3-***C***H_2), 64.3 ($CO_2\boldsymbol{C}H_2$).

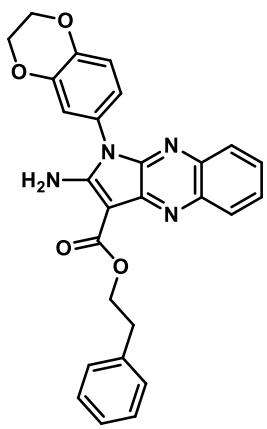

Phenethyl 2-amino-1-(2,3-dihydrobenzo[*b*][1,4]dioxin-6-yl)-1*H*-pyrrolo[2,3-*b*]quinoxaline-3-carboxylate (40p). 2,3-Dihydrobenzo[*b*][1,4]dioxin-6-amine (**29**) (47 mg, 0.31 mmol, 1.5 eq.) was reacted with phenethyl (*Z*)-2-(3-chloroquinoxalin-2(1*H*)-ylidene)-2-cyanoacetate (**42p**) (75 mg, 0.21 mmol, 1 eq.) in 9 mL EtOH and 3 mL THF in accordance with general procedure 2. The reaction was monitored by LCMS. The reaction mixture was cooled and a white precipitate crashed out which was filtered under vacuum and washed with cold MeOH (10 mL) to yield a white solid of the title

compound (49 mg, 49 %). LC/MS *m/z* calculated for $C_{27}H_{23}N_4O_4$: $[M+H]^+$: 467.2, found: 467.0, t_R 5.42 min (long run). HRMS (TOF ES^+) calculated: 467.1714, found: 467.1724. **^{1}H NMR (400 Hz, DMSO-*d*$_6$)**- *δ* 7.97 (d, *j*= 8.2 Hz, 1H, pyrroloquinoxaline-5-C***H***), 7.87 (broad s, 2H, amine-N***H***$_2$), 7.76 (d, *j*= 8.2 Hz, 1H, pyrroloquinoxaline-8-C***H***), 7.64-7.54 (m, 3H, pyrroloquinoxaline-6-C***H***, phenyl-3-C***H***, phenyl-5-C***H***), 7.49 (t, *j*= 7.2 Hz, 1H, pyrroloquinoxaline-7-C***H***), 7.31 (t, *j*= 7.5 Hz, 2H, phenyl-1-C***H***, phenyl-6-C***H***), 7.22 (t, *j*= 7.7 Hz, 1H, phenyl-4-C***H***), 7.14-7.07 (m, 2H, benzodioxane-7-C***H***, benzodioxame-5-C***H***), 7.00 (d, *j*= 8.6 Hz, 1H, benzodioxane-8-C***H***), 4.46 (t, *j*= 6.7 Hz, 2H, $CO_2C\boldsymbol{H}_2$), 4.35 (s, 4H, benzodioxane-2-C***H***$_2$, benzodioxane-3-C***H***$_2$), 3.08 (t, *j*= 6.7 Hz, 2H, $CO_2CH_2C\boldsymbol{H}_2$). **^{13}C NMR (101 Hz, DMSO-*d*$_6$)**- *δ* 164.6 (***C***=O), 159.9 (pyrroloquinoxaline-8a-***C***), 144.2 (benzodioxane-8a-***C***), 143.7 (benzodioxane-4a-***C***), 143.1 (pyrroloquinoxaline-9a-***C***), 141.3 (pyrroloquinoxaline-3a-***C***), 140.5 (pyrroloquinoxaline-4a-***C***), 138.4 (phenyl-1-***C***), 136.7 (benzodioxane-6-***C***), 129.2 (phenyl-3-***C***H, phenyl-5-***C***H), 128.0 (phenyl-2-***C***H, phenyl-6-C***H***), 127.3 (pyrroloquinoxaline-5-***C***H), 127.2 (pyrroloquinoxaline-8-***C***H), 126.5 (pyrroloquinoxaline-6-***C***H), 126.1 (pyrroloquinoxaline-7-***C***H), 125.3 (phenyl-4-***C***H), 124.6 (pyrroloquinoxaline-2-***C***), 121.7 (benzodioxane-8-***C***H), 117.8 (benzodioxane-7-***C***H), 117.7 (benzodioxane-5-***C***H), 80.5 (pyrroloquinoxaline-3-***C***), 64.0 (benzodioxane-2-$\boldsymbol{C}H_2$), 63.9 (benzodioxane-3-$\boldsymbol{C}H_2$), 63.6 ($CO_2\boldsymbol{C}H_2$), 34.7 ($CO_2CH_2\boldsymbol{C}H_2$).

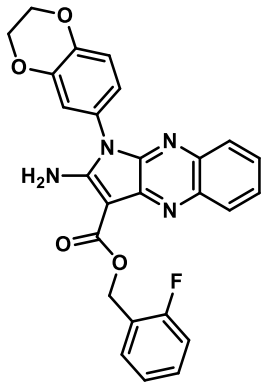

2-Fluorobenzyl 2-amino-1-(2,3-dihydrobenzo[*b*][1,4]dioxin-6-yl)-1*H*-pyrrolo[2,3-*b*]quinoxaline-3-carboxylate (40q). Conducted by student Ng Yu Yang. 2,3-Dihydrobenzo[*b*][1,4]dioxin-6-amine (**29**) (140 mg, 0.93 mmol, 1.6 eq.) was reacted with 4-fluorobenzyl (*Z*)-2-(3-chloroquinoxalin-2(1*H*)-ylidene)-2-cyanoacetate (**42q**) (208 mg, 0.58 mmol, 1.0 eq.) in 7.5 mL EtOH and 2.5 mL THF in accordance with general procedure 2. The reaction was monitored by TLC conditions 1:9 MeOH: DCM. The reaction mixture was cooled and a white precipitate crashed out which was filtered under vacuum and washed with cold MeOH (10 mL) to yield a beige solid of the title compound (114 mg, 41 %). R_f= 0.77 (10 % MeOH in DCM). LC/MS *m/z* calculated for

$C_{26}H_{20}FN_4O_4$: $[M+H]^+$: 471.1, found: 471.2, t_R 2.99 min. HRMS (TOF ES^+) calculated: 471.1463, found: 471.1472. **^{1}H NMR (400 Hz, $CDCl_3$)**- δ 8.15 (d, *j*= 8.4 Hz, 1H, pyrroloquinoxaline-5-C***H***), 7.93 (t, *j*= 7.3 Hz, 1H, benzyl-4-C***H***), 7.88 (d, *j*= 6.5 Hz, 1H, pyrroloquinoxaline-8-C***H***), 5.59 (t, *j*= 7.1 Hz, 1H, pyrroloquinoxaline-6-C***H***), 7.50 (t, *j*= 7.9 Hz, 1H, pyrroloquinoxaline-7-C***H***), 7.31 (q, *j*= 7.0 Hz, 1H, benzyl-3-C***H***), 7. 21 (t, *j*= 7.5 Hz, 1H, benzyl-6-C***H***), 7.15-7.03 (m, 2H, benzyl-5-C***H***, benzodioxane-7-C***H***), 7.02 (s, 1H, benzodioxane-5-C***H***), 6.96 (d, *j*= 8.1 Hz, 1H, benzodioxane-8-C***H***), 5.61 (s, 2H, $CO_2C\boldsymbol{H}_2$), 4.32 (s, 4H, benzodioxane-2-C$\boldsymbol{H}_2$, benzodioxane-3-C$\boldsymbol{H}_2$). **^{13}C NMR (101 Hz, $CDCl_3$)**- δ 165.1 (***C***=O), 161.6 (benzyl-2-***C***), 159.0 (pyrroloquinoxaline-8a-***C***), 144.9 (benzodioxane-8a-***C***), 144.7 (benzodioxane-4a-***C***), 142.8 (pyrroloquinoxaline-9a-***C***), 141.5 (pyrroloquinoxaline-3a-***C***), 141.3 (pyrroloquinoxaline-4a-***C***), 137.7 (benzodioxane-6-***C***), 129.9 (benzyl-1-***C***), 129.4 (benzyl-4-***C***H), 129.35 (benzyl-6-***C***H), 128.6 (pyrroloquinoxaline-5-***C***H), 127.9 (pyrroloquinoxaline-8-***C***H), 126.9 (pyrroloquinoxaline-6-H***C***H), 126.2 (pyrroloquinoxaline-7-***C***H), 124.3 (pyrroloquinoxaline-2-***C***), 124.2 (benzyl-5-***C***H), 121.0 (benzodioxane-8-***C***H), 118.9 (benzodioxane-7-***C***H), 117.2 (benzodioxane-5-***C***H), 115.3 (benzyl-3-***C***H), 82.5 (pyrroloquinoxaline-3-***C***), 64.4 (benzodioxande-2-***C***H_2), 64.3 (benzodioxane-3-***C***H_2), 59.4 ($CO_2\boldsymbol{C}H_2$). **^{19}F NMR (377 Hz, $CDCl_3$)**- δ -118.8 (m, 1F, C***F***).

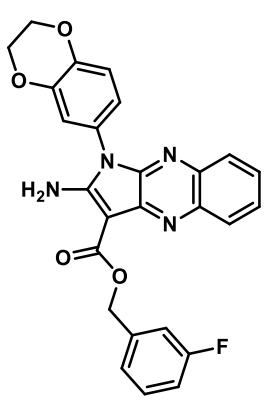

3-Fluorobenzyl 2-amino-1-(2,3-dihydrobenzo[*b*][1,4]dioxin-6-yl)-1*H*-pyrrolo[2,3-*b*]quinoxaline-3-carboxylate (40r). Conducted by student Ng Yu Yang. 2,3-Dihydrobenzo[*b*][1,4]dioxin-6-amine (**29**) (92 mg, 0.61 mmol, 2.3 eq.) was reacted with 3-fluorobenzyl (*Z*)-2-(3-chloroquinoxalin-2(1*H*)-ylidene)-2-cyanoacetate (**42r**) (97 mg, 0.26 mmol, 1.0 eq.) in 3 mL EtOH and 1 mL THF in accordance with general procedure 2. The reaction was monitored by LCMS. The reaction mixture was cooled and a white precipitate crashed out which was filtered under vacuum and washed with cold MeOH (10 mL) to yield a white solid of the title compound (24 mg, 19 %). LC/MS *m/z* calculated for $C_{26}H_{20}FN_4O_4$: $[M+H]^+$: 471.1, found 471.2, t_R 5.03 min (long run). HRMS (TOF ES^+)

calculated: 471.1463, found: 471.1466. **^{1}H NMR (400 Hz, $CDCl_3$)**- *δ* 8.18 (d, *j*= 8.3 Hz, 1H, pyrroloquinoxaline-5-C***H***), 7.90 (d, *j*= 8.1 Hz, 1H, pyrroloquinoxaline-8-C***H***), 7.65-7.48 (m, 3H, pyrroloquinoxaline-7-C***H***, pyrroloquinoxaline-6-C***H***, benzyl-5-C***H***), 7.42-7.31 (m, 2H, benzyl-2-C***H***, benzyl-6-C***H***), 7.11 (d, *j*= 8.7 Hz, benzyl-4-C***H***), 7.07-6.96 (m, 3H, benzodioxane-7-C***H***, benzodoxane-8***H***CN, benzodioxane-5-C***H***), 5.53 (s, 2H, $CO_2C\boldsymbol{H}_2$), 4.35 (s, 4H, benzodioxane-2-C$\boldsymbol{H}_2$, benzodioxane-3-C$\boldsymbol{H}_2$). **^{13}C NMR (101 Hz, $CDCl_3$)**- *δ* 164.4 (***C***=O), 161.9 (benzyl-3-***C***), 159.0 (pyrroloquinoxaline-8a-***C***), 145.0 (benzodioxane-8a-***C***), 144.8 (benzodioxane-4a-***C***), 142.8 (pyrroloquinoxaline-9a-***C***), 141.5 (pyrroloquinoxaline-3a-***C***), 139.8 (pyrroloquinoxaline-4a-***C***), 139.7 (benzyl-1-***C***), 137.7 (benzodioxane-6-***C***), 129.9 (benzyl-5-***C***H), 128.7 (pyrroloquinoxaline-5-***C***H), 128.0 (pyrroloquinoxaline-8-***C***H), 127.0 (pyrroloquinoxaline-6-***C***H), 126.3 (pyrroloquinoxaline-7-***C***H), 124.2 (pyrroloquinoxaline-2-***C***), 122.6 (benzyl-6-***C***H), 121.0 (benzodioxane-8-***C***H), 118.9 (benzodioxane-7-***C***H), 117.2 (benzodioxane-5-***C***H), 114.6 (benzyl-4-***C***H), 114.3 (benzyl-2-***C***H), 82.5 (pyrroloquinoxaline-3-***C***), 64.5 ($CO_2\boldsymbol{C}H_2$), 64.4 (benzodioxane-2-$\boldsymbol{C}H_2$), 64.3 (benzodioxane-3-$\boldsymbol{C}H_2$). **^{19}F NMR (377 Hz, $CDCl_3$)**- *δ* -112.89- -112.99 (m, 1F, C***F***).

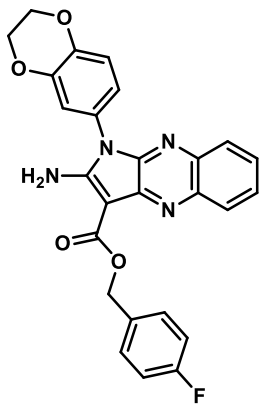

4-Fluorobenzyl 2-amino-1-(2,3-dihydrobenzo[*b*][1,4]dioxin-6-yl)-1*H*-pyrrolo[2,3-*b*]quinoxaline-3-carboxylate (40s). Conducted by student Ng Yu Yang. 2,3-Dihydrobenzo[*b*][1,4]dioxin-6-amine (**29**) (78 mg, 0.52 mmol, 1.4 eq.) was reacted with 4-fluorobenzyl (*Z*)-2-(3-chloroquinoxalin-2(1*H*)-ylidene)-2-cyanoacetate (**42s**) (135 mg, 0.38 mmol, 1.0 eq.) in 7.5 mL EtOH and 2.5 mL THF in accordance with general procedure 2. The reaction was monitored by TLC conditions 1:9 MeOH: DCM. The reaction mixture was cooled and a white precipitate crashed out which was filtered under vacuum and washed with cold MeOH (10 mL) to yield a beige solid of the title compound (28 mg, 16 %). R_f= 0.77 (1:9 MeOH: DCM). LC/MS *m/z* calculated for $C_{26}H_{20}FN_4O_4$: $[M+H]^+$: 471.1, found: 471.2, t_R 4.94 min (long run). HRMS (TOF ES^+) calculated: 471.1463, found: 471.1462. **^{1}H NMR (400 Hz, $CDCl_3$)**- *δ* 8.14 (d, *j*=

8.4 Hz, 1H, pyrroloquinoxaline-5-C***H***), 7.88 (d, *j*= 8.1 Hz, 1H, pyrroloquinoxaline-8-C***H***), 7.68-7.56 (m, 3H, benzyl-2-C***H***, benzyl-6-C***H***, pyrroloquinoxaline-6-C***H***), 7.51 (t, *j*= 7.3 Hz, 1H, pyrroloquinoxaline-7-C***H***), 7.13-7.05 (m, 3H, benzodioxane-7-C***H***, benzyl-3-C***H***, benzyl-5-C***H***), 7.02 (s, 1H, benzodioxane-5-C***H***), 6.96 (d, *j*= 8.1 Hz, 1H, benzodioxane-8-C***H***), 5.50 (s, 2H, $CO_2C\boldsymbol{H}_2$), 4.33 (s, 4H, benzodioxane-2-C$\boldsymbol{H}_2$, benzodioxane-3-C$\boldsymbol{H}_2$). **^{13}C NMR (101 Hz, $CDCl_3$)**- *δ* 163.8 (***C***=O), 161.3 (benzyl-4-***C***), 159.2 (pyrroloquinoxaline-8a-***C***), 145.1 (benzodioxane-8a-***C***), 144.8 (benzodioxane-4a-***C***), 142.9 (pyrroloquinoxaline-9a-***C***), 141.6 (pyrroloquinoxaline-3a-***C***), 141.3 (pyrroloquinoxaline-4a-***C***), 137.8 (benzodioxane-6-***C***), 133.0 (benzyl-1-***C***), 129.7 (benzyl-2-***C***H, benzyl-6-***C***H), 128.7 (pyrroloquinoxaline-5-***C***H), 128.1 (pyrroloquinoxaline-8-***C***), 127.0 (pyrroloquinoxaline-6-***C***H), 126.4 (pyrroloquinoxaline-7-***C***H), 124.4 (pyrroloquinoxaline-2-***C***), 121.1 (benzodioxane-8-***C***H), 119.0 (benzodioxane-7-***C***H), 117.3 (benzodioxane-5-***C***H), 115.6 (benzyl-3-CH, benzyl-5-***C***H), 82.7 (pyrroloquinoxaline-3-***C***), 64.8 ($CO_2\boldsymbol{C}H_2$), 64.5 (benzodioxane-2-***C***H_2), 64.4 (benzodioxane-3-***C***H_2). **^{19}F NMR (377 Hz, $CDCl_3$)**- *δ* -114.8 (m,1F, C***F***).

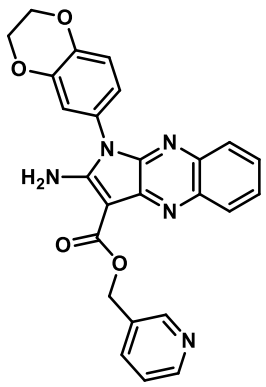

Pyridin-3-ylmethyl 2-amino-1-(2,3-dihydrobenzo[*b*][1,4]dioxin-6-yl)-1*H*-pyrrolo[2,3-*b*]quinoxaline-3-carboxylate (40b). 2-cyanoacetic acid (**31**) (311 mg, 3.5 mmol, 1.0 eq.) was reacted with pyridin-3-ylmethanol (0.35 ml, 3.5 mmol, 1.0 eq.), DCC (766 mg, 3.7 mmol, 1.1 eq.) and DMAP (43 mg, 0.35 mmol, 0.1 eq.) in DCM 10 mL according to general procedure 4. TLC showed desired ester formation R_f= 0.29 (3:97 MeOH: DCM). The reaction mixture was filtered to remove the white solid urea by-product washing with cold DCM (100 mL). The resulting filtrated was washed with distilled water (50 mL) and sodium bicarbonate (50 mL), phases separated then dried over $MgSO_4$, filtered, and concentrated under reduced pressure with no heating. To the crude material was added 2,3-dichloroquinoxaline (**26**) (1.396 g, 7.0 mmol, 2.0 eq.), CS_2CO_3 (5.73 g, 17.6 mmol, 5.0 eq.) in 15 mL DMF in accordance with general procedure 1(a). TLC confirmed desired intermediate formation, R_f= 0.40 (3:97 MeOH: DCM). DMF was removed using

high vacuum at 30 °C. Acetonitrile was added to the crude material sonicated and filtered to remove the Cs_2CO_3, the filtrated was concentrated under reduced pressure without heating. To the crude intermediate was added 2,3-dihydrobenzo[*b*][1,4]dioxin-6-amine (**29**) (140 mg, 0.93 mmol, 1.6 eq.) in 9 mL EtOH and 3 mL THF in accordance with general procedure 2. The reaction was monitored by TLC conditions 3:97 MeOH: DCM. A white solid crashed out upon cooling of the reaction mixture which was filtered under vacuum washing with cold MeOH (20 mL). Recrystallization of the solid was conducted in a 3:1 mixture of EtOH and THF to yield a cream solid of the title compound (553 mg, 35 %). R_f= 0.1 (3% MeOH in DCM). LC/MS *m/z* calculated for $C_{25}H_{20}N_5O_4$: $[M+H]^+$: 454.1, found: 454.1, t_R 4.08 min (long run). HRMS (TOF ES^+) calculated: 454.1510, found: 545.1500. **^{1}H NMR (400 Hz, $CDCl_3$)**- δ 8.86 (s, 1H, pyridine-2-C***H***), 8.54 (d, 4.4 Hz, 1H, pyridine-4-C***H***), 8.06 (d, *j*= 7.6 Hz, 1H, pyridine-6-C***H***), 8.02-7.92 (m, 3H, amine-N$\boldsymbol{H_2}$, pyrroloquinoxaline-5-C***H***), 7.76 (d, *j*= 8.2 Hz, 1H, pyrroloquinoxaline-8-C***H***), 7.58 (t, *j*= 6.8 Hz, 1H, pyrroloquinoxaline-6-C***H***), 7.53-7.44 (m, 2H, pyrroloquinoxaline-7-C***H***, pyridine-5-C***H***), 7.16-7.07 (m, 2H, benzodioxane-7-C***H***, benzodioxane-5-C***H***), 7.02 (d, *j*= 8.9 Hz, 1H, benzodioxane-8-C***H***), 5.47 (s, 2H, $CO_2C\boldsymbol{H_2}$), 4.35 (s, 4H, benzodioxane-2-C$\boldsymbol{H_2}$, benzodioxane-3-C$\boldsymbol{H_2}$). **^{13}C NMR (101 Hz, $CDCl_3$)**- δ 164.8 (***C***=O), 160.7 (pyrroloquinoxaline-8a-***C***), 149.2 (pyridine-2-***C***H, pyridine-4-***C***H), 144.9 (benzodioxane-8a-***C***), 144.4 (benzodioxane-4a-***C***), 143.8 (pyrroloquinoxaline-9a-***C***), 142.0 (pyrroloquinoxaline-3a-***C***), 141.1 (pyrroloquinoxaline-4a-***C***), 137.4 (benzodioxane-6-***C***), 135.6 (pyridine-1-***C***), 133.5 (pyridine-6-***C***H), 128.0 (pyrroloquinoxaline-5-***C***H), 127.9 (pyrroloquinoxaline-8-***C***H), 126.9 (pyrroloquinoxaline-6-***C***H), 126.0 (pyrroloquinoxaline-7-***C***H), 125.1 (pyridine-5-***C***H), 123.9 (pyrroloquinoxaline-2-***C***), 122.3 (benzodioxane-8-***C***H), 118.4 (benzodioxane-7-***C***H), 118.3 (benzodioxane-5-***C***H), 81.0 (pyrroloquinoxaline-3-***C***), 64.6 (benzodioxane-2-***C***H_2), 64.5 (benzodioxane-3-***C***H_2), 62.3 ($CO_2\boldsymbol{C}H_2$).

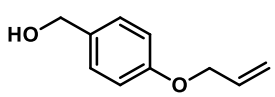

(4-(Allyloxy)phenyl)methanol (44u). 4-Hydroxybenzyl alcohol (**43**) (500 mg, 4 mmol, 1.0 eq.), allyl bromide (487 mg, 4 mmol, 1.0 eq.) and potassium carbonate (668 mg, 4.1 mmol, 1.0 eq.) was suspended in DMF 5 mL

before heating to 80 °C for 24 hours. Reaction determined complete by TLC conditions 2:3 EtOAc: cyclohexane. The DMF was removed under high vacuum before the crude material was extracted into DCM (200 mL) and washed with distilled water (200 mL). The phases were separated, the organic dried over $MgSO_4$, filtered and concentrated under reduced pressure. The crude material was then purified by column chromatography on a 25g silica column using solvent conditions 0-70 % EtOAc in cyclohexane over 13 CV. The desired product co-eluted with an impurity, the fractions were combined and concentrated under reduced pressure. A second column was ran on a 25 g silica column using solvent conditions 0- 50% EtOAc in cyclohexane 13 CV. Desired fractions were combined and concentrated under reduced pressure to yield the title compound as a colourless oil (255 mg, 39 %). R_f= 0.26 (2:3 EtOAc: cyclohexane). **^{1}H NMR (400 Hz, $CDCl_3$)**- δ 7.21 (d, *j*= 7.7 Hz, 2H, phenyl-2-C***H***, phenyl-6-C***H***), 6.89 (d, *j*= 7.7 Hz, 2H, phenyl-3-C***H***, phenyl-4-C***H***), 6.03 (dddd, *j*= 16.0, 9.2, 5.9, 4.6 Hz, 1H, $OCH_2C\boldsymbol{H}CH_2$), 5.38 (d, *j*= 17.0 Hz, 1H, 1x $OCH_2CHC\boldsymbol{H}_2$), 5.24 (d, *j*= 10.1 Hz, 1H, 1x $OCH_2CHC\boldsymbol{H}_2$), 5.03 (t, *j*= 5.6 Hz, 1H, methanol-O***H***), 4.54 (d, *j*= 4.1 Hz, 2H, $OC\boldsymbol{H}_2CHCH_2$), 4.41 (d, *j*= 5.6 Hz, 2H, methanol-$C\boldsymbol{H}_2$).**^{13}C NMR (101 Hz, $CDCl_3$)**- δ 157.5 (phenyl-4-***C***), 135.2 ($OCH_2\boldsymbol{C}HCH_2$), 134.3 (phenyl-1-***C***), 128.4 (phenyl-2-CH, phenyl-6-***C***H), 117.7 ($OCH_2CH\boldsymbol{C}H_2$), 114.7 (phenyl-3-C***H***, phenyl-5-***C***H), 68.6 ($O\boldsymbol{C}H_2CHCH_2$), 63.0 (methanol-$\boldsymbol{C}H_2$).

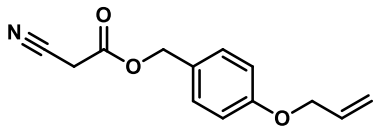

4-(Allyloxy)benzyl 2-cyanoacetate (41u). 2-Cyanoacetic acid (**31**) (130 mg, 1.5 mmol, 1.0 eq.) was reacted with (4-(allyloxy)phenyl)methanol (**44u**) (250 mg, 1.5 mmol, .01 eq.), DCC (314 mg, 1.5 mmol, 1.0 eq.) and DMAP (18 mg, 0.15 mmol, 0.1 eq.) in DCM 5 mL according to general procedure 4. The reaction was monitored by TLC conditions 2:3 EtOAc: cyclohexane. The crude material was purified by column chromatography on a 12g silica column using solvent conditions 0-40 % EtOAc in cyclohexane over 12 CV. The desired fractions were combined and concentrated under reduced pressure to yield a colourless oil of the title compound (240 mg, 68 %). R_f= 0.5 (2:3 EtOAc: cyclohexane). LC/MS *m/z* calculated for $C_{13}H_{14}NO_3$: $[M+H]^+$: 231.1, no mass found, t_R 2.73 min. **^{1}H**

NMR (400 Hz, $CDCl_3$)- δ 7.30 (d, *j*= 7.8 Hz, 2H, benzyl-2-C***H***, benzyl-6-C***H***), 6.92 (d, *j*= 7.6 Hz, 2H, benzyl-3-C***H***, benzyl-5-C***H***), 6.1205.98 (m, 1H, $OCH_2C\boldsymbol{H}CH_2$), 5.41 (d, *j*= 17.3 Hz, 1H, 1x $OCH_2CHC\boldsymbol{H}_2$), 5.30 (d, *j*= 10.6 Hz, 1H, 1x $OCH_2CHC\boldsymbol{H}_2$), 7.16 (s, 2H, $CO_2C\boldsymbol{H}_2$), 4.55 (d, *j*= 4.9 Hz, 2H, $OC\boldsymbol{H}_2CHCH_2$), 3.46 (s, 2H, cyanoacetate-2-C***H***$_2$). **^{13}C NMR (101 Hz, $CDCl_3$)**- δ 162.8 (***C***=O), 159.2 (benzyl-4-***C***), 133.0 ($OCH_2\boldsymbol{C}HCH_2$), 130.6 (benzyl-2-***C***H, benzyl-6-***C***H), 126.6 (benzyl-1-***C***), 117.9 ($OCH_2CH\boldsymbol{C}H_2$), 114.9 (benzyl-3-***C***H, benzyl-5-***C***H), 112.9 (nitrile-***C***N), 68.9 ($O\boldsymbol{C}H_2CHCH_2$), 68.4 ($CO_2\boldsymbol{C}H_2$), 24.9 (cyanoacetate-2-***C***H_2).

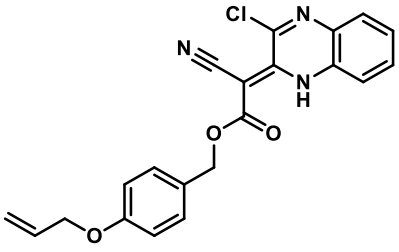

4-(Allyloxy)benzyl (*Z*)-2-(3-chloroquinoxalin-2(1*H*)-ylidene)-2-cyanoacetate (42u). 2,3-Dichloroquinoxaline (**26**) (202 mg, 1.0 mmol, 1.0 eq.) was reacted with of 4-(allyloxy)benzyl 2-cyanoacetate (**41u**) (230 mg, 1.0 mmol, 1.0 eq.), CS_2CO_3 (1.630 g, 5 mmol, 5.0 eq.) in 5 mL DMF in accordance with general procedure 1(a). The reaction was monitored by TLC conditions 2:3 EtOAc: cyclohexane. The DMF was removed under high vacuum before the crude material was extracted into EtOAc (100 mL) washing with water (100 mL), and brine (100 mL). The phases were separated, organic combined, dried over $MgSO_4$ before being filtered and concentrated under reduced pressure. The crude material was purified by column chromatography on a 12g silica column using solvent conditions 0-60 % EtOAc in cyclohexane over 19 CV. The desire fractions were combined and concentrated under reduced pressure to yield an orange solid of the title compound (210 mg, 54 %). R_f= 0.43 (2:3 EtOAc: cyclohexane). LC/MS *m/z* calculated for $C_{21}H_{17}ClN_3O_3$: $[M+H]^+$: 394.1, found: 394.2, t_R 3.11min. **^{1}H NMR (400 Hz, $CDCl_3$)**- δ 14.4 (broad s, 1H, quinoxaline-1-N***H***), 7.80 (d, *j*= 8.2 Hz, 1H, quinoxaline-8-C***H***), 7.62 (t, *j*= 7.6 Hz, 1H, quinoxaline-7-C***H***), 7.46 (t, *j*= 7.6 Hz, 1H, quinoxaline-6-C***H***), 7.39 (d, *j*= 8.2 Hz, 3H, quinoxaline-5-C***H***, benzyl-2-C***H***, benzyl-6-C***H***), 6.92 (d, *j*= 8.2 Hz, 2H, benzyl-3-C***H***, benzyl-5-C***H***), 6.12-5.89 (m, 1H, $OCH_2C\boldsymbol{H}CH_2$), 6.41 (d, *j*= 17.2 Hz, 1H, 1x $OCH_2CHC\boldsymbol{H}_2$), 5.33-5.24 (m, 3H, $CO_2C\boldsymbol{H}_2$, $OCH_2CHC\boldsymbol{H}_2$), 4.54 (1d, *j*= 4.9 Hz, 2H, $OC\boldsymbol{H}_2CHCH_2$). **^{13}C NMR (101 Hz, $CDCl_3$)**- δ 170.9 (***C***=O), 158.9 (benzyl-4-***C***), 146.4 (quinoxaline-3-***C***), 143.9 (quinoxaline-2-***C***), 134.5 (quinoxaline-8a-***C***), 133.3 (quinoxaline-4a-***C***), 132.5

(OCH_2***C***HCH_2), 129.9 (benzyl-2-***C***H, benzyl-6-***C***H), 128.9 (benzyl-1-***C***), 128.4 (quinoxaline-5-***C***H), 127.8 (quinoxaline-6-***C***H), 126.9 (quinoxaline-6-***C***H), 117.9 (OCH_2CH***C***H_2), 116.7 (quinoxaline-8-***C***H), 116.6 (nitrile-***C***N), 115.0 (benzyl-3-***C***H, benzyl-5-***C***H), 69.6 (O***C***H_2CHCH_2), 69.0 (cyanoacetate-2-***C***), 67.4 (CO_2***C***H_2).

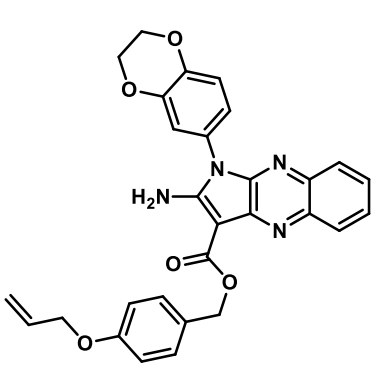

4-(Allyloxy)benzyl 2-amino-1-(2,3-dihydrobenzo[*b*][1,4]dioxin-6-yl)-1*H*-pyrrolo[2,3-*b*]quinoxaline-3-carboxylate (47). 2,3-Dihydrobenzo[*b*][1,4]dioxin-6-amine (**29**) (118 mg, 0.78 mmol, 1.5 eq.) was reacted with 4-(allyloxy)benzyl (*Z*)-2-(3-chloroquinoxalin-2(1*H*)-ylidene)-2-cyanoacetate (**42u**) (205 mg, 0.52 mmol, 1.0 eq.) in 9 mL EtOH and 3 mL THF in accordance with general procedure 2. The reaction was monitored by LCMS. The reaction mixture was cooled and a white precipitate crashed out which was filtered under vacuum and washed with cold MeOH (10 mL). The crude material was purified by reverse phase chromatography on a 12g C18 column using solvent conditions 10-90 % Acetonitrile in water over 13 CV. The desired fractions were combined and concentrated under reduced pressure to yield a white solid of the title compound (93 mg, 35 %). LC/MS m/z calculated for $C_{29}H_{25}N_4O_5$: $[M+H]^+$: 509.2, found: 509.1, t_R 5.61 min (long run). HRMS (TOF ES^+) calculated: 509.1819, found: 509.1818. **^{1}H NMR (400 Hz, $CDCl_3$)**- *δ* 7.97-7.90 (m, 3H, amine-N***H***$_2$, pyrroloquinoxaline-5-C***H***), 7.75 (d, *j*= 8.1 Hz, 1H, pyrroloquinoxaline-8-C***H***), 7.61-7.43 (m, 4H, pyrroloquinoxaline-7-C***H***, pyrroloquinoxaline-6-C***H***, benzyl-2-C***H***, benzyl-6-C***H***), 7.15-7.07 (m, 2H, benzodioxane-7-C***H***, benzodioxane-6-C***H***), 7.07-6.95 (m, 3H, benzodioxane-5-C***H***, benzyl-3-C***H***, benzyl-5-C***H***), 6.11-5.97 (m, 1H, OCH_2C***H***CH_2), 5.54- 5.31 (m, 3H, CO_2C***H***$_2$, 1x OCH_2CHC***H***$_2$), 5.25 (d, *j*= 10.6 Hz, 1H, 1x OCH_2CHC***H***$_2$), 4.57 (d, *j*= 5.5 Hz, 1H, OC***H***$_2CHCH_2$), 4.35 (s, 4H, benzodioxane-2-C***H***$_2$, benzodioxane-3-C***H***$_2$).**^{13}C NMR (101 Hz, $CDCl_3$)**- *δ* 164.8 (***C***=O), 160.5 (benzyl-4-***C***), 157.9 (pyrroloquinoxaline-8a-***C***), 144.6 (benzodioxane-8a-***C***), 144.1 (benzodioxane-4a-***C***), 143.5 (pyrroloquinoxaline-9a-***C***), 141.7 (pyrroloquinoxaline-3a-***C***), 140.8 (pyrroloquinoxaline-4a-***C***), 137.1 (benzodioxane-6-***C***), 133.9 (OCH_2C***H***CH_2), 129.8 (benzyl-1-***C***), 129.3 (benzyl-2-***C***H, benzyl-6-***C***H), 127.8

(pyrroloquinoxaline-5-***C***H), 127.6 (pyrroloquinoxaline-8-***C***H), 126.6 (pyrroloquinoxaline-6-***C***H), 125.8 (pyrroloquinoxaline-7-***C***H), 125.0 (pyrroloquinoxaline-2-***C***), 122.1 (benzodioxane-8-***C***H), 118.2 (benzodioxane-7-***C***H), 118.1 ($OCH_2CH\mathbf{C}H_2$), 117.6 (benzodioxane-5-***C***H), 114.7 (benzyl-3-***C***H, benzyl-5-***C***H), 81.0 (pyrroloquinoxaline-3-***C***), 68.4 ($O\mathbf{C}H_2CHCH_2$), 64.4 (benzodioxane-2-$\mathbf{C}H_2$), 64.3 (benzodioxane-3-$\mathbf{C}H_2$), 63.9 ($CO_2\mathbf{C}H_2$).

8.2 Pharmacology experimental

8.2.1 *Cell culture*

Cell lines- For binding studies HEK293T cell line (ATTC CRL3216) expressing p3.1neo(+)-EP_2-tsNluc was generated and provided by Dr J Farmer (University of Nottingham, UK) [289]. This stably expressed the human prostaglandin EP_2 receptor (Genbank: AY275471) tagged via the C terminus to the thermostable version of nanoluciferase (tsNluc), in the pcDNA3.1neo(+) plasmid for high level mammalian expression (Life Technologies, Paisley, UK) [285]. The thermostable nanoluciferase includes point mutations removing cysteine residues to improve nanoluciferase stability [285]. For arrestin NanoBiT assays, dual expressing HEK293T cells were used as generated and provided by Dr N Dijon (University of Notitngham, UK) [286]. These co-expressed (i) either the human EP_2 or human EP_4 (Genbank NM 00058) receptors, C terminally tagged with the large nanoluciferase fragment LgBiT, in pcDNA3.1neo(+), and (ii) human β-arrestin2 (Genbank NM 004313) tagged at the N terminus via a 5x Ser/Gly linker with the small Nanoluciferase peptide SmBiT, in pcDNA3.1zeo(+) [221]. Due to the length and flexibility of the C-termini of the EP_2 receptors, a peptide linker was not required between the receptors and the LgBiT/NLuc tag.

Cell maintenance and passaging- HEK293T cell lines were maintained in Dulbecco's modified Eagle's medium (DMEM D6429) supplemented with glucose (4.5 g/L) and L-glutamine (2.5 mM), and with 10 % foetal bovine serum (FBS)(Life Technologies, Paisley, U. K.), in a humidified atmosphere of 5 % CO_2 at 37 ^{o}C. Medium was supplemented with

the appropriate concentration of the relevant antibiotic to maintain selection pressure on the expressed plasmids. The p3.1neo(+)-EP_2-tsNluc expressing cell line required addition of 0.2 mg/mL G418 (Sigma), whereas the p3.1neo EP-LgBiT, p3.1zeo β-arrestin2-SmBiT tagged cell lines required addition of both 0.2 mg/mL G418 and 50 µg/mL Zeocin. Cells were passaged at 70-90 % confluency, with a splitting ratio between 1:2 and 1:30 and maintained in sterile polystyrene flasks (25, 75 or 175 cm^2 growing surface, termed T25, T75 and T175 respectively). During splitting the media was aspirated and the cells washed with sterile phosphate buffered saline (PBS). PBS was aspirated and 1 mL of sterile trypsin solution was added to the flask before incubating for 5 minutes at 37 ^oC. Physical agitation, by tapping the flask, encouraged the detachment of cells which were collected with the addition of 10 mL DMEM/10% FBS media into a 25 mL sterile universal tube. The cells were centrifuged (1000 g, 5 minutes) to form a pellet and the supernatant decanted into the waste to remove the trypsin. The pellet of cells was resuspended into 10 mL of DMEM/10%FCS and split according to required ratio or seeded into plates following a sample count.

Cell counting and plate seeding- Cells were seeded 24 hours prior to NanoBiT complementation assays. To ensure adherence of HEK293T cells, 96 well plates were first coated with 50 µL /well of filter sterilised 10 µg/mL poly-D-lysine (prepared in H_2O from P6407 Sigma, Poole, UK) on the day of seeding and incubated for 30 minutes at room temperature. Poly-d-lysine was then aspirated, and the wells were washed with 100 µL of sterile DMEM/10%FBS prior to seeding. Cells were removed from the flask and pelleted and resuspended according to procedures described above. A sample of the resuspended mixture was added to a haemocytometer and cells were counted within the grid (1 mm^2, with a depth of 0.1 mm- volume 0.1 µL). The cell count was then multiplied by 10,000 to determine the number of cells per mL. For a 96 well plate each well required the addition of 40,000 cells in 100 µL volume of DMEM/10%FBS in the different asssays. The required volume of cell resuspension was calculated using the following equation:

$$Volume\ of\ cell\ suspension\ required\ (mL) = \frac{Number\ of\ cells\ required\ (mL) x\ Required\ seeding\ volume\ (mL)}{Number\ of\ counted\ cells\ (per\ mL)}$$

The volume of cell resuspension required was diluted up the seeding solution volume using DMEM/10%FBS and seeded into the poly-D-lysine coated plates using an Eppendorf Multipipette Combitip dispenser.

Procedure for freezing and thawing cells-For freezing, cells were grown to 90 % confluency in multiple T75 flasks which were combined and centrifuged to form a pellet (methods cell culture 1). The cell pellet was resuspended in 2 mL FBS/10%DMSO, with 1 mL added to two cryovials and placed in a room temperature freezing container (Nalgene Mr Frosty, containing isopropyl to ensure cooling at a rate of 1 °C/min at -80 °C). The freezing container was placed into a -80 °C freezer for 24 hours before being transferred into liquid nitrogen storage. For thawing cells, the cryovial was removed from storage and warmed to room temperature until defrosted. The freezing media, with cells, was added to 10 mL DMEM/10%FCS and centrifuged (1000 g, 5 mins) to form a pellet. The supernatant was decanted, and the pellet resuspended in 1 mL DMEM/10%FBS before addition to a T25 flask. The cells were incubated for 24 hours in an atmosphere of 5 % CO_2 at 37 °C before the media was replaced and antibiotics added for selection maintenance.

8.2.2 NanoBRET competition binding assay

Membrane preparation- Membranes were prepared from the HEK293 cell line expressing p3.1neo(+)-EP_2-tsNluc described in Chapter 3.1.3. Cells were grown in four T175 flasks to 90 % confluency before being harvested by addition of 10 mL PBS and use of scraping to remove cells from the flask. The cell suspensions were collected in a sterile 25 mL universal flask before being spun in the centrifuge (2000 rpm, 10 minutes) to obtain a cell pellet. The supernatant was removed, and the cell pellets were frozen at -80 °C until required for membrane preparation. When required the cell pellets were thawed on ice to prevent receptor degradation before addition of 20 mL wash buffer (10 mm HEPES, 10 mM EDTA, pH: 7.4). The pellet was homogenised using an electrical

homogeniser, Ultra-Turrax, position 4, 8 short bursts (Ika-Werk GmbH & Co. KG, Staufen, Germany), before being centrifuged at 48,000 g, 4 °C for 30 minutes. The supernatant was discarded before an additional 20 mL wash buffer was added and centrifugation was repeated. The supernatant was discarded, and the pellet resuspended in 1.5 mL cold 10 mM HEPES with 0.1 mM EDTA (pH 7.4). Membrane protein concentration was determined using a bicinchoninic acid (BCA) assay kit (Sigma-Aldrich, Pool, UK). The BCA assay quantifies protein content by measuring the change in light absorption occurring with the interaction of copper (II) ions with the protein alpha helical structure and comparing against known standard bovine serum albumin (BSA). To a 96 well, clear bottom plate (Greiner) was added a serial dilution of BSA in distilled ultra high pure H_2O from 1000 mg/mL- 0 mg/mL (in 200 mg/mL increments), 25 µL/ well in triplicate. The membrane test sample was diluted by 2 with a final volume of 100 uL and added in triplicate (25 µL/ well) to the plate. A green solution was prepared containing 160 µL 1M copper (II) sulphate solution and 8 mL bicinchoninic acid, before 200 µL of the solution was added to each well using a multichannel pipette. The plate was incubated at 37 °C for 30 minutes before being read on a well by well basis on a PHERAstar FS plate reader (BMG, Labtech Germany), measuring absorbance at 560 nm. The control BSA data was plotted against protein concentration and a calibration curve constructed from simple linear regression. The sample data was then interpolated from the standard curve to calculate the membrane protein concentration in µg/mL. The membrane samples were aliquoted into Eppendorf tubes at suitable volumes for addition of 1 µg/well membrane for a full 384-well plate and stored at -80 °C.

NanoBRET assay protocol- The NanoBRET saturation and competition binding assays used the previously described membrane preparations expressing p3.1neo(+)-EP_2-tsNluc, and were performed as previously described by Farmer et al [219, 289]. A low sodium assay binding buffer (25 mM HEPES, 1% DMSO, 0.1 mg/ml Saponin, 0.02 % w/v Pluronic acid F127, 1 mM MgCl2 and 0.2 % bovine serum albumin (BSA, pH 7.4)) was used throughout in 384-well Optiplates (product number: 6007290, PerkinElmer LAS Ltd, UK).

Binding of the fluorescent probe TMR-Gαs19cha18 (as described by Farmer et al, synthesized Genscript, Oxford, UK; stored as aqueous 10 mM aliquots at -20 °C) binding was first characterised by addition of varying concentrations (78 nM–10 μM) to 1 μg/well Hek- EP_2-tsNluc cell membranes (added last), in which donor luciferase luminescence was stimulated with the addition of furimazine (Promega, Southampton, UK; 1/240 dilution from manufacturer's stock) in the absence or presence of the orthosteric agonist 10 μM PGE_2 (final assay volume, 40 μl). Saturations curves were also performed in the absence and presence of 40 μM **25b** to define non-specific binding (NSB). Incubations in assay buffer were performed at 37 °C, with endpoint measurements at 30- and 60- minute timepoints post incubation taken using a PHERAstar FS (BMG Labtech, Germany) to record the BRET ratio between donor nanoluciferase luminescence (450-80 nm emission filter) and acceptor TMR-Gαs19cha18 fluorescence (550 nm long pass emission filter). The BRET ratio was used to indicate TMR-Gαs19cha18 concentration dependent binding to the EP_2-tsNluc receptor.

To determined unlabelled ligand affinities using competition binding, assays in standard assay buffer employed 500 nM TMR -Gαs19cha18, a range of competing ligand (NAM) concentrations (10^{-5} M to $10^{-11.5}$ M in half log serial dilutions) or vehicle, combined with 40 μM PGE_2 (Sigma-Aldrich, Pool, UK) per well and 1 μg/ well HEK-EP_2-tsNluc cell membranes were then pre-incubated for 60 mins at 37 °C prior to addition of 1/960 dilution of furimazine (final volume, 50 μL). Luminescence output was recorded as the BRET ratio using the PHERAstar FS plate reader (BMG Labtech, Germany, 550 nm/450 nm ratio) measurements were taken every 2.8 minutes over a 30-minute interval after the 60 min incubation with NAMs.

NanoBRET data analysis- The NanoBRET assays were performed in technical duplicate. For saturation binding data, mean BRET ratiometric data from individual experiments were fitted to a one site binding model to allow derivation of TMR-Gαs19cha18 (tracer) dissociation constant (K_D) through:

$$\text{Specific binding} = B_{max}\frac{[\text{Tracer}]}{[\text{Tracer}] + K_D}$$

Where specific binding is determined through subtraction of NSB data in the presence of competitor **25b** from total BRET measurements (total binding – NSB). B_{max} indicates the maximum specific binding as determined by the BRET ratio. K_D represents the concentration of probe required to occupy 50 % of the available receptor binding sites at equilibrium.

In competition binding studies, the individual experimental data was normalised to total binding in the absence of competing ligands (vehicle, 100 %) and the top concentration 40 μM of the reference antagonist **25b** defining non-specific binding in the plate (0 %). In the presence of increasing concentrations of an unlabelled intracellular ligand we would expect to see a reduction in the BRET ratio and % specific binding due to its competition with the fluorescent tracer for the intracellular EP_2 site [219]. The inhibitory concentration for half maximum inhibition of specific binding, IC_{50} value, can be calculated for each unlabelled ligand using the 4 parameter equation:

$$\text{Tracer Bound (\%)} = \text{Total Specific binding (100\%)}.\frac{{IC_{50}}^{n}}{[\text{Competing Ligand}]^{n} + {IC_{50}}^{n}}$$

Where n is the Hill slope representing the steepness of the curve.

If it is assumed that the unlabelled ligands compete with the fluorescent probe competitively and reversibly the K_i can then be estimated using the Cheng-Prusoff correction:[198]

$$K_i = \frac{IC_{50}}{1 + \frac{[\text{Tracer}]}{K_{\text{Tracer}}}}$$

Where [Tracer] and K_{Tracer} are the concentration and equilibrium dissociation constant for the TMR-Gαs19cha18 fluorescent tracer.

All data analysis was conducted using Prism 10.0 (GraphPad Software, San Diego, USA). Ligand binding affinities were reported as their pK_i value, the negative log of the K_i, and data from a minimum of five individual experiments were pooled as mean ± standard error of the mean (SEM).

8.2.3 Assessment of receptor-arrestin interactions using the NanoBiT complementation assay

NanoBiT complementation assay protocol- HEK-EP_2-LgBiT/SmBiT-β-arrestin2 or HEK-EP_4-LgBiT/SmBiT-β-arrestin2 cells were seeded into poly-D lysine (10 µg/mL) coated white, clear-bottomed, 96 well plates (Greiner Bio-One, Stonehouse, UK), at 35,000-40,000 cells per well, incubated at 37 °C/5 % CO_2 for 24 h prior to the assay. All assays were conducted in HEPES balanced salt solution containing 0.1 % BSA (pH 7.4) made up of: 10 mM HEPES, 2 mM sodium pyruvate, 146 nM NaCl, 5 mM KCl, 1mM $MgSO_4$, 1.7 mM $CaCl_2$, 1.5 mM $NaHCO_3$, 5 mM D-glucose.

For experiments determining agonist concentration response curves, cells were washed and replaced with 40 µL pre-warmed assay buffer and incubated for 10 minutes. 10 µL NanoGlo furimazine substrate (1:750; final assay dilution from Promega stock) was added and incubated for 5 mins. The basal measure of luminescence was monitored for 5 mins before the addition of 10 µL vehicle (assay buffer) or agonist (PGE_2, butaprost, or evatanepag at 6 X final concentration) at a final concentration range 10^{-5} M to 10^{-9} M in half log serial dilutions made up in pre-warmed assay buffer to the desired wells. Luminescence measurements were obtained from 1 min post agonist addition, for 30 mins, at 120 second intervals, maintained at 37 °C throughout the assay (Pherastar FS; BMG Labtech).

In the second set of experiments, concentration inhibition curves were constructed for NAM test ligands. In this assay, cells were washed and replaced with 40 µL pre-warmed assay buffer containing NAMs (or vehicle) with a concentration range $10^{-4.5}$ M to 10^{-9} M in half log serial dilutions. Cells were incubated for 10 mins at 37 °C, before addition of 10 µL NanoGlo furimazine substrate (1:750; final assay dilution from Promega stock) incubating for 5 mins. The basal measure of luminescence was monitored for 5 mins before the addition of 10 µL vehicle (assay buffer) or agonist PGE_2 (at the final EC_{80} concentration =164 nM) to the assay wells. Luminescence measurements (Pherastar FS) were obtained from 1 min post PGE_2 addition, for 30 mins, at 120 second intervals, maintained at 37 °C throughout the assay.

Finally, for determining agonist concentration response curves in the presence of NAMs, cells were washed and replaced with 40 µL of either pre-warmed assay buffer only or containing 1 µM or 30 µM (FAC) of our unlabelled NAMs. Cells were incubated for 10 mins at 37 °C, before addition of 10 µL NanoGlo furimazine substrate (1:750; final assay dilution from manufacturer's stock) incubating for 5 mins. The basal measure of luminescence was monitored for 5 mins before the addition of 10 µL vehicle (assay buffer) or agonist at a concentration range 10^{-5} M to 10^{-9} M in half log serial dilutions made up in pre-warmed assay buffer to the desired wells. Luminescence measurements were obtained from 1 min post agonist addition, for 30 mins, at 120 second intervals, maintained at 37 °C throughout the assay.

Functional arrestin assay data analysis- Functional arrestin assays were performed in technical duplicate, and curves were fitted as follows to individual experiments:

For agonist concentration response curves in the absence or presence of NAM a four-parameter equation was used:

$$\text{Response} = \frac{\text{Rmax. } [\text{agonist}]^{n}}{([\text{agonist}]^{n} + \text{EC}_{50}{}^{n}) + \text{Basal}}$$

Where R_{max} is the maximal agonist response, EC_{50} is the concentration of agonist to provide half maximal response, basal is unstimulated measurement and n is Hill slope. An EC_{80} was calculated as EC_{80}= 4 x EC_{50} (assuming unit Hill slope) where required. R_{max} values for different agonists were normalised for comparison to the maximal 10 µM PGE_2 concentration (as 100 %)

For functional concentration inhibition curves, individual experiment data were first normalised to PGE_2 only responses (100 %) and vehicle only (in the absence of PGE_2, 0 %):

$$\begin{aligned}\text{Response (\%)} &= [\text{Response at Max Inhibition}] + (\text{PGE}_2 \text{ response (100 \%)} \\ &- [\text{Response at Max Inhibition}]).\frac{\text{IC}_{50}{}^{n}}{[\text{Competing Ligand}]^{n} + \text{IC}_{50}{}^{n}}\end{aligned}$$

In this instance the NAM IC_{50} represents a functional inhibitory potency as the concentration of the ligand to inhibit the PGE_2 response to 50 % of its maximal effect. The maximal inhibition of the ligand (Imax) was defined as (100-[PGE_2 response at max inhibition]). The Hill slope n defined the steepness of the curve.

Concentration dependent parameters (e.g. EC_{50}, IC_{50}, EC_{80}) were also expressed as their negative logarithms (p) as needed (e.g. pEC_{50}). All pooled data are presented as mean ± SEM from 3-5 individual replicates. Data were analysed and collated using GraphPad Prism 10.0 (GraphPad Software, Sand Diego, USA).

Statistical analysis (e.g. chapter 5) between two pooled data groups was performed by Student's t test. For multiple comparisons, one way analysis of variance (ANOVA) followed by Dunnett's post test against a control group was performed. A p value of $p < 0.05$ was considered significant.

8.3 Computational modelling experimental

The BLAST search was performed using the PDB website tool. The Protein Data Bank was used to retrieve the crystal structures of the desired receptors. The homology models were acquired from GPCRdb and uploaded to Maestro from the Schrödinger suite [421]. The computational model first underwent protein preparation with Maestro's protein preparation wizard under default settings [422]. Maestro's sitemap tool was then used on the prepared protein to identify the top-ranked potential receptor binding sites using default settings [423, 424]. The generated binding pockets (discounting the orthosteric PGE_2 binding site) were then manually analysed comparing their respective size, using the measure tool, with the size of the ligands to identify sites where binding is reasonable. The structures of ligands were generated in Maestro using the 2D sketcher tool and prepared with LigPrep retaining their specific chirality and not including charged compounds [448]. IDF was conducted using Maestro selecting the prepared ligands, choosing the centroid of workspace ligand as an atom in the centre of the sitemap binding pocket, and docking ligands with a length <= 20 Å [425-427]. The

IDFs produced were then manually analysed, identifying consistent ligand binding poses and docking scores then comparing this information against our known SAR dataset of active and inactive compounds. IDF models of interest were then re-docked with our compound library using Maestro's Ligand Docking tool on default settings without constraints. A second round of site mapping was conducted which was used generate a receptor grid for this docking, selecting an entry in the centre of the site-mapped pocket and using the default settings. A second round of manual analysis for each IDF-based computational model was conducted comparing the produced docking scores/poses against our generated SAR dataset. The most representative computational model when compared to our SAR data was selected. For all known ligands displaying EP_2 binding affinity the highest and most consistent docking poses have been reported. The EP_2 receptor computational model bound to **25a** was overlayed with CXCR2-00767013 bound CXCR2 receptor and 'Compound 15' bound β2AR crystal structures using PyMOL [158, 183, 449].

Chapter 9- References

1. Furman, D., et al., *Chronic inflammation in the etiology of disease across the life span. Nat. Med.*, 2019. **25**(12): p. 1822-1832.
2. Slavich, G.M., *Understanding inflammation, its regulation, and relevance for health: a top scientific and public priority. Brain Behav. Immun.*, 2015. **45**: p. 13-4.
3. Pahwa, R., A. Goyal, and I. Jialal, *Chronic Inflammation*, in *StatPearls*. 2025, StatPearls Publishing: Treasure Island (FL).
4. Goswami, K.K., A. Bose, and R. Baral, *Macrophages in tumor: An inflammatory perspective. Clin. Immunol.*, 2021. **232**: p. 108875.
5. Spielman, L.J., J.P. Little, and A. Klegeris, *Inflammation and insulin/IGF-1 resistance as the possible link between obesity and neurodegeneration. J. Neuroimmunol.*, 2014. **273**(1): p. 8-21.
6. Gopalan, C. and E. Kirk, *Chapter 3 - Inflammation*, in *Biology of Cardiovascular and Metabolic Diseases*, C. Gopalan and E. Kirk, Editors. 2022, Academic Press. p. 53-66.
7. *Global, regional, and national age-sex-specific mortality for 282 causes of death in 195 countries and territories, 1980-2017: a systematic analysis for the Global Burden of Disease Study 2017. Lancet*, 2018. **392**(10159): p. 1736-1788.
8. Slavich, G.M., *Understanding inflammation, its regulation, and relevance for health: A top scientific and public priority. Brain Behav. Immun.*, 2015. **45**: p. 13-14.
9. Aristizabal, B. and A. Gonzalez, *Innate immune system*, in *Autoimmunity: From Bench to Bedside*, J.M. Anaya, Y. Shoenfeld, and A. Rojas-Villarraga, Editors. 2013: El Rosario University Press.
10. Rosales, C., *Neutrophil: A Cell with Many Roles in Inflammation or Several Cell Types? Front. Physiol.*, 2018. **9**: p. 113.
11. Sawalha, A.H., *Chapter 15 - Neutrophils in Systemic Lupus Erythematosus*, in *Systemic Lupus Erythematosus*, G.C. Tsokos, Editor. 2016, Academic Press: Boston. p. 127-130.
12. Frauwirth, K.A. and C.B. Thompson, *Activation and inhibition of lymphocytes by costimulation. J. Clin. Invest.*, 2002. **109**(3): p. 295-9.
13. Chi, H., M. Pepper, and P.G. Thomas, *Principles and therapeutic applications of adaptive immunity. Cell*, 2024. **187**(9): p. 2052-2078.
14. Cano, R.L.E. and H.D.E. Lopera, *Autoimmunity: From Bench to Bedside*, in *Introduction to T and B lymphocytes*, J.M. Anaya, Y. Shoenfeld, and A. Rojas-Villarraga, Editors. 2013, Rosario University Press: National Library of Medicine.
15. Dunkelberger, J.R. and W.C. Song, *Complement and its role in innate and adaptive immune responses. Cell Res.*, 2010. **20**(1): p. 34-50.
16. Janeway, C.A.J., P. Travers, and M. Walport, *Immunobiology: The Immune System in Health and Disease*, in *The complement system and innate immunity*. 2001: National Library of Medicine.

17. Malik, A. and T.D. Kanneganti, *Function and regulation of IL-1α in inflammatory diseases and cancer. Immunol. Rev.*, 2018. **281**(1): p. 124-137.
18. Tesmer, L.A., et al., *Th17 cells in human disease. Immunol. Rev.*, 2008. **223**: p. 87-113.
19. Srirangan, S. and E.H. Choy, *The role of interleukin 6 in the pathophysiology of rheumatoid arthritis. Ther. Adv. Musculoskelet. Dis.*, 2010. **2**(5): p. 247-56.
20. Gabay, C., *Interleukin-6 and chronic inflammation. Arthritis Res. Ther.*, 2006. **8**(2): p. S3.
21. Jang, D.I., et al., *The Role of Tumor Necrosis Factor Alpha (TNF-α) in Autoimmune Disease and Current TNF-α Inhibitors in Therapeutics. Int. J. Mol. Sci.*, 2021. **22**(5).
22. Parameswaran, N. and S. Patial, *Tumor necrosis factor-α signaling in macrophages. Crit. Rev. Eukaryot. Gene Expr.*, 2010. **20**(2): p. 87-103.
23. Cai, R., et al., *Tumor Necrosis Factor Alpha Deficiency Improves Endothelial Function and Cardiovascular Injury in Deoxycorticosterone Acetate/Salt-Hypertensive Mice. Biomed. Res. Int.*, 2020. **2020**: p. 3921074.
24. Elgazzar, A.H., *Inflammation*, in *Synopsis of Pathophysiology in Nuclear Medicine*, A.H. Elgazzar, Editor. 2014, Springer International Publishing: Cham. p. 41-57.
25. *Chronic Granulomatous Lymphadenitis*, in *Diagnostic Pathology: Lymph Nodes and Extranodal Lymphomas (Second Edition)*, L.J. Medeiros and R.N. Miranda, Editors. 2018, Elsevier. p. 20-27.
26. Ju, Z., et al., *Recent development on COX-2 inhibitors as promising anti-inflammatory agents: The past 10 years. Acta Pharmaceutica Sinica B.*, 2022. **12**(6): p. 2790-2807.
27. Bindu, S., S. Mazumder, and U. Bandyopadhyay, *Non-steroidal anti-inflammatory drugs (NSAIDs) and organ damage: A current perspective. Biochem. Pharmacol.*, 2020. **180**: p. 114147.
28. Ray, W.A., et al., *Educational program for physicians to reduce use of non-steroidal anti-inflammatory drugs among community-dwelling elderly persons: a randomized controlled trial. Med. Care*, 2001. **39**(5): p. 425-35.
29. Narumiya, S., Y. Sugimoto, and F. Ushikubi, *Prostanoid receptors: structures, properties, and functions. Physiol. Rev.*, 1999. **79**(4): p. 1193-226.
30. Smith, W.L. and R. Langenbach, *Why there are two cyclooxygenase isozymes. J. Clin. Invest.*, 2001. **107**(12): p. 1491-5.
31. Biringer, R.G., *The enzymology of the human prostanoid pathway. Mol. Biol. Rep.*, 2020. **47**(6): p. 4569-4586.
32. Hirata, T. and S. Narumiya, *Prostanoid receptors. Chem. Rev.*, 2011. **111**(10): p. 6209-30.
33. Abdalla, S.I., I.R. Sanderson, and R.C. Fitzgerald, *Effect of inflammation on cyclooxygenase (COX)-2 expression in benign and malignant oesophageal cells. Carcinog.*, 2005. **26**(9): p. 1627-1633.
34. Radi, Z.A. and N.K. Khan, *Effects of cyclooxygenase inhibition on the gastrointestinal tract. Exp. Toxicol. Pathol.*, 2006. **58**(2): p. 163-173.

35. Varga, Z., S.R.A. Sabzwari, and V. Vargova, *Cardiovascular Risk of Nonsteroidal Anti-Inflammatory Drugs: An Under-Recognized Public Health Issue. Cureus*, 2017. **9**(4): p. e1144.
36. Busse, W.W., *Leukotrienes and inflammation. Am. J. Respir. Crit. Care Med.*, 1998. **157**(6 Pt 2): p. S210-3; discussion S247-8.
37. Hedi, H. and G. Norbert, *5-Lipoxygenase Pathway, Dendritic Cells, and Adaptive Immunity. J. Biomed. Biotechnol.*, 2004. **2004**(2): p. 99-105.
38. Schrör, K., *Aspirin and platelets: the antiplatelet action of aspirin and its role in thrombosis treatment and prophylaxis. Semin. Thromb. Hemost.*, 1997. **23**(4): p. 349-56.
39. Wakefield, T.W., A.T. Obi, and P.K. Henke, *An aspirin a day to keep the clots away: can aspirin prevent recurrent thrombosis in extended treatment for venous thromboembolism? Circulation*, 2014. **130**(13): p. 1031-3.
40. Marcum, Z.A. and J.T. Hanlon, *Recognizing the Risks of Chronic Nonsteroidal Anti-Inflammatory Drug Use in Older Adults. Ann. Longterm Care*, 2010. **18**(9): p. 24-27.
41. Griffin, M.R., *Epidemiology of nonsteroidal anti-inflammatory drug-associated gastrointestinal injury. Am. J. Med.*, 1998. **104**(3a): p. 23S-29S; discussion 41S-42S.
42. Gupta, M. and G.M. Eisen, *NSAIDs and the gastrointestinal tract. Curr. Gastroenterol. Rep.*, 2009. **11**(5): p. 345-53.
43. Wright, J.M., *The double-edged sword of COX-2 selective NSAIDs. Can. Med. Assoc. J.*, 2002. **167**(10): p. 1131-7.
44. Zhang, J., E.L. Ding, and Y. Song, *Adverse effects of cyclooxygenase 2 inhibitors on renal and arrhythmia events: meta-analysis of randomized trials. J. AM. Med. Assoc.*, 2006. **296**(13): p. 1619-32.
45. Basith, S., et al., *Exploring G Protein-Coupled Receptors (GPCRs) Ligand Space via Cheminformatics Approaches: Impact on Rational Drug Design. Front. Pharmacol.*, 2018. **9**: p. 128.
46. Zhao, J., et al., *G Protein-Coupled Receptors (GPCRs) in Alzheimer's Disease: A Focus on BACE1 Related GPCRs. Front. Aging Neurosci.*, 2016. **8**: p. 58.
47. Rosenbaum, D.M., S.G. Rasmussen, and B.K. Kobilka, *The structure and function of G-protein-coupled receptors. Nature*, 2009. **459**(7245): p. 356-63.
48. Oprea, T.I., et al., *Unexplored therapeutic opportunities in the human genome. Nat. Rev. Drug Discov.*, 2018. **17**(5): p. 317-332.
49. Hauser, A.S., et al., *Trends in GPCR drug discovery: new agents, targets and indications. Nat. Rev. Drug. Discov.*, 2017. **16**(12): p. 829-842.
50. Zhang, M., et al., *G protein-coupled receptors (GPCRs): advances in structures, mechanisms and drug discovery. Signal Transduct. Target Ther.*, 2024. **9**(1): p. 88.
51. Sun, X. and Q. Li, *Prostaglandin EP2 receptor: Novel therapeutic target for human cancers (Review). Int. J. Mol. Med.*, 2018. **42**(3): p. 1203-1214.
52. Ferguson, S.S., *Phosphorylation-independent attenuation of GPCR signalling. Trends Pharmacol. Sci.*, 2007. **28**(4): p. 173-9.

53. Fredriksson, R., et al., *The G-protein-coupled receptors in the human genome form five main families. Phylogenetic analysis, paralogon groups, and fingerprints. Mol. Pharmacol.*, 2003. **63**(6): p. 1256-72.
54. Kennedy, I., et al., *Studies on the characterisation of prostanoid receptors: a proposed classification. Prostaglandins*, 1982. **24**(5): p. 667-89.
55. Coleman, R.A., et al., *Prostanoid receptors — the development of a working classification. Trends Pharmacol. Sci.*, 1984. **5**: p. 303-306.
56. Breyer, R.M., et al., *Prostanoid receptors: subtypes and signaling. Annu. Rev. Pharmacol. Toxicol.*, 2001. **41**: p. 661-90.
57. Toh, H., A. Ichikawa, and S. Narumiya, *Molecular evolution of receptors for eicosanoids. FEBS Lett.*, 1995. **361**(1): p. 17-21.
58. Huang, Z.L., Y. Urade, and O. Hayaishi, *Prostaglandins and adenosine in the regulation of sleep and wakefulness. Curr. Opin. Pharmacol.*, 2007. **7**(1): p. 33-8.
59. Wu, J., et al., *Anti-inflammatory effects of the prostaglandin D2/prostaglandin DP1 receptor and lipocalin-type prostaglandin D2 synthase/prostaglandin D2 pathways in bacteria-induced bovine endometrial tissue. Vet. Res.*, 2022. **53**(1): p. 98.
60. Matsuoka, T., et al., *Prostaglandin D2 as a mediator of allergic asthma. Science*, 2000. **287**(5460): p. 2013-7.
61. Pettipher, R., *The roles of the prostaglandin D(2) receptors DP(1) and CRTH2 in promoting allergic responses. Br. J. Pharmacol.*, 2008. **153 Suppl 1**(Suppl 1): p. S191-9.
62. Peinhaupt, M., et al., *DP1 receptor signaling prevents the onset of intrinsic apoptosis in eosinophils and functions as a transcriptional modulator. J. Leukoc. Biol.*, 2018. **104**(1): p. 159-171.
63. Domingo, C., et al., *The prostaglandin D2 receptor 2 pathway in asthma: a key player in airway inflammation. Respir. Res.*, 2018. **19**(1): p. 189.
64. Domingo, C., et al., *The prostaglandin D(2) receptor 2 pathway in asthma: a key player in airway inflammation. Respir. Res.*, 2018. **19**(1): p. 189.
65. Brightling, C.E., G. Brusselle, and P. Altman, *The impact of the prostaglandin D(2) receptor 2 and its downstream effects on the pathophysiology of asthma. Allergy*, 2020. **75**(4): p. 761-768.
66. Biringer, R.G., *A Review of Prostanoid Receptors: Expression, Characterization, Regulation, and Mechanism of Action. J. Cell. Commun. Signal.*, 2021. **15**(2): p. 155-184.
67. Andreasson, K., *Emerging roles of PGE2 receptors in models of neurological disease. Prostaglandins Other Lipid Mediat.*, 2010. **91**(3-4): p. 104-12.
68. Lohitaksha, K., et al., *Eicosanoid signaling in neuroinflammation associated with Alzheimer's disease. Eur. J. Pharmacol.*, 2024. **976**: p. 176694.
69. Nagamachi, M., et al., *Facilitation of Th1-mediated immune response by prostaglandin E receptor EP1. J. Exp. Med.*, 2007. **204**(12): p. 2865-74.
70. Sood, R., et al., *Upregulation of prostaglandin receptor EP1 expression involves its association with cyclooxygenase-2. PLoS One*, 2014. **9**(3): p. e91018.

71. Aoki, T., et al., *Prostaglandin E2-EP2-NF-κB signaling in macrophages as a potential therapeutic target for intracranial aneurysms. Sci. Signal.*, 2017. **10**(465).
72. Shin, V.Y., et al., *Inhibition of EP2 receptor suppresses tumor growth and chemoresistance of gastric cancer. Am. J. Cancer Res.*, 2022. **12**(10): p. 4680-4692.
73. Jiang, J. and R. Dingledine, *Prostaglandin receptor EP2 in the crosshairs of anti-inflammation, anti-cancer, and neuroprotection. Trends Pharmacol. Sci.*, 2013. **34**(7): p. 413-23.
74. Kalinski, P., *Regulation of immune responses by prostaglandin E2. J. Immunol.*, 2012. **188**(1): p. 21-8.
75. Nakamura, Y., et al., *Prostaglandin EP3 receptor-expressing preoptic neurons bidirectionally control body temperature via tonic GABAergic signaling. Sci. Adv.*, 2022. **8**(51): p. eadd5463.
76. Xu, H., et al., *Prostaglandin E2 receptor EP3 regulates both adipogenesis and lipolysis in mouse white adipose tissue. J. Mol. Cell. Biol.*, 2016. **8**(6): p. 518-529.
77. Lazarus, M. and C.B. Saper, *CHAPTER 15 - The Differential Role of Prostaglandin E2 Receptors in the CNS Response to Systemic Immune Challenge*, in *Psychoneuroimmunology (Fourth Edition)*, R. Ader, Editor. 2007, Academic Press: Burlington. p. 319-336.
78. Wang, L., et al., *Roles of EP Receptors in the Regulation of Fluid Balance and Blood Pressure.* Front Endocrinol (Lausanne), 2022. **13**: p. 875425.
79. Natura, G., et al., *Neuronal prostaglandin E2 receptor subtype EP3 mediates antinociception during inflammation. Proc. Natl. Acad. Sci. U.S.A.*, 2013. **110**(33): p. 13648-53.
80. Yokoyama, U., et al., *The Prostanoid EP4 Receptor and Its Signaling Pathway. Pharmacol. Rev.*, 2013. **65**(3): p. 1010-1052.
81. Konya, V., et al., *E-type prostanoid receptor 4 (EP4) in disease and therapy. Pharmacol. Ther.*, 2013. **138**(3): p. 485-502.
82. Zhang, J., Y. Gong, and Y. Yu, *PG F2α Receptor: A Promising Therapeutic Target for Cardiovascular Disease. Front. Pharmacol.*, 2010. **Volume 1 - 2010**.
83. Asaki, T., et al., *Selexipag: An Oral and Selective IP Prostacyclin Receptor Agonist for the Treatment of Pulmonary Arterial Hypertension. J. Med. Chem.*, 2015. **58**(18): p. 7128-7137.
84. Friedman, E.A., et al., *Understanding the role of prostaglandin E2 in regulating human platelet activity in health and disease. Thromb. Res.*, 2015. **136**(3): p. 493-503.
85. Smolenski, A., *Novel roles of cAMP/cGMP-dependent signaling in platelets. J. Thromb. Haemost.*, 2012. **10**(2): p. 167-176.
86. Watts, S.W., N.L. Kanagy, and J.H. Lombard, *Chapter 7 - Receptor-Mediated Events in the Microcirculation*, in *Microcirculation (Second Edition)*, R.F. Tuma, W.N. Durán, and K. Ley, Editors. 2008, Academic Press: San Diego. p. 285-348.
87. Bogatcheva, N.V., et al., *Arachidonic acid cascade in endothelial pathobiology. Microvasc. Res.*, 2005. **69**(3): p. 107-127.

88. Ricciotti, E. and G.A. FitzGerald, *Prostaglandins and inflammation. Arterioscler. Thromb. Vasc. Biol.*, 2011. **31**(5): p. 986-1000.
89. Bley, K.R., et al., *The role of IP prostanoid receptors in inflammatory pain. Trends Pharmacol. Sci.*, 1998. **19**(4): p. 141-147.
90. Eckenstaler, R. and R.A. Benndorf, *Insights into the Expression, Structure, and Function of the Thromboxane A2 Receptor in Vascular Biology. ACS Pharmacol. Transl. Sci.*, 2025. **8**(9): p. 2887-2907.
91. Capra, V., et al., *Impact of vascular thromboxane prostanoid receptor activation on hemostasis, thrombosis, oxidative stress, and inflammation. J. Thromb. Haemost.*, 2014. **12**(2): p. 126-37.
92. Ekambaram, P., et al., *The thromboxane synthase and receptor signaling pathway in cancer: an emerging paradigm in cancer progression and metastasis. Cancer Metastasis Rev.*, 2011. **30**(3-4): p. 397-408.
93. Ershov, P.V., et al., *Prostanoid Signaling in Cancers: Expression and Regulation Patterns of Enzymes and Receptors. Biology (Basel)*, 2022. **11**(4).
94. Lima, I.V., et al., *Role of prostaglandins in neuroinflammatory and neurodegenerative diseases. Mediators Inflamm.*, 2012. **2012**: p. 946813.
95. Tuteja, N., *Signaling through G protein coupled receptors. Plant Signal. Behav.*, 2009. **4**(10): p. 942-7.
96. Wang, M., et al., *Prostaglandin E(2)/EP(2) receptor signalling pathway promotes diabetic retinopathy in a rat model of diabetes. Diabetologia*, 2019. **62**(2): p. 335-348.
97. Sassone-Corsi, P., *The cyclic AMP pathway. Cold. Spring. Harb. Perspect. Biol.*, 2012. **4**(12).
98. Zhang, H., et al., *Complex roles of cAMP–PKA–CREB signaling in cancer. Exp. Hematol. Oncol.*, 2020. **9**(1): p. 32.
99. Jiang, J. and R. Dingledine, *Role of prostaglandin receptor EP2 in the regulations of cancer cell proliferation, invasion, and inflammation. J. Pharmacol. Exp. Ther.*, 2013. **344**(2): p. 360-7.
100. Cheng, X., et al., *Epac and PKA: a tale of two intracellular cAMP receptors. Acta. Biochim. Biophys. Sin. (Shanghai)*, 2008. **40**(7): p. 651-62.
101. Jean-Charles, P.Y., S. Kaur, and S.K. Shenoy, *G Protein-Coupled Receptor Signaling Through β-Arrestin-Dependent Mechanisms. J. Cardiovasc. Pharmacol.*, 2017. **70**(3): p. 142-158.
102. Shukla, A.K. and H. Dwivedi-Agnihotri, *Structure and function of β-arrestins, their emerging role in breast cancer, and potential opportunities for therapeutic manipulation. Adv. Cancer Res.*, 2020. **145**: p. 139-156.
103. Tobin, A.B., *G-protein-coupled receptor phosphorylation: where, when and by whom. Br. J. Pharmacol.*, 2008. **153 Suppl 1**(Suppl 1): p. S167-76.
104. Martínez-Morales, J.C., et al., *Roles of Receptor Phosphorylation and Rab Proteins in G Protein-Coupled Receptor Function and Trafficking. Mol. Pharmacol.*, 2022. **101**(3): p. 144-153.
105. Carman, C.V. and J.L. Benovic, *G-protein-coupled receptors: turn-ons and turn-offs. Curr. Opin. Neurobiol.*, 1998. **8**(3): p. 335-44.

106. Houslay, K.F., et al., *Identification of a multifunctional docking site on the catalytic unit of phosphodiesterase-4 (PDE4) that is utilised by multiple interaction partners. Biochem. J.*, 2017. **474**(4): p. 597-609.
107. Chun, K.S., et al., *The prostaglandin receptor EP2 activates multiple signaling pathways and beta-arrestin1 complex formation during mouse skin papilloma development. Carcinogenesis*, 2009. **30**(9): p. 1620-7.
108. Aoki, T. and S. Narumiya, *Prostaglandin E(2)-EP2 signaling as a node of chronic inflammation in the colon tumor microenvironment. Inflamm. Regen.*, 2017. **37**: p. 4.
109. Liu, T., et al., *NF-κB signaling in inflammation. Signal Transduct. Target. Ther.*, 2017. **2**: p. 17023-.
110. Boniface, K., et al., *Prostaglandin E2 regulates Th17 cell differentiation and function through cyclic AMP and EP2/EP4 receptor signaling. J. Exp. Med.*, 2009. **206**(3): p. 535-48.
111. Napolitani, G., et al., *Prostaglandin E2 enhances Th17 responses via modulation of IL-17 and IFN-gamma production by memory CD4+ T cells. Eur. J. Immunol.*, 2009. **39**(5): p. 1301-12.
112. Cho, J.S., et al., *Prostaglandin E2 Induces IL-6 and IL-8 Production by the EP Receptors/Akt/NF-κB Pathways in Nasal Polyp-Derived Fibroblasts. Allergy Asthma Immunol. Res.*, 2014. **6**(5): p. 449-57.
113. Lee, J., et al., *T cell-intrinsic prostaglandin E(2)-EP2/EP4 signaling is critical in pathogenic T(H)17 cell-driven inflammation. J. Allergy Clin. Immunol.*, 2019. **143**(2): p. 631-643.
114. Medeiros, A.I., et al., *Efferocytosis impairs pulmonary macrophage and lung antibacterial function via PGE2/EP2 signaling. J. Exp. Med.*, 2009. **206**(1): p. 61-8.
115. Ganesh, T., *Prostanoid receptor EP2 as a therapeutic target. J. Med. Chem.*, 2014. **57**(11): p. 4454-65.
116. Ganesh, T., *Targeting EP2 Receptor for Drug Discovery: Strengths, Weaknesses, Opportunities, and Threats (SWOT) Analysis. J. Med. Chem.*, 2023. **66**(14): p. 9313-9324.
117. Matsuo, M., Y. Matsuoka, and M. Tanito, *Efficacy and Patient Tolerability of Omidenepag Isopropyl in the Treatment of Glaucoma and Ocular Hypertension. Clin. Ophthalmol.*, 2022. **16**: p. 1261-1279.
118. Cui, F.B., et al., *Investigation on the regulatory effect of PGE2 on ESCC cells through the trans-activation of EGFR by EP2 and the relevant mechanism. Eur. Rev. Med. Pharmacol. Sci.*, 2017. **21**(24): p. 5668-5676.
119. Wang, Q., et al., *Prostaglandin Pathways: Opportunities for Cancer Prevention and Therapy. Cancer Res.*, 2022. **82**(6): p. 949-965.
120. Zhao, H., et al., *Inflammation and tumor progression: signaling pathways and targeted intervention. Signal Transduct. Target. Ther.*, 2021. **6**(1): p. 263.
121. Shacter, E. and S.A. Weitzman, *Chronic inflammation and cancer. Onc.*, 2002. **16**(2): p. 217-26, 229; discussion 230-2.
122. Thumkeo, D., et al., *PGE(2)-EP2/EP4 signaling elicits immunosuppression by driving the mregDC-Treg axis in inflammatory tumor microenvironment. Cell Rep.*, 2022. **39**(10): p. 110914.

123. Yang, L., et al., *Cancer-associated immunodeficiency and dendritic cell abnormalities mediated by the prostaglandin EP2 receptor. J. Clin. Invest.*, 2003. **111**(5): p. 727-35.
124. Punyawatthananukool, S., et al., *Prostaglandin E(2)-EP2/EP4 signaling induces immunosuppression in human cancer by impairing bioenergetics and ribosome biogenesis in immune cells. Nat. Commun.*, 2024. **15**(1): p. 9464.
125. Wu, V.H., et al., *The GPCR-Gα(s)-PKA signaling axis promotes T cell dysfunction and cancer immunotherapy failure. Nat. Immunol.*, 2023. **24**(8): p. 1318-1330.
126. Larkin, J., et al., *Combined Nivolumab and Ipilimumab or Monotherapy in Untreated Melanoma. N. Engl. J. Med.*, 2015. **373**(1): p. 23-34.
127. Ritter, B. and F.R. Greten, *Modulating inflammation for cancer therapy. J. Exp. Med.*, 2019. **216**(6): p. 1234-1243.
128. Mantovani, A., et al., *Cancer-related inflammation. Nature*, 2008. **454**(7203): p. 436-44.
129. Wang, X., S.J. Baek, and T. Eling, *COX inhibitors directly alter gene expression: role in cancer prevention? Cancer Metastasis Rev.*, 2011. **30**(3-4): p. 641-57.
130. Rayburn, E.R., S.J. Ezell, and R. Zhang, *Anti-Inflammatory Agents for Cancer Therapy. Mol. Cell. Pharmacol.*, 2009. **1**(1): p. 29-43.
131. Zhang, W., et al., *Role of neuroinflammation in neurodegeneration development. Signal Transduct. Target Ther.*, 2023. **8**(1): p. 267.
132. *2020 Alzheimer's disease facts and figures. Alzheimers Dement.*, 2020.
133. Otani, K. and T. Shichita, *Cerebral sterile inflammation in neurodegenerative diseases. Inflamm. Regen.*, 2020. **40**(1): p. 28.
134. Heneka, M.T., M.P. Kummer, and E. Latz, *Innate immune activation in neurodegenerative disease. Nat. Rev. Immunol.*, 2014. **14**(7): p. 463-77.
135. Hansen, D.V., J.E. Hanson, and M. Sheng, *Microglia in Alzheimer's disease. J. Cell. Biol.*, 2018. **217**(2): p. 459-472.
136. Johansson, J.U., et al., *Prostaglandin signaling suppresses beneficial microglial function in Alzheimer's disease models. J. Clin. Invest.*, 2015. **125**(1): p. 350-64.
137. Pooler, A.M., et al., *Prostaglandin E2 regulates amyloid precursor protein expression via the EP2 receptor in cultured rat microglia. Neurosci. Lett.*, 2004. **362**(2): p. 127-30.
138. Kinney, J.W., et al., *Inflammation as a central mechanism in Alzheimer's disease. Alzheimers Dement. (N.Y.)*, 2018. **4**: p. 575-590.
139. Tansey, M.G., et al., *Inflammation and immune dysfunction in Parkinson disease. Nat. Rev. Immunol.*, 2022. **22**(11): p. 657-673.
140. Szeto, J.Y. and S.J. Lewis, *Current Treatment Options for Alzheimer's Disease and Parkinson's Disease Dementia. Curr. Neuropharmacol.*, 2016. **14**(4): p. 326-38.
141. Wold, E.A., et al., *Allosteric Modulation of Class A GPCRs: Targets, Agents, and Emerging Concepts. J. Med. Chem.*, 2019. **62**(1): p. 88-127.
142. Townsend, C., *Ion Channels*, in *Reference Module in Biomedical Sciences*. 2021, Elsevier.
143. Nussinov, R. and C.J. Tsai, *The different ways through which specificity works in orthosteric and allosteric drugs. Curr. Pharm. Des.*, 2012. **18**(9): p. 1311-6.

144. Langmead, C.J. and A. Christopoulos, *Functional and structural perspectives on allosteric modulation of GPCRs. Curr. Opin. Cell. Biol.*, 2014. **27**: p. 94-101.
145. Grover, A.K., *Use of allosteric targets in the discovery of safer drugs. Med. Princ. Pract.*, 2013. **22**(5): p. 418-26.
146. Gregory, K.J., P.M. Sexton, and A. Christopoulos, *Overview of receptor allosterism. Curr. Protoc. Pharmacol.*, 2010. **Chapter 1**: p. Unit 1.21.
147. Christopoulos, A. and T. Kenakin, *G protein-coupled receptor allosterism and complexing. Pharmacol. Rev.*, 2002. **54**(2): p. 323-74.
148. Wold, E.A. and J. Zhou, *GPCR Allosteric Modulators: Mechanistic Advantages and Therapeutic Applications. Curr. Top. Med. Chem.*, 2018. **18**(23): p. 2002-2006.
149. Kenakin, T.P., *Biased signalling and allosteric machines: new vistas and challenges for drug discovery. Br. J. Pharmacol.*, 2012. **165**(6): p. 1659-1669.
150. Fan, L. and S. Wang, *Biased GPCR Signaling: Possible Mechanisms and Therapeutic Applications. Biochem.*, 2025. **64**(6): p. 1180-1192.
151. Valant, C., et al., *Probe dependence in the allosteric modulation of a G protein-coupled receptor: implications for detection and validation of allosteric ligand effects. Mol. Pharmacol.*, 2012. **81**(1): p. 41-52.
152. Zhang, M., et al., *G protein-coupled receptors (GPCRs): advances in structures, mechanisms, and drug discovery. Signal Transduct. Target Ther.*, 2024. **9**(1): p. 88.
153. Bueno, A.B., et al., *Structural insights into probe-dependent positive allosterism of the GLP-1 receptor. Nat. Chem. Biol.*, 2020. **16**(10): p. 1105-1110.
154. Liu, X., et al., *Mechanism of β(2)AR regulation by an intracellular positive allosteric modulator. Science*, 2019. **364**(6447): p. 1283-1287.
155. Liu, X., et al., *An allosteric modulator binds to a conformational hub in the β(2) adrenergic receptor. Nat. Chem. Biol.*, 2020. **16**(7): p. 749-755.
156. Christopher, J.A., et al., *Fragment and Structure-Based Drug Discovery for a Class C GPCR: Discovery of the mGlu5 Negative Allosteric Modulator HTL14242 (3-Chloro-5-[6-(5-fluoropyridin-2-yl)pyrimidin-4-yl]benzonitrile). J. Med. Chem.*, 2015. **58**(16): p. 6653-64.
157. Liu, K., et al., *Structural basis of CXC chemokine receptor 2 activation and signalling. Nature*, 2020. **585**(7823): p. 135-140.
158. Liu, X., et al., *Mechanism of intracellular allosteric β(2)AR antagonist revealed by X-ray crystal structure. Nature*, 2017. **548**(7668): p. 480-484.
159. Rawat, A., et al., *Targeted intracellular delivery of therapeutics: an overview.* Pharmazie. , 2007. **62**(9): p. 643-58.
160. Qu, C., et al., *Ligand recognition, unconventional activation, and G protein coupling of the prostaglandin E(2) receptor EP2 subtype. Sci. Adv.*, 2021. **7**(14).
161. Isberg, V., et al., *Generic GPCR residue numbers - aligning topology maps while minding the gaps. Trends. Pharmacol. Sci.*, 2015. **36**(1): p. 22-31.
162. Saleem, S., et al., *PGD(2) DP1 receptor protects brain from ischemia-reperfusion injury. Eur. J. Neurosci.*, 2007. **26**(1): p. 73-8.
163. Song, W.L., et al., *Niacin and biosynthesis of PGD_2 by platelet COX-1 in mice and humans. J. Clin. Invest.*, 2012. **122**(4): p. 1459-68.

164. Xu, H., et al., *VSMC-specific EP4 deletion exacerbates angiotensin II-induced aortic dissection by increasing vascular inflammation and blood pressure. Proc. Natl. Acad. Sci. U.S.A.*, 2019. **116**(17): p. 8457-8462.
165. Swan, C.E. and R.M. Breyer, *Prostaglandin E2 modulation of blood pressure homeostasis: studies in rodent models. Prostaglandins Other Lipid Mediat.*, 2011. **96**(1-4): p. 10-3.
166. Pickles, H. and J. O'Grady, *Side effects occurring during administration of epoprostenol (prostacyclin, PGI2), in man. Br. J. Clin. Pharmacol.*, 1982. **14**(2): p. 177-85.
167. Ma, Y., B. Patterson, and L. Zhu, *Biased signaling in GPCRs: Structural insights and implications for drug development. Pharmacol. Ther.*, 2025. **266**: p. 108786.
168. Loperfido, A., et al., *Strategies for Tapering the Dosage of Biologics Targeting Type 2 Inflammation: A Systematic Review. Curr. Allergy Asthma Rep.*, 2025. **25**(1): p. 32.
169. Jiang, J., et al., *Small molecule antagonist reveals seizure-induced mediation of neuronal injury by prostaglandin E2 receptor subtype EP2. Proc. Natl. Acad. Sci. U.S.A.*, 2012. **109**(8): p. 3149-54.
170. Ganesh, T., et al., *Discovery and characterization of carbamothioylacrylamides as EP(2) selective antagonists. ACS Med. Chem. Lett.*, 2013. **4**(7): p. 616-621.
171. af Forselles, K.J., et al., *In vitro and in vivo characterization of PF-04418948, a novel, potent and selective prostaglandin EP_2 receptor antagonist. Br. J. Pharmacol.*, 2011. **164**(7): p. 1847-56.
172. Fox, B.M., et al., *A selective prostaglandin E2 receptor subtype 2 (EP2) antagonist increases the macrophage-mediated clearance of amyloid-beta plaques. J. Med. Chem.*, 2015. **58**(13): p. 5256-73.
173. Hou, R., Y. Yu, and J. Jiang, *Prostaglandin E2 in neuroblastoma: Targeting synthesis or signaling? Biomed. Pharmacother.*, 2022. **156**: p. 113966.
174. Tejwani, V., et al., *Glycoengineering in CHO Cells: Advances in Systems Biology.* Biotechnol. J., 2018. **13**(3): p. e1700234.
175. Wang, C., et al., *Targeting the EP2 receptor ameliorates inflammatory bowel disease in mice by enhancing the immunosuppressive activity of T(reg) cells. Mucosal Immunol.*, 2025. **18**(2): p. 418-430.
176. Sanguinetti, M.C. and M. Tristani-Firouzi, *hERG potassium channels and cardiac arrhythmia.* Nature, 2006. **440**(7083): p. 463-9.
177. Conn, P.J., A. Christopoulos, and C.W. Lindsley, *Allosteric modulators of GPCRs: a novel approach for the treatment of CNS disorders. Nat. Rev. Drug Discov.*, 2009. **8**(1): p. 41-54.
178. Christopoulos, A., et al., *International Union of Basic and Clinical Pharmacology. XC. multisite pharmacology: recommendations for the nomenclature of receptor allosterism and allosteric ligands. Pharmacol. Rev.*, 2014. **66**(4): p. 918-47.
179. Jiang, C., et al., *An Agonist Dependent Allosteric Antagonist of Prostaglandin EP2 Receptors. ACS Chem. Neurosci.*, 2020. **11**(10): p. 1436-1446.
180. Cree, I.A. and P.E. Andreotti, *Measurement of cytotoxicity by ATP-based luminescence assay in primary cell cultures and cell lines. Toxicol. In Vitro*, 1997. **11**(5): p. 553-6.

181. Toyoda, Y., et al., *Ligand binding to human prostaglandin E receptor EP(4) at the lipid-bilayer interface. Nat. Chem. Biol.*, 2019. **15**(1): p. 18-26.
182. Regan, J.W., *EP2 and EP4 prostanoid receptor signaling. Life Sci.*, 2003. **74**(2-3): p. 143-53.
183. Zheng, Y., et al., *Structure of CC chemokine receptor 2 with orthosteric and allosteric antagonists. Nature*, 2016. **540**(7633): p. 458-461.
184. Oswald, C., et al., *Intracellular allosteric antagonism of the CCR9 receptor. Nature*, 2016. **540**(7633): p. 462-465.
185. Colquhoun, D., *Affinity, efficacy and receptor classification: is the classical theory still useful?* 1987. p. 103-114.
186. Stephenson, R.P., *A modification of receptor theory. Br. J. Pharmacol. Chemother.*, 1956. **11**(4): p. 379-93.
187. Hill, A.V. and A. Paganini-Hill, *The possible effects of the aggregation of the molecules of haemoglobin on its dissociation curves. J. Physiol.* **40**: p. 4-7.
188. Gesztelyi, R., et al., *The Hill equation and the origin of quantitative pharmacology. Arch. Hist. Exact. Sci.*, 2012. **66**(4): p. 427-438.
189. De Lean, A., J.M. Stadel, and R.J. Lefkowitz, *A ternary complex model explains the agonist-specific binding properties of the adenylate cyclase-coupled beta-adrenergic receptor. J. Biol. Chem.*, 1980. **255**(15): p. 7108-17.
190. Costa, T. and A. Herz, *Antagonists with negative intrinsic activity at delta opioid receptors coupled to GTP-binding proteins. Proc. Natl. Acad. Sci. U.S.A.*, 1989. **86**(19): p. 7321-5.
191. Samama, P., et al., *A mutation-induced activated state of the beta 2-adrenergic receptor. Extending the ternary complex model. J. Biol. Chem.*, 1993. **268**(7): p. 4625-36.
192. Weiss, J.M., et al., *The cubic ternary complex receptor-occupancy model. III. resurrecting efficacy. J. Theor. Biol.*, 1996. **181**(4): p. 381-97.
193. Weis, W.I. and B.K. Kobilka, *The Molecular Basis of G Protein-Coupled Receptor Activation. Annu. Rev. Biochem.*, 2018. **87**: p. 897-919.
194. Jakubík, J., et al., *The operational model of allosteric modulation of pharmacological agonism. Sci. Rep.*, 2020. **10**(1): p. 14421.
195. Ferguson, D.C., *Chapter 3 - Principles of Pharmacodynamics and Toxicodynamics*, in *Haschek and Rousseaux's Handbook of Toxicologic Pathology (Third Edition)*, W.M. Haschek, C.G. Rousseaux, and M.A. Wallig, Editors. 2013, Academic Press: Boston. p. 61-76.
196. Meineke, I. and C.H. Gleiter, *Assessment of drug accumulation in the evaluation of pharmacokinetic data. J. Clin. Pharmacol.*, 1998. **38**(8): p. 680-4.
197. Srinivasan, B. and M.D. Lloyd, *Dose–Response Curves and the Determination of IC50 and EC50 Values. J. Med. Chem.*, 2024. **67**(20): p. 17931-17934.
198. Cheng, Y. and W.H. Prusoff, *Relationship between the inhibition constant (K1) and the concentration of inhibitor which causes 50 per cent inhibition (I50) of an enzymatic reaction. Biochem. Pharmacol.*, 1973. **22**(23): p. 3099-108.
199. Cheng, H.C., *The power issue: determination of KB or Ki from IC50: A closer look at the Cheng–Prusoff equation, the Schild plot and related power equations. J. Pharmacol. Toxicol. Methods*, 2001. **46**(2): p. 61-71.

200. Srinivasan, B. and M.D. Lloyd, *Dose-Response Curves and the Determination of IC(50) and EC(50) Values. J. Med. Chem.*, 2024. **67**(20): p. 17931-17934.
201. Maguire, J.J., R.E. Kuc, and A.P. Davenport, *Radioligand binding assays and their analysis. Methods Mol. Biol.*, 2012. **897**: p. 31-77.
202. Stoddart, L.A., et al., *Fluorescence- and bioluminescence-based approaches to study GPCR ligand binding. Br. J. Pharmacol.*, 2016. **173**(20): p. 3028-37.
203. Förster, T., *Zwischenmolekulare Energiewanderung und Fluoreszenz (Intermolecular energy migration and fluoresence). Ann. Phys. 2*, 1948. **437**(1-2): p. 55-75.
204. Sykes, D.A. and S.J. Charlton, *Single Step Determination of Unlabeled Compound Kinetics Using a Competition Association Binding Method Employing Time-Resolved FRET. Methods Mol. Biol.*, 2018. **1824**: p. 177-194.
205. Nørskov-Lauritsen, L., A.R. Thomsen, and H. Bräuner-Osborne, *G protein-coupled receptor signaling analysis using homogenous time-resolved Förster resonance energy transfer (HTRF®) technology. Int. J. Mol. Sci.*, 2014. **15**(2): p. 2554-72.
206. Sajkowska, J.J., C.H. Tsang, and P. Kozielewicz, *Application of FRET- and BRET-based live-cell biosensors in deorphanization and ligand discovery studies on orphan G protein-coupled receptors. SLAS Discov.*, 2024. **29**(6): p. 100174.
207. Fung, J.J., et al., *Ligand-regulated oligomerization of beta(2)-adrenoceptors in a model lipid bilayer. Embo J.*, 2009. **28**(21): p. 3315-28.
208. Vilardaga, J.P., *Studying ligand efficacy at G protein-coupled receptors using FRET. Methods Mol. Biol.*, 2011. **756**: p. 133-48.
209. Zwier, J.M., et al., *A fluorescent ligand-binding alternative using Tag-lite® technology. J. Biomol. Screen.*, 2010. **15**(10): p. 1248-59.
210. Emami-Nemini, A., et al., *Time-resolved fluorescence ligand binding for G protein-coupled receptors. Nat. Protoc.*, 2013. **8**(7): p. 1307-20.
211. Heuninck, J., et al., *Time-Resolved FRET-Based Assays to Characterize G Protein-Coupled Receptor Hetero-oligomer Pharmacology. Methods Mol. Biol.*, 2019. **1947**: p. 151-168.
212. Hall, M.P., et al., *Engineered luciferase reporter from a deep sea shrimp utilizing a novel imidazopyrazinone substrate. ACS Chem. Biol.*, 2012. **7**(11): p. 1848-57.
213. England, C.G., E.B. Ehlerding, and W. Cai, *NanoLuc: A Small Luciferase Is Brightening Up the Field of Bioluminescence. Bioconjug. Chem.*, 2016. **27**(5): p. 1175-1187.
214. Bonardi, A., et al., *Behind the glow: unveiling the nature of NanoLuc reactants and products. Phys. Chem. Chem. Phys.*, 2024. **26**(43): p. 27447-27458.
215. Pfleger, K.D. and K.A. Eidne, *Illuminating insights into protein-protein interactions using bioluminescence resonance energy transfer (BRET). Nat. Methods*, 2006. **3**(3): p. 165-74.
216. Stoddart, L.A., L.E. Kilpatrick, and S.J. Hill, *NanoBRET Approaches to Study Ligand Binding to GPCRs and RTKs. Trends Pharmacol. Sci.*, 2018. **39**(2): p. 136-147.
217. Stoddart, L.A., et al., *Application of BRET to monitor ligand binding to GPCRs. Nat. Methods*, 2015. **12**(7): p. 661-663.

218. Soave, M., et al., *Use of a new proximity assay (NanoBRET) to investigate the ligand-binding characteristics of three fluorescent ligands to the human β(1)-adrenoceptor expressed in HEK-293 cells. Pharmacol. Res. Perspect.*, 2016. **4**(5): p. e00250.
219. Farmer, J.P., et al., *Development of fluorescent peptide G protein-coupled receptor activation biosensors for NanoBRET characterization of intracellular allosteric modulators. Faseb J.*, 2022. **36**(11): p. e22576.
220. Walker, J.R., et al., *Highly Potent Cell-Permeable and Impermeable NanoLuc Luciferase Inhibitors. ACS Chem. Biol.*, 2017. **12**(4): p. 1028-1037.
221. Dixon, A.S., et al., *NanoLuc Complementation Reporter Optimized for Accurate Measurement of Protein Interactions in Cells. ACS Chem. Biol.*, 2016. **11**(2): p. 400-8.
222. Dijon, N.C., D.N. Nesheva, and N.D. Holliday, *Luciferase Complementation Approaches to Measure GPCR Signaling Kinetics and Bias. Methods Mol. Biol.*, 2021. **2268**: p. 249-274.
223. Wan, Q., et al., *Mini G protein probes for active G protein-coupled receptors (GPCRs) in live cells. J. Biol. Chem.*, 2018. **293**(19): p. 7466-7473.
224. Carpenter, B. and C.G. Tate, *Engineering a minimal G protein to facilitate crystallisation of G protein-coupled receptors in their active conformation. Protein Eng. Des. Sel.*, 2016. **29**(12): p. 583-594.
225. Waller, D. and A. Sampson, *Principles of pharmacology and mechanisms of drug action*, in *Medical Pharmacology and Therapeutics (Fifth Edition*. 2018. p. 3-31.
226. Kawasaki, Y. and E. Freire, *Finding a better path to drug selectivity. Drug Discov. Today*, 2011. **16**(21-22): p. 985-90.
227. Kise, R. and A. Inoue, *GPCR signaling bias: an emerging framework for opioid drug development. J. Biochem.*, 2024. **175**(4): p. 367-376.
228. Fiser, A., *Template-based protein structure modeling. Methods Mol. Biol.*, 2010. **673**: p. 73-94.
229. Loeffler, J.R., et al., *STACKED - Solvation Theory of Aromatic Complexes as Key for Estimating Drug Binding. J. Chem. Inf. Model.*, 2020. **60**(4): p. 2304-2313.
230. Adhav, V.A. and K. Saikrishnan, *The Realm of Unconventional Noncovalent Interactions in Proteins: Their Significance in Structure and Function. ACS Omega*, 2023. **8**(25): p. 22268-22284.
231. Kumari, S., et al., *Amide Bond Bioisosteres: Strategies, Synthesis, and Successes. J. Med. Chem.*, 2020. **63**(21): p. 12290-12358.
232. Snape, T., A. Astles, and J. Davies, *Understanding the chemical basis of drug stability and degradation. Pharm. J.*, 2010. **285**.
233. Laizure, S.C., et al., *The role of human carboxylesterases in drug metabolism: have we overlooked their importance? J. Pharmacother.*, 2013. **33**(2): p. 210-22.
234. Powers, E.T., S. Deechongkit, and J.W. Kelly, *Backbone–Backbone H-Bonds Make Context-Dependent Contributions to Protein Folding Kinetics and Thermodynamics: Lessons from Amide-to-Ester Mutations*, in *Advances in Protein Chemistry*. 2005, Academic Press. p. 39-78.

235. Lipinski, C.A., et al., *Experimental and computational approaches to estimate solubility and permeability in drug discovery and development settings. Adv. Drug Deliv. Rev.*, 1997. **23**(1): p. 3-25.
236. Hou, T.J. and X.J. Xu, *ADME Evaluation in Drug Discovery. 3. Modeling Blood-Brain Barrier Partitioning Using Simple Molecular Descriptors. J. Chem. Inf. Comput. Sci.*, 2003. **43**(6): p. 2137-2152.
237. Teague, S.J., *Implications of protein flexibility for drug discovery. Nat. Rev. Drug Discov.*, 2003. **2**(7): p. 527-41.
238. Feixas, F., et al., *Exploring the role of receptor flexibility in structure-based drug discovery. Biophys. Chem.*, 2014. **186**: p. 31-45.
239. Caron, G., et al., *Flexibility in early drug discovery: focus on the beyond-Rule-of-5 chemical space. Drug Discov. Today*, 2020. **25**(4): p. 621-627.
240. Veber, D.F., et al., *Molecular Properties That Influence the Oral Bioavailability of Drug Candidates. J. Med. Chem.*, 2002. **45**(12): p. 2615-2623.
241. Ertl, P., *Polar Surface Area*, in *Molecular Drug Properties*. 2007. p. 111-126.
242. Achar, A., R. Myers, and C. Ghosh, *Drug Delivery Challenges in Brain Disorders across the Blood–Brain Barrier: Novel Methods and Future Considerations for Improved Therapy. Biomed.*, 2021. **9**(12): p. 1834.
243. Hughes, L.D., et al., *Why Are Some Properties More Difficult To Predict than Others? A Study of QSPR Models of Solubility, Melting Point, and Log P. J. Chem. Inf. Model.*, 2008. **48**(1): p. 220-232.
244. Jorgensen, W.L. and E.M. Duffy, *Prediction of drug solubility from structure. Adv. Drug Deliv. Rev.*, 2002. **54**(3): p. 355-66.
245. Obafemi, C.A. and W. Pfleiderer, *Synthesis and some reactions of 3-chloro-2-(cyanomethylene)-1,2-dihydroquinoxalines. Molecules*, 2004. **9**(4): p. 223-31.
246. Otomasu, H., S. Ohmiya, and T. Sekiguchi, *Synthesis of Condensed Quinoxalines. II. A New Synthesis of Pyrrolo- [2,3-b] quinoxalines. Chem. Pharm. Bull.*, 1970. **18**: p. 2065-2069.
247. Yates, K. and R.A. McClelland, *Mechanisms of ester hydrolysis in aqueous sulfuric acids. J. Am. Chem. Soc.*, 1967. **89**(11): p. 2686-2692.
248. Johnson, S.L., *General Base and Nucleophilic Catalysis of Ester Hydrolysis and Related Reactions*, in *Advances in Physical Organic Chemistry*, V. Gold, Editor. 1967, Academic Press. p. 237-330.
249. Sing Lim, K., *Structure-Activity Relationship studies of intracellular allosteric modulators for the Prostaglandin E2 Receptor 2 (EP2)*, in *School Of Pharmacy*. 2022, University of Nottingham: Internal. p. 40.
250. Khaki, M., *Structure-Activity Relationship studies of intracellular allosteric modulators for the Prostaglandin E2 Receptor 2 (EP2)*, in *School Of Pharmacy*. 2022, University of Nottingham: Internal. p. 30.
251. Kurasawa, Y. and A. Takada, *Characteristic tautomerism and isomerization in the quinoxaline chemistry. Heterocycles*, 1986. **24**: p. 2322-2355.
252. Pfaff, D., G. Nemecek, and J. Podlech, *A Lewis acid-promoted Pinner reaction. Beilstein J. Org. Chem.*, 2013. **9**: p. 1572-7.

253. Li, J.J., *Name Reactions: A Collection of Detailed Mechanisms and Synthetic Applications- Fischer-Speier esterification*. Fifth ed. 2014: Springer International Publishing.
254. Chen, Y. and Y. Li, *Bicyclic and tricyclic inhibitors of sumoylation enzymes and methods for their use.*, in *Patent Scope*, W.I. P., Editor. 2012: U. S.
255. Krieble, V.K. and C.I. Noll, *The Hydrolysis of Nitriles with Acids. J. Am. Chem. Soc.*, 1939. **61**(3): p. 560-563.
256. M. Wei, et al., *Design, synthesis and biological evaluation of a series of novel 2-benzamide-4-(6-oxy-N-methyl-1-naphthamide)-pyridine derivatives as potent fibroblast growth factor receptor (FGFR) inhibitors.* Eur. J. Med. Chem., 2018. **154**: p. 9-28.
257. Kurihara, T., K. Nakamura, and H. Hirano, *Studies on indenopyridine derivatives and related compounds. I. Syntheses and stereochemistries of 1-substituted 1,2,3,4,4a,9a-hexahydro-4-hydroxy-9H-indeno(2,1-b)pyridines and related compounds. Chem. Pharm. Bull. (Tokyo)*, 1974. **22**(8): p. 1839-45.
258. McIsaac Jr, J.E., R.E. Ball, and E.J. Behrman, *Mechanism of the base-catalyzed conversion of nitriles to amides by hydrogen peroxide. J. Org. Chem.*, 1971. **36**(20): p. 3048-3050.
259. Yamasaki, R., et al., *Synthesis and properties of phenylogous amides. Tetrahedron*, 2012. **68**(40): p. 8450-8456.
260. Casiraghi, G., et al., *The vinylogous aldol reaction: a valuable, yet understated carbon-carbon bond-forming maneuver. Chem. Rev.*, 2000. **100**(6): p. 1929-72.
261. Curti, C., et al., *New Developments of the Principle of Vinylogy as Applied to π-Extended Enolate-Type Donor Systems. Chem. Rev.*, 2020. **120**(5): p. 2448-2612.
262. Ouellette, R.J. and J.D. Rawn, *21 - Carboxylic Acid Derivatives*, in *Organic Chemistry*, R.J. Ouellette and J.D. Rawn, Editors. 2014, Elsevier: Boston. p. 699-745.
263. Neises, B. and W. Steglich, *Simple Method for the Esterification of Carboxylic Acids. Angew. Chem. Int. Ed. Engl.*, 1978. **17**(7): p. 522-524.
264. Pon, R.T., S. Yu, and Y.S. Sanghvi, *Rapid Esterification of Nucleosides to Solid-Phase Supports for Oligonucleotide Synthesis Using Uronium and Phosphonium Coupling Reagents. Bioconjug. Chem.*, 1999. **10**(6): p. 1051-1057.
265. Yang, N.Y., *Synthesis of analogues of a negative allosteric modulator of the prostaglandin E2 receptor EP2*, in *School of Pharmacy*. 2023, University of Nottingham: Internal. p. 67.
266. Machetti, F., et al., *Neat reaction of carboxylic acid methyl esters and amines for efficient parallel synthesis of scaffold amide libraries. C. R. Chim.*, 2003. **6**(5): p. 631-633.
267. Hu, L., et al., *Spiro urea compounds as RSV antiviral compounds*, WIPO, Editor. 2015.
268. Babu, P.V., et al., *Ligand/PTC-free intramolecular Heck reaction: synthesis of pyrroloquinoxalines and their evaluation against PDE4/luciferase/oral cancer cell growth in vitro and zebrafish in vivo. Org. Biomol. Chem.*, 2013. **11**(39): p. 6680-6685.

269. Szychowski, J., et al., *Discovery of an Orally Bioavailable and Selective PKMYT1 Inhibitor, RP-6306. J. Med. Chem.*, 2022. **65**(15): p. 10251-10284.
270. Abou-Shehada, S., et al., *Lewis Acid Activation of Pyridines for Nucleophilic Aromatic Substitution and Conjugate Addition. ChemSusChem*, 2015. **8**(6): p. 1083-1087.
271. Kirby, A.J. and W.P. Jencks, *Base Catalysis of the Reaction of Secondary Amines with p-Nitrophenyl Phosphate. Kinetic Evidence for an Addition Intermediate in Nucleophilic Aromatic Substitution1. J. Am. Chem. Soc.*, 1965. **87**(14): p. 3217-3224.
272. Thabit, M., S. El Bialy, and M. Nasr, *Synthesis and biological evaluation of new 3-(4-subsituted phenyl)aminoquinoxaline derivatives as anticancer agents. Heterocycl. Commun.*, 2015. **21**.
273. Yi, X., et al., *Copper-Catalyzed Radical N-Demethylation of Amides Using N-Fluorobenzenesulfonimide as an Oxidant. Org. Lett.*, 2020. **22**(12): p. 4583-4587.
274. Teng, Q.H., et al., *Visible-light Induced Cerium-catalyzed N-Demethylation of N-Methyl Amides under Air Conditions. Adv. Synth. Catal.*, 2023. **365**(3): p. 307-311.
275. Golkowski, M. and T. Ziegler, *The 2-(triphenylsilyl)ethoxycarbonyl-("Tpseoc"-) group: a new silicon-based, fluoride cleavable oxycarbonyl protecting group highly orthogonal to the Boc-, Fmoc- and Cbz-groups. Molecules*, 2011. **16**(6): p. 4695-718.
276. Barcelos, M.P., et al., *Lead Optimization in Drug Discovery*, in *Research Topics in Bioactivity, Environment and Energy: Experimental and Theoretical Tools*, C.A. Taft and S.R. de Lazaro, Editors. 2022, Springer International Publishing: Cham. p. 481-500.
277. Miller, R.T., et al., *A mutation that prevents GTP-dependent activation of the alpha chain of Gs. Nature*, 1988. **334**(6184): p. 712-5.
278. Hirsch, J.P., C. Dietzel, and J. Kurjan, *The carboxyl terminus of Scg1, the G alpha subunit involved in yeast mating, is implicated in interactions with the pheromone receptors. Genes Dev.*, 1991. **5**(3): p. 467-74.
279. Hamm, H.E., et al., *Site of G protein binding to rhodopsin mapped with synthetic peptides from the alpha subunit. Science*, 1988. **241**(4867): p. 832-5.
280. Conklin, B.R., et al., *Substitution of three amino acids switches receptor specificity of Gq alpha to that of Gi alpha. Nature*, 1993. **363**(6426): p. 274-6.
281. Palm, D., et al., *Identification of a Gs-protein coupling domain to the beta-adrenoceptor using site-specific synthetic peptides. Carboxyl terminus of Gs alpha is involved in coupling to beta-adrenoceptors. FEBS Lett.*, 1990. **261**(2): p. 294-8.
282. Rasenick, M.M., et al., *Synthetic peptides as probes for G protein function. Carboxyl-terminal G alpha s peptides mimic Gs and evoke high affinity agonist binding to beta-adrenergic receptors. J. Biol. Chem.*, 1994. **269**(34): p. 21519-25.
283. Mannes, M., et al., *Development of Generic G Protein Peptidomimetics Able to Stabilize Active State G(s) Protein-Coupled Receptors for Application in Drug Discovery. Angew. Chem. Int. Ed.*, 2021. **60**(18): p. 10247-10254.

284. Mannes, M., et al., *Development of Generic G Protein Peptidomimetics Able to Stabilize Active State Gs Protein-Coupled Receptors for Application in Drug Discovery. Angew. Chem. Int. Ed.*, 2021. **60**(18): p. 10247-10254.
285. Hoare, B.L., et al., *ThermoBRET: A Ligand-Engagement Nanoscale Thermostability Assay Applied to GPCRs. Chembiochem*, 2024. **25**(2): p. e202300459.
286. Dijon, N.C., *Novel complementation biosensors to investigate G protein coupled receptor kinetics and signalling*, in *Cell Signalling Research Group*. 2022, University of Nottingham: Nottingham eThesis. p. 330.
287. Soave, M., et al., *Monitoring Allosteric Interactions with CXCR4 Using NanoBiT Conjugated Nanobodies. Cell. Chem. Biol.*, 2020. **27**(10): p. 1250-1261.e5.
288. Yano, H., et al., *Luciferase complementation based-detection of G-protein-coupled receptor activity. Biotechniques*, 2018. **65**(1): p. 9-14.
289. Farmer, J.P., *Universal sensors for identifying use-dependent intracellular allosteric modulators of G protein coupled receptors.*, in *School of Life Sciences*. 2024, University of Nottingham: Nottingham eTheses. p. 324.
290. Katritch, V., et al., *Allosteric sodium in class A GPCR signaling.* Trends Biochem. Sci., 2014. **39**(5): p. 233-44.
291. Karas, L.J., et al., *Hydrogen bond design principles. Wiley Interdiscip. Rev. Comput. Mol. Sci.*, 2020. **10**(6).
292. Bootsma, A.N., A.C. Doney, and S.E. Wheeler, *Predicting the Strength of Stacking Interactions between Heterocycles and Aromatic Amino Acid Side Chains. J. Am. Chem. Soc.*, 2019. **141**(28): p. 11027-11035.
293. Bitencourt-Ferreira, G., M. Veit-Acosta, and W.F. de Azevedo, Jr., *Van der Waals Potential in Protein Complexes. Methods Mol. Biol.*, 2019. **2053**: p. 79-91.
294. Hubbard, R.E. and M. Kamran Haider, *Hydrogen Bonds in Proteins: Role and Strength*, in *eLS*. 2010: Wiley Online Library.
295. P., C.N., D. Auld, and P. Roby, *Compound-mediated assay interferences in homogenous proximity assays.*, in *The assay guidance manual*. 2020: National Library of Medicine.
296. Pelay-Gimeno, M., et al., *Structure-Based Design of Inhibitors of Protein–Protein Interactions: Mimicking Peptide Binding Epitopes. Angew. Chem. Int. Ed.*, 2015. **54**(31): p. 8896-8927.
297. Villén, J., et al., *Rational Dissection of Binding Surfaces for Mimicking of Discontinuous Antigenic Sites. Chem. Biol.*, 2006. **13**(8): p. 815-823.
298. Bang, I. and H.J. Choi, *Structural features of β2 adrenergic receptor: crystal structures and beyond. Mol. Cells*, 2015. **38**(2): p. 105-11.
299. Gardiner, P.J., *Characterization of prostanoid relaxant/inhibitory receptors (psi) using a highly selective agonist, TR4979. Br. J. Pharmacol.*, 1986. **87**(1): p. 45-56.
300. Cameron, K.O., et al., *Discovery of CP-533536: An EP2 receptor selective prostaglandin E2 (PGE2) agonist that induces local bone formation. Bioorg. Med. Chem. Lett.*, 2009. **19**(7): p. 2075-2078.
301. Hirata, T. and S. Narumiya, *Prostanoid Receptors. Chem. Rev.*, 2011. **111**(10): p. 6209-6230.

302. Wilson, R.J., et al., *Functional pharmacology of human prostanoid EP2 and EP4 receptors*. *Eur. J. Pharmacol.*, 2004. **501**(1-3): p. 49-58.
303. Chan, K.M. and R.L. Jones, *Partial agonism of taprostene at prostanoid IP receptors in vascular preparations from guinea-pig, rat, and mouse*. *J. Cardiovasc. Pharmacol.*, 2004. **43**(6): p. 795-807.
304. Gress, K., et al., *A comprehensive review of partial opioid agonists for the treatment of chronic pain*. *Best Pract. Res. Clin. Anaesthesiol.*, 2020. **34**(3): p. 449-461.
305. Sugimoto, Y. and S. Narumiya, *Prostaglandin E receptors*. *J. Biol. Chem.*, 2007. **282**(16): p. 11613-7.
306. Vleeshouwers, W., et al., *Characterization of the Signaling Modalities of Prostaglandin E2 Receptors EP2 and EP4 Reveals Crosstalk and a Role for Microtubules*. *Front. Immunol.*, 2020. **11**: p. 613286.
307. Paolini, G.V., R.A. Lyons, and P. Laflin, *How desirable are your IC50s? A way to enhance screening-based decision making*. *J. Biomol. Screen.*, 2010. **15**(10): p. 1183-93.
308. Di, L. and E.H. Kerns, *Chapter 5 - Lipophilicity*, in *Drug-Like Properties (Second Edition)*, L. Di and E.H. Kerns, Editors. 2016, Academic Press: Boston. p. 39-50.
309. Bennion, B.J., et al., *Predicting a Drug's Membrane Permeability: A Computational Model Validated With in Vitro Permeability Assay Data*. *J. Phys. Chem. B.*, 2017. **121**(20): p. 5228-5237.
310. Hoare, S.R.J., *The Problems of Applying Classical Pharmacology Analysis to Modern In Vitro Drug Discovery Assays: Slow Binding Kinetics and High Target Concentration*. *SLAS Discovery*, 2021. **26**(7): p. 835-850.
311. Ong, S., H. Liu, and C. Pidgeon, *Immobilized-artificial-membrane chromatography: measurements of membrane partition coefficient and predicting drug membrane permeability*. *J. Chromatogr. A.*, 1996. **728**(1-2): p. 113-28.
312. Gilchrist, A., et al., *G alpha minigenes expressing C-terminal peptides serve as specific inhibitors of thrombin-mediated endothelial activation*. *J. Biol. Chem.*, 2001. **276**(28): p. 25672-9.
313. Gilchrist, A., et al., *Antagonists of the receptor-G protein interface block Gi-coupled signal transduction*. *J. Biol. Chem.*, 1998. **273**(24): p. 14912-9.
314. Eiger, D.S., et al., *GPCR systems pharmacology: a different perspective on the development of biased therapeutics*. Am. J. Physiol. Cell Physiol., 2022. **322**(5): p. C887-c895.
315. McCallum, M.M., et al., *A fluorescence-based high throughput assay for the determination of small molecule-human serum albumin protein binding*. Anal. Bioanal. Chem., 2014. **406**(7): p. 1867-75.
316. Moore, M.N., et al., *Design of allosteric modulators that change GPCR G protein subtype selectivity*. *bioRxiv*, 2024.
317. Wang, T., et al., *Measurements of cAMP for Gas- and Gai protein-coupled receptors (GPCRs)*, in *The assay guidance manual*, S. Markossian, A. Grossman, and H. Baskir, Editors. 2017: national library of medicine.

318. Conigrave, A.D. and A.H. Franks, *Allosteric activation of plasma membrane receptors—physiological implications and structural origins. Prog. Biophys. Mol. Biol.*, 2003. **81**(3): p. 219-240.
319. Yanamala, N., K.C. Tirupula, and J. Klein-Seetharaman, *Preferential binding of allosteric modulators to active and inactive conformational states of metabotropic glutamate receptors. BMC Bioinformatics*, 2008. **9 Suppl 1**(Suppl 1): p. S16.
320. Mech, P., et al., *Calculations of pKa Values of Selected Pyridinium and Its N-Oxide Ions in Water and Acetonitrile. J. Phys. Chem. A.*, 2020. **124**(3): p. 538-551.
321. Manallack, D.T., *The pK(a) Distribution of Drugs: Application to Drug Discovery. Perspect. Medicin. Chem.*, 2007. **1**: p. 25-38.
322. Pennington, L.D. and D.T. Moustakas, *The Necessary Nitrogen Atom: A Versatile High-Impact Design Element for Multiparameter Optimization. J. Med. Chem.*, 2017. **60**(9): p. 3552-3579.
323. Galland, N., C. Laurence, and J.Y. Le Questel, *The pKBHX Hydrogen-Bond Basicity Scale: From Molecules to Anions. J. Org. Chem.*, 2022. **87**(11): p. 7264-7273.
324. Laurence, C., et al., *The pKBHX Database: Toward a Better Understanding of Hydrogen-Bond Basicity for Medicinal Chemists. J. Med. Chem.*, 2009. **52**(14): p. 4073-4086.
325. Berthelot, M., et al., *Hydrogen-bond basicity pKHB scale of six-membered aromatic N-heterocycles. J. Chem. Soc. Perkin. Trans. 2*, 1998(2): p. 283-290.
326. Shah, M.B., et al., *Halogen-π Interactions in the Cytochrome P450 Active Site: Structural Insights into Human CYP2B6 Substrate Selectivity. ACS Chem. Biol.*, 2017. **12**(5): p. 1204-1210.
327. Shah, M.B., et al., *Halogen-π Interactions in the Cytochrome P450 Active Site: Structural Insights into Human CYP2B6 Substrate Selectivity.* ACS Chem Biol, 2017. **12**(5): p. 1204-1210.
328. Mitra, D., et al., *C-halogen...pi interactions in nucleic acids: a database study. J. Chem. Sci.*, 2020. **132**(1): p. 93.
329. Kanao, E., et al., *Separation of halogenated benzenes enabled by investigation of halogen–π interactions with carbon materials. Chem. Sci.*, 2020. **11**(2): p. 409-418.
330. Zhang, J., et al., *Unexpected effect of halogenation on the water solubility of small organic compounds. Comput. Biol. Med.*, 2024. **172**: p. 108209.
331. Benlakhdar, F., et al., *Effect of halogen substitution on the electronic and optical behavior of $C_{16}H_{10}X_2O_2$(X = F, cl, Br and I) organic semiconductors. Sci. Rep.*, 2025. **15**(1): p. 25891.
332. Villaluenga, J. and A. Tabe-Mohammadi, *A review on the separation of benzene/cyclohexane mixtures by pervaporation process. J. Membr. Sci.*, 2000. **169**: p. 159-174.
333. Chiodi, D. and Y. Ishihara, *The role of the methoxy group in approved drugs. Eur. J. Med. Chem.*, 2024. **273**: p. 116364.
334. Wiles, L.A., *The Methoxyl Group. Chem. Rev.*, 1956. **56**(2): p. 329-385.

335. Ling, Y., et al., *The Expanding Role of Pyridine and Dihydropyridine Scaffolds in Drug Design*. *Drug Des. Devel. Ther.*, 2021. **15**(null): p. 4289-4338.
336. King, J.F., et al., *Nucleophilic substitution factors. 1. Coplanar vs. orthogonal bimolecular substitution at a benzylic carbon. X-ray structure of 2-isobutyl-1,3-dihydrobenzo[c]thiophenium perchlorate*. *J. Am. Chem. Soc.*, 1985. **107**(11): p. 3224-3232.
337. Sharma, I. and G.A. Kaminski, *Calculating pKa values for substituted phenols and hydration energies for other compounds with the first-order Fuzzy-Border continuum solvation model*. *J. Comput. Chem.*, 2012. **33**(30): p. 2388-99.
338. Dunker, C., K. Schlegel, and A. Junker, *Phenol (bio)isosteres in drug design and development*. *Archiv der Pharmazie*, 2025. **358**(1): p. e2400700.
339. Robinson, S., *The design and synthesis of allosteric modulators for the prosanoid EP2 receptor*, in *School of Pharmacy*. 2024, University of Nottingham: Internal. p. 30.
340. Singh, B., *Exploration of the intracellular allosteric binding sites of G protein-coupled receptors.*, in *School of Pharmacy*. 2024, University of Nottingham: Internal. p. 50.
341. Yang, N.Y., *Synthesis of analogues of a negative allosteric modulator of the prostaglandin E2 receptor EP2*, in *School of Pharmacy*. 2024, University of Nottingham: Internal. p. 67.
342. Komarova, A.O., G.R. Dick, and J.S. Luterbacher, *Diformylxylose as a new polar aprotic solvent produced from renewable biomass*. *Green Chem.*, 2021. **23**(13): p. 4790-4799.
343. Donello, J.E., *Substituted 6,7-dialkoxy-3-isoquinolinol derivatives as inhibitors of phosphodiestrease 10 (PDE10A)*, in *Patent cooperation treaty*, W.I.P. Organisation, Editor. 2012. p. 128.
344. Kulkarni, P.P., et al., *Demethylation of Methyl Aryl Ethers using Pyridine Hydrochloride in Solvent-free Conditions under Microwave Irradiation*. *J. Chem. Res. Synop.*, 1999(6): p. 394-395.
345. Bandgar, B.P. and S.P. Kasture, *Protection of phenols as t-butyl ethers under mild conditions†‡*. *J. Chem. Res.*, 2000. **2000**(5): p. 252-253.
346. Yu, D.D., et al., *Identification of novel inverse agonists of estrogen-related receptors ERRγ and ERRβ*. *Bioorg. Med. Chem.*, 2017. **25**(5): p. 1585-1599.
347. Quesneau, V., et al., *Reinvestigation of the synthesis of "covalent-assembly" type probes for fluoride ion detection. Identification of novel 7-(diethylamino)coumarins with aggregation-induced emission properties*. *Tettrahedron Lett.*, 2019. **60**(48): p. 151279.
348. Polat, M.F., *Synthesis of Asebogenin and Balsacone A Precursor by a Novel Synthetic Strategy: Recent Opportunities for and Challenges of Total Synthesis of Balsacone A*. *Molecules*, 2022. **27**(11): p. 3523.
349. Ishizaki, M., et al., *Palladium charcoal-catalyzed deprotection of O-allylphenols*. *Tetrahedron*, 2004. **60**(36): p. 7973-7981.
350. Vutukuri, D.R., et al., *A mild deprotection strategy for allyl-protecting groups and its implications in sequence specific dendrimer synthesis*. *J. Org. Chem.*, 2003. **68**(3): p. 1146-9.

351. Bailey, W.F., et al., *Facile O-deallylation of allyl ethers via S(N)2' reaction with tert-butyllithium. Org. Lett.*, 2000. **2**(4): p. 489-91.
352. Effenberger, F. and J. Jäger, *Synthesis of the Adrenergic Bronchodilators (R)-Terbutaline and (R)-Salbutamol from (R)-Cyanohydrins1. J. Org. Chem.*, 1997. **62**(12): p. 3867-3873.
353. Atienza, B.J.P., N. Truong, and F.J. Williams, *Reliably Regioselective Dialkyl Ether Cleavage with Mixed Boron Trihalides. Org. Lett.*, 2018. **20**(20): p. 6332-6335.
354. Dakin, H.D., *The oxidation of hydroxy derivatives of benzaldehyde, acetophenone, and related substances. J. Am. Chem. Soc.*, 1909. **42**(6): p. 477-498.
355. Corma, A., et al., *One-pot synthesis of phenols from aromatic aldehydes by Baeyer–Villiger oxidation with H2O2 using water-tolerant Lewis acids in molecular sieves. J. Catal.*, 2004. **221**(1): p. 67-76.
356. Weaver, M.G. and T.R.R. Pettus, *7.15 Synthesis of para- and ortho-Quinones*, in *Comprehensive Organic Synthesis (Second Edition)*, P. Knochel, Editor. 2014, Elsevier: Amsterdam. p. 373-410.
357. Chen, S. and F.W. Foss, Jr., *Aerobic Organocatalytic Oxidation of Aryl Aldehydes: Flavin Catalyst Turnover by Hantzsch's Ester. Org. Lett.*, 2012. **14**(19): p. 5150-5153.
358. Lin, H. and D. Sun, *Recent synthetic developments and applications of the ullmann reaction. A review. Org. Prep. Proced. Int.*, 2013. **45**(5).
359. Mann, G., et al., *Palladium-Catalyzed C−O Coupling Involving Unactivated Aryl Halides. Sterically Induced Reductive Elimination To Form the C−O Bond in Diaryl Ethers. J. AM. Chem. Soc.*, 1999. **121**(13): p. 3224-3225.
360. Ma, D. and Q. Cai, *N,N-Dimethyl Glycine-Promoted Ullmann Coupling Reaction of Phenols and Aryl Halides. Org. Lett.*, 2003. **5**(21): p. 3799-3802.
361. Li, G., S. Ma, and M. Szostak, *Amide Bond Activation: The Power of Resonance. Trends Chem.*, 2020. **2**(10): p. 914-928.
362. Cameron, K.O., et al., *Discovery of CP-533536: an EP2 receptor selective prostaglandin E2 (PGE2) agonist that induces local bone formation. Bioorg. Med. Chem. Lett.*, 2009. **19**(7): p. 2075-8.
363. Wyllie, D.J. and P.E. Chen, *Taking the time to study competitive antagonism. Br. J. Pharmacol.*, 2007. **150**(5): p. 541-51.
364. Schild, H.O., *pAx and competitive drug antagonism. Br. J. Pharmacol. Chemother.*, 1949. **4**(3): p. 277-80.
365. Lazareno, S. and N.J. Birdsall, *Estimation of competitive antagonist affinity from functional inhibition curves using the Gaddum, Schild and Cheng-Prusoff equations. Br. J. Pharmacol.*, 1993. **109**(4): p. 1110-9.
366. Gaddum, J.H., *Theories of drug antagonism. Pharmacol. Rev.*, 1957. **9**(2): p. 211-8.
367. Johnson, D.K. and J. Karanicolas, *Druggable protein interaction sites are more predisposed to surface pocket formation than the rest of the protein surface. PLOS Comput. Biol.*, 2013. **9**(3): p. e1002951.
368. Zheng, X., et al., *Pocket-based drug design: exploring pocket space. AAPS J.*, 2013. **15**(1): p. 228-41.

369. Bosma, R., et al., *Probe dependency in the determination of ligand binding kinetics at a prototypical G protein-coupled receptor. Sci. Rep.*, 2019. **9**(1): p. 7906.
370. Conner, A.C., et al., *The use of site-directed mutagenesis to study GPCRs. Methods Mol. Biol.*, 2011. **746**: p. 85-98.
371. Di, L. and E.H. Kerns, *Biological assay challenges from compound solubility: strategies for bioassay optimization. Drug Discov. Today*, 2006. **11**(9): p. 446-451.
372. Sou, T. and C.A.S. Bergström, *Automated assays for thermodynamic (equilibrium) solubility determination. Drug Discov. Today Technol.*, 2018. **27**: p. 11-19.
373. Bharate, S.S. and R.A. Vishwakarma, *Thermodynamic equilibrium solubility measurements in simulated fluids by 96-well plate method in early drug discovery. Bioorg. Med. Chem. Lett.*, 2015. **25**(7): p. 1561-7.
374. Munson, P.J. and D. Rodbard, *An exact correction to the "Cheng-Prusoff" correction. J. Recept. Res.*, 1988. **8**(1-4): p. 533-46.
375. Kenakin, T., *Analytical pharmacology and allosterism: the importance of quantifying drug parameters in drug discovery. Drug Discov. Today: Technol.*, 2013. **10**(2): p. e229-e235.
376. Kenakin, T., *Allosteric theory: taking therapeutic advantage of the malleable nature of GPCRs. Curr. Neuropharmacol.*, 2007. **5**(3): p. 149-56.
377. Gentry, P.R., P.M. Sexton, and A. Christopoulos, *Novel Allosteric Modulators of G Protein-coupled Receptors. J. Biol. Chem.*, 2015. **290**(32): p. 19478-88.
378. Jakubik, J. and E.E. El-Fakahany, *Current Advances in Allosteric Modulation of Muscarinic Receptors. Biomolecules*, 2020. **10**(2).
379. Ghanouni, P., et al., *Functionally Different Agonists Induce Distinct Conformations in the G Protein Coupling Domain of the β2Adrenergic Receptor*. J. Biol. Chem.*, 2001. **276**(27): p. 24433-24436.
380. Sum, C.S., et al., *Pharmacological characterization of GPCR agonists, antagonists, allosteric modulators and biased ligands from HTS hits to lead optimization*, S. Markossian, A. Grossman, and H. Baskir, Editors. 2019: U.S. National Library of Medicine. p. 27.
381. Munk, C., et al., *Integrating structural and mutagenesis data to elucidate GPCR ligand binding. Curr. Opin. Pharmacol.*, 2016. **30**: p. 51-58.
382. Olsen, R.H.J., et al., *TRUPATH, an open-source biosensor platform for interrogating the GPCR transducerome. Nat. Chem. Biol.*, 2020. **16**(8): p. 841-849.
383. DiBerto, J.F., et al., *Agonist and antagonist TRUPATH assays for G protein-coupled receptors. STAR Protoc.*, 2022. **3**(2): p. 101259.
384. Kim, N., S. Shin, and S.W. Bae, *cAMP Biosensors Based on Genetically Encoded Fluorescent/Luminescent Proteins. Biosensors (Basel)*, 2021. **11**(2).
385. Sugimoto, Y. and S. Narumiya, *Prostaglandin E Receptors. J. Biol. Chem.*, 2007. **282**(16): p. 11613-11617.
386. Dore, S. and A.S. Ahmad, *Cryoprotective role of prostaglandin D2 DP1 receptor against neuronal injury following acute excitotoxicity and cerebral ischemia*, in

Brain neurotrauma: molecular, neuropsychological, and rehabilitation aspects, F.H. Kobeissy, Editor. 2015, CRC Press/ Taylor & Francis.
387. Wang, J.J., et al., *Molecular recognition and activation of the prostacyclin receptor by anti-pulmonary arterial hypertension drugs. Sci. Adv.*, 2024. **10**(6): p. eadk5184.
388. Meher, M., S. Pradhan, and S.R. Pradhan, *Risk Factors Associated With Hypertension in Young Adults: A Systematic Review. Cureus*, 2023. **15**(4): p. e37467.
389. Zou, F., et al., *DP1 (Prostaglandin D2 Receptor 1) Activation Protects Against Vascular Remodeling and Vascular Smooth Muscle Cell Transition to Myofibroblasts in Angiotensin II–Induced Hypertension in Mice. Hypertension*, 2022. **79**(6): p. 1203-1215.
390. Ahmad, A.S., et al., *Role of the L-PGDS-PGD2-DP1 receptor axis in sleep regulation and neurologic outcomes. Sleep*, 2019. **42**(6).
391. Garrido, A., et al., *hERG toxicity assessment: Useful guidelines for drug design. Eur. J. Med. Chem.*, 2020. **195**: p. 112290.
392. Lynch, J.J., 3rd, et al., *Potential functional and pathological side effects related to off-target pharmacological activity. J. Pharmacol. Toxicol. Methods*, 2017. **87**: p. 108-126.
393. Blundell, T.L. and S. Patel, *High-throughput X-ray crystallography for drug discovery. Curr. Opin. Pharmacol.*, 2004. **4**(5): p. 490-496.
394. Aitipamula, S. and V.R. Vangala, *X-Ray Crystallography and its Role in Understanding the Physicochemical Properties of Pharmaceutical Cocrystals. J. Indian. Inst. Sci.*, 2017. **97**(2): p. 227-243.
395. Li, L., et al., *An Updated Review on Developing Small Molecule Kinase Inhibitors Using Computer-Aided Drug Design Approaches. Int. J. Mol. Sci.*, 2023. **24**(18).
396. Smyth, M.S. and J.H. Martin, *x ray crystallography. Mol. Pathol.*, 2000. **53**(1): p. 8-14.
397. García-Nafría, J. and C.G. Tate, *Structure determination of GPCRs: cryo-EM compared with X-ray crystallography. Biochem. Soc. Trans.*, 2021. **49**(5): p. 2345-2355.
398. Tate, C.G., *Practical considerations of membrane protein instability during purification and crystallisation. Methods Mol. Biol.*, 2010. **601**: p. 187-203.
399. Heo, L. and M. Feig, *Multi-state modeling of G-protein coupled receptors at experimental accuracy. Proteins*, 2022. **90**(11): p. 1873-1885.
400. Kühlbrandt, W., *The Resolution Revolution. Science*, 2014. **343**(6178): p. 1443-1444.
401. Milne, J.L., et al., *Cryo-electron microscopy--a primer for the non-microscopist. Febs. J.*, 2013. **280**(1): p. 28-45.
402. Vyas, V.K., et al., *Homology modeling a fast tool for drug discovery: current perspectives. Indian J. Pharm. Sci.*, 2012. **74**(1): p. 1-17.
403. Werner, T., et al., *Structural modelling and dynamics of proteins for insights into drug interactions. Adv. Drug. Deliv. Rev.*, 2012. **64**(4): p. 323-343.
404. Chothia, C. and A.M. Lesk, *The relation between the divergence of sequence and structure in proteins. Embo. J.*, 1986. **5**(4): p. 823-6.

405. Mirny, L.A. and E.I. Shakhnovich, *Protein structure prediction by threading. why it works and why it does not11Edited by F. Cohen. J. Mol. Biol.*, 1998. **283**(2): p. 507-526.
406. Pan, X. and T. Kortemme, *Recent advances in de novo protein design: Principles, methods, and applications. J. Biol. Chem.*, 2021. **296**: p. 100558.
407. Varadi, M., et al., *AlphaFold Protein Structure Database: massively expanding the structural coverage of protein-sequence space with high-accuracy models. Nucleic Acids Res.*, 2022. **50**(D1): p. D439-d444.
408. Jumper, J., et al., *Highly accurate protein structure prediction with AlphaFold. Nature*, 2021. **596**(7873): p. 583-589.
409. Moult, J., et al., *A large-scale experiment to assess protein structure prediction methods. Proteins*, 1995. **23**(3): p. ii-v.
410. Kryshtafovych, A., et al., *Critical assessment of methods of protein structure prediction (CASP)-Round XIII. Proteins*, 2019. **87**(12): p. 1011-1020.
411. Rose, P.W., et al., *The RCSB protein data bank: integrative view of protein, gene and 3D structural information. Nucleic Acids Res.*, 2017. **45**(D1): p. D271-d281.
412. Altschul, S.F., et al., *Basic local alignment search tool. J. Mol. Biol.*, 1990. **215**(3): p. 403-410.
413. Muhammed, M.T. and E. Aki-Yalcin, *Homology modeling in drug discovery: Overview, current applications, and future perspectives. Chem. Biol. Drug Des.*, 2019. **93**(1): p. 12-20.
414. Fernandez-Fuentes, N., et al., *Comparative protein structure modeling by combining multiple templates and optimizing sequence-to-structure alignments. Bioinformatics*, 2007. **23**(19): p. 2558-65.
415. Davis, I.W., et al., *MolProbity: all-atom contacts and structure validation for proteins and nucleic acids. Nucleic Acids Res.*, 2007. **35**(Web Server issue): p. W375-83.
416. Laskowski, R.A., et al., *PROCHECK: a program to check the stereochemical quality of protein structures. J. Appl. Crystallogr.*, 1993. **26**(2): p. 283-291.
417. Hooft, R.W., et al., *Errors in protein structures. Nature*, 1996. **381**(6580): p. 272.
418. Toyoda, Y., et al., *Ligand binding to human prostaglandin E receptor EP4 at the lipid-bilayer interface. Nat. Chem. Biol.*, 2019. **15**(1): p. 18-26.
419. Pettersen, E.F., et al., *UCSF Chimera--a visualization system for exploratory research and analysis. J. Comput. Chem.*, 2004. **25**(13): p. 1605-12.
420. Costanzi, S., *Homology modeling of class a G protein-coupled receptors. Methods Mol. Biol.*, 2012. **857**: p. 259-79.
421. *Schrodinger Release 2024-3*. 2024, Maestro, Schrodinger, LLC, New York, NY.
422. Sastry, G.M., et al., *Protein and ligand preparation: parameters, protocols, and influence on virtual screening enrichments. J. Comput. Aided Mol. Des.*, 2013. **27**(3): p. 221-34.
423. Halgren, T.A., *Identifying and Characterizing Binding Sites and Assessing Druggability. J. Chem. Inf. Model.*, 2009. **49**(2): p. 377-389.
424. Halgren, T., *New method for fast and accurate binding-site identification and analysis. Chem. Biol. Drug Des.*, 2007. **69**(2): p. 146-8.

425. Miller, E.B., et al., *Reliable and Accurate Solution to the Induced Fit Docking Problem for Protein–Ligand Binding. J. Chem. Theory Comput.*, 2021. **17**(4): p. 2630-2639.
426. Xu, T., et al., *Induced-Fit Docking Enables Accurate Free Energy Perturbation Calculations in Homology Models. J. Chem. Theory Comput.*, 2022. **18**(9): p. 5710-5724.
427. Coskun, D., et al., *Using AlphaFold and Experimental Structures for the Prediction of the Structure and Binding Affinities of GPCR Complexes via Induced Fit Docking and Free Energy Perturbation. J. Chem. Theory Comput.*, 2024. **20**(1): p. 477-489.
428. Madan, R., et al., *Principles and aspects of molecular docking: A bird's eye view. H.S.S.*, 2020.
429. Brylinski, M., *Nonlinear scoring functions for similarity-based ligand docking and binding affinity prediction.* J. Chem. Inf. Model, 2013. **53**(11): p. 3097-112.
430. Isberg, V., et al., *Generic GPCR residue numbers - aligning topology maps while minding the gaps. Trends Pharmacol. Sci.*, 2015. **36**(1): p. 22-31.
431. van der Kant, R. and G. Vriend, *Alpha-bulges in G protein-coupled receptors. Int. J. Mol. Sci.*, 2014. **15**(5): p. 7841-64.
432. Rominger, D.H., et al., *Biased ligands: pathway validation for novel GPCR therapeutics. Curr. Opin. Pharmacol.*, 2014. **16**: p. 108-115.
433. Borchardt, A.J., et al., *Heterocyclic inhibitors of histamine receptors for the treatment of disease*, W.I.P. Organization, Editor. 2011.
434. Landquist, J.K., *567. Quinoxaline N-oxides. Part I. The oxidation of quinoxaline and its Bz-substituted derivatives. J. Chem. Soc.*, 1953(0): p. 2816-2821.
435. Farmer, J.P., et al., *An industrial perspective on ligand bias in GPCR drug discovery. Neuropharmacology*, 2026. **284**: p. 110782.
436. Violin, J.D., et al., *Selectively engaging β-arrestins at the angiotensin II type 1 receptor reduces blood pressure and increases cardiac performance. J. Pharmacol. Exp. Ther.*, 2010. **335**(3): p. 572-9.
437. Pang, P.S., et al., *Biased ligand of the angiotensin II type 1 receptor in patients with acute heart failure: a randomized, double-blind, placebo-controlled, phase IIB, dose ranging trial (BLAST-AHF). Eur. Heart J.*, 2017. **38**(30): p. 2364-2373.
438. Piña, M., et al., *Tetrel bonds involving CF3 group participate in protein-drug recognition: A combined crystallographic and computational study. Phys. Chem. Chem. Phys.*, 2023.
439. Bauzá, A., A. Frontera, and T.J. Mooibroek, *π-Hole Interactions Involving Nitro Aromatic Ligands in Protein Structures. Chemistry*, 2019. **25**(58): p. 13436-13443.
440. Jeffries, B., et al., *Lipophilicity trends upon fluorination of isopropyl, cyclopropyl and 3-oxetanyl groups. Beilstein J. Org. Chem.*, 2020. **16**: p. 2141-2150.
441. Bunally, S.B., C.N. Luscombe, and R.J. Young, *Using Physicochemical Measurements to Influence Better Compound Design. SLAS Discov.*, 2019. **24**(8): p. 791-801.
442. Maric, J., et al., *Prostaglandin E(2) suppresses human group 2 innate lymphoid cell function. J. Allergy Clin. Immunol.*, 2018. **141**(5): p. 1761-1773.e6.

443. Maseda, D., et al., *mPGES1-Dependent Prostaglandin E(2) (PGE(2)) Controls Antigen-Specific Th17 and Th1 Responses by Regulating T Autocrine and Paracrine PGE(2) Production. J. Immunol.*, 2018. **200**(2): p. 725-736.
444. Cuenca-Escalona, J., et al., *EP2/EP4 targeting prevents tumor-derived PGE2-mediated immunosuppression in cDC2s. J. Leukoc. Biol.*, 2024. **116**(6): p. 1554-1567.
445. Bortnichuk, L., A. Pashchenko, and Y. Kheilik, *Microsomal stability assay for human and mouse liver microsomes - drug metabolism v1*. 2024.
446. Carione, P., *Cytochrome P450-Mediated Metabolic Stability Assay in Liver Microsomes*, in *Cytochrome P450: In Vitro Methods and Protocols*, Z. Yan and G.W. Caldwell, Editors. 2021, Springer US: New York, NY. p. 229-242.
447. Leung, C., et al., *An Integrated Hepatocyte Stability Assay for Simultaneous Metabolic Stability Assessment and Metabolite Profiling. Drug Metab. Dispos.*, 2024. **52**(5): p. 377-389.
448. *Schrödinger Release 2025-3: LigPrep, Schrödinger, LLC, New York, NY, 2025*.
449. *The PyMOL Molecular Graphics System, Version 3.0 Schrödinger, LLC, 2025*.